

**SOLAR HYDROGEN GENERATION THROUGH OVERALL WATER SPLITTING ON
GALLIUM-ZINC OXYNITRIDE VISIBLE-LIGHT ACTIVATED PHOTOCATALYST**

by

Babak Adeli Koudehi

B.Sc., Iran University of Science and Technology, Iran, 2007

M.Sc., Sharif University of Technology, Iran, 2009

A THESIS SUBMITTED IN PARTIAL FULFILLMENT OF
THE REQUIREMENTS FOR THE DEGREE OF

DOCTOR OF PHILOSOPHY

in

THE FACULTY OF GRADUATE AND POSTDOCTORAL STUDIES

(Chemical and Biological Engineering)

THE UNIVERSITY OF BRITISH COLUMBIA

(Vancouver)

January 2017

© Babak Adeli Koudehi, 2017

Abstract

In this study, novel approaches for the development of solar-responsive photocatalysts for water splitting are investigated, with a focus on the gallium-zinc oxynitride solid solution (GaN:ZnO).

A facile synthesis technique was developed for the fabrication of nanoporous GaN:ZnO photocatalyst. The synthesis time was reduced substantially to 12 min (from original 10+ h) as the result of effective solid–solid and gas–solid reactant interactions at the nanoscale. The synthesized photocatalyst samples were characterized for their optical, structural, and photochemical properties. Despite the short synthesis time, the prepared nanoporous GaN:ZnO photocatalyst maintained the overall visible-light water splitting activities at reasonable rates, reaching to the maximum apparent quantum efficiency of 2.71% at 420–440 nm.

Decoration of the photocatalyst surface with the optimal amount of various hydrogen and oxygen evolution co-catalyst materials through photo-deposition and impregnation was investigated. Our experimental and characterization data suggest a mechanism for minimizing the effect of the undesired charge recombination and reverse reaction through the utilization of structural nanopores as the active water splitting regions.

To reduce the recombination of photo-excited charges, the hybridization of GaN:ZnO photocatalyst on highly conductive graphene support was studied. Effective electrochemical interaction between composite components was confirmed through material characterization, photo-induced conversion of graphene oxide to reduced graphene oxide (rGO), and visual observation of co-catalyst nanoparticles on the surface of the conductive nanosheets. The

GaN:ZnO-rGO composite photocatalyst exhibited ~70% improvement in photocatalytic hydrogen evolution.

Finally, a number of approaches for the synthesis of one-dimensional (1-D) GaN:ZnO photocatalysts were studied. A novel direct fabrication route for 1-D GaN:ZnO through gold-catalyzed atmospheric pressure chemical vapour deposition was proposed. The material characterization data indicated that the proposed method is capable of preparing 1-D GaN:ZnO nanostructures with a wide range of morphologies, including nanofibers and nanowires, via vapour–liquid–solid epitaxy. In addition, via the proposed method, the dimensions of the obtained nanomaterials can be tailored. The synthesized GaN:ZnO nanowires demonstrated promising sacrificial hydrogen evolution compared to the powder and nanofiber photocatalysts.

The work presented in this research provides an in-depth understanding of the nanoscale fabrication and optimization of GaN:ZnO photocatalysts for visible-light hydrogen generation.

Preface

All the presented data in this thesis were obtained by the author, under supervision of Prof. Fariborz Taghipour at the University of British Columbia (UBC). Several equipment and apparatuses were used for fabrication, characterization, and performance evaluation of gallium-zinc oxynitride solid solution (GaN:ZnO) photocatalyst, its surface modified, hybridized, and thin film materials. Most of the experiments were conducted in the Photo-Reaction Engineering Laboratory in the Department of Chemical and Biological Engineering at UBC. Several tests and analysis, particularly material fabrication and characterizations, were performed at:

- Clean Energy Research Center (CERC), UBC
- Chemistry Department, UBC
- Advanced Materials and Process Engineering Laboratory (AMPEL), UBC
- Material Engineering Department, UBC
- Centre for High-Throughput Phenogenomics, UBC
- Bioimaging Facility, UBC
- 4D LABS, Simon Fraser University (SFU)

Throughout the entire research, Prof. Taghipour has largely contributed to the development of research objectives and experimental plans, as well as evaluation of the obtained data.

Materials provided in Chapters 1–5 were presented in:

- Adeli, B. (2016) Towards Solar Hydrogen. UBC Multidisciplinary Undergraduate Research Conference, Vancouver, BC.

- Adeli, B. and Taghipour, F. (2015) Nanoporous Gallium Zinc Oxynitride Photocatalyst for Overall Water Splitting. PacifiChem 2015: The International Chemical Congress of Pacific Basin Societies, Honolulu, HI.
- Adeli, B. and Taghipour, F. (2015) Toward Solar Hydrogen Generation: GaN:ZnO Solid Solution-Reduced Graphene Oxide Nanocomposite. EEST 2015: International Conference on Electrochemical Energy Science and Technology, Vancouver, BC.
- Adeli, B. and Taghipour, F. (2015) GaN:ZnO-Graphene Composite for Overall Water Splitting. 27th International Conference on Photochemistry, Jeju, Korea.
- Adeli, B. and Taghipour, F. (2014) Nanoporous Gallium Zinc Oxynitride Photocatalyst for Visible Light Hydrogen Generation. NanoGe 2014: International Conference on New Advances in Materials Research for Solar Fuels Production, Montreal, QC.
- Adeli, B. and Taghipour, F. (2013) Toward Solar Hydrogen Generation: Developing Visible Light Active Photocatalyst for Overall Water Splitting. HFC 2013: International Conference on Hydrogen and Fuel Cell, Vancouver, BC.

Materials presented in Chapters 1, 2, 3, 5, and 6 are summarized in four publications written by the author of this thesis with inputs and guidance from Prof. Taghipour:

[1] B. Adeli, and F. Taghipour, “Synthesis of Gallium-Zinc Oxynitride Nanowires through Atmospheric Pressure Chemical Vapor Deposition”, *under review for publication*.

[2] B. Adeli, and F. Taghipour, “Morphology Engineering of Graphene Hybridized Gallium-Zinc Oxynitride Photocatalyst”, *under review for publication*.

[3] B. Adeli, and F. Taghipour, “Facile Synthesis of Highly Efficient Nano-structured Gallium Zinc Oxynitride Solid Solution Photocatalyst for Visible-light Overall Water Splitting”, *Applied Catalysis A: General*, 521, 250–258 (2016). DOI: 10.1016/j.apcata.2016.01.001

[4] B. Adeli, and F. Taghipour, “Reduced Graphene Oxide Composite of Gallium Zinc Oxynitride Photocatalyst with Improved Activity for Overall Water Splitting”, *Chemical Engineering & Technology*, 39 (1) 142–148 (2016). DOI: 10.1002/ceat.201500239 - *featured as back-cover*.

[5] B. Adeli, and F. Taghipour, “A Review of Synthesis Techniques for Gallium-Zinc Oxynitride Solar-Activated Photocatalyst for Water Splitting”, *ECS Journal of Solid-state Science and Technology*, 2, Q118–Q126 (2013). DOI: 10.1149/2.022307jss

In addition, two manuscripts were prepared from the materials presented in Chapters 4 and 6, and will be submitted for publication in peer-reviewed journals.

Table of Contents

Abstract.....	ii
Preface.....	iv
Table of Contents	vii
List of Tables	xiii
List of Figures.....	xv
List of Symbols	xxv
List of Abbreviations	xxvii
Acknowledgements	xxxii
Dedication	xxxii
Chapter 1: Introduction	1
1.1 Principles of photocatalytic overall water splitting	2
1.2 Knowledge gap	11
1.3 Research objectives.....	13
1.4 Thesis outline	14
1.5 Problem statement.....	15
1.5.1 Solid-state synthesis of GaN:ZnO solid solution photocatalyst	15
1.5.2 Utilization of HER and OER catalysts.....	20
1.5.3 Utilization of conductive support.....	22
1.5.4 One-dimensional nanostructures of GaN:ZnO	27
Chapter 2: Approaches and Methods	31
2.1 Materials	31

2.2	Preparation of nanoporous GaN:ZnO solid solution photocatalyst	32
2.2.1	Precursors.....	32
2.2.1.1	Mixed precursor (physical approach)	32
2.2.1.2	Layered double hydroxide precursor (chemical approach)	32
2.2.2	Nanoporous GaN:ZnO solid solution	33
2.3	Traditional GaN:ZnO solid solution	33
2.4	Co-catalysts nanoparticles deposition.....	33
2.4.1	Co-catalysts impregnation	34
2.4.2	Co-catalysts photo-deposition.....	34
2.5	Preparation of GaN:ZnO hybridized reduced graphene oxide (GaN:ZnO-rGO)	34
2.5.1	Graphene oxide (GO).....	34
2.5.2	GO/rGO-GaN:ZnO composite.....	35
2.6	Fabrication of GaN:ZnO thin film	35
2.6.1	Chemical-bath growth of nanowires (NWs).....	35
2.6.1.1	ZnO seeding.....	35
2.6.1.2	ZnO nanowires (NWs).....	36
2.6.1.3	Impregnation of ZnO NWs with Ga ³⁺	36
2.6.2	Chemical vapor deposition of GaN:ZnO solid solution	37
2.6.2.1	Au-catalyst coating	37
2.6.2.2	GaN:ZnO thin-film growth via atmospheric pressure chemical vapor deposition (APCVD)	37
2.6.2.3	Photo-deposition of Rh co-catalyst on the thin film samples	38
2.7	Material characterizations.....	38

2.7.1	Scanning electron microscopy (SEM) and energy-dispersive X-ray (EDX) spectroscopy.....	38
2.7.2	X-ray diffraction (XRD) analysis	40
2.7.3	Surface area.....	41
2.7.4	X-ray photoelectron spectroscopy (XPS)	41
2.7.5	Transmission electron microscopy (TEM) and scanning transmission electron microscopy (STEM).....	42
2.7.6	UV-visible spectroscopy.....	43
2.7.7	Photoluminescence (PL) analysis	44
2.8	Water-splitting reaction	45
2.8.1	Center-irradiated photo-reactor.....	45
2.8.2	Pyrex side-irradiated photo-reactor.....	45
2.8.3	Top-irradiated photo-reactor.....	46
2.9	Photocatalytic performance evaluation.....	46
2.9.1	Quantum efficiency.....	46
2.9.2	Powder samples	47
2.9.2.1	Independent analysis.....	47
2.9.2.2	Comparative studies.....	47
2.9.3	Immobilized photocatalysts panel.....	48
Chapter 3: Facile Synthesis of Gallium-Zinc Oxynitride Solid Solution.....		50
3.1	Effective interaction between solid and gaseous reactants using urea nitrogen source	51
3.2	Preparation of Ga and Zn mixed-metal precursor.....	52
3.3	Synthesis mechanism	54

3.4	Heat source of solid-state synthesis	56
3.5	Surface and bulk structure	62
3.6	Optical characterization	68
3.7	Photocatalytic performance	70
3.8	Durability analysis	75
3.8.1	Deactivation mechanism.....	83
Chapter 4: Utilization of Hydrogen and Oxygen Evolution Co-catalysts		85
4.1	Co-catalysts deposition method	87
4.2	Optimal loading of co-catalyst active sites	91
4.3	Undesired reverse reaction catalyzed by HER active sites	99
Chapter 5: GaN:ZnO-Reduced Graphene Oxide (rGO) Composite		103
5.1	Formation of functional GaN:ZnO-rGO composite	105
5.2	Structure of the prepared GaN:ZnO-rGO composite.....	110
5.3	Photo-deposition of co-catalyst active sites	116
5.4	Life-time of the photo-excited charges	120
5.5	Photocatalytic performance	121
Chapter 6: One-Dimensional Gallium Zinc Oxynitride Solid Solution.....		126
6.1	Charge separation and recombination in 1-D nanostructures	126
6.2	Approaches to fabricate GaN:ZnO thin film	130
6.3	Impregnation of ZnO NWs with Ga ³⁺	133
6.4	Direct growth of Ga-Zn 1-D nanostructures.....	135
6.5	CVD growth of GaN:ZnO 1-D nanostructures	137
6.5.1	Non-epitaxial CVD growth of GaN:ZnO 1-D nanostructures.....	141

6.5.2	Epitaxial CVD growth of GaN:ZnO 1-D nanostructures	144
6.5.3	Controlling the morphology of the thin film.....	158
6.6	Photocatalytic performance	169
Chapter 7: Conclusions and Recommendations		173
7.1	Conclusions.....	173
7.1.1	Development of a facile synthesis method for GaN:ZnO photocatalyst	173
7.1.2	Utilization of hydrogen and oxygen evolution active sites.....	176
7.1.3	GaN:ZnO photocatalysts hybridized with reduced graphene oxide	178
7.1.4	Fabrication of GaN:ZnO 1-D nanostructure	179
7.1.4.1	Nitridation of Ga ³⁺ decorated ZnO nanowires.....	180
7.1.4.2	Direct solution-base growth of Ga-Zn nanowires.....	180
7.1.4.3	Atmospheric pressure chemical vapor deposition (APCVD) via vapor-liquid- solid epitaxy (VLSE) mechanism	180
7.2	Recommendations.....	183
7.2.1	Apparatuses.....	183
7.2.2	Fabrication	184
7.2.2.1	Nanoporous GaN:ZnO solid solution	184
7.2.2.2	Surface modification with co-catalyst materials.....	186
7.2.2.3	Hybridization with graphene oxide.....	188
7.2.2.4	Fabrication of 1-D GaN:ZnO.....	189
7.2.3	Photocatalytic performances	191
Bibliography		193
Appendices.....		214

Appendix A: Photo-reactor apparatuses	214
A.1 Center-irradiated photo-reactor.....	214
A.2 Pyrex side irradiated photo-reactor.....	216
A.3 Top irradiated photo-reactor	217
Appendix B: Microwave-assisted synthesis	218
B.1 Method	218
B.2 Photocatalytic performance	218
Appendix C: Surface and bulk elemental composition of nanoporous GaN:ZnO samples....	219
C.1 XPS spectra.....	219
C.2 EDX spectra.....	222
Appendix D: Cost analysis and scalability	225
Appendix E: Morphology of the ZnO NWs impregnated with Ga ³⁺ using concentrated Ga salt solution.....	228
Appendix F: Morphology of the samples obtained through experiments described in Table 6.2: Direct growth of Zn-Ga NWs	229
Appendix G: Substrates orientation for epitaxial APCVD growth of 1-D nanostructures.....	231
Appendix H: Formation of catalysts liquid droplets at different temperatures	232

List of Tables

Table 1.1: Crystal lattice constants (a , b , and c) of wurtzite GaN and ZnO [53,54].	10
Table 3.1: Effect of synthesis temperature and time on the photocatalytic activity of the GaN:ZnO-LDHs. The model precursor is Ga-Zn LDHs with $x = 0.20$. N: not active, L: low activity, M: medium activity, and H: high activity. The obtained photocatalytic data were normalized to 1.00 and categorized as follows: No OWS activities were observed: N, 0.00–0.20: L, 0.20–0.60: M, and 0.60–1.00: H.	57
Table 3.2: Crystallographic features estimated from the diffraction patterns in Figure 3.3 and equation (9) and (10).	60
Table 3.3: Compositional data of the LDHs precursors and GaZnON-LDHs photocatalysts prepared in 12 min at 900 °C. $x = [\text{Zn}]/[\text{Zn}+\text{Ga}]$	64
Table 3.4: Lattice parameters of the fresh and used photocatalysts estimated from the XRD pattern in Figure 3.14, using the equation (9) and (10).	78
Table 4.1: Impacts of OER and HER catalysts co-loading, and the OER catalyst deposition method on the OWS performances of the nanoporous GaN:ZnO photocatalyst. The OWS data of the bare and surface modified photocatalyst were obtained using the same GaZnON-LDHs 3 photocatalyst samples, which were decorated with HER and OER co-catalyst materials at various loadings. Details of the sample preparation for comparative studies are described in Chapter 2.	98
Table 6.1: Summary of the 1-D GaZnON fabrication routes proposed in the literature and the techniques developed in this research (shaded area).	132
Table 6.2: Summary of the experiments, as well as the morphology of the materials on the substrate and inside the processing solution for direct growth of Ga-Zn NWs through the	

chemical bath technique. Stoichiometric amount of $\text{Ga}(\text{NO}_3)_3 \cdot x\text{H}_2\text{O}$ and HMT were used as the source of gallium and selective capping reagent, respectively. SEM images of the samples are presented in Appendix F. 136

Table 6.3: Conditions and study range of the parameters (shaded area) for the APCVD growth of the 1-D GaN:ZnO solid solution. 141

Table 6.4: Elemental composition of the NWs synthesized at $T_s = 1000 \text{ }^\circ\text{C}$ for 30 min ($D = 8 \text{ cm}$). 151

Table 6.5: Composition of NFs synthesized at $1100 \text{ }^\circ\text{C}$ for 5 min at $D = 0$ 166

Table C.1: Surface composition of prepared photocatalysts obtained by XPS. 221

Table C.2: Summary of the EDX bulk elemental analysis. 224

Table D.3: Amount of materials and their cost per batch of the nanoporous GaN:ZnO solid solution synthesis. 225

Table D.4: Amount of materials and their cost per batch of the traditional GaN:ZnO solid solution synthesis. 226

Table D.5: Cost of electricity for preparation of one batch of nanoporous and traditional solid solution photocatalysts. 226

Table D.6: Total cost of synthesis of per gram of photocatalyst through urea-assisted technique proposed in this research and traditional solid-state reaction. 226

List of Figures

Figure 1.1: Band gap energy (E_g), valence band (VB) and conduction band (CB) potentials of a semiconductor. Processes (photo-excitation, charge transportation, and charge recombination) occur once a light photon with energy greater than E_g strikes the surface of a semiconductor are depicted. Redox reactions at the CB energy state are listed for solar fuel generation reactions (water splitting and CO_2 conversion).....	5
Figure 1.2: Energy band structure of some semiconductors and their limitation for visible-light overall water splitting application [6].....	8
Figure 1.3: Wurtzite crystalline structure of GaN [52].....	9
Figure 1.4: Band gap reduction in GaN:ZnO solution.....	11
Figure 1.5: Possible solid-state routes using Ga_2O_3 and ZnO as the starting materials.....	16
Figure 1.6: Ion-exchange preparation of mesoporous ZnGa_2O_4 [56,74]..... Error! Bookmark not defined.	
Figure 1.7: Metal- Cr_2O_3 core-shell HER co-catalyst (a) the mechanism in which Cr_2O_3 shell suppresses the undesired water formation [99], and (b) HRTEM image of Rh- Cr_2O_3 core-shell fabricated via in-situ photo-deposition [86].....	22
Figure 1.8: Schematic illustration of the effectiveness of graphene in enhancing the efficiencies of the photocatalytic water splitting reactions.	25
Figure 1.9: Charge separation mechanism driven by the electrical field in the space-charge region of an individual n-type nanowire (1) semiconductor NW, (2) photo-excited electrons highway, and (3) substrate [6].	28
Figure 3.1: Examples of physical and chemical approaches to prepare mixed-metal precursors. 52	

Figure 3.2: Comparison between two solid-state synthesis mechanisms. (a) High exposure of the starting materials to NH₃ gas within the Ga³⁺ and Zn²⁺ LDHs distributed within the urea foam, and (b) diffusion of NH₃ gas into the bulk precursor in the traditional route. 55

Figure 3.3: Overview (a) and wurtzite diffraction enlarged view (b) XRD pattern of the GaN:ZnO-LDHs ([Zn]/[Zn+Ga] = 0.20) photocatalyst prepared at various temperatures for 12 min. 58

Figure 3.4: XRD patterns of GaN:ZnO-LDHs ([Zn]/[Zn+Ga] = 0.20) photocatalyst prepared at 900 °C for various times..... 61

Figure 3.5: Digital photo of the prepared GaN:ZnO solid solution samples with different compositions. 62

Figure 3.6: SEM images of (a) the synthesized GaN:ZnO particles, and (b) nanoporosity on the surface..... 63

Figure 3.7: (a) TEM, and (b) HRTEM images of the synthesized GaN:ZnO photocatalyst. 66

Figure 3.8: Bright (a) and dark-field (b) STEM micrograph of the prepared GaN:ZnO, accompanied by The EDX elemental maps for Ga (c), N (d), Zn (e), and O (f). 67

Figure 3.9: Effect of solid solution composition on the (a) optical absorption, and (b) band gap energy of the synthesized GaN:ZnO solid solutions..... 68

Figure 3.10: PL spectra of GaZnON-LDHs and GaZnON-M samples. Inset shows the effect of [Zn]/[Zn+Ga] ratio on the PL characteristics of the GaZnON-LDHs-3 and GaZnON-LDHs-6 samples..... 69

Figure 3.11: Rate of H₂ and O₂ evolution for GaZnON-LDHs 1–6. Error bars indicate 90% confident interval. 71

Figure 3.12: Comparison of the OWS performances of the GaN:ZnO samples prepared by processing of LDHs (GaZnON-LDHs) and mixed precursors (GaZnON-M).....	74
Figure 3.13: H ₂ and O ₂ evolution rates from the Rh-loaded GaN:ZnO solid solution photocatalyst.	76
Figure 3.14: Diffraction pattern of the fresh and used GaN:ZnO photocatalyst (after 20 h) along with that of the standard ZnO and GaN.	77
Figure 3.15: (a) Ga2p, and (b) Zn2p high resolution XPS spectra of the fresh and used GaN:ZnO photocatalysts.....	79
Figure 3.16: Evolved hydrogen from fresh (Cycle 1) and recycled photocatalysts (Cycles 2 and 3).	82
Figure 4.1: Schematic illustration of techniques used in this research for deposition of co-catalyst active sites on the surface of the photocatalyst (a) impregnation, and (b) photo-deposition of Pt.	88
Figure 4.2: Comparison between impregnation and photo-deposition methods for the photocatalysts surface modification with Pt co-catalyst. Comparative studies of HER deposition technique (this figure) and HER photocatalysts materials/loading (Figure 4.5) were conducted using the same GaZnON-LDHs 3 photocatalyst sample. Details of the sample preparation for comparative studies are described in Chapter 2.....	89
Figure 4.3: (a-c) Interruption of the co-catalysts precursors film during the impregnation on a porous structure; steps showing co-catalysts salt is dislodged from the pores during evaporation and thermal treatment. Comparison between co-catalyst active sites density (d) Egg-shell structure, and (e) uniform deposition.....	90

Figure 4.4: Changes in the appearance of the photocatalyst before and after 1 wt% Rh loading
(a). Individual Rh NPs, marked by black arrows in the HRTEM image (b). 92

Figure 4.5: Dependency of the visible-light H₂ evolution rate to HER co-catalyst materials and their loading amount. Comparative studies of the HER deposition technique (this figure) and HER photocatalysts materials/loading (Figure 4.2) were conducted using the same GaZnON-LDHs 3 photocatalyst sample. Details of sample preparation for comparative studies are described in Chapter 2. 93

Figure 4.6: Selected angles HAADF STEM tomography images of a nanoporous GaN:ZnO particle..... 94

Figure 4.7: Effect of OER co-catalysts materials and loading on the O₂ evolution from 5 mM AgNO₃ solution. Oxygen evolution results of the bare and surface modified photocatalyst were obtained using the same GaN:ZnO- GaZnON-LDHs 3 photocatalyst samples, which were decorated with IrO_x and Mn₃O₄ at various loadings. Details of sample preparation for comparative studies are described in Chapter 2..... 95

Figure 4.8: Rapid deactivation of OER co-catalyst by formation of Ag deposits onto photo-deposited OER sites during sacrificial O₂ evolution in AgNO₃ solution. 97

Figure 4.9: STEM (a) and HRTEM (b) image showing the formation of Rh aggregates wrapped in Cr-base film, and blocked the space between two photocatalyst surfaces. 100

Figure 4.10: STEM-EDX compositional profile of the region displayed in Figure 4.9. Ga (a), N (b), Zn (c), O (d), Rh (e), and Cr (f)..... 101

Figure 5.1: Chemical reduction of GO in hydrazine vapor. Band gap energy and schematic structure of the nanosheets at various stages of reduction are also depicted [228]. 104

Figure 5.2: XRD pattern of GaN:ZnO solid solution, GaN, and ZnO (a) wurtzite structure, and (b) diffraction pattern shift.....	105
Figure 5.3: XRD pattern of pristine graphite, prepared GO, and GaN:ZnO-rGO composites. ..	106
Figure 5.4: XPS spectra of (a) graphite, (b) GO, (c) GaN:ZnO, and (d) GaN:ZnO-rGO composite.	107
Figure 5.5: TEM image of GaN:ZnO-rGO composite showing the photocatalysts particles are wrapped in a monolayer rGO nanosheet.....	108
Figure 5.6: High resolution C1s spectra of (a) graphite, (b) GO, and (c) GaN:ZnO-rGO composite.	110
Figure 5.7: SEM image of graphite flakes (a) before and (b) after ultra-sonication for 3 h in pure water.....	111
Figure 5.8: TEM image of a monolayer GO nanosheet prepared through modified Hummers method using pre-exfoliated graphite as the starting material.	112
Figure 5.9: SEM images of the prepared (a) GO, (b) GaN:ZnO, (C) GO composite, and (d) rGO composite.	113
Figure 5.10: Dark (a) and bright (b) field STEM images of the GaN:ZnO-rGO composite.	115
Figure 5.11: EDX elemental profile of the area selected in Figure 5.10 for (a) Ga, (b) N, (c) Zn and (d) O.	115
Figure 5.12: High resolution SEM images of the GaN:ZnO-rGO composite loaded with Rh-Cr ₂ O ₃ NPs. White arrows show co-catalysts clusters.	117
Figure 5.13: HRTEM image of the Rh-GaN:ZnO-rGO composite.	118
Figure 5.14: High resolution STEM image of the rGO surface loaded with Rh NPs (a and c), and Rh elemental map of the area indicated with the green rectangle in a and c (b and d). The inset in	

(b) displays the estimated Rh party size distribution from the area indicated with the white rectangle in (a). The size distribution of the nanoparticles is presented as obtained with no statistical estimation. Image processing was conducted using ImajeJ 1.50i..... 119

Figure 5.15: PL emission of GaN:ZnO solid solution and GaN:ZnO-rGO composite. 121

Figure 5.16: Overall water splitting performance of GaN:ZnO solid solution and its corresponding 2 wt% rGO composite..... 122

Figure 5.17: Effect of GO content of the composite on the visible-light hydrogen evolution. OWS data of the bare and reduced graphene oxide hybridized photocatalyst were obtained using the same traditional photocatalyst sample. Details of sample preparation for the comparative studies are described in Chapter 2. 123

Figure 5.18: Effect of GO loading on the visible light H₂ production of the rGO composite of nanoporous GaN:ZnO solid solution. OWS data of the bare and reduced graphene oxide hybridized photocatalyst were obtained using the same GaZnON-LDHs 3 photocatalyst sample. Details of sample preparation for the comparative studies are described in Chapter 2..... 124

Figure 6.1: Charge separation in n-type semiconductors depletion layer (space-charge region). Figure also displays the charge recombination in the bulk (J_{br}), depletion layer (J_{dr}), and surface states (J_{sr}) of the semiconductor..... 127

Figure 6.2: Charge separation mechanism in an n-type semiconductor nanowire. Figure also shows the OWS process using nanowire photocatalyst. 129

Figure 6.3: SEM image of (a) ZnO NWs prepared by chemical bath method. inset shows the hexagonal tip of a ZnO NW, scale bar = 100 nm, and (b) ZnO-Ga³⁺ thin film prepared by impregnation of ZnO NWs using 5 mM Ga(NO₃)₃.xH₂O solution. 134

Figure 6.4: Vapor-solid (VS) growth mechanism..... 138

Figure 6.5: Vapor-liquid-solid (VLS) growth mechanism.	138
Figure 6.6: Schematic illustration of the utilized APCVD apparatus. Figure also displays the schematic profile of the reactants concentration and growth temperature.	140
Figure 6.7: Digital photos of the quartz substrates process at the downstream of Ga ₂ O ₃ -ZnO source (Ts = 1000 °C) for 30 min (a) D = 8 cm, (b) D = 13 cm, and (C) D = 21 cm.	142
Figure 6.8: SEM image of the quartz substrate at D = 8 cm in the downstream of Ga ₂ O ₃ -ZnO source (Ts = 1000 °C) for 30 min. (a) low resolution image. Arrows show the Au-catalyzed growth. Black: complete growth, white: surface growth (crawling). (b) High resolution image of an individual Au-capped NW.	143
Figure 6.9: Schematic display of epitaxial GaN and ZnO nucleation on the Si (100) substrate. Image was taken from reference [277] and modified for the purpose of this discussion.	145
Figure 6.10: (a) Low resolution SEM image, and (b) digital photo of the Si (100) substrate processed at Ts = 1000 °C and D = 8 cm for 30 min.	147
Figure 6.11: High resolution SEM image of the Si (100) substrate processed at Ts = 1000 °C and D = 8 cm for 30 min. Inset shows an individual Au-capped NW – scale bar = 500 nm.	148
Figure 6.12: Elemental profile of the synthesized NWs along (a) tip cross-section acquired at 20 keV and (b) growth direction, obtained at 5 keV.	152
Figure 6.13: XRD pattern of the GaN:ZnO thin film fabricated at 1000 °C for 30 min at D = 8 cm on Si (100) substrate.	153
Figure 6.14: Low resolution STEM image of a NW prepared at at 1000 °C for 30 min at D = 8 cm, showing the growth direction, along the exposed facets on the side and tip.	154

Figure 6.15: HRTEM images of a NW prepared at 1000 °C for 30 min at D = 8 cm on the Si substrate showing the growth direction and distance between the adjacent lattice fringes. Inset: SAED pattern.	155
Figure 6.16: High resolution SEM image of a NW with exposed (1011) and (1011) facets.	157
Figure 6.17: Dependence of 1-D nanostructures diameter (d) and length (L) to Au-catalyst film thickness (L _{Au}), source temperature (T _s), growth temperature (T _g), Au catalyst droplet size (d _{Au}), distance between precursor and substrate (D), and reactants concentration (C).....	158
Figure 6.18: SEM image of the samples prepared via APCVD at T _s = 1100 °C and t = 5 min on Si (100) substrate at various distances from precursor boat (a) NFs at D = 0 – scale bar = 5 μm, (b) long NWs at D = 8 cm – scale bar = 20 μm, (c) short NWs at D = 13 cm – scale bar = 10 μm, and (d) hollow polyhedral cages at D = 21 cm – scale bar = 50 μm.	160
Figure 6.19: Dependency of the Au droplet size to the growth temperature and local concentration of the building blocks.....	161
Figure 6.20: Various regions of the furnace for growth of structures with different morphologies.	162
Figure 6.21: Low resolution SEM image of the Au-coated Si substrate processed at 1000 °C for 30 min in the dead-zone illustrated in Figure 6.20. Inset: SEM image of the Au coated Si substrate processed at 1100 °C for 5 min. scale bar = 3 μm.	163
Figure 6.22: High resolution SEM micrograph of synthesized NFs on the Au-coated Si substrate processed at 1100 °C for 5 min in the NF-zone (D = 0) illustrated in Figure 6.20. (a) The smooth lateral surface, and (b) Au-catalyst on the tip of an individual NF.....	164
Figure 6.23: Low resolution SEM image of NFs synthesized on the Au-coated Si substrate processed at 1100 °C for 5 min in NFs-zone (D = 0) illustrated in Figure 6.20.	165

Figure 6.24: SEM images of the bulk structures on the surface of Si substrate prepared at various temperatures and durations in the bulk-structure zone displayed in Figure 6.20. (a) Polyhedral cages with hollow structure – scale bar = 10 μm , (b) thick film – scale bar = 20 μm , (c) and (d) low and high magnification images of micro-balls – scale bars = 200 μm and 2 μm , respectively. Low resolution SEM image of the polyhedral cages is presented in Figure 6.18 (d)..... 168

Figure 6.25: (a) STEM, and (b) HRTEM image of an Rh co-catalyst NP on the surface of a GaN:ZnO NW..... 170

Figure 6.26: Sacrificial hydrogen evolution in 10 V% methanol solution for the GaN:ZnO nanowires (GaN:ZnO-NW), nanoporous particles (GaN:ZnO-P), and nanofibers (GaN:ZnO-NF). Data also displayed for the blank Si (100) substrate..... 171

Figure A.1: Center-irradiated photo-reactor apparatus. (a) Light source and (b) 900 mL photo-reactor. 214

Figure A.2: UV-Vis absorption spectra of 2M NaNO₂..... 214

Figure A.3: UV-Vis output of the USHIO high pressure 100 W Hg lamp with and without use of the quartz sleeve and 2M NaNO₂ UV cut-off filter. 215

Figure A.4: Digital photo of the center-irradiated photo-reactor..... 215

Figure A.5: UV-Vis output of the Osram XBO 75 W Xe lamp with and without use of the UV cut-off filter. 216

Figure A.6: The Pyrex side-irradiated photo-reactor..... 216

Figure A.7: Top-irradiated photo-reactor. 217

Figure B.8: Hydrogen evolution of the 3 wt% Pt-GaN:ZnO solid solution under visible light irradiation from pure water. All samples were prepared at 800 W for 12 min..... 218

Figure C.9: XPS spectra of LHD-1 to LDH-6 photocatalysts. Surface x values are presented in Table 3.3.	220
Figure C.10: EDX spectra of LHD-1 to LDH-6 photocatalysts.	224
Figure E.11: Low resolution SEM image of the ZnO thin film impregnated with concentrated (35 mM) Ga(NO ₃) ₃ .xH ₂ O solution. Inset shows the high resolution SEM micrograph of the continuous film, scale bar = 3 μm.....	228
Figure F.12: SEM image of the structures precipitated inside the growth solution during chemical bath growth in HMT solution using zinc nitrate as Zn source (entry 1 in Table 6.2).....	229
Figure F.13: SEM image of the structures precipitated inside the processing solution during chemical bath growth in HMT solution using zinc acetate as the Zn source (entry 2 in Table 6.2). Inset shows the high resolution SEM image of the precipitates.	230
Figure F.14: SEM image of the structures observed on the ZnO-seeded quartz substrate during chemical bath growth in HMT solution using zinc acetate as the Zn source (entry 2 in Table 6.2).	230
Figure G.15: Face-down substrates layout at D = 0.....	231
Figure G.16: APCVD substrate holder.	231
Figure G.17: Schematic illustration of the chemical vapor deposition hydrodynamics modification to enhance the density of the building blocks in the growth region using the vertical sample holder.	231
Figure H.18: Dependency of metal particles diameter to their melting temperature [291].....	232

List of Symbols

a, b, c	Lattice constants (nm)
c	Speed of light in vacuum ($m s^{-1}$)
C	Concentration ($mol L^{-1}$)
d	1-D nanostructures diameter (nm)
$d_{(hkl)}$	Lattice spacing of the (hkl) plane (nm)
d_p	Particle diameter (nm)
D	Distance from the center of the furnace (cm)
E_g	Band gap energy (eV)
E_p	Photon's energy (eV)
$F(R)$	Kubelka-Munk function
h	Planck constant ($eV s$)
h, k, l	1 st , 2 nd , and 3 rd Miller indices
H	Number of the evolved hydrogen molecules
I	Number of the irradiated photons
J	Diffusion flux of gasses to Au nanoparticle ($\mu mol nm^{-2} s^{-1}$)
J_{br}	Bulk recombination rate (s^{-1})
J_{dr}	Depletion layer recombination rate (s^{-1})
J_{sr}	Surface recombination rate (s^{-1})
K	Shape factor in Scherrer equation
L	1-D nanostructures length (μm)

L_{Au}	Thickness of the Au film (nm)
L_s	Depletion layer thickness (nm)
R	Portion of the reflected light (%)
s	Scattering coefficient (nm^{-1})
S	Specific surface area ($m^2 g^{-1}$)
T_g	Growth temperature ($^{\circ}C$)
T_s	Source temperature ($^{\circ}C$)
v	Velocity ($m s^{-1}$)
V	Electrochemical potential (eV)
x	Atomic composition of ZnO in GaN:ZnO solid solution ($atm\%$)
Δd_p	Rate of changes in Au nanoparticles diameter ($nm s^{-1}$)
ΔG^0	Standard Gibbs free energy of reaction ($KJ mol^{-1}$)
α	Absorption coefficient (nm^{-1})
β	Peak full width at half maximum (rad)
λ	Wavelength (nm)
θ	Diffraction angle ($degree$)
ρ	Bulk density ($g ml^{-1}$)
\emptyset	Apparent quantum efficiency (%)
δ_p	Photo-penetration depth (nm)

List of Abbreviations

1-D	One-dimensional
ad	Adsorbed
AM	Air-mass
APCVD	Atmospheric pressure chemical vapor deposition
AQE	Apparent quantum efficiency
BET	Brunauer-Emmett-Teller
BSE	Back-scattered electron
CB	Conduction band
CNT	Carbon nanotube
CVD	Chemical vapor deposition
DFT	Density functional theory
EDX	Energy dispersive X-ray
ETA	Ethanolamine
ETD	Everhart-Thornley detector
FTO	Fluorine-doped tin oxide
FWHM	Full width at half maximum
GBC	Graphene-base composite
GC	Gas chromatography
GO	Graphene oxide
HAADF	High-angle annular dark-field

HER	Hydrogen evolution reaction
HMT	Hexamethylenetetramine
HOMO	Highest occupied molecular orbital
HRTEM	High resolution transmission electron microscopy
ITO	Indium tin oxide
LDH	Layered double hydroxide
LED	Light-emitting diode
LUMO	Lowest unoccupied molecular orbital
MBE	Molecular beam epitaxy
MM	Mixed-metal
MOCVD	Metal-organic chemical vapor deposition
MW	Microwave
NF	Nanofiber
NHE	Normal hydrogen electrode
NIST	National Institute of Standards and Technology
NP	nanoparticle
NR	Nanorod
NT	Nanotube
NW	Nanowire
OER	Oxygen evolution reaction
OWS	Overall water splitting
PEC	Photo-electro-chemical

PL	Photoluminescence
PTFE	Polytetrafluoroethylene
QD	Quantum dot
QE	Quantum efficiency
rGO	Reduced graphene oxide
RHE	Reversible hydrogen electrode
SAED	Selected area electron diffraction
SE	Secondary electron
SEM	Scanning electron microscopy
STEM	Scanning transmission electron microscopy
SWCNT	Single-wall carbon nanotube
TCD	Thermal conductivity detector
TEM	Transmission electron microscopy
TLD	Through the Lens Detector
TW	Terawatt = 10^{12} W
TGA	Thermo-gravimetric analysis
UV	Ultra-violet
VB	Valence band
Vis	Visible
VLS	Vapor-liquid-solid
VLSE	Vapor-liquid-solid epitaxy
VS	Vapor-solid

VSS	Vapor-solid-solid
XPS	X-ray photoelectron spectroscopy
XRD	X-ray diffraction

Acknowledgements

Writing this note of thanks is the finishing touch on my thesis. It has been an intense and exciting learning process for me, not only in the scientific arena, but also on a personal level. Being part of the UBC community has had a big impact on me, which I hope that will stay with me throughout my life. I would like to reflect on the people who have supported and helped me so much throughout this period.

Firstly, I would like to express my sincere gratitude to my research supervisor Prof. Taghipour for the continuous support of my Ph.D. study and related research, for his patience, motivation, and immense knowledge. His guidance helped me in all the time of research.

I would also like to thank my thesis committee, Prof. Wilkinson, and Prof. MacLachlan, for their insightful comments.

I offer my enduring gratitude to the faculty, staff and my fellow students at UBC and other people who have inspired me throughout my PhD program.

I would like to thank my fellow colleagues at the Photo-Reaction Engineering Laboratory for the stimulating discussions, for the nights we were working together before deadlines, and for all the fun we have had.

My sincere appreciation goes to Kevin Reilly, and Sina Tebianian for their friendship.

I would like to thank my family: my parents and my brother for supporting me spiritually throughout my PhD program, writing this thesis, and my life in general.

To My Family

Chapter 1: Introduction

Providing clean and renewable energy is arguably the most important challenge facing humanity in the 21st century [1]. World's energy demand is projected to more than double by mid-century and to more than triple by 2100 [2]. Holding the atmospheric CO₂ levels to its current values would require invention and development of new technologies [3].

Among the various clean and renewable energy sources, sunlight is by far the largest. More energy from sunlight strikes the Earth in one hour (4.3×10^{20} J) than all the energy consumed on the planet in a year (4.1×10^{20} J) [2]. However, the utilization of sunlight as a clean energy source depends on the efficiency of the devices which capture, convert, store, and distribute solar energy.

In general, there are three routes to utilize solar energy: in the form of heat (thermochemical), fuel (photo-electrochemical) or electricity (electrolysis). Despite the enormous energy flux supplied by sunlight to the Earth, the contribution of all three conversion routes is only a fraction of our current needs [1]. The contribution of solar heat in providing residential and industrial energy has been significantly lower than solar electricity, owing to the advantages of photovoltaic systems, including their low cost, facile installation, and less required maintenance [4]. Today the average cost of energy from solar photovoltaic in U.S. is reported to be about the same as the average retail rate [5]. Yet, fossil fuels still provide 87% of the global primary supply, while renewable sources are about to reach a 10 % overall share [6]. Such slow growth is attributed to the fact that the solar electricity and heat are not storable and not compatible with current infrastructures.

The most attractive method of solar energy conversion and storage is in the form of the chemical bonds of an energy carrier such as hydrogen or light hydrocarbons (*i.e.* solar fuel generation via water splitting or CO₂ conversion), which does not experience energy loss via

thermal transformation (thermochemical) and conversion of solar energy to electricity (electrolysis) [7]. Direct production of fuel from sunlight is an appealing technology because it inherently provides a method for extracting energy during the evening and for dispatching and distributing energy through the existing infrastructure for use in the residential, industrial and transportation sectors [8].

Conversion of sunlight into chemical fuels through splitting of water into H₂ and O₂ is an existing technology; however, the current rate of solar water splitting reaction is very low. Besides, the cost of the utilized materials and processing techniques for fabrication of functional photocatalysts are substantially high. Moreover, the photocatalysts that have studied so far cannot readily provide the energy levels that would be required to support a TW-level (Terawatt = 10¹² W) implementation [9]. Thereby, in-depth understanding of solar hydrogen production process, and facile production of highly efficient photocatalyst materials with superior characteristics are crucial.

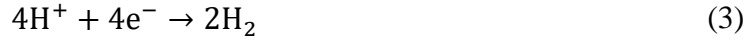
In this chapter, the principles, obstacles, and opportunities of solar water splitting technology are explained. This section is followed by elaborating the potentials of gallium-zinc oxynitride solid solution as a visible-light activated photocatalyst for water splitting application. Finally, the research motivations, objectives and a review on the relevant studies in the literature are presented.

1.1 Principles of photocatalytic overall water splitting

Thermodynamically, overall water splitting (OWS) is an uphill reaction with a large positive change in the Gibbs free energy ($\Delta G^{\circ} = 238 \text{ kJ mol}^{-1}$) [10].



The oxidation and reduction half-reactions are described as follows:



Equation (2), the so called water oxidation reaction, can be also written as $2\text{H}_2\text{O} + 4\text{h}^+ \rightarrow \text{O}_2 + 4\text{H}^+$, where h^+ is photo-induced hole, which is the vacancy of an electron in the atomic orbital of a semiconductor. In regards to the changes in Gibbs free energy, photocatalytic water splitting is distinguished from photocatalytic degradation reactions, such as photo-oxidation of organic compounds using oxygen molecules that are generally downhill reactions. These reactions are regarded as photo-induced processes and have been extensively studied using titanium dioxide (TiO_2) photocatalyst [11,12].

Photocatalytic water splitting systems can be classified as immobilized thin film, suspended slurry (the focus of this research), and fluidized bed systems. Utilization of immobilized photocatalysts are hindered by their complex design, limited amount of the photocatalyst surface area in contact with the electrolyte, and inefficient mass transport at the liquid-film interface [13]. In contrast, the suspended slurry systems can be designed at substantially lower cost, and maintain an excellent mass-transfer, as well as provide maximum active surface area and radiation distribution. However, the slurry systems are hardly scalable. The fluidized bed photocatalysts are known to have an improved light absorption, and mass transfer, as compared to immobilized thin film photocatalysts. On the other hand, their high operating cost, as well as the photocatalyst degradation because of surface damages and attritions are considered as major obstacles for this systems [14].

Photocatalytic splitting of water is a promising, yet challenging and complicated process. For instance, the rate of water splitting reaction (*i.e.* rate of H₂ and O₂ evolution) is a function of many competing factors such as reaction kinetics, energy states of photo-induced charge carriers, morphology, crystalline structure, exposed crystallographic facets and the surface properties of the utilized photocatalyst and redox active sites [15]. Once a photon strikes the surface of a semiconductor material, a photo-induced charge pair (*i.e.* electron-hole pair) is generated near the surface of the photocatalyst [16]. The energy levels of these photo-induced charges are relative to the electronic band structure of the semiconductor, whereas the electrons possess the energy of the lowest unoccupied molecular orbital (LUMO), while the holes contain the potential energy of the highest occupied molecular orbital (HOMO) [17]. These energy states are also known as the bottom of the semiconductor's conduction band (CB), and the top of the semiconductor's valence band (VB), respectively. The energy gap between VB and CB is called band gap energy (E_g), which is the minimum required energy to activate a semiconductor photocatalyst [17]. These energy states are demonstrated in Figure 1.1.

For a photocatalytic reaction to proceed, the photo-induced charges must pose suitable energy levels corresponding to that of the redox reactions. For solar water splitting reaction, the photo-excited holes and electrons must contain more positive and more negative energy compared to that of the water oxidation potential, reaction (2), equal to 1.23 eV vs normal hydrogen electrode (NHE), and proton reduction potential, reaction (3), equal to 0.00 eV vs NHE, respectively [17]. Upon photo-excitation, the charge carriers can reach to the photocatalyst-electrolyte interface and participate in the redox reactions at the CB and VB energy levels.

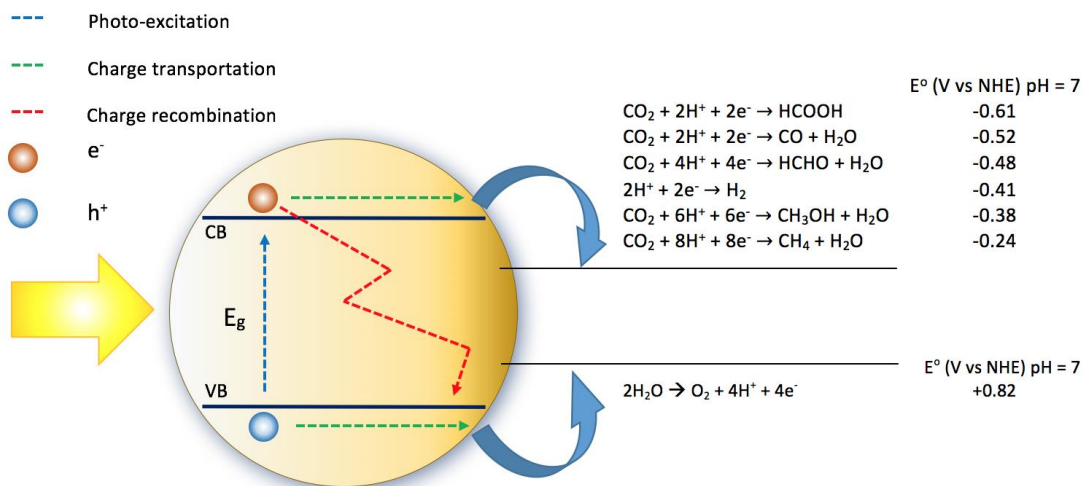


Figure 1.1: Band gap energy (E_g), valence band (VB) and conduction band (CB) potentials of a semiconductor. Processes (photo-excitation, charge transportation, and charge recombination) occur once a light photon with energy greater than E_g strikes the surface of a semiconductor are depicted. Redox reactions at the CB energy state are listed for solar fuel generation reactions (water splitting and CO_2 conversion).

Processes occur upon absorption of a light photon with energy greater than the band gap of the photocatalyst ($E_p > E_g$) are schematically illustrated in Figure 1.1, and can be described by the following steps:

- I. Generation of photo-induced holes and electrons at VB and CB of the semiconductor, respectively (photo-excitation step which is demonstrated by blue dash-line)
- II. Diffusion of the photo-induced holes and electrons within the crystal lattice of the photocatalyst towards the surface (charge transportation step which is shown by green dash-lines) and interaction with active species in the electrolyte (redox reactions which are indicated by blue arrows)

III. Recombination of photo-induced holes and electrons at the crystal defects and grain boundaries in the bulk or on the surface of the photocatalyst (charge recombination step which is displayed by red dash-line)

Difference between the potentials of the hydrogen and oxygen evolution half-reactions (reactions 2 and 3) is only 1.23 eV, which corresponds to the light photon with wavelength around 1000 nm, calculated from the Planck equation (4).

$$E_p = \frac{hc}{\lambda} \quad (4)$$

where E_p (eV) is the photon's energy, h is the Planck constant (eV s), c is the speed of light in vacuum ($m s^{-1}$) and λ (nm) is the photon's wavelength. Thus, overall water splitting can be driven with both visible and near-infrared light. However, there is an activation barrier in the charge-transfer process between photocatalysts and electrolyte that requires energy levels much greater than those of the theoretical redox half-reactions to drive the overall water splitting reaction at a reasonable rate [18]. Moreover, the formation of water molecules from evolved hydrogen and oxygen, so called backward reaction [11,19], and more importantly, the recombination of photo-generated electrons and holes must be strictly inhibited [11,20].

The first experimental demonstration of photo-electro-chemical (PEC) water splitting was reported by Fujishima and Honda [21]. In their study, a TiO_2 photo-anode electrode for water oxidation half-reaction (2) was coupled with a platinum (Pt) cathode electrode for proton reduction half-reaction (3), and illuminated with UV-irradiation. As the result of reaction of the photo-excited charges with electrolyte, stoichiometric rate hydrogen and oxygen evolution was observed. Since the pioneering work of Fujishima and Honda, photocatalytic water splitting has grasped

considerable attention, owing to its promises for addressing the future energy crisis. In recent years, advances in solid-state chemistry and nanofabrication triggered a global research effort for synthesis and utilization of various semiconductors and their hybridized materials for solar hydrogen production. Despite the application of advanced metal oxide, sulfide, and nitride photocatalysts, as well as their solid solution and composite materials, the efficiencies of the solar fuel generation processes have remained too low for them to be feasibly commercialized [15,19,22,23]. In the last few years, strategies with emphasis on the engineering of the semiconductor's band gap, morphology and exposed crystallographic facets, as well as increasing the number of redox active sites led to remarkable progresses, yet not enough to set the commercialization of solar water splitting within sight [15,19,22,23]. The major obstacle in the development of the desired photocatalyst is a lack of a suitable compound that meets the following requirements [24]:

- I. Band gap energy narrower than 3.0 eV to harvest the visible portion of the solar spectrum,
- II. Suitable VB and CB band-edge potentials corresponding to the redox potentials of overall water splitting,
- III. Highly crystalline structure to minimize the photo-excited electrons-holes recombination, and
- IV. Stable chemistry in the water splitting reaction condition.

Figure 1.2 shows some photocatalyst materials which were studied for photo-induced water splitting reaction and the difficulties associated with their use.

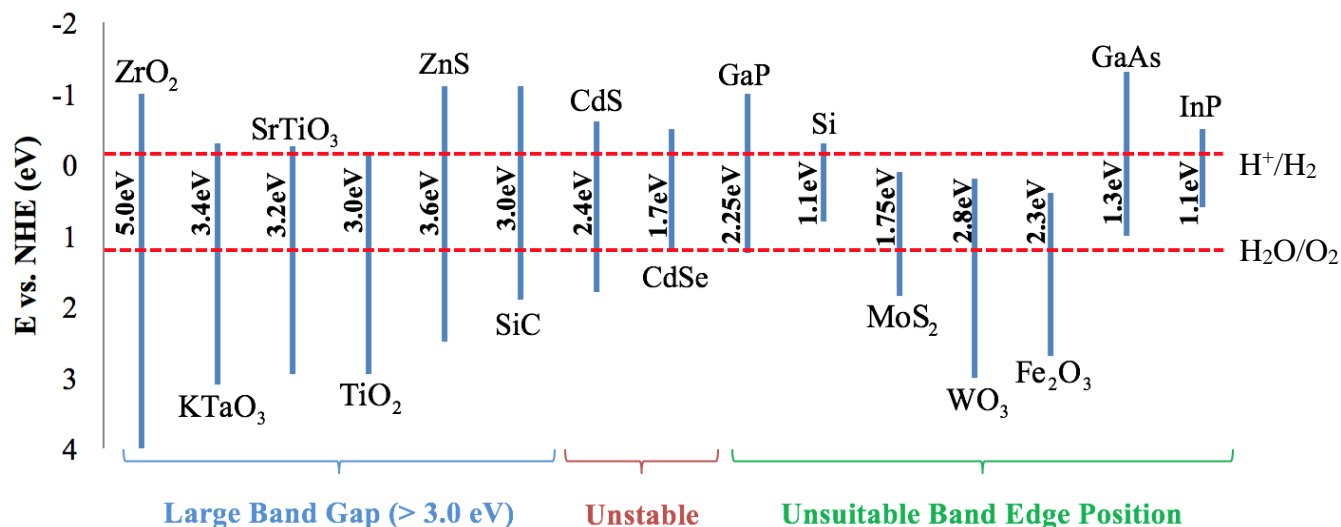


Figure 1.2: Energy band structure of some semiconductors and their limitation for visible-light overall water splitting application [9].

Gallium-zinc oxynitride solid solution (GaN:ZnO), also known as $(\text{Ga}_{1-x}\text{Zn}_x)(\text{N}_{1-x}\text{O}_x)$, is one of the few materials that meets all the required conditions, and exhibited outstanding stability and OWS performances within the visible-region [25–27].

GaN is a wide band gap semiconductor ($E_g = 3.3\text{--}3.4\text{ eV}$ [28–30]) and has been studied extensively for applications such as light-emitting diodes (LEDs) and lasers [26,27]. GaN exhibited water oxidation under UV irradiation in PEC configuration [33–35]. Domen and co-workers reported overall water splitting of pristine and surface modified GaN photocatalyst powder [36,37]. Recently, outstanding overall water splitting activities were reported by Wang et al. from the surface modified GaN nanowires (NWs) fabricated via molecular beam epitaxy (MBE) [38]. P-type doping of GaN NWs and fabrication of multiband heterostructures of GaN-base NWs led to remarkable improvements in the overall water splitting performances under UV-visible irradiation [39–43].

ZnO with a band gap of 3.2–3.4 eV [30,44,45] has been studied for many applications such as LEDs and gas sensors [46–48]. Surface and structure modified ZnO have been investigated comprehensively for water splitting application [49–53]. However, ZnO is not active under visible light irradiation and reported to be unstable at the water splitting reaction condition, since it undergoes photo-corrosion by consuming the photo-induced holes, according to reaction (5) [54–56].



GaN and ZnO possess the same wurtzite hexagonal crystalline configuration, as illustrated in Figure 1.3, with relatively identical unit crystal dimensions, defined by a , b , and c lattice constants, as summarized in Table 1.1.

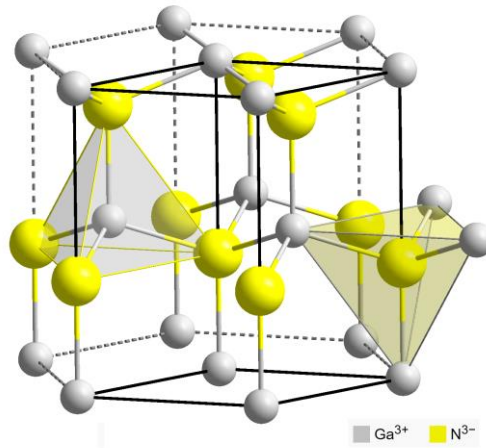


Figure 1.3: Wurtzite crystalline structure of GaN [57].

Table 1.1: Crystal lattice constants (a , b , and c) of wurtzite GaN and ZnO [58,59].

Material	Lattice constants		Mismatch to GaN	
	$a = b$ (nm)	c (nm)	a (%)	c (%)
GaN	0.318	0.518	-	-
ZnO	0.325	0.520	2.1	0.4

Because of the similar crystal lattice parameters of GaN and ZnO, a solid solution with the same crystalline structure can be formed between the two. As mentioned, GaN and ZnO are not active under visible-light irradiation; on the other hand, the oxynitride solid solution phase of the two exhibited visible-light activity with band gap dependency to the solid solutions composition (x) between 2.1–2.8 eV corresponding to photon’s energy up to 590 nm [27,30,60–65]. The origin of such band gap reduction, as illustrated in Figure 1.4, is under debate. Shi et al. suggested that the repulsion between p and d orbitals is responsible for the changes in the VB maximum potentials and band gap bowing [66]. Lee and co-workers observed similar band gap reduction for the germanium-zinc oxynitride solid solution (GeN:ZnO) synthesized through high temperature solid-state reaction [67]. It was proposed that the repulsion forces between the p and d orbitals in II-VI semiconductors shifts the VB maximum upward without affecting the CB minimum [68]. Presence of Zn3d, N2p, and O2p electrons in the upper states of the GeN:ZnO valence band causes a strong repulsion between electrons in the p and d orbitals and shifts the top of the VB upwards, thus narrowing the band gap [67]. Similarly, it can be hypothesized that the formation of the VB maximum by Zn3d, N2p, and O2p atomic orbitals (Figure 1.4) causes the p-d repulsion in GaN:ZnO solid solution and; therefore, is responsible for shifting the its VB to the higher energy states [66,69].

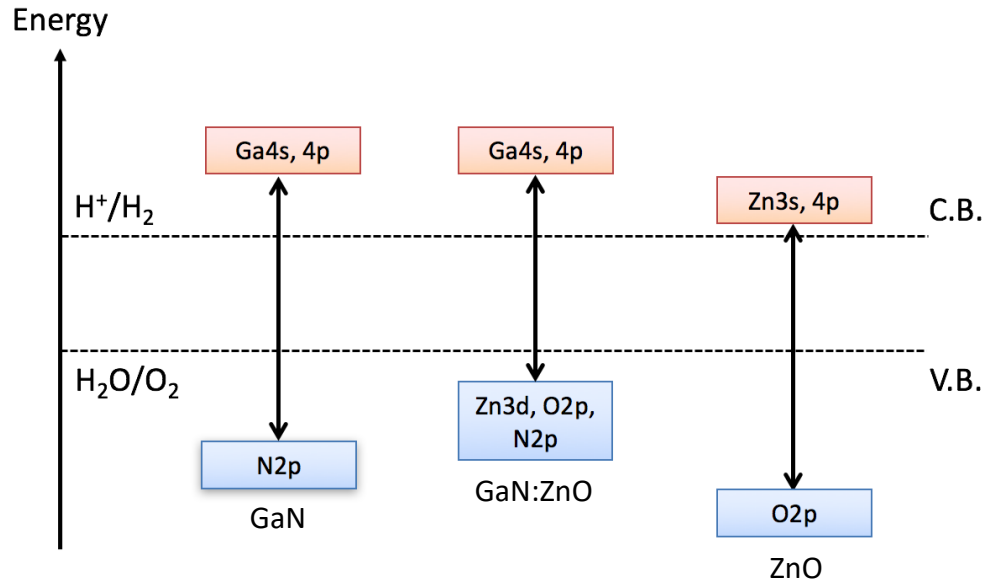


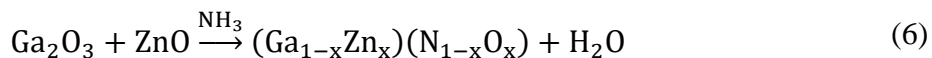
Figure 1.4: Band gap reduction in GaN:ZnO solution.

This hypothesis is in agreement with experimental observations indicating band gap reduction with increase in the Zn-content of the solid solution photocatalyst [6,20,22,25,55,56,58,60,65,66].

Due to the interesting properties of GaN:ZnO solid solution in tailoring the optical band gap, as well as the outstanding OWS activities reported for this photocatalyst, the focus of this research was centered on the synthesis, characterization, and performance evaluation of GaN:ZnO solid solution photocatalyst for visible light hydrogen production.

1.2 Knowledge gap

GaN:ZnO solid solution photocatalyst is typically synthesized through the nitridation of a mixture of Ga_2O_3 and ZnO at high temperatures (850 °C) for 5–18 h (typically 15 h) under flow of ammonia ($250 \text{ mL}^{-1} \text{ min}$) via the solid-state reaction (6) [25–27], the so called traditional synthesis technique.



During the solid-state synthesis, atoms of Ga are replaced by Zn, while N atoms from the nitrogen source diffuse into the lattice and substitute the O atoms. It is documented that the insertion of atoms into the host material's lattice causes crystalline defects that serve as trap sites for the photo-excited charges, thus reduce their transfer to the surface of the photocatalyst [11,17]. Due to the similar lattice dimensions of GaN and ZnO, it is expected that controlled solid-state synthesis of GaN:ZnO minimizes the density of structural defects, thereby enhance the rate of photo-induced charge migration to photocatalyst-electrolyte interface.

Although the photocatalyst prepared through the traditional method exhibited promising OWS activities, long synthesis time, at high synthesis temperature and consumption of toxic gaseous ammonia are considered as the drawback of this method. Moreover, the Zn/Ga ratio of the traditionally prepared solid solution is low due to the evaporation of ZnO at high temperatures [9,27,60,61,63,65], even at shorter synthesis durations ($x = 0.42$ at 30 min [72]). Considering that the visible-light harvesting of the solid solution photocatalyst is attributed to the Zn-content of the prepared photocatalyst, development of highly efficient solid solution materials demands new synthesis strategies that inhibit Zn evaporation. Several studies investigated the kinetic and mechanism of oxynitride phase formation from its oxide and hydroxide precursors [56,69,70,71,66,72]. Our extensive literature review concluded that there are several potential approaches for development of visible-light responsive photocatalysts based on gallium-zinc oxynitride solid solution through improved routes, which have hitherto not been studied in depth. These approaches include:

- Effect of the starting materials characteristics, and their interaction at the nanoscale, which impact the solid-state synthesis mechanism, as well as the composition, morphology, crystallinity, and ultimately the photocatalytic performance of the obtained photocatalyst.
- Effect of photocatalysts surface modification with optimal amount of hydrogen and oxygen evolution co-catalysts, which provides active sites for redox reactions, and potentially enhances the density of the charges on the surface.
- Effect of hybridization of GaN:ZnO photocatalyst with highly conductive support, which reduces the recombination losses by enhancing the rate of charge separation.
- Effect of growing the GaN:ZnO photocatalyst in the form of one-dimensional (1-D) nanostructures, which is a morphological approach to separate the photo-generated electrons and holes, to provide high active surface area, and to enhance light absorption.

This thesis aims to study the aforementioned effects.

1.3 Research objectives

The overall objective of this research is set to explore a number of potentially promising approaches to develop visible-light active photocatalysts based on GaN:ZnO solid solution with tailored structural, optical, and photochemical properties for visible light hydrogen generation. In order to address the overall goal, the following four objectives were defined for this research:

1. To develop an efficient synthesis technique for GaN:ZnO photocatalyst by exploring the role of solid-state synthesis effective parameters (*e.g.* solid-solid and solid-gas interaction, synthesis temperature and preparation time).
2. To investigate the effect of different hydrogen and oxygen evolution co-catalysts, and their loading conditions.

3. To determine the impact of graphene as the conductive support material in composite with GaN:ZnO solid solution photocatalyst.
4. To develop an effective route for the fabrication of GaN:ZnO solid solution photocatalyst in the form of 1-D nanostructures.

1.4 Thesis outline

In this introduction chapter, the principles of photocatalytic water splitting are explained, and potentials of GaN:ZnO solid solution as a visible light activated photocatalyst are described. Further, a literature review is represented in respect to the research objectives, discussing the recent advances in the preparation and surface modification of GaN:ZnO solid solution, as well as the merits of graphene-based nanocomposites, and opportunities offered by the fabrication of semiconductor thin films.

In Chapter 2, approaches and methods used in this research are described. Procedures for material fabrication, characterization and performance evaluation are explained.

The outcomes of this study are presented in Chapters 3, 4, 5, and 6. Each chapter starts with a brief introduction and addresses the obtained results thereafter.

Chapter 3 is dedicated to the development of a facile synthesis technique for nanoporous GaN:ZnO solid solution. In this chapter, the synthesis mechanism is explained, and the material characterization results along with the photocatalytic overall water splitting performances of the prepared GaN:ZnO are discussed.

Surface modification of nanoporous GaN:ZnO solid solution photocatalyst with hydrogen evolution reaction (HER) and oxygen evolution reaction (OER) catalysts is argued in Chapter 4,

where the obtained results for various deposition techniques, co-catalysts materials and optimal loading are presented.

In Chapter 5, the preparation and characterization of graphene oxide (GO), reduced graphene oxide (rGO), and their hybridized materials with GaN:ZnO solid solution photocatalyst are explored. Further, the overall water splitting performance of the prepared composite photocatalysts and optimal GO integration are investigated.

The preparation of GaN:ZnO solid solution thin film is described in Chapter 6, where various techniques have been studied for fabrication of 1-D solid solution of GaN and ZnO. This chapter placed an emphasis on the atmospheric pressure chemical vapor deposition (APCVD) growth of 1-D GaN:ZnO solid solution through vapor-liquid-solid epitaxy (VLSE) mechanism.

The overall conclusion of this study and recommendations for future work are presented in the last chapter of this thesis.

1.5 Problem statement

In this section, recent advances with respect to the defined research objectives are reviewed. The works conducted by other researchers have been a significant help to this study. Through the last few years, we have consistently monitored the reports related to photocatalytic dissociation of water, particularly those regarding GaN:ZnO solid solutions, and compiled these materials to design and implement the research plans and experiments.

1.5.1 Solid-state synthesis of GaN:ZnO solid solution photocatalyst

The synthesis of the GaN:ZnO photocatalyst and its OWS performance were first reported in 2005–2006 by Prof. Domen's research team at the University of Tokyo [25,26], who contributed

significantly in the development of highly efficient oxynitride photocatalysts such as GaN:ZnO, GeN:ZnO, TaON, and MTiO₂N (M = La, Ca, Sr, and Ba). The outcomes of their research are summarized in recently published reviews [77,78]. Their work inspired many research groups globally and triggered a scientific endeavor for understanding the solid-state mechanism, as well as the properties of the prepared oxynitride photocatalysts. In addition to the traditional solid-state synthesis described earlier, a few alternative preparation routes were reported lately [60,61,65,71,73]. The general solid-state synthesis pathways of GaN:ZnO solid solution photocatalyst is depicted in Figure 1.5, indicating the important role of the metal oxides starting materials and nitrogen source in the synthesis kinetic, along with the possible products of the high temperature solid-state preparation.

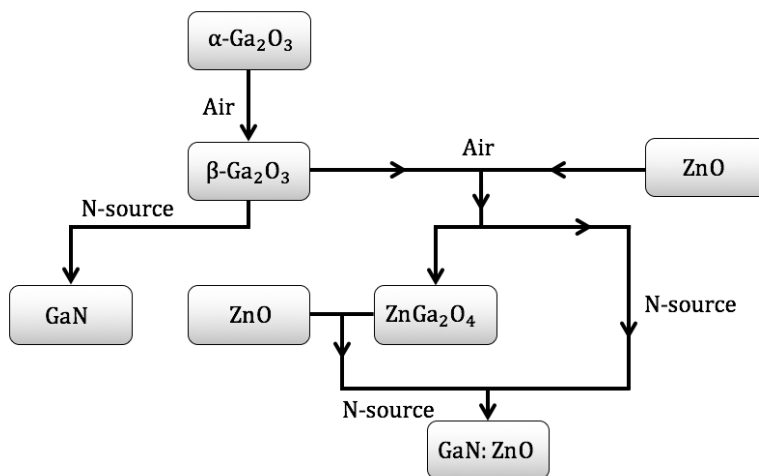


Figure 1.5: Possible solid-state routes using Ga₂O₃ and ZnO as the starting materials.

Yan et al. proposed a two-step medium-temperature solid-state synthesis via nitridation of mesoporous nanocrystalline zinc gallate (ZnGa_2O_4) under ammonia flow (250 mL min^{-1}) for 6 h at $680 \text{ }^\circ\text{C}$ [61,79]. Hydrothermal ion-exchange reaction between mesoporous NaGaO_2 colloid

precursor and Zn salt resulted in ZnGa_2O_4 with mesoporous morphology [79], as described in reaction (7) and illustrated in Figure 1.6.

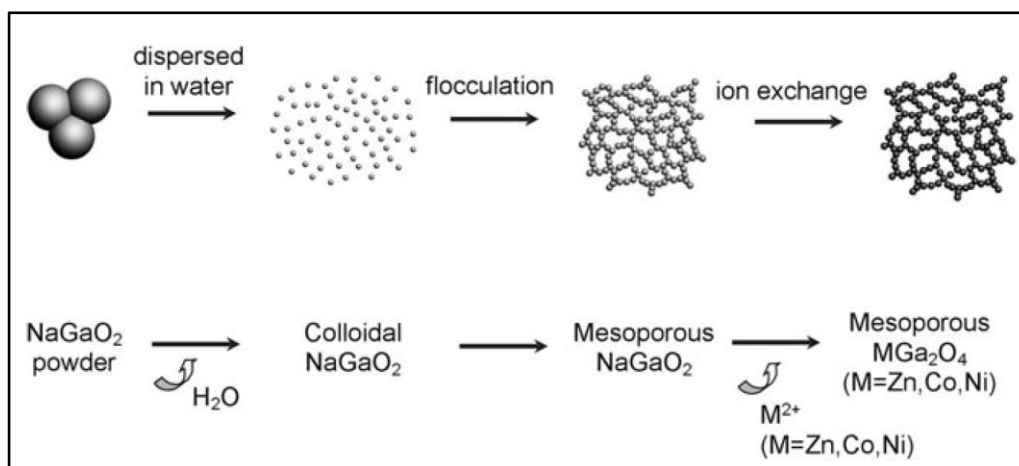
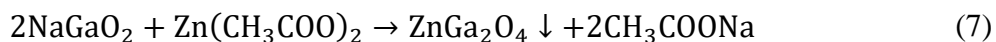


Figure 1.6: Ion-exchange preparation of mesoporous ZnGa_2O_4 [79]. Reprinted with permission from (Angew. Chem. Int. Ed. 2010, 49, 6400–6404). Copyright (2006) Wiley-VCH Verlag GmbH & Co. KGaA, Weinheim.

Highly crystalline mesoporous zinc gallate was reported to be an effective precursor for synthesis of GaN:ZnO solid solution [79]. High surface area for solid-state reaction can be provided using the mesoporous precursor; thus, less nitridation time is required for the solid-solid diffusion step. Therefore, higher Zn/Ga ratios and greater visible-light harvesting can be maintained through the medium-temperature solid-state technique, as compared to the traditional method [9]. Hisatomi et al. reported that use of fine ZnO particles with higher surface area enhances the solid-state diffusion flux, and evaporation rate of ZnO [80]; thus, by controlling the ZnO particle size distribution in the starting materials, transformation from oxide to oxynitride

phase can be realized at lower nitridation times and temperatures. The VB potential of the mesoporous photocatalyst is laid at 1.51–1.73 eV, with band-gap energy of 2.34–2.57 eV, which makes it thermodynamically capable to drive overall water-splitting reaction under visible light irradiation.

Wang and co-workers proposed a novel approach for the preparation of GaN:ZnO photocatalyst through nitridation of gallium and zinc layered double hydroxides (LDHs) precursor [63]. LDHs have been extensively studied for many applications including energy conversion and storage, as well as environment and catalysis [81]. The basic features of their structure, including positively charged brucite-like layers containing divalent and trivalent metal cations, charge-balancing anions and water in interlayer galleries, are well documented [82]. Because of their ease of synthesis, LHDs were extensively studied as cost-effective, durable, versatile host materials, catalyst supports and precursors with controlled chemical and physical properties [82]. In particular, mixed metal compounds prepared by the precipitation in the form of LDHs with large specific surface areas ($100\text{--}300\text{ m}^2\text{ g}^{-1}$ [82]) have been widely utilized for catalysis applications [83].

Studies have provided examples of LDHs with Zn as the divalent cation and trivalent metals such as Al, Fe, Cr and Co in various compositions [84–86]. Their structural configuration suggest that LDHs are excellent host materials for preparation of mix-zinc-gallium hydroxide precursors [9,63]. The GaN:ZnO photocatalyst was obtained by nitridation of zinc-gallium LDHs under 300 mL min^{-1} ammonia flow for 30 min at $800\text{ }^\circ\text{C}$. Decreasing the nitridation time to 30 min (from its original 10+ h for the traditional method) is likely attributed to: 1) Effective diffusion of NH_3 into the interlayer spacing of LDHs, enhancing the surface area of the gas-solid interaction,

and 2) formation of a homogeneous mixture of Zn^{2+} and Ga^{3+} at an atomic scale; therefore, increasing the solid-solid diffusion rate. The solid solution prepared through the LDHs precursor reported to be uniform in composition, owing to the atomic level interaction between precursor's components. Due to the lower synthesis time and temperature, Zn-rich GaN:ZnO photocatalyst (up to $x = 0.81$) was successfully prepared. High stability of the structural zinc of the solid solution photocatalyst was confirmed through elemental analysis, showing relatively constant Zn-content for longer nitridation times up to 5 h [63]. The band gap energy of the prepared solid solution was estimated ~ 2.60 eV at $x = 0.46$, confirming the effective optical tuning via oxynitride phase formation using LDHs precursor.

An efficient microwave (MW)-assisted method was proposed by Yang et al. for synthesis of GaN:ZnO solid solution photocatalyst [60]. Microwave heating, as a new energy source, has proven to be an effective technology for endothermic reactions in materials chemistry. Conduction and convection heating are arguably slow and inefficient strategies for transferring energy through the reaction vessel. However, MW irradiation provides efficient heating by direct coupling with the polar molecules in the reaction domain (*e.g.* solvents, reagents and catalysts) [87]. Over the last few years, it has been demonstrated that the synthesis of nanoporous metal oxides can be improved by more than an order of magnitude using MW irradiation [88].

Yang and colleagues employed MW irradiation for treatment of metal oxides and urea (nitrogen source) mixture and successfully synthesized GaN:ZnO solid solution in 10 min [60]. The band gap of the MW-treated GaN:ZnO solid solution was estimated equal to 2.47 eV, which is lower than the photocatalyst obtained through the traditional method via 13 h nitridation. The

short preparation time may not be sufficient for the solid-solid interface diffusion; thus, the formation of various phases and residues through side reactions are inevitable [9].

Lee et al. developed a multi-step route for the preparation of single crystal GaN:ZnO nanoparticles ($d_p \sim 18$ nm) using ultra-fine $ZnGa_2O_4$ and ZnO nanocrystallites as the starting materials [71]. High rate of solid-state reaction via effective nanoscale solid-solid interfacial contact resulted in a lower synthesis temperature (650 °C) and fabrication of zinc-rich solid solutions with Zn-content as high as $x = 0.87$. The solar absorption of the Zn-rich photocatalyst increased by 260%, compared to the photon absorption observed for the solid solution with $x = 0.42$ [72].

Alternative synthesis routes in the literature indicate that by precise control of the solid-state synthesis kinetic at the nanoscale, preparation of GaN:ZnO with well-defined crystalline structures can be realized at reduced temperatures (650 °C) and/or durations (10 min). Recently, we have proposed a facile method for the synthesis of nanoporous GaN:ZnO photocatalyst by utilizing Ga-Zn LDHs and urea as the uniform mixed metal oxide precursor and source of nitrogen, respectively [65]. The synthesis mechanism and material characterization of the obtained samples are presented in Chapter 3 of this thesis.

1.5.2 Utilization of HER and OER catalysts

Even if the photo-generated electrons and holes contain thermodynamically sufficient potentials for water splitting half-reactions, they essentially recombine if active sites for the redox reactions do not exist on the surface of the photocatalyst. The surface of the photocatalyst is usually decorated with co-catalyst materials such as Pt, rhodium (Rh), gold (Au) and nickel (Ni) to

introduce active sites for H₂ evolution, because the CB levels of many photocatalysts are not high enough for the H₂ evolution reaction without catalytic assistance [89]. Particularly, metal nitride and oxynitride photocatalysts are not active for overall water splitting without surface modifications with co-catalysts, due to lack of HER active sites on their surface. Decoration of the surface of these photocatalysts with HER co-catalysts led to remarkable visible-light water splitting performances [42,90–93].

Co-catalysts are typically applied as nanoparticles (NPs) to the photocatalyst surface by impregnation or photo-deposition methods [94]. In the impregnation method, co-catalysts salts are randomly anchored to the photocatalyst surface, where activation takes place in the post-processing steps [91,92]. In contrast, photo-deposition allows the co-catalyst NPs to be located selectively at the reaction sites, where usually no post-activation step is required [97–99]. Due to such deposition mechanism, samples modified by photo-deposition route have exhibited superior photocatalytic performances, compared to those treated via impregnation technique [100].

It is known that HER active sites also catalyze the water splitting reverse reaction (*i.e.* formation of water from evolved H₂ and O₂), which limits their role for OWS application. Various approaches have been studied to suppress the back-reaction. For instance, Sayama and Arakawa, and Abe et al. showed that the rate of back-reaction on Pt catalysts surface can be nearly suppressed during OWS by adding Na₂CO₃ or NaI to water splitting solution [101,102]. Very recently, Pan et al. proposed an amorphous Si-Ti oxyhydroxide surface coating that not only stabilizes photocatalysts surface from deactivation, but also inhibited the undesired reverse reaction [103]. Domen and co-workers engineered a metal-Cr₂O₃ core-shell co-catalytic system that suppresses the undesired reaction of H₂ and O₂ [91,94,99]. As demonstrated in Figure 1.7, the Cr₂O₃ shell

surrounding the metal NPs inhibits the access of the evolved O_2 molecules to the HER active sites, while maintaining the flow of H^+ ions for H_2 production.

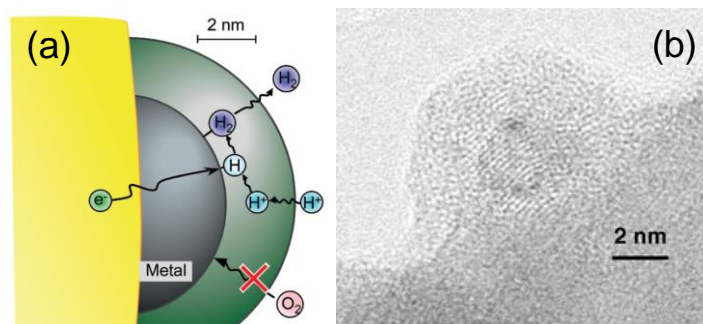


Figure 1.7: Metal- Cr_2O_3 core-shell HER co-catalyst (a) the mechanism in which Cr_2O_3 shell suppresses the undesired water formation [104], reprinted with permission from (J. Phys. Chem. C, 2009, 113 (23), pp 10151–10157). Copyright (2009) American Chemical Society, and (b) HRTEM image of Rh- Cr_2O_3 core-shell fabricated via in-situ photo-deposition [91], reprinted with permission from (Angew. Chem. Int. Ed. 2006, 45, 7806–7809). Copyright (2006) Wiley-VCH Verlag GmbH & Co. KGaA, Weinheim.

Maeda et al. studied the co-loading of the GaN:ZnO solid solution photocatalyst with Rh- Cr_2O_3 (HER) and Mn_3O_4 (OER) catalysts [105]. Their study concluded that decoration of the Rh- Cr_2O_3 -GaN:ZnO photocatalysts surface with 0.05 wt% of Mn_3O_4 enhances the rates of gases evolution by ~1.5-folds. Xiong et al. reported a similar observation by applying RuO_2 and IrO_x OER co-catalysts, although 0.02 wt% was identified as the optimal loading of the OER catalysts [100].

1.5.3 Utilization of conductive support

The majority of the photo-generated carriers are recombined within the bulk of the GaN:ZnO photocatalyst at the crystalline defects and grain boundaries [106]. It is well-

documented that the low efficiency of the photocatalytic systems, which inhibits their commercial realization, is mostly attributed to the recombination of the photo-induced charges [107–109]. Therefore, decreasing the rate of recombination losses is the most important task in developing an efficient photocatalyst, since these charges are the basis of the photocatalytic activity. In the past decade, various strategies, including crystal modifications, band gap engineering, interfacial hetero-structuring, and surface sensitization of semiconductor photocatalysts have been attempted to improve their performances [110].

In recent years, immobilization of photocatalyst materials onto conductive supports has emerged as a promising strategy to enhance solar fuel generation efficiencies. Conductive supports provide effective separation of charge carriers, thus minimizing the photo-recombination losses [10,108,109].

Dating back to October 2004, a revolution in science and technology was triggered when Geim and Novoselov [113] prepared two-dimensional sheets of carbon atoms: graphene. Graphene, as an allotrope of carbon, is composed of layers of atoms packed into a honeycomb network that can be exfoliated from bulk graphite. Graphene shortly became one of the attractive components in photonics, energy conversion and storage, as well as environment, sensing and catalysis, owing to its outstanding mechanical, thermal, optical, and electrical properties [114–116]. The characteristics of graphene are highly similar to those of single-walled carbon nanotubes (SWCNTs), while it can be prepared at significantly lower costs [117]. In particular, graphene's massive theoretical specific surface area ($\sim 2,600 \text{ m}^2 \text{ g}^{-1}$ [116]), high mobility of charge carriers ($200,000 \text{ cm}^2 \text{ V}^{-1} \text{ s}^{-1}$ at room temperature [114]), excellent thermal conductivity ($3,000\text{--}5,000 \text{ W m}^{-1} \text{ K}^{-1}$ [118]), with 97.7% optical transmittance, and $<0.1\%$ reflectance [119], make it an excellent choice for light harvesting and energy conversion devices fabrication. Within a few years,

graphene-derivative materials such as graphene oxide (GO), reduced graphene oxide (rGO), nanoribbons, quantum dots (QDs), and their functionalized counterparts demonstrated peculiar and fascinating properties.

GO is a two-dimensional carbon nanomaterial with many merits such as low manufacturing cost, facile mass production, tunable chemistry and semiconducting behavior [120]. The surface of GO nanosheets is decorated with epoxide ($-O-$) and hydroxyl ($-OH$) groups; while carbonyl ($-C=O$) and carboxyl ($-COOH$) groups are linked to the edges of the nanosheets [121]. These functionalities allow GO and rGO to interact with a wide range of precursors and structures through non-covalent, covalent and/or ionic interactions [119,113]. Chemical interactions in the GO structures are categorized into sp^2 and sp^3 hybridizations. The sp^2 hybridization is attributed to the bonding of carbon atoms to the neighboring carbon atoms (which are not connected with hydroxyl or epoxy groups) or oxygen in the form of carbonyl or carboxyl groups. On the other hand, sp^3 hybridization forms when a carbon atom is bonded to epoxy or hydroxyl functional groups [123]. Various densities of sp^3 hybridization in GO structure create a wide range of interesting characteristics. In addition to their role in tailoring the electrochemical characteristics, the optical properties of GO is a strong function of sp^2 and sp^3 hybridization densities and their electrical interaction [124] [125].

Graphene QDs, as zero dimensional layers of sp^2 hybridized honeycomb carbon, have grasped enormous attention and been studied extensively for wide range of applications, energy conversion in particular [126,127]. Within their ultra-small sizes (typically less than 10 nm), their optical and electrical properties can be tailored precisely and a well-defined band gap can be formed [126,127]. To that regard, graphene QDs are very similar to highly crystalline inorganic

semiconductor QDs with physically and chemically reactive facets, owing to their dense surface functionalities [128].

Integration of highly conductive graphene nanosheets with massive surface area into an efficient photocatalytic system could improve the separation of photo-excited charges, while dedicating different sites for evolution of hydrogen and oxygen, as displayed in Figure 1.8. Due to the differences in energy band structures of photocatalyst and graphene, photo-excited electrons can be injected to the conductive nanosheets and efficiently interact with protons in the electrolyte, while water oxidation reaction occurs on the surface of the photocatalyst.

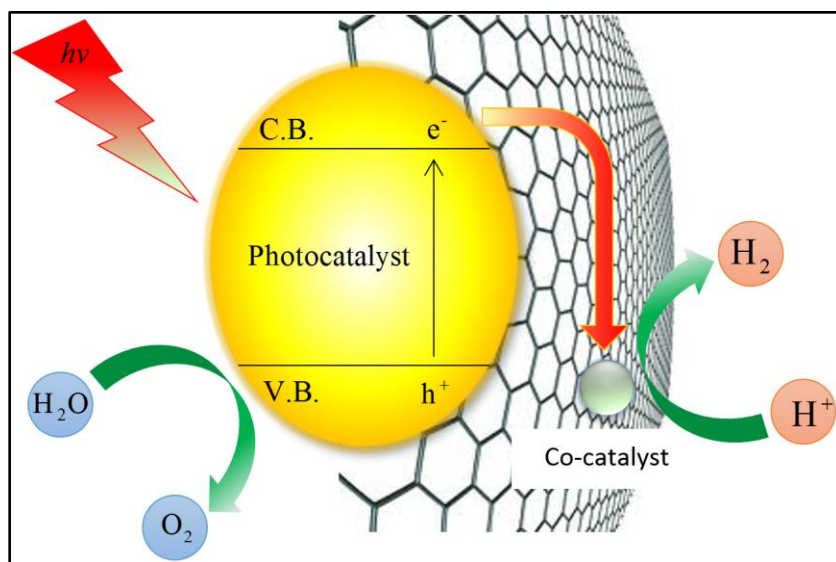


Figure 1.8: Schematic illustration of the effectiveness of graphene in enhancing the efficiencies of the photocatalytic water splitting reactions.

The first report on the fabrication of graphene-based composites (GBCs) was made by Stankovich and co-workers who demonstrated the effectiveness of graphene in tuning the electrical conductivity of polymers [129]. Since then, tremendous efforts were dedicated to the tailoring of

optical, structural, and electrochemical characteristics of GBCs at the nanoscale, resulting in remarkable improvements. The effectiveness of graphene as a conductive support for water splitting application has been extensively studied for oxide, sulfide, their alloys, and ternary composites [116,130]. Despite the outstanding photocatalytic performances of metal nitride and oxynitride photocatalysts, the majority of studies have focused on the GBCs of graphitic carbon nitride (g-C₃N₄). In recent years, surface and structure modification of g-C₃N₄-rGO composites resulted in fascinating enhancements in the photocatalytic activities, primarily attributed to the fast charge separation and high surface area of the composite photocatalysts [131–133]. For oxynitride semiconductors on the other hand, reports are limited to a few recent studies. Mukherji et al. investigated the effect of Sr₂Ta₂O₇ nitrogen doping on the optical absorption, as well as integration of rGO nanosheets, as the electron transport “highway”, on the charge-carrier migration [134]. In this system, nitrogen doping narrowed down the band gap and led to 87% increase in the H₂ evolution rate, and incorporation of 5 wt% GO and 0.5 wt% Pt resulted in an additional 80% improvement. The Pt-Sr₂Ta₂O_{7-x}N_x-rGO composite reached to 6.45% sacrificial QE under 280–550 nm irradiation, over 2.7-times higher than the undoped Sr₂Ta₂O₇.

Our group recently reported enhanced photocatalytic activity of the GaN:ZnO solid solution through rGO hybridization [135]. A facile ultra-sonication/blending route driven by electrostatic self-assembly resulted in uniform distribution of the photocatalysts particles over rGO nanosheets. To our knowledge, the work presented in the Chapter 5 of this thesis (published in [135]) is the first report on the fabrication, characterization and performance evaluation of the GaN:ZnO solid solution GBCs. Very recently, Li et al. prepared GaN:ZnO-rGO composite by nitridation of hydrothermally synthesized nanocrystallite ZnGa₂O₄-GO composite under ammonia

at 700 °C for 6 h [136]. The prepared composite exhibited higher photocatalytic hydrogen generation by almost 4.5-times, compared to the blank photocatalyst.

1.5.4 One-dimensional nanostructures of GaN:ZnO

It is generally accepted that one-dimensional (1-D) nanostructures provide versatile systems to investigate the dependency of optical, and electrochemical properties on dimensionality and size reduction (quantum confinement) [137]. In the last decade, semiconductor nanofibers (NFs), nanowires (NWs) and nanotubes (NTs) have become the focus of intensive research. This interest arises from their peculiar properties originating from their 1-D nanostructure, which is responsible for their high active surface area, short distances of charge carrier transport, tailored diffusion path length for the positive and negative charges, enhanced light trapping in high-density arrays, and controlled size and composition over a wide range [138–140].

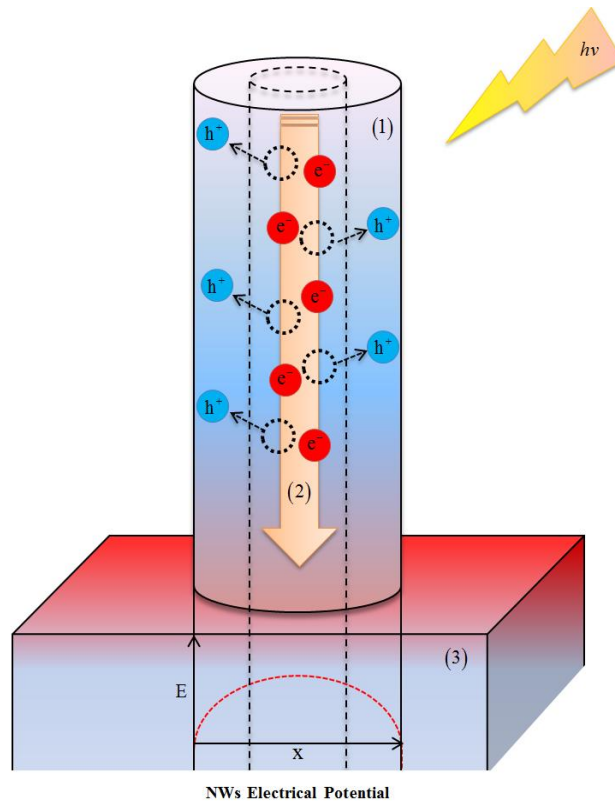


Figure 1.9: Charge separation mechanism driven by the electrical field in the space-charge region of an individual n-type nanowire (1) semiconductor NW, (2) photo-excited electrons highway, and (3) substrate [9].

Photo-generated charges in bulk structures and close-packed crystallites tend to recombine at the structural defects and grain boundaries [108,109]. On the other hand, due to the strong electrical field at the space-charge region near their lateral surface, 1-D nanostructures minimize the charge recombination, because the majority charge carriers (electrons in n-type semiconductors) can be collected and transported along the individual nanowires axis [141], while minority charge carriers (holes in n-type semiconductors) travel towards the surface. This process is schematically illustrated in Figure 1.9.

The synthesis of ZnO and GaN NWs and NTs has been studied extensively in the last decade. The preparation of single crystal ZnO NWs with tailored diameters and aspect ratios can

be realized through various techniques including solution-based methods, and vapor phase transfer routes [142,143]. The fabrication of single crystal GaN NWs is also reported through ultra-vacuum chemical vapor deposition (CVD) [144–146]. Due to the very high temperature required for the CVD preparation of GaN NWs (typically >1000 °C), metal-organic CVD (MOCVD) has been the focus of several studies for fabrication of GaN NWs at medium temperature (~ 550 °C) or atmospheric pressure [147,148]. Recently, Mi and co-workers fabricated a series of doped and multiband heterostructure NWs based on GaN through molecular beam epitaxy (MBE), which exhibited high photocatalytic activities at UV and visible regions [33,35,36,38,146,147].

Within the last few years, some studies have been conducted on the synthesis and application of GaN:ZnO solid solution NWs and NTs. For the first time, preparation of GaN:ZnO solid solution NWs was reported in 2010 by Han et al. who investigated the effectiveness of vacuum CVD at 900 °C using ZnGa_2O_4 NPs as the source material [64]. The CVD growth of single crystal GaN:ZnO NWs with $x = 0.12$ was confirmed through vapor-liquid-solid (VLS) mechanism.

In 2012, Hahn and colleagues reported an epitaxial casting approach, in which the GaN:ZnO solid solution NTs were synthesized through diffusion of the ZnO core into the GaN shell at high temperature [151]. The prepared NTs with $x = 0.10$ demonstrated 1.5–2 times improvements in the sacrificial H_2 and O_2 generation, compared to those of the powder solid solution photocatalyst with similar composition. In a similar approach, Zhong and co-workers proposed a two-step template-based fabrication route for highly ordered and dense NW arrays of ZnO-GaN:ZnO core-shell through high temperature (1150 °C) vapor-phase diffusion of Ga and N into single crystal ZnO NWs lattice [152]. The ZnO-GaN:ZnO core-shell NWs photo-anode exhibited highly stable water splitting under visible light irradiation with 0.3 V_{RHE} onset potential.

Very recently, Jiang et al. demonstrated the fabrication of Zn-rich GaN:ZnO solid solution nanorods (NRs) through sol-gel solid-state growth followed by nitridation under ammonia flow at 800–900 °C for 30–120 min [62]. The Zn-rich NRs (up to $x = 0.95$) prepared in this study strongly responded to the photons with wavelength up to 590 nm which is significantly higher than the one reported for the powder photocatalyst around 440 nm [74,153,154].

In this research, various routes for the fabrication of 1-D nanostructures containing Ga, Zn, O, and N (GaZnON) have been developed, where focus is placed on the catalyzed vapor phase approaches. The outcomes of this study are presented in Chapter 6.

Chapter 2: Approaches and Methods

Development of several photocatalyst materials through various techniques has been practiced in this research. The synthesized samples structure, morphology and optical properties were characterized thoroughly, and their photocatalytic performances were examined accordingly. The following chapter describes the approaches and methods, as well as the experimental apparatuses applied in this research.

2.1 Materials

The following materials have been used for processing of various samples as received, without further purifications:

Ga₂O₃ (99.99+%, Sigma-Aldrich), ZnO (99+%, Sigma-Aldrich), Zn (99+%, Sigma-Aldrich), urea (Sigma-Aldrich), NaOH (≥97%, Fisher Scientific), Na₂CO₃ (≥99.50%, Fisher Scientific), Na₃RhCl₆ (Sigma-Aldrich), H₂PtCl₆.6H₂O (≥37.50% Pt basis, Sigma-Aldrich), Ni(NO₃)₂.6H₂O (99.999%, Sigma-Aldrich), K₂CrO₄ (≥99%, Sigma-Aldrich), Na₂IrCl₆.6H₂O (99.9%, Sigma-Aldrich), KMnO₄ (99%, EMD Millipore), NaNO₂ (≥99%, Sigma-Aldrich), natural graphite flakes (Sigma-Aldrich), H₂SO₄ (98%, Sigma-Aldrich), NaNO₃ (99%, Sigma-Aldrich), H₂O₂ (30–32 wt% in water, Sigma-Aldrich), Zn(NO₃)₂.xH₂O (99.999%, Sigma-Aldrich), Ga(NO₃)₃.xH₂O (99.99%, Sigma-Aldrich), Zn(CH₃COO)₂ (99.99%, Sigma-Aldrich), Hexamethylenetetramine (≥99%, Sigma-Aldrich), and Ethanolamine (≥99.50%, Sigma-Aldrich).

Ultra-pure gasses (N₂, Ar, and NH₃), polished quartz plates and Si (100) substrates were purchased from Praxair, TGP, and Ted Pella Inc., respectively.

2.2 Preparation of nanoporous GaN:ZnO solid solution photocatalyst

2.2.1 Precursors

Two precursors were used for the synthesis of GaN:ZnO solid solution photocatalyst. Urea was used as the source of nitrogen, while mixture of Ga₂O₃ and ZnO (mixed precursor) or Ga³⁺-Zn²⁺ layered double hydroxides (Ga-Zn LDHs) were employed as the source of Ga and Zn.

2.2.1.1 Mixed precursor (physical approach)

For the preparation of the precursor via physical approach, a powder mixture of Ga₂O₃, ZnO, Zn, and urea was prepared as follows: A stoichiometric amount of Ga₂O₃ and pre-synthesized (600 °C for 1 h) ZnO ([Zn]/[Zn+Ga] = 0.06–0.67) was added to appropriate amount of Zn ([Zn]/[Ga] = 0.25) and urea powders. The prepared mixture was ball-milled (SPEX SamplePrep 8000-series Mixer/Mills) for 10 min to obtain a uniform mixed precursor.

2.2.1.2 Layered double hydroxide precursor (chemical approach)

The layered double hydroxide (LDHs) of Ga³⁺ and Zn²⁺ was prepared through the procedure described in the literature [63], with some modifications. Various amount of Ga₂O₃ and ZnO powder with [Zn]/[Zn+Ga] = 0.06–0.67 were dissolved in 8M HCl at boiling temperature. The pH of the solution was adjusted to 9 with a mixed aqueous solution of 2M NaOH and 1M Na₂CO₃, added drop-wise to the acidic solution under vigorous stirring. The obtained slurry was aged in the mother liquor for 18–24 h at 80 °C. The precipitates were collected and washed thoroughly with pure water and ethanol, and subsequently dried overnight in a laboratory oven at 80 °C. The dried LDHs powder was mixed with Zn ([Zn]/[Ga] = 0.25) and urea powders in a stainless steel ball-mill jar for 10 min to obtain a uniform precursor.

2.2.2 Nanoporous GaN:ZnO solid solution

The nanoporous GaN:ZnO solid solution was prepared through the technique we have reported recently [65]. In a typical synthesis, the prepared precursor was loaded into a semi-sealed alumina synthesis vessel and placed in a preheated laboratory muffle furnace for solid-state preparation at various temperatures and durations. The thermally treated samples were collected, refluxed in 10 V% ethanol aqueous solution at 60 °C for 4 h and washed with pure water. The washed photocatalysts were dried in the oven overnight and annealed in air at 600 °C for 1 h. The photocatalyst samples prepared using LDHs and mixed precursor are denoted as GaZnON-LDHs and GaZnON-M, respectively.

2.3 Traditional GaN:ZnO solid solution

The traditional GaN:ZnO solid solution was prepared using a method described elsewhere [25] with modifications. A uniform mixture of Ga₂O₃ and ZnO powders ([Zn]/[Ga] = 1) was prepared by 10 min ball-milling in a stainless steel jar. Nitridation of this uniform mixture was carried out under 250 mL min⁻¹ NH₃ at 850 °C for 13 h. The obtained photocatalyst was thermally treated at 550 °C for 1 h in air.

2.4 Co-catalysts nanoparticles deposition

Co-catalysts nanoparticles were loaded on the surface of the synthesized photocatalyst samples through impregnation and photo-deposition techniques. In this research, various hydrogen evolution and oxygen evolution co-catalysts have been tested for their catalytic behavior. Na₃RhCl₆, H₂PtCl₆.6H₂O, Ni(NO₃)₂.6H₂O, K₂CrO₄, Na₃IrCl₆.6H₂O, and KMnO₄ precursors were used for deposition of Rh, Pt, NiO_x, Cr₂O₃, IrO_x, and Mn₃O₄ co-catalysts, respectively. The values

stated in this thesis for co-catalysts loading (wt%) are based on the metallic contents in the deposition solution.

2.4.1 Co-catalysts impregnation

Co-catalysts impregnation was carried out through the procedure described in [99], with modifications. In a typical procedure, co-catalysts salt is dissolved in 3–4 mL of pure water and added to the synthesized photocatalyst powder. The paste is continuously mixed with a glass rod on a hot plate at 40 °C until dryness. The dried powder was kept at room temperature for 18–24 h to ensure complete dryness at a slow evaporation rate. The powder was transferred to a laboratory muffle furnace for thermal treatment at 350 °C for 1 h. the loaded sample was cooled down at room temperature and collected for further use.

2.4.2 Co-catalysts photo-deposition

Co-catalysts nanoparticles were deposited through photo-deposition as described previously [99], with modifications. The synthesized photocatalyst was stirred in pure water and purged with ultra-pure nitrogen for several hours to obtain an oxygen-free suspension. An oxygen-free solution containing appropriate amount of co-catalysts salt was introduced to the photocatalyst suspension in the dark and purged with ultra-pure nitrogen for another 2 h, when the suspension was irradiated with visible light for 4–6 h. The catalysts-loaded photocatalyst was collected, washed with pure water and dried overnight. The powder was processed at 350–400 °C for 1 h.

2.5 Preparation of GaN:ZnO hybridized reduced graphene oxide (GaN:ZnO-rGO)

2.5.1 Graphene oxide (GO)

Pre-exfoliated graphite was used as the starting material of the modified Hummer's method for GO synthesis [155]. A few gram of natural graphite flakes was ultra-sonicated in pure water

for 3 h, reduced in grain size to pre-exfoliated graphite. The pre-exfoliated graphite was collected and dried at 80 °C overnight. 1 g of the pre-exfoliated graphite powder was added to a mixture of 23 mL concentrated H₂SO₄ and 500 mg of NaNO₃ in an ice bath. 3 g of KMnO₄ was slowly added to the suspension to avoid any violent or explosive reactions. The rate of addition was controlled carefully to prevent the temperature of the suspension from exceeding 20 °C. The dark green suspension was removed from the ice bath and gradually heated to 35–45 °C for an hour. The resulted paste was diluted with 40 mL pure water, when its temperature reached to 98 °C, which was then maintained at this temperature for another 15 min. Thereafter, 40 mL of 10 wt% H₂O₂ was added to the paste to react with KMnO₄ residues. The prepared GO was collected and washed with 5 V% H₂SO₄ and H₂O₂ mixture, and pure water thoroughly, and dried at 80 °C overnight.

2.5.2 GO/rGO-GaN:ZnO composite

1 mg ml⁻¹ GO solution was prepared by ultra-sonication of an appropriate amount of the prepared GO in pure water for 1–2 h. The GaN:ZnO-GO composite was prepared by 1 h sonication and several hours mixing of GaN:ZnO uniform suspension and GO solution. The prepared suspension was then purged with ultra-pure nitrogen and exposed to visible-light irradiation for 4–6 h to obtain the GaN:ZnO-rGO composite.

2.6 Fabrication of GaN:ZnO thin film

2.6.1 Chemical-bath growth of nanowires (NWs)

2.6.1.1 ZnO seeding

A polished quartz substrate was cleaned in 50-50 V% isopropanol-ethanol solution and seeded with ZnO nanoparticles (NPs) by applying some modifications to the method described in the literature [142]. 0.5 µL of a 5 mM zinc acetate solution in ethanol was triple spin coated on the

clean quartz substrate at ~2000 rpm. The substrate was dried by for 30 s on the spin coater and thermally treated for 5 min on the hot plate at 180 °C between each coating, to ensure an adequate adhesion of NPs. The coated substrate was annealed in a laboratory muffle furnace at 250 °C for 20 min and cooled down at room temperature.

2.6.1.2 ZnO nanowires (NWs)

A thin film of ZnO NWs was prepared by the technique described in [156], with modifications. The seeded quartz substrate was placed up-side-down in a stoichiometry aqueous solution of 35 mM $\text{Zn}(\text{NO}_3)_2 \cdot x\text{H}_2\text{O}$ and HMT in a glass vial. The vial was placed in a laboratory oven at 93 °C for 6 h. The obtained NWs were washed with pure water, and ethanol, and subsequently annealed in furnace at 350 °C for 30 min.

This procedure was repeated for direct growth of Zn-Ga mix-metal oxide NWs by adding stoichiometric solution (35 mM) of $\text{Ga}(\text{NO}_3)_3 \cdot x\text{H}_2\text{O}$ to the growth solution, use of zinc acetate as an alternative source of Zn, as well as application of ETA and HMT as the morphology-regulating reagents.

2.6.1.3 Impregnation of ZnO NWs with Ga^{3+}

The prepared ZnO NWs were placed inside a plastic petri dish, where its surface was covered with a few droplets of 5–35 mM $\text{Ga}(\text{NO}_3)_3 \cdot x\text{H}_2\text{O}$ aqueous solution. The petri dish was kept static until complete dryness. The Ga^{3+} -ZnO NWs were washed with pure water to remove the residues of the solvents, and subsequently annealed at 350 °C for 30 min.

2.6.2 Chemical vapor deposition of GaN:ZnO solid solution

2.6.2.1 Au-catalyst coating

Deposition of the Au-catalyst thin film was conducted in a high-vacuum Leica EM MED 020 coating system for planar magnetron sputtering, equipped with a quartz crystal film thickness monitor. A few substrates were ultra-sonicated in 50-50 V% isopropanol-ethanol solution, dried at the room temperature and subjected to 10 nm Au coating. The coated substrates were stored in a clean desiccator for further use.

2.6.2.2 GaN:ZnO thin-film growth via atmospheric pressure chemical vapor deposition (APCVD)

The APCVD growth of GaN:ZnO thin film was performed in a 40 mm quartz tube inside a 400 mm single-zone NANYANG XINYU FURNACES-SK2-4-12TPB4 tube furnace with ± 1 °C constant temperature control precision. A uniform mixture of Ga₂O₃ and ZnO (1:1 wt) was loaded in an alumina boat and placed at the center of the heated zone. The Au-coated substrates were secured at the various locations of the quartz tube as described in the text. Quartz tube was purged with ultra-pure Ar gas for 1 h when the flow was switched to ammonia 30 min prior to heating. Reaction tube was heated at 20 °C min⁻¹ while NH₃ gas was flowing at 250 mL min⁻¹ at atmospheric pressure. After a given growth time, furnace heating was terminated automatically and the substrates were cool down at the room temperature under ammonia flow. The synthesized thin films were washed with pure water and 10 V% ethanol aqueous solution for several times to ensure their surface cleanness from the ammonia residues. The coated substrates were stored in a clean desiccator for further characterizations and tests.

2.6.2.3 Photo-deposition of Rh co-catalyst on the thin film samples

Rh co-catalysts nanoparticles were deposited on the surface of the prepared GaN:ZnO thin film via a procedure similar to the one described earlier for the particulate photocatalyst. In a typical procedure, coated substrate was placed in a top-irradiated photo-reactor filled with appropriate amount of Na_3RhCl_6 in 5 V% ethanol solution. The reaction chamber was evacuated and re-filled with ultra-pure nitrogen for several times prior to irradiation. The coated substrate was irradiated with visible light for 30 min. After this period, the irradiation was terminated and the Rh-loaded GaN:ZnO thin film was taken out, washed with pure water, dried at room temperature and subsequently treated at 350 °C for 20 min.

2.7 Material characterizations

2.7.1 Scanning electron microscopy (SEM) and energy-dispersive X-ray (EDX) spectroscopy

To study the surface morphology of the samples and their bulk composition, SEM analysis was conducted at the Centre for High-Throughput Phenogenomics, University of British Columbia (UBC), using an FEI Helios NanoLab 650 dual beam scanning electron microscope equipped with an EDAX TEAM Pegasus energy dispersive X-ray spectrometer. For imaging, samples were coated with 4–8 nm Ir using a high-vacuum Leica EM MED 020 sputter coater. The edges of the samples were painted with silver suspension to ensure adequate conductivity. Imaging was conducted at an applied voltage of 2–5 keV and a current of 13–50 pA in the secondary electron (SE) and back-scattered electron (BSE) modes, using the Through the Lens Detector (TLD) and Everhart-Thornley Detector (ETD).

ImageJ 1.50i software was used for analyzing the SEM images. The average dimensions (diameter and length) of the 1-D nanostructures were estimated from the SEM images in four regions of the substrate. For estimation of the aerial density, the number of nanowires with dominant morphology was counted in four regions of the substrate. The number of gold nanoparticles on the substrate was estimated using the “Analyze particle” function at an adjusted threshold to obtain the highest resolution.

To ensure minimal background detection, EDX elemental data were obtained at 5–20 keV applied voltage, depending on the dimensions of the analyzed samples. Based on the applied voltage, Ga $L\alpha$ (1.098 keV) and $K\alpha$ (9.251 keV), Zn $L\alpha$ (1.012 keV) and $K\alpha$ (8.637 keV), N $K\alpha$ (0.392 keV), O $K\alpha$ (0.525 keV), Rh $L\alpha$ (2.697 keV), Cr $K\alpha$ (5.415 keV), Si $K\alpha$ (1.740 keV), and Au $M\alpha$ (2.123 keV) energy lines were employed for material identification and quantification [157]. For particulate samples, to enhance the reliability of EDX elemental data, the compositions obtained from a wider area at low magnification (typically a few microns field of view) were compared to the high resolution data. Further density analysis at BSE mode was employed to identify the contaminations, unreacted compounds and residues. The obtained EDX data were corrected by normalizing the composition of the materials to no-carbon-basis (due to high carbon background signal from carbon tape). The same procedure was applied to the composition of Si for the thin film samples, due to the intense Si $K\alpha$ signal from the substrate. The presented elemental data for various samples were selected by considering the lowest deviations from the average composition.

2.7.2 X-ray diffraction (XRD) analysis

X-ray diffraction (XRD) analysis was conducted at the Powder X-ray Diffraction Laboratory, Chemistry Department, UBC. A Bruker D8 Advance X-ray diffractometer in Bragg-Brentano configuration with Cu K-alpha radiation was used to determine the crystalline phases and the structures of the prepared precursors and samples through X-ray diffraction measurements. For powder XRD, some of the collected XRD data were aligned in respect to the low intensity peaks at $2\theta \sim 90^\circ$, which found to be unchanged for various samples. For the thin film samples on the Si substrate, analysis was terminated at $2\theta = 65^\circ$, due to the intense Si peak observed at $2\theta \sim 67^\circ$. Scherrer equation (8) was used to calculate the mean size of the ordered crystalline domain (nm) of the samples [158].

$$d_{\text{crystallites}} = \frac{K\lambda}{\beta \cos(\theta)} \quad (8)$$

where K is a dimensionless shape factor with a typical value equal to 0.9, λ is the X-ray wavelength equal to 1.54 Å, β is the peak full width at the half of the maximum intensity (FWHM) in radians, and θ (degree) is the diffraction angle (2θ) divided by 2. The d-spacing of the crystallographic planes were calculated using the Bragg's law (9) and the lattice parameters were calculated by equation (10) for the hexagonal crystal structure [158]:

$$d_{(h,k,l)} = \frac{\lambda}{2\sin(\theta)} \quad (9)$$

$$d_{h,k,l}^{-2} = \frac{4}{3} \frac{h^2 + hk + k^2}{a^2} + \frac{l^2}{c^2} \quad (10)$$

where h , k , and l are the crystal facets Miller indices, while a and c (Å) are lattice constants.

2.7.3 Surface area

The surface area (S_{BET}) measurement of the samples was conducted at the Catalysis Laboratory, Department of Chemical and Biological Engineering (CHBE), UBC, through the single-point Brunauer–Emmett–Teller (BET) analysis, using a Micrometrics FlowSorbII 2300. Appropriate amount of sample was loaded in a Pyrex BET tube and degassed for several hours prior to the test. The average particle size was estimated from equation (11) [159]:

$$d_p = \frac{6}{S_{\text{BET}} \times \rho} \quad (11)$$

where ρ (g mL^{-1}) is the bulk density. The bulk density of the samples was estimated by dividing the mass (m) of powder (g) occupies a certain volume (V) of the graduate cylinder (mL), as described in equation (12).

$$\rho = \frac{m}{V} \quad (12)$$

2.7.4 X-ray photoelectron spectroscopy (XPS)

The surface chemical states and compositions of the samples were analyzed at the Interfacial Analysis & Reactivity Laboratory (IARL), Advanced Material and Process Engineering Laboratory (AMPEL), UBC, using a Leybold MAX200 X-ray photoelectron spectrometer with Al K-alpha and Mg K-alpha X-ray sources. Ga composition was used as the baseline for converting the data obtained from the Mg K-alpha X-ray source to the Al K-alpha X-ray source. Since carbon can be easily adsorbed on the surface of solid samples from ambient environment, the obtained elemental data were corrected to no-carbon-basis.

High resolution XPS data were analyzed with XPSPEAK 4.1 software to identify the chemical states and their corresponding compositions. Standard binding energies were obtained from the National Institute of Standards and Technology (NIST) database [160].

2.7.5 Transmission electron microscopy (TEM) and scanning transmission electron microscopy (STEM)

The synthesized photocatalysts crystalline structure, co-catalyst nanoparticles deposition, and elemental distributions were investigated through transmission electron microscopy (TEM) and scanning transmission electron microscopy (STEM) using:

- 1) FEI Tecnai TEM equipped with a 200 kV LaB6 filament capable of 1.4 Å point-to-point resolution (Bioimaging Facility, UBC).
- 2) FEI Tecnai Osiris S/TEM system equipped with Analytical TWIN (A-TWIN) objective lens integrated with Super-X EDX detection system, Gatan Ultrascan CCD camera, HAADF, and BF STEM detectors, capable of STEM/EDX mapping (Esprit), and S/TEM tomography (4D LABS, Simon Fraser University).

For the TEM/STEM sample preparation, the powder samples were dispersed in ethanol and sonicated for a given time. 200 µL of the photocatalyst suspension was drop casted on a Ted Pella carbon Type-B, 200 mesh TEM grid, and dried at the room temperature. The coated grids were stored in a clean TEM grid storage inside a desiccator for further analysis.

Due to difficulties in transferring the samples synthesized on the Si substrate to ethanol solution by the above procedure (ultra-sonication), the following methods were applied:

- 1) Scratching method: The coated Si substrate was covered with a few droplets of ethanol and its surface was scratch with a knife for several times. The obtained suspension was ultrasonicated for 30 min, and drop casted on the TEM grid as described earlier.
- 2) Freezing method: The surface of the coated Si substrate was covered with a few droplets of pure water, and placed in a laboratory fridge for 1 h to obtain a frozen layer. The frozen film was detached from the surface of the substrate and used for the preparation of TEM grid, as described earlier.

The high angle annular dark field (HAADF) tomography was conducted by acquiring the STEM image of an individual particle between $\mp 70^\circ$ angles at 2° intervals.

The TEM images were analyzed using ImageJ 1.50i software. The Rh co-catalyst size distribution on the surface of the reduced graphene oxide was estimated using the “Analyze particles” function, adjusting the threshold to obtain the highest resolution. The sizes of the Rh nanoparticles on the surface of the nanoporous photocatalyst were estimated manually using ImageJ 1.50i. The crystalline structures of the samples (crystallographic fringes and angles) were also estimated manually using ImageJ 1.50i.

2.7.6 UV-visible spectroscopy

UV-Vis diffuse reflectance of the samples was measured at the Photo-Reaction Engineering Laboratory, CHBE, UBC, using an Ocean Optics Flame UV-Vis detector with a laboratory-grade reflectance probe, equipped with a DH-2000-BAL tungsten/deuterium light source, calibrated to a Polytetrafluoroethylene (PTFE) reflectance standard. The absorption spectra of the samples were estimated using the Kubelka-Munk method, equation (13) [161]:

$$F(R) = \frac{(1 - R)^2}{2R} = \frac{\alpha}{s} \quad (13)$$

where $F(R)$ is the Kubelka-Munk function, R is the portion of the reflected light, α is the absorption coefficient which is function of wavelength, and s is the scattering coefficient. Since s is independent from wavelength, the Kubelka-Munk function can be assumed proportion to α only; therefore, the absorption spectrum can be approximated from $F(R)$.

Due to the high level of noises at the UV region, for estimation of the absorption coefficient, data were collected from the visible and near UV-region. The custom-made apparatus utilized for the diffuse reflectance measurements found to be very sensitive to the angle and distance of the spectrometer probe from the samples surface, and the density of the photocatalyst film; therefore, slight shifts in the measured absorption spectra are anticipated.

The band gap energy (E_g) of the samples was estimated through incorporation of the onset wavelength (abscissa) of the absorption spectra to Equation (4).

2.7.7 Photoluminescence (PL) analysis

The lifetime and rate of recombination of the photo-excited charges as well as the density of the crystal defects were analyzed for various samples at the Laboratory for Advanced Spectroscopy and Imaging Research (LASIR), UBC. The photoluminescence (PL) spectra of the samples were acquired using a combined system consisting of a Princeton Instruments SP2300i and a Hamamatsu C7700 streak camera. The excitation source was an EKSPLA PL2241 picosecond laser with a 10 Hz repetition rate and 30 ps pulse duration at 355 nm. The samples were deposited on the glass slide through drop casting. A blank slide was used to capture the background PL emittance.

2.8 Water-splitting reaction

Various photo-reactor apparatuses were employed in this study for surface modification of the prepared samples, photo-assisted reduction, and photocatalytic performance evaluation.

2.8.1 Center-irradiated photo-reactor

Throughout this research, the following apparatus was used as the primary performance evaluation apparatus, unless stated otherwise.

Photocatalytic water-splitting reactions were conducted in a 900 mL (reaction volume) borosilicate glass reactor (Cansci Glass Product Ltd., Canada), where a USHIO 100 W high pressure UV-Vis Hg lamp was located at the center, in a quartz sleeve. The near-UV portion ($\lambda \leq 420$ nm) of the lamp's output was filtered by 2M NaNO₂ solution. The gaseous products of the photocatalytic reactions in this apparatus can be sampled manually via a sealed syringe or injected automatically to the gas chromatograph (GC) via a stainless steel tube. The flow diagram of the center-irradiated photo-reactor, absorption spectra of 2M NaNO₂ solution, the light-sources spectra and digital photos of the apparatus can be find in Appendix A.

2.8.2 Pyrex side-irradiated photo-reactor

A 400 mL (reaction volume) Pyrex photo-reactor with side illumination was used occasionally for photo-deposition of co-catalyst nanoparticles. An Osram Sylvania XBO 75W Ozone Free Short Arc Xe Lamp and a UV cut-off filter ($\lambda \geq 420$ nm, <0.5% transmission 300–410 nm, Kupo Co., Taiwan) were used as the light-source and filter, respectively. The gaseous products from this photo-reactor can be sampled manually, via a sealed syringe, or injected automatically to GC via a stainless steel tube. XBO Xe light source spectrum and digital photos of the side-irradiated Pyrex apparatus are presented in Appendix A.

2.8.3 Top-irradiated photo-reactor

To test the performance of the photocatalyst thin films, a top irradiated photo-reactor connected to a vacuum pump and ultra-pure nitrogen supply was used. The USHIO 100 W high pressure UV-Vis Hg lamp was secured at the top of the chamber (~3.0 cm above the quartz top) and a UV cut-off filter ($\lambda \geq 420$ nm, <0.5% transmission 300–410 nm, Kupo Co., Taiwan) was located between the lamp and the quartz top. The gaseous products from the photocatalytic reactions were sampled manually via a sealed syringe and injected to GC for quantification. Digital photo of the top-irradiated photo-reaction is displayed in Appendix A.

2.9 Photocatalytic performance evaluation

2.9.1 Quantum efficiency

For performance evaluation of powder photocatalysts, appropriate amount of samples was dispersed in the test solution inside the photo-reactor and purged with ultra-pure nitrogen or argon gas for several hours prior to reaction. Analysis of the evolved gases was carried out using an Agilent 7890A gas chromatograph equipped with two thermal conductivity detectors (TCD), each modified for detection of hydrogen or oxygen. The apparent quantum efficiency (AQE) of the photocatalyst samples was calculated from equation (14).

$$\phi(\%) = \frac{2 \times H}{I} \times 100 \quad (14)$$

where H and I are the number of evolved hydrogen molecules and irradiated photons, respectively. The spectrum of the light-sources was measured by an Ocean Optics USB2000+ UV-Vis-NIR spectrometer equipped with a DET2B-200-850 detector. The measured spectrum of the light

source with, and without the quartz sleeve and 2M NaNO₂ solution (UV cut-off) are displayed in Appendix A.

The following reaction conditions were adjusted for photocatalytic tests:

2.9.2 Powder samples

2.9.2.1 Independent analysis

The independent analysis in this research includes the followings:

- 1) Effect of synthesis temperature and time on the photocatalytic performance of the nanoporous GaN:ZnO (results are presented in Table 3.1).
- 2) Effect of Zn content of the synthesized nanoporous GaN:ZnO on the photocatalytic performance (results are presented in Figure 3.11).
- 3) Effect of the employed precursor on the photocatalytic performance of nanoporous GaN:ZnO (results are presented in Figure 3.12).
- 4) Deactivation of nanoporous GaN:ZnO photocatalyst (results are presented in Figure 3.13).

A total of 300 mg of the photocatalyst decorated with appropriate amount of co-catalyst materials (metallic basis) was dispersed in pure water inside the photo-reactor. The photo-reactor was purged with ultra-pure nitrogen until oxygen-free suspension was obtained. In the presented data, $t = 0$ is the time when the lamp reaches its maximum power, typically 7–10 min after launching the experiment.

2.9.2.2 Comparative studies

To maintain a reliable comparison and exclude the variations in the photocatalytic performance of the synthesized photocatalyst samples, an appropriate amount of photocatalyst was

prepared through a number of batches, mixed, and used for experiments, as described for the independent analysis.

Comparative studies in this research examined the following:

- 1) Effect of physical surface treatment on the regeneration of the nanoporous photocatalyst (results are presented in Figure 3.16).
- 2) Effect of co-catalyst loading technique as well as hydrogen evolution co-catalyst materials and amount on the photocatalytic performance of the nanoporous GaN:ZnO photocatalyst (results are presented in Figure 4.2 and Figure 4.5).
- 3) Effect of oxygen evolution co-catalyst and loading amount on the sacrificial oxygen evolution of the nanoporous GaN:ZnO photocatalyst (results are presented in Figure 4.7).
- 4) Effect of hydrogen and oxygen evolution catalyst co-loading on the photocatalytic performance of the nanoporous photocatalyst (results are presented in Table 4.1).
- 5) Effect of reduced graphene oxide hybridization and its loading amount on the photocatalytic performance of the traditional GaN:ZnO photocatalyst (results are presented in Figure 5.16 and Figure 5.17, respectively).
- 6) Effect of reduced graphene oxide hybridization and its loading amount on the photocatalytic performance of the nanoporous GaN:ZnO photocatalyst (results are presented in Figure 5.18).

2.9.3 Immobilized photocatalysts panel

For the samples on the substrate, one photocatalyst panel loaded with 1 wt% Rh (metallic basis) was placed inside the reaction vessel of the top-irradiated photo-reactor filled with a 10 V% methanol solution. The reaction vessel was evacuated and re-filled with ultra-pure nitrogen

several times prior to reaction. In the presented data, $t = 0$ is the time when the lamp reaches its maximum power, typically 7–10 min after launching the experiment.

Chapter 3: Facile Synthesis of Gallium-Zinc Oxynitride Solid Solution

Temperatures ranging from 650 °C to 900 °C and durations mostly over hours have been reported for the fabrication of GaN:ZnO solid solutions with various properties, and functionalities corresponding to the composition, morphologies, and structures of the starting materials [25,63,64,71,74,80,162–164]. Lee et al. highlighted that high synthesis temperature (>850 °C) enhances the rate of solid-state reaction; however, it adversely affects the characteristics of the prepared photocatalyst at the nanoscale [71]. It is desired to develop a synthesis method that solid-state reaction can take place at a reasonably high rate, and efficient operating conditions (low temperature or short duration).

At relatively low nitridation temperatures (<700 °C), the chemical transformation from the spinel ZnGa_2O_4 to the wurtzite oxynitride phase is slow, due to insufficient energy to overcome the nitridation activation barrier, and the slow diffusion rates of atoms, within and between the component's structures. It is documented that the formation of spinel phase is the key step of solid-state reaction; while the phase transition from the spinel ZnGa_2O_4 to wurtzite GaN:ZnO solid solution can take place in time order of minutes at 850 °C [74,164], or temperatures as low as 650 °C [71]. It is suggested that an intimate contact between the starting materials plays a crucial role in controlling the rate of solid-state reaction [61,63]. Since the nitridation kinetics are a strong function of solid-solid and solid-gas diffusion flux, the crystallinity and structure of the starting precursor, as well as its introduction into an active nitrogen source are arguably the most important parameters. Without a massive contact between solid-solid starting materials and gas-solid reactants, synthesis time increases substantially. Therefore, a uniform nanostructured precursor with a high active surface area in contact with an effective and sufficient source of nitrogen is essential for the efficient preparation of GaN:ZnO solid solution.

3.1 Effective interaction between solid and gaseous reactants using urea nitrogen source

Urea, as an abundant and non-toxic organic compound, is suitable for large-scale production, and has been extensively studied for the preparation of nitrides and nitrogen-doped materials [165–168]. At elevated temperatures, urea is decomposed via pyrolysis, transforms into nanoscale foam that has been frequently applied as a soft template for synthesis of inorganic nanocrystals and porous structures [169,170]. Compared to other template-based routes, this technique is very convenient and avoids the introduction of impurities [169], suitable for synthesis of nanoporous nitride and oxynitride semiconductors.

Effectiveness of urea as an active source of nitrogen for reducing the synthesis time of wurtzite semiconductors has been reported previously [60,167]. Qiu and colleagues reported an efficient preparation route for GaN powder from gallium-urea complex at 500–600 °C in 1 h, significantly lower compared to the traditional techniques that take place at higher preparation temperatures (>850 °C) for extended periods [167]. Similar observations were reported by Yang et al. who synthesized GaN:ZnO solid solution using urea nitrogen source with a facile microwave technique, that led to a remarkable reduction in synthesis time to 10 min [60].

Kinetic studies of the urea pyrolysis reaction, as well as analysis of the evolved gases indicate the dominance of NH₃; although, the end products of the thermal decomposition are highly dependent on the temperature, heating rate, and decomposition environment [171,172]. This is attributed to the corresponding variation in efflux rates of the different reactants, *e.g.* a higher heating rate leads to a higher gas phase concentration of possible reactants [172].

For the facile preparation of GaN:ZnO solid solution powder photocatalyst in this research, urea was employed as the source of nitrogen. Mixtures of urea with various Zn and Ga mix-metal

compounds was processed as the precursor in the preparation of GaN:ZnO solid solution at various synthesis temperatures and durations.

3.2 Preparation of Ga and Zn mixed-metal precursor

In general, mixed-metal (MM) precursors can be prepared through physical and chemical approaches, such as grinding, ball-milling, and ultra-sonication (physical), as well as chemical reactions and co-precipitation (chemical). Physical methods can be applied to any mixture of metal compounds, while feasible chemical routes must be developed for chemical transformation of metallic salts into MM phases. Common physical and chemical techniques in the preparation of mixed-metal precursors are illustrated in Figure 3.1.

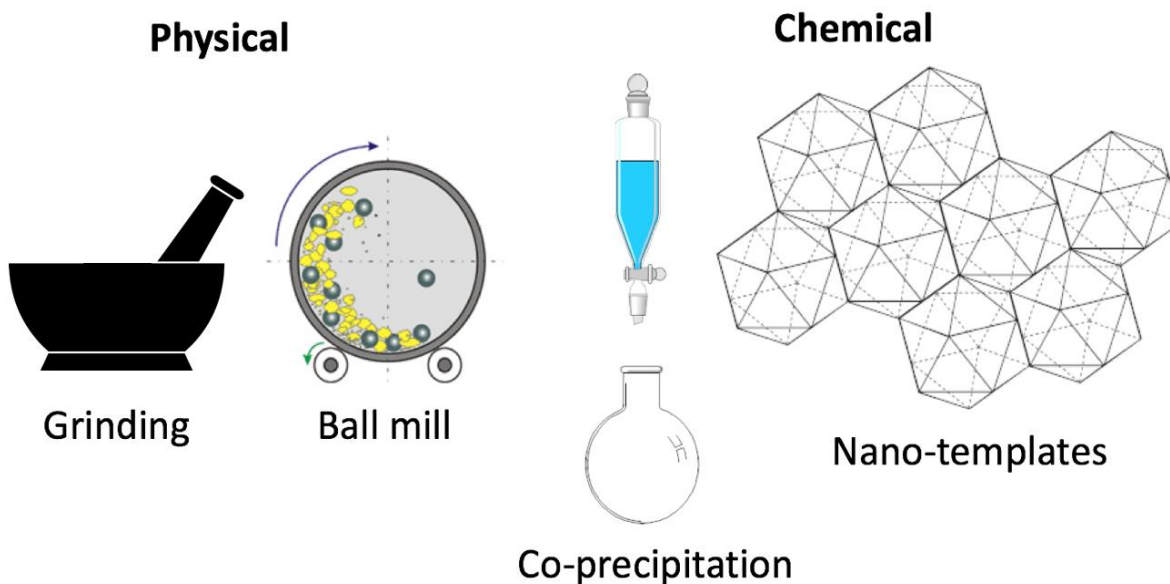


Figure 3.1: Examples of physical and chemical approaches to prepare mixed-metal precursors. Reprint with permission: [CC-BY-SA](<http://creativecommons.org/licenses/by-sa/3.0/>)

In this study, both physical and chemical approaches have been attempted for the preparation of mixed-metal precursors, in which emphasis are centered on the ball-milling (physical) and nano-template-based co-precipitation (chemical) methods.

Use of a nano-template for fabrication of uniform Ga-Zn mixed-metal compound in favor of the GaN:ZnO solid solution synthesis is investigated in this research. A wide range of fabrication techniques is called nano-template-based preparation. In general, transformation of ions and/or disordered structures inside the fluid phase (solution) to materials with tailor-made structure of a template is defined as template-based preparation [173]. To this regard, template-based approaches are similar to co-precipitation, but instead of nucleation and growth freely inside the solution, atoms are arranged inside an ordered structure of a nano-template.

Layered double hydroxides (LDHs) nano-template have been widely studied for the preparation of uniform MM precursors. LDHs are synthetic anionic materials that were discovered in the mid-19th century. LDHs structure, consisting of metal divalent and trivalent hydroxides layers with 7–12 Å basal spacing filled with anions and water molecules, can be represented as $[(M^{2+})_{1-m}(M^{3+})_m(OH)_2]^{m+}(A^{n-})_{m/n} \cdot yH_2O$ [81]. MM hydroxides prepared by the precipitation in the form of LDHs through replacement of divalent cations (M^{2+}) by trivalent ions (M^{3+}) on the brucite-like layers, creates large specific surface areas ($100\text{--}300\text{ m}^2\text{ g}^{-1}$) suitable for many applications [82]. The characteristics of the positively charged layers, and the interlayer anion (A^{n-}), as well as their relative composition (m), can be varied over a wide range [81]. LDHs template is an excellent host for Ga and Zn MM-hydroxide precursor for the solid-state synthesis of GaN:ZnO photocatalyst. Due to the homogeneity of divalent and trivalent cations at the atomic level, in addition to the efficient gas diffusion within the layered structures, synthesis time can be reduced substantially. Wang and co-workers utilized LDHs precursor for GaN:ZnO solid solution

synthesis through NH_3 nitridation. The synthesized photocatalyst was characterized as well-crystalline wurtzite phase, with high photocatalytic activity towards Cr^{6+} ions reduction under visible light [63].

Inspired by the proposed fabrication routes in the literature, a facile preparation technique is proposed in this research that addresses the inefficiencies associated with the traditional synthesis, by utilizing urea and Ga-Zn MM as the starting materials. The synthesis procedures and conditions have been optimized based on the photocatalytic performance of the crystalline Ga^{3+} and Zn^{2+} LDHs precursor that exhibited the highest promise in regards to OWS efficiencies. The proposed approach reduced the synthesis time significantly, while maintaining the nanoscale structure of the final products. To our knowledge, this study is the first demonstration of the efficient synthesis and overall water splitting performance evaluation of the nanoporous GaN:ZnO prepared from the LDHs precursor, and the first contribution to the fundamental understanding of its optical, structural, and photochemical characteristics.

3.3 Synthesis mechanism

At a high heating rate (obtained by placing the precursor in the preheated muffle furnace) and low oxygen atmosphere, urea creates a homogenous foam with massive surface area. This foam has been employed as the nanostructured soft template to help the synthesis of inorganic nanocrystals and formation of nanoporous structures with high active surface areas [169,170,174]. Mixing the uniform MM precursor with urea results in the distribution of the starting materials on this random structure. During the thermal decomposition of urea, the uniform precursor is exposed to oxygen and NH_3 at the high synthesis temperature within the massive surface area of nano/micro foam. This effective interaction between solid-solid and gas-solid reactants at the high preparation

temperature is sufficient for both formation of the spinel ZnGa_2O_4 , and its phase transition to the wurtzite $\text{GaN}:\text{ZnO}$ solid solution. As a result, the solid-solid and gas-solid diffusion rates are significantly enhanced, as illustrated for urea- Ga^{3+} and Zn^{2+} LDHs precursor in Figure 3.2 (a), and the synthesis time is reduced to 12 min in the proposed technique, from the 10+ h reported for the traditional solid-state reaction (slow gas-solid diffusion) depicted in Figure 3.2 (b).

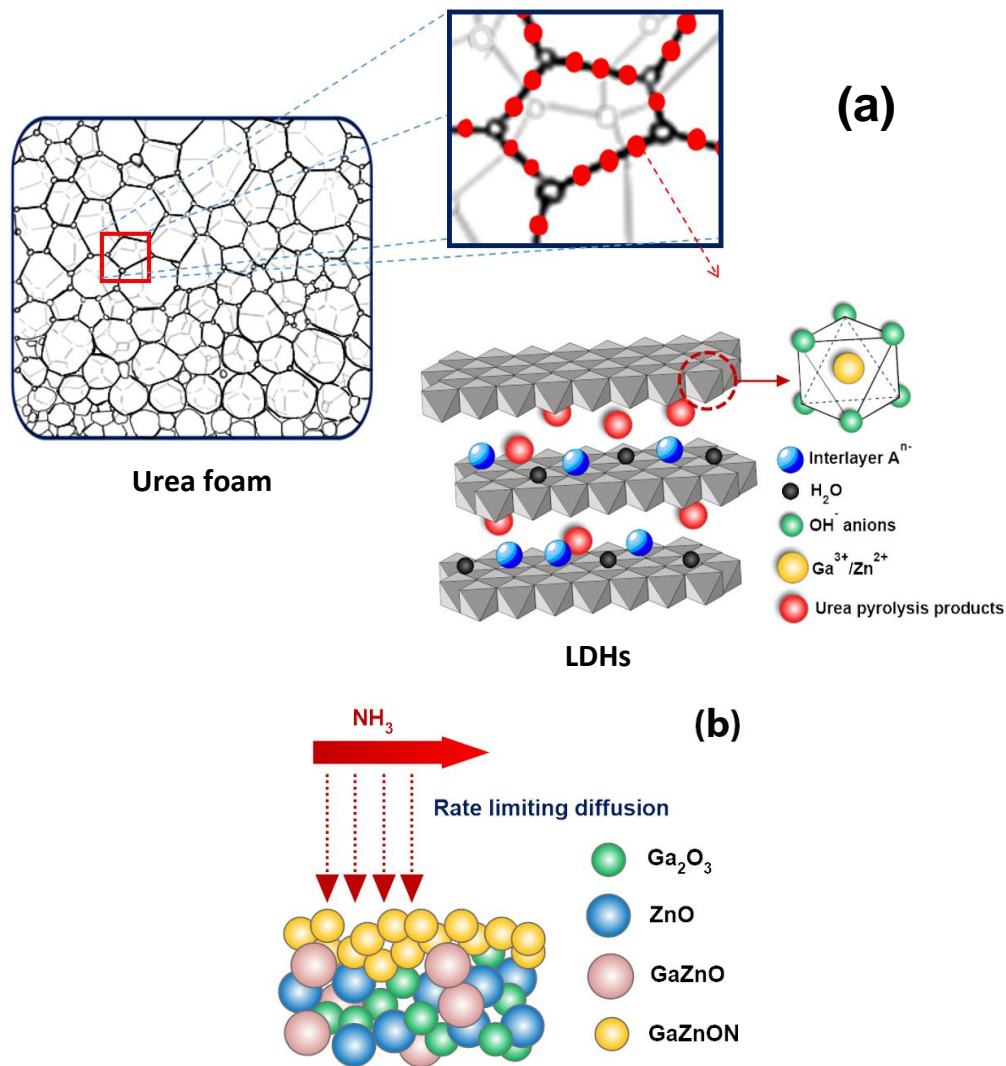


Figure 3.2: Comparison between two solid-state synthesis mechanisms. (a) High exposure of the starting materials to NH_3 gas within the Ga^{3+} and Zn^{2+} LDHs distributed within the urea foam, and (b) diffusion of NH_3 gas into the bulk precursor in the traditional route.

The OWS activity data of the samples prepared by thermal treatment of various MM precursors indicated that:

- 1) The samples prepared by grinding are not active for OWS.
- 2) The OWS activities of the LDHs samples are superior than those of the mixed precursor with similar compositions.

Therefore, LDHs precursor has been selected as the model precursor of this research, and most of the results presented in this chapter were obtained from treatment of this precursor.

3.4 Heat source of solid-state synthesis

Thermal treatment of the prepared precursors has been carried out in a laboratory muffle furnace and a microwave (MW) oven. Despite the high activities observed for some samples prepared in the microwave oven, the preparation of samples with consistent characteristics were not realized. Variations in the photocatalytic performances of the samples prepared in the microwave oven under same configuration are displayed in Appendix B. Inconsistent performance of the MW-synthesized samples is likely attributed to the non-uniform irradiation of the employed domestic microwave. The fabrication of GaN:ZnO under controlled conditions may result in steady evolution of hydrogen at a promising rate. Due to the difficulties associated with MW heat source, a laboratory muffle furnace was employed as the primary heating source of the solid-state preparation.

The optimal synthesis temperature provides sufficient energy for complete transformation of the precursors into the wurtzite phase, and maintain the nanoscale morphology formed during urea decomposition, while inhibiting the evaporation of the structural Zn.

Table 3.1: Effect of synthesis temperature and time on the photocatalytic activity of the GaN:ZnO-LDHs. The model precursor is Ga-Zn LDHs with $x = 0.20$. N: not active, L: low activity, M: medium activity, and H: high activity. The obtained photocatalytic data were normalized to 1.00 and categorized as follows: No OWS activities were observed: N, 0.00–0.20: L, 0.20–0.60: M, and 0.60–1.00: H.

		Temperature (°C)							
		650	700	750	800	850	900	950	1000
Time (min)	4	N	N	N	N	N	N	N	N
	8	N	N	L	M	M	M	L	N
	12	N	N	L	H	H	H	L	N
	20	L	L	N	L	L	L	N	N
	30	N	N	N	N	N	N	N	N

To identify the optimal synthesis temperature and duration, a comprehensive combinatorial experiment was conducted, where the LDHs precursor with $[Zn]/[Zn+Ga] = 0.20$ was treated at $T = 650\text{--}1000$ °C and $t = 4\text{--}30$ min. The photocatalytic performances of the prepared GaN:ZnO-LDHs samples are summarized in Table 3.1. Data obtained from experiments unveiled a trend for the functionality of the synthesis temperature and time within the study range: 1) neither long synthesis durations ($t \geq 20$ min), nor high preparation temperatures ($T \geq 950$ °C) are suitable for the synthesis of active solid solution samples. 2) Short synthesis durations ($t \leq 8$ min) and low preparation temperatures ($T \leq 700$ °C) are not sufficient for the formation of the wurtzite oxynitride phase. These areas are indicated with red and letter “N” (not active) in Table 3.1. On the other hand, highly active photocatalysts can be prepared at medium synthesis temperatures (800–900 °C) and durations (~12 min), as marked with green and letter “H” (highly active) in Table 3.1. Low (“L”, gray) and medium (“M”, blue) activities were observed for the samples prepared at the temperatures and times that deviated from the optimal synthesis conditions. Evidenced by the data

presented in Table 3.1, fabrication of active GaN:ZnO photocatalyst can be realized at a significantly lower synthesis time, when the solid-state mechanism is engineered and the preparation is performed at the nanoscale.

To further understand the role of synthesis temperature, the prepared GaN:ZnO solid solution samples were characterized for their crystalline structure and chemical phases via X-ray diffraction (XRD). Figure 3.3 (a) illustrates the XRD patterns of the solid solutions samples prepared from LDHs precursor at different temperatures in 12 min, along with those of the standard GaN and ZnO for comparison.

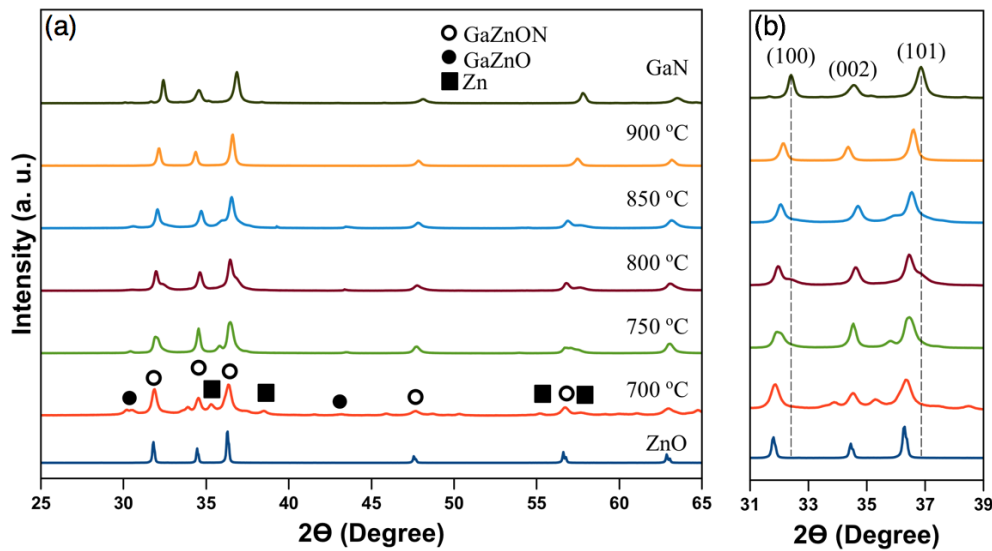


Figure 3.3: Overview (a) and wurtzite diffraction enlarged view (b) XRD pattern of the GaN:ZnO-LDHs ([Zn]/[Zn+Ga] = 0.20) photocatalyst prepared at various temperatures for 12 min.

The crystallographic data revealed that at $T < 700\text{ }^{\circ}\text{C}$, the XRD pattern of the samples contains the characteristics of the starting LDHs precursor. At $700\text{ }^{\circ}\text{C}$, the diffraction peaks of the wurtzite phase are appeared, along with the spinel peaks of ZnGa_2O_4 at $2\theta \sim 31^{\circ}$ and 43° , as well

as the metallic Zn residues. From $T = 700\text{--}800\text{ }^{\circ}\text{C}$, the cubic spinel peaks disappear and the fraction of wurtzite phase increases. The prepared samples exhibit nearly single-phase diffraction pattern assigned to the hexagonal wurtzite structure, similar to those of GaN and ZnO, at temperatures above $850\text{ }^{\circ}\text{C}$.

The enlarged view of the wurtzite diffraction pattern displayed in Figure 3.3 (b), suggesting (100) and (101) peaks as the favorable crystallite growth directions, evidenced by their high intensities. The diffraction patterns of the wurtzite phase in Figure 3.3 (b) exhibit a successive shift to lower angles as compared to those of GaN, which is similar to the reported data [25]. The slight shift of the diffraction pattern confirms the formation of a solid solution of GaN and ZnO, rather than the physical mixture of the two. This shift is expected, since the ionic radius of Zn^{2+} (0.74 Å) is larger than that of Ga^{3+} (0.61 Å) [70].

Shoulders and minor peaks that appear at various temperatures in Figure 3.3 (b) suggest minor fractions of metal oxides, spinel ZnGa_2O_4 , metallic Zn, and GaN phases. Although the proposed technique reduces the synthesis time significantly, presence of phases other than the wurtzite GaN:ZnO is considered as its drawback. These phases are mostly semiconductors with large band gap energies ($E_g > 3.0\text{ eV}$) that absorb UV portion of the solar spectrum only, thus reducing the visible light activity of the prepared photocatalyst. Moreover, bulk and surface impurities, produced through rapid urea pyrolysis, could introduce defects, surface dangling bonds (imperfect atomic bonds), and undesired surface states (energy states within photocatalysts band gap); thus reduce the overall water splitting reaction efficiencies [151,171,172].

Crystallite size of the prepared samples was estimated between 20–34 nm via Scherrer Equation (8). The size of the particles was estimated from Equation (11) ~51–87 nm. Differences between the size of the single crystal domain and that of the particles suggests polycrystalline

characteristics of the prepared samples. This difference could also be attributed to the formation of clusters by aggregation of solid solution particles. Lattice spacing ($d_{h,k,l}$) and constants (a and c) were estimated from equation (9) and (10) are summarized in Table 3.2.

Table 3.2: Crystallographic features estimated from the diffraction patterns in Figure 3.3 and equation (9) and (10).

Materials	Lattice constants (nm)		d-spacing (nm)	
	a	c	d_{100}	d_{101}
GaN	0.319	0.518	0.276	0.244
900 °C	0.321	0.520	0.278	0.245
850 °C	0.322	0.518	0.279	0.246
800 °C	0.323	0.519	0.280	0.246
750 °C	0.323	0.517	0.280	0.246
700 °C	0.324	0.520	0.280	0.247
ZnO	0.324	0.520	0.281	0.247

From the data represented in Table 3.2, it is apparent that the variations in the dimension of the prepared wurtzite crystals can be assigned to the crystallographic mismatch between GaN and ZnO towards the 6-fold hexagonal side-walls (2.1%) and along the c -axis (0.4%).

X-ray diffraction was employed to investigate the GaN:ZnO synthesis timeline. As shown in Figure 3.4, XRD data of the samples were obtained at $t = 0$ (LDHs), 4, 8, and 12 min at $T = 900$ °C. At $t = 0$, the diffraction pattern exhibits the characteristic features of layered structures, showing the basal peak and higher-order reflections at low angles [81,177]. The XRD pattern of the sample at $t = 4$ min reflects crystalline ZnCN phase, along with the spinel $ZnGa_2O_4$, and mixed-

metal oxynitride phases. From $t = 4$ min to 8 min, the composition of ZnCN phase decreases significantly, while the fractions of the spinel and oxynitride phases have enhanced slightly. Nearly single wurtzite phase is obtained at $t = 12$ min, when peaks of spinel and ZnCN phases have disappeared.

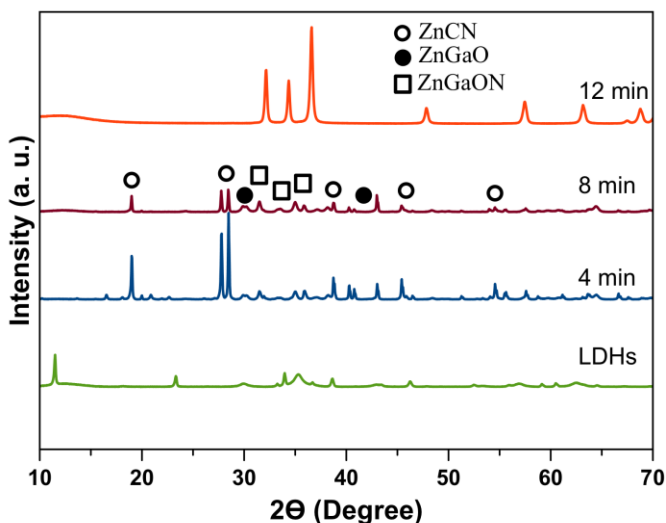


Figure 3.4: XRD patterns of GaN:ZnO-LDHs ($[\text{Zn}]/[\text{Zn}+\text{Ga}] = 0.20$) photocatalyst prepared at 900 °C for various times.

Interestingly, the optimal synthesis temperature and duration obtained from the diffraction data in Figure 3.3 and Figure 3.4 are in agreement with those obtain from the combinatorial experiment presented in Table 3.1. This is important, since it directly links the photocatalytic activity of the prepared GaN:ZnO photocatalyst to its crystalline structure and composition, which could be optimized by applying modifications into the proposed fabrication technique.

3.5 Surface and bulk structure

Thermal treatment of LDHs precursors with various compositions resulted in a powder with range of colors in respect to the composition (x) of the samples. Figure 3.5 shows the prepared GaN:ZnO samples with various compositions.



Figure 3.5: Digital photo of the prepared GaN:ZnO solid solution samples with different compositions.

The synthesized GaN:ZnO solid solution samples were examined for their surface morphology through scanning electron microscopy (SEM) analysis. As demonstrated in Figure 3.6 (a), samples contains particles with non-uniform shape distribution, up to 3 μm in size. Wide size and shape distribution could be attributed to high-temperature sintering of the smaller particles and formation of aggregates. Decomposition of these clusters is advantageous; because the particles in the center of these clusters are not exposed to the incident photons, and the photo-generated charges are trapped in the grain boundaries, thus do not participate in the water splitting reaction.

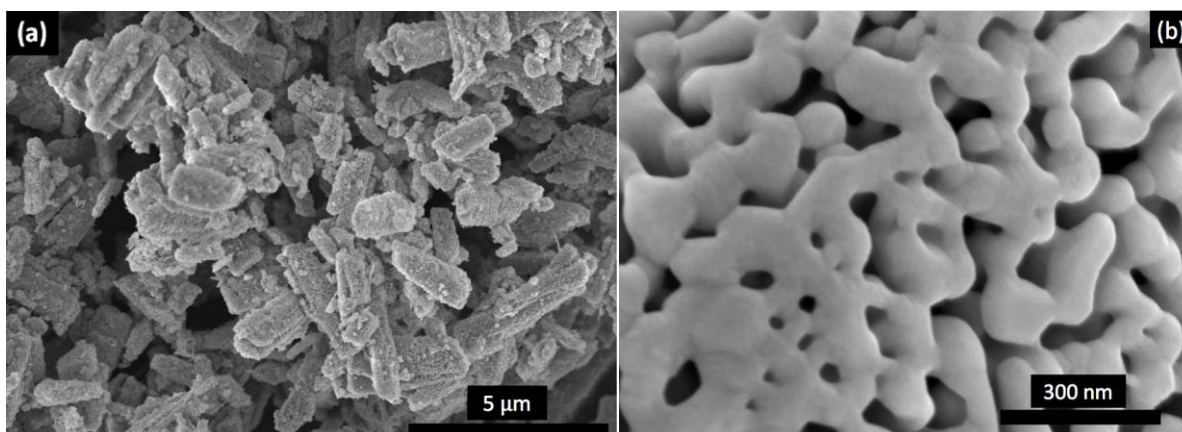


Figure 3.6: SEM images of (a) the synthesized GaN:ZnO particles, and (b) nanoporosity on the surface.

Thermal decomposition of urea at a high heating rate leads to evolution of micro-gas bubbles [169,170,174]. These gaseous off-products cause local nano- and micro-scale disruption in the precursor mixture and create random structures in the bulk and on the surface of the product. High resolution SEM image in Figure 3.6 (b) shows the surface nanoporosity formed as the result of such disruption. Surface of the synthesized samples contains uniform nanoporous morphology with narrow pore size distribution, which could increase the active surface area of the sample to a significant degree. The single-point BET surface area of various samples was estimated ~ 36.4 – $53.1 \text{ m}^2 \text{ g}^{-1}$, which is significantly higher than the analogous surface area reported for the traditional photocatalyst ($S_{\text{BET}} = 3.7$ – $8.1 \text{ m}^2 \text{ g}^{-1}$ [70]).

The surface and bulk composition of the prepared samples were measured by X-ray photoelectron spectroscopy (XPS) and energy-dispersive X-ray (EDX) spectroscopy. The elemental spectra and samples compositions are presented in Appendix C. Comparing the composition of the elements in the synthesized samples to the solid solution formula $(\text{Ga}_{1-x}\text{Zn}_x)(\text{N}_{1-x}\text{O}_x)$ suggests sub-stoichiometric Zn-content ($[\text{Zn}]/[\text{O}] < 1$), as well as N-

deficiency ($[Ga]/[N] > 1$) in the bulk of the samples. This deviation from the stoichiometric composition could be attributed to:

- 1) Surface absorption of oxygen from ambient, which increases $[O]$ and reduces the $[Zn]/[O]$ ratio from its stoichiometric value of 1.
- 2) High temperature evaporation of Zn, which reduces the $[Zn]/[O]$ ratio from its stoichiometric value of 1. This case has been also reported in the literature [27].
- 3) Partial collapse of Ga–N and Zn–N bonds at high temperature due to oxidation which increases the $[Ga]/[N]$, as well as decreases the $[Zn]/[O]$ ratios from their stoichiometric value of 1.
- 4) Incomplete solid-state nitridation due to low synthesis time which results in high, and low composition of oxygen and nitrogen respectively; therefore, reduces the $[Zn]/[O]$ and enhances the $[Ga]/[N]$ ratios.

Table 3.3: Compositional data of the LDHs precursors and GaZnON-LDHs photocatalysts prepared in 12 min at 900 °C. $x = [Zn]/[Zn+Ga]$

Sample	Calculated x		Measured x	
	Prepared LDHs	Precursor	GaZnON (Surface)	GaZnON (Bulk)
GaZnON-LDHs-1	0.06	0.24	0.14	0.16
GaZnON-LDHs-2	0.11	0.27	0.20	0.21
GaZnON-LDHs-3	0.20	0.33	0.30	0.32
GaZnON-LDHs-4	0.33	0.43	0.35	0.39
GaZnON-LDHs-5	0.50	0.56	0.49	0.55
GaZnON-LDHs-6	0.67	0.70	0.53	0.66

The metallic-basis surface and bulk elemental compositions of the samples are summarized in Table 3.3. The surface and bulk $x = [\text{Zn}]/[\text{Zn}+\text{Ga}]$ for the prepared samples were smaller than those in the precursor, which is similar to the observation reported previously [70]. Despite the fact that the evaporation of Zn-compounds is inevitable at high temperature, due to the lower synthesis time, the rate of Zn evaporation in this study was reduced, as such the x values in the bulk of the photocatalyst is comparable to those in the precursor. The higher Zn-content in the precursor, as compared to that in the prepared LDHs, is attributed to the metallic Zn, which was found to be beneficial for the photocatalytic activity of the newly synthesized photocatalyst. The effectiveness of metallic Zn in the proposed synthesis technique is attributed to the enhanced separation rate of the photo-induced charges, caused by the formation of acceptor mid-band energy levels in the forbidden gap to increase the concentration and mobility of carriers [178–183]. Due to low Zn evaporation, the proposed technique was found to be effective for the synthesis of Zn-rich solid solutions with x up to 0.66. The preparation of Zn-rich GaN:ZnO solid solution is desired, considering its essential role in the visible light absorption, by shifting the VB energy state upward; thus narrowing the band gap of the photocatalyst [70].

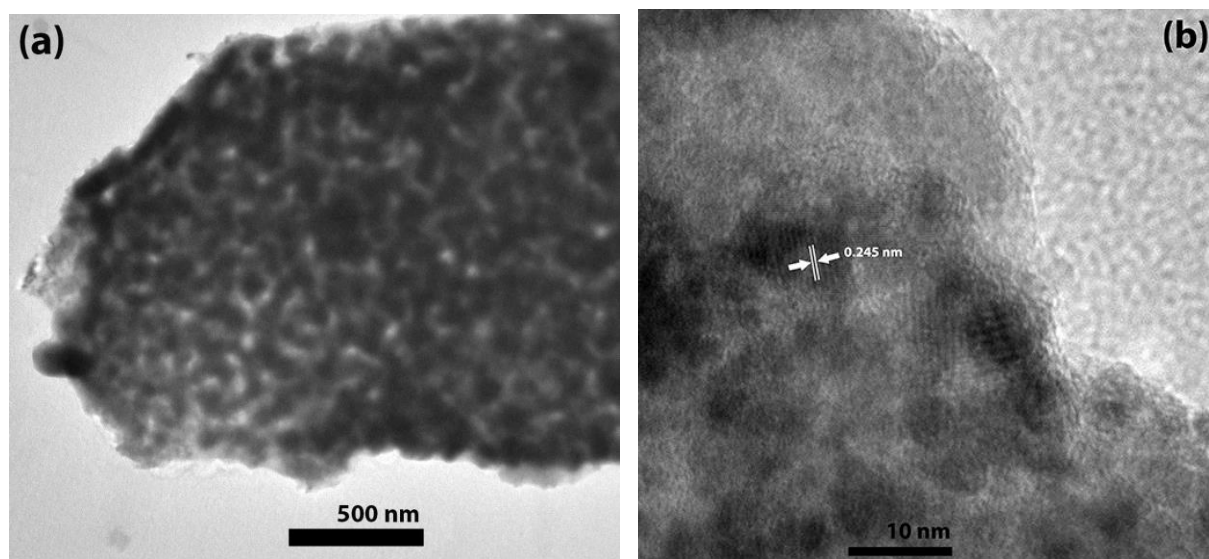


Figure 3.7: (a) TEM, and (b) HRTEM images of the synthesized GaN:ZnO photocatalyst.

Transmission electron microscopy (TEM) analysis was carried out to investigate the crystalline structure of the synthesized samples and phases. The low-resolution TEM image in Figure 3.7 (a) reveals that the nanopores formed during the urea-assisted synthesis are distributed uniformly over the structure of the particles. Bulk nanoporosity not only increases the active surface area for photocatalytic reaction (at least by 4.5-folds in this study, compared to the one reported for the traditional GaN:ZnO [70]), but also reduces the diffusion length of the photo-excited charges to the surface, thus minimizing their recombination rate. The structural nanopores also provide greater surface area for deposition of co-catalyst nanoparticles, without blocking the photocatalysts surface from the incident photons. This construction provides a morphological approach to address the solar water splitting obstacles such as charge recombination, and likely undesired reverse reaction.

Lattice d-spacing ~ 0.245 nm was estimated from the high resolution TEM (HRTEM) image in Figure 3.7 (b), which is equal to that obtained from the XRD data, and is between the d-

spacing of ZnO (101) \sim 0.247 nm and GaN (101) \sim 0.244 nm. Therefore, the (101) plane, which also exhibited the most intense diffraction peak in Figure 3.3, is the favorable growth direction of the crystallites. The synthesized samples were identified as poly-nano-crystalline, since various crystalline lattices in different growth directions with nanoscale domain size were observed by HRTEM analysis. Presence of various phases with different crystalline structures was also observed in the XRD data, and presumably attributed to the untransformed phases during rapid solid-state reaction.

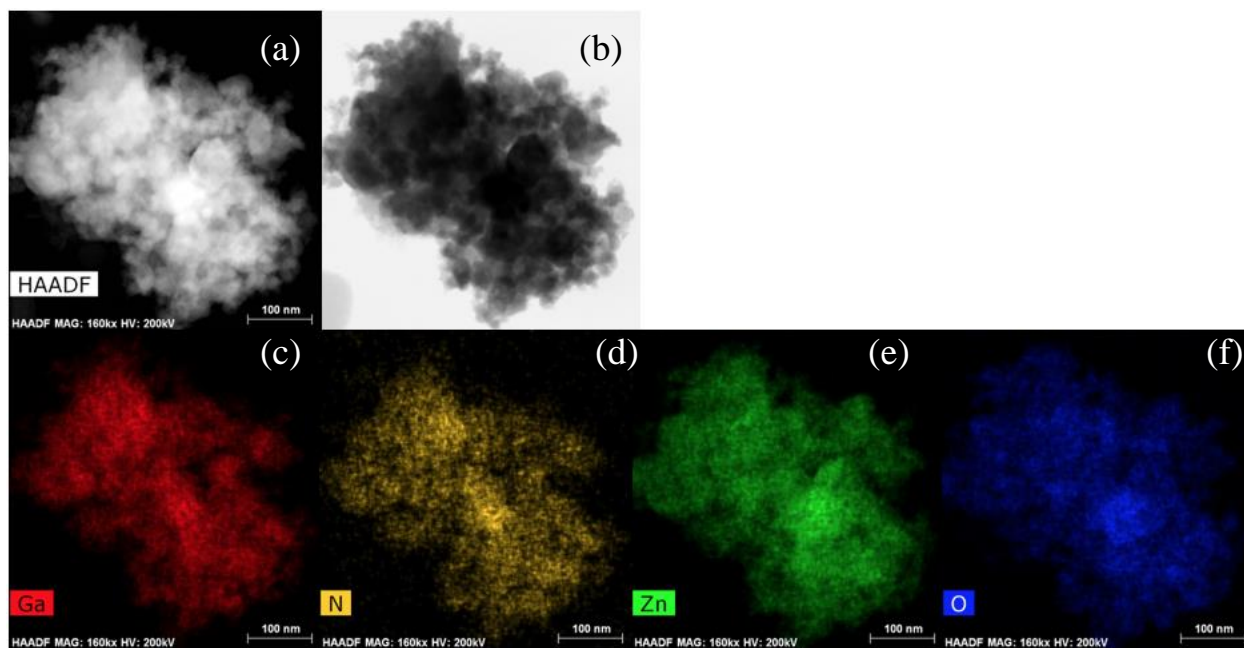


Figure 3.8: Bright (a) and dark-field (b) STEM micrograph of the prepared GaN:ZnO, accompanied by The EDX elemental maps for Ga (c), N (d), Zn (e), and O (f).

Scanning transmission electron microscopy (STEM) images of the prepared sample, along with compositional map of the key solid solution elements are displayed in Figure 3.8. While the STEM micrograph in Figure 3.8 (a and b) display the nanoporous structure of the synthesized

GaN:ZnO solid solution photocatalyst, the EDX elemental maps in Figure 3.8 (c–f) confirms the uniform distribution of Ga, N, Zn and O respectively, with no sign of aggregation, isolated phases or elemental islands.

3.6 Optical characterization

The prepared oxynitride photocatalysts were subjected to optical characterization. Figure 3.9 (a) demonstrates the Kubelka-Munk UV-Vis diffuse absorption spectra of the samples with various Zn-content (GaZnON-LDHs 1–6 in Table 3.3). In agreement with the data in the literature [25,27,63,70,80], a red-shift can be observed in the absorption spectra of the samples from the UV region for GaN and ZnO to the visible region for the samples with higher Zn-content.

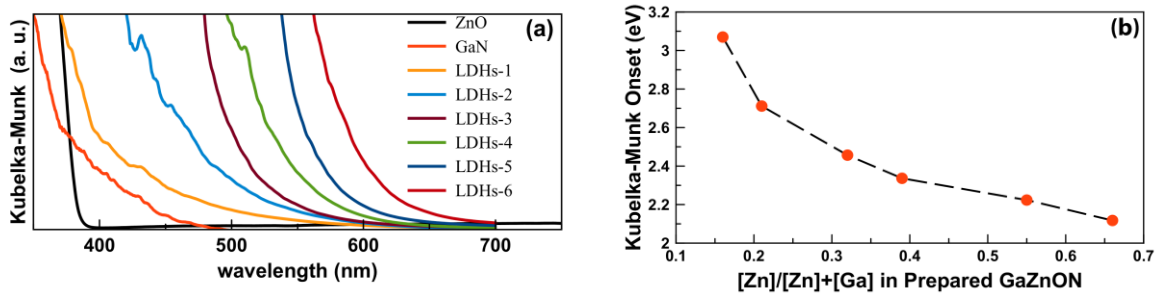


Figure 3.9: Effect of solid solution composition on the (a) optical absorption, and (b) band gap energy of the synthesized GaN:ZnO solid solutions.

The band gap energies (E_g) of the samples estimated from the onset of the absorption spectra in Figure 3.9 (a) are presented in Figure 3.9 (b) as a function of the samples composition (x), varies in 2.1–3.1 eV range when $0.16 \leq x \leq 0.66$. The large band gap (> 3.0 eV) for samples

with lower Zn-content is likely related to the remaining spinel, metal oxide, and metal nitride phases that have not transformed into the wurtzite phase, evidenced by the XRD and TEM data.

Photoluminescence (PL) spectra of the GaN:ZnO samples prepared through urea decomposition of LDHs (GaZnON-LDHs) and mixed (GaZnON-M) precursors are illustrated in Figure 3.10. PL emission can be related to the structural defects of materials, due to the recombination of the photo-induced charges generated at the excitation stage [184,185]. Thus, more intense PL emissions can be interpreted to greater densities of crystalline defects.

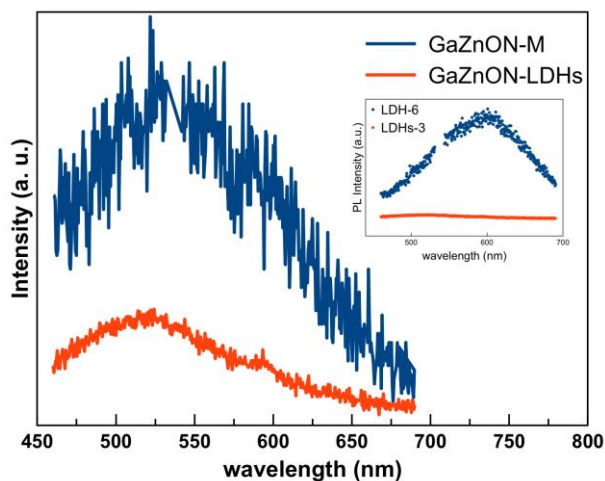


Figure 3.10: PL spectra of GaZnON-LDHs and GaZnON-M samples. Inset shows the effect of $[Zn]/[Zn+Ga]$ ratio on the PL characteristics of the GaZnON-LDHs-3 and GaZnON-LDHs-6 samples.

The PL emission of the samples revealed that the density of the crystal defects is significantly higher for the GaZnON-M sample compared to the GaZnON-LDHs photocatalyst. The GaZnON-M sample shows the PL peak at slightly higher wavelength compared to the GaZnON-LDHs, which is likely accounted to its higher Zn-content. Similar trend can be observed

for the GaZnON-LDHs samples, as illustrated in the inset of Figure 3.10, whereas the PL peak of the GaZnON-LDHs-3 ($x = 0.32$) at ~ 520 nm is shifted to longer wavelengths around 590 nm for the GaZnON-LDHs-6 ($x = 0.66$). The broad PL bands of the prepared samples are attributable to the several narrower bands of Zn acceptor, from the blue and orange PL bands for the GaZnON-LDHs-3 to the orange and red inter-bands for the GaZnON-LDHs-6, picturing the role of Zn as the acceptor impurity to enhance the sample's photo-excitation and charge mobility, as well as its function in the disruption of the GaN host's crystal structure [186].

3.7 Photocatalytic performance

The UV-Vis absorption spectra of the solid solution samples shown in Figure 3.9 (a) revealed absorption edge shifts proportional to the Zn-content of the samples, suggesting the formation of visible-light responsive phase. However, due to the complexity of photochemical water splitting reaction kinetics, performance evaluation tests with respect to the visible light hydrogen evolution must be conducted.

Photocatalysts with various compositions were tested for their photocatalytic activity in pure water under visible light irradiation. The as prepared GaZnON-LDHs samples did not exhibit considerable OWS activity, due to lack of active hydrogen evolution sites on their surface. As highlighted by Miseki et al., most photocatalysts lack surface H_2 evolution sites [11]. Maeda and co-workers also reported that the surface sites of the traditional GaN:ZnO photocatalyst are not active for proton reduction reaction [105,187]. To promote the hydrogen evolution reaction, surface of the nanoporous GaN:ZnO samples were decorated with 1 wt% Rh NPs through photo-deposition. In the base-line tests, 1 wt% Rh-loaded Ga_2O_3 , ZnO, and GaN did not produce hydrogen or oxygen at the experiments condition.

The elemental analysis of the Rh-loaded samples reflected 0.31–0.53 wt% of Rh on the surface of photocatalysts samples. Although individual 2–4 nm Rh nanoparticles were observed on the surface, it is believed that a portion of the active sites was deposited inside the nanopores of the photocatalyst. Despite the fact that photon absorption occurs on the near-surface region of the bulk particles, the resulting photo-excited charges can be transferred inside the bulk, in response to the variations in charge densities. Therefore, even though the nanopores are not exposed to the incident photons, they could be considered as the active regions for water splitting reaction.

The rate of hydrogen and oxygen evolution in Figure 3.11 indicates the strong dependency of the OWS activities to the photocatalysts composition. This trend is influenced by the Zn-content of the photocatalyst, which is responsible for the visible-light absorption, as well as the structural defects.

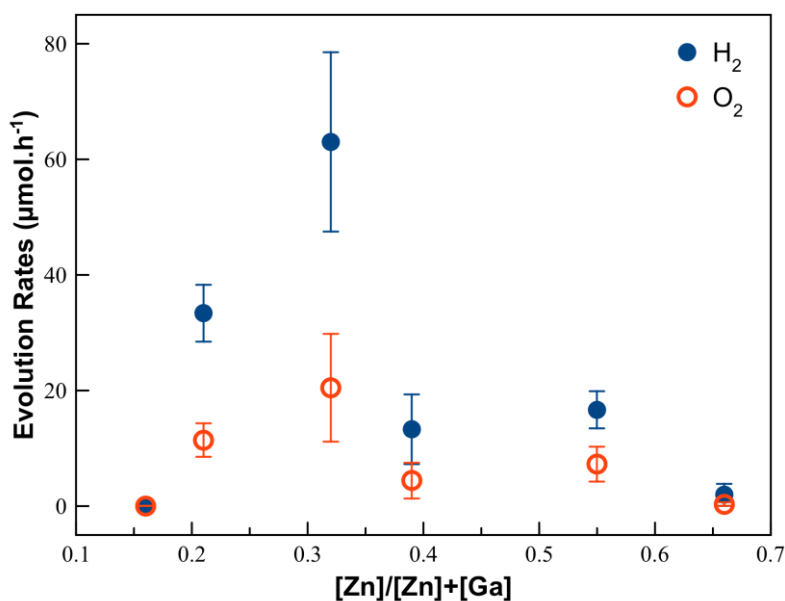


Figure 3.11: Rate of H₂ and O₂ evolution for GaZnON-LDHs 1–6. Error bars indicate 90% confident interval.

Among the samples, those with $x = 0.21, 0.32, 0.39,$ and 0.55 (LDHs 2–5) demonstrated visible light OWS activities. The dependency of the photocatalytic activities to the composition of the prepared samples can be explained through the solid solution's optical and structural characteristics. Incorporation of ZnO into the lattice of GaN host results in red-shifts in the absorption spectra, and reduces the semiconductor E_g , as observed in Figure 3.9, therefore increasing the rate of photo-excited charges generation. For the traditional GaN:ZnO solid solution, the highest rate of OWS has been reported at $x = 0.12$ – 0.18 [154]. However, the highest hydrogen evolution rate for the newly synthesized nanoporous GaN:ZnO photocatalyst was noted for the sample with $x = 0.32$ (LDHs-3), reaching the maximum apparent quantum efficiency (AQE) of 2.71% at 420–440 nm. This difference is attributed to differences in the crystalline structure and morphology between the two. Unlike the traditional solid solution, the photocatalytic activity of the nanoporous photocatalyst is attributed to its higher surface area. Therefore, the mechanisms that cause the generation and transfer of charges are considerably different from those in the traditional solid solution. Moreover, the sample obtained from the rapid solid-state reaction consists of residues and untransformed phases, such as metallic zinc, oxides, and nitrides, which make the comparisons based on the Zn content of the photocatalysts difficult.

Although the absorption of the photocatalysts improves by increasing the Zn-content, for $x > 0.32$, the activity of the photocatalyst reduces due to the stronger effect of the crystalline defects. Despite the promising OWS activity of the synthesized samples, the ratio of evolved hydrogen to oxygen do not match to the stoichiometric value of 2. Some of the prepared samples exhibited no activity for OWS; the reason of such occurrence is not fully known. It is hypothesized that chemical composition of these samples are significantly deviated from that of the solid

solution GaN:ZnO. Nitrogen deficiency and intense oxidation could also be responsible for the lack of OWS activity of these samples.

Maeda et al. reported negligible hydrogen evolution for the 1 wt% noble-metal-loaded GaN:ZnO solid solution prepared through the traditional technique [99]. In their study, the photocatalyst demonstrated considerable improvements in hydrogen evolution just after surface modification with Cr₂O₃ shell, to suppress the undesirable reverse reaction. On the other hand, in the case of the nanoporous photocatalyst, deposition of Cr₂O₃ did not improve, but reduced the evolution of gasses. Low photocatalytic activity of the Cr-loaded photocatalyst could be associated to the blockage of the pores by increasing the size of the active sites and/or formation of a Cr-base film at the pores entry. The newly synthesized photocatalyst is capable of OWS under visible light irradiation at a considerable rate, using only a single co-catalyst. The insignificant effect of the back-reaction on the gas evolution rate for the nanoporous photocatalyst is not clear at this point; however, the following explanation may be offered: Due to the existence of nanopores on the surface and in the bulk of the photocatalyst, hypothetically the majority of Rh active sites are deposited inside the pores, rather than on the surface of the photocatalyst. As a result, the limiting mass transfer could have hindered the diffusion of the evolved gases inside the pores to reach to the surface of the Rh NPs and participate in the water splitting back-reaction.

Water splitting experiments were performed in pure water with pH = 6.4–6.8, and the solution pH was not changed noticeably after 12 h of reaction (pH = 5.9–6.2). Experiments at various pH values indicated higher photocatalytic activities at mild-acidic (pH = 4.5±0.2) electrolyte and unstable performances at harsh acidic (pH = 3.0±0.2) and alkaline (pH = 11.2±0.2) electrolytes. Apparently, rapid decomposition (oxidation) and surface hydrolysis are responsible for the instable activity of photocatalyst in the harsh acidic and alkaline conditions.

Heating of urea to temperatures up to 550 °C typically leads to the formation of graphitic carbon nitride polymer (g-C₃N₄) which has induced promising activity in photocatalysis [169,170,188–190]. However, due to the synthesis temperature of the nanoporous GaN:ZnO solid solution in this study, gas evolutions cannot be assigned to g-C₃N₄, given the thermogravimetric analysis (TGA) of g-C₃N₄ indicates complete decomposition at temperatures less than 700 °C [191–193]. Moreover, the intense (002) peak of g-C₃N₄ at $2\theta = 27^\circ$ [169,170,189–193] was not detected in the XRD pattern of the prepared samples illustrated in Figure 3.3.

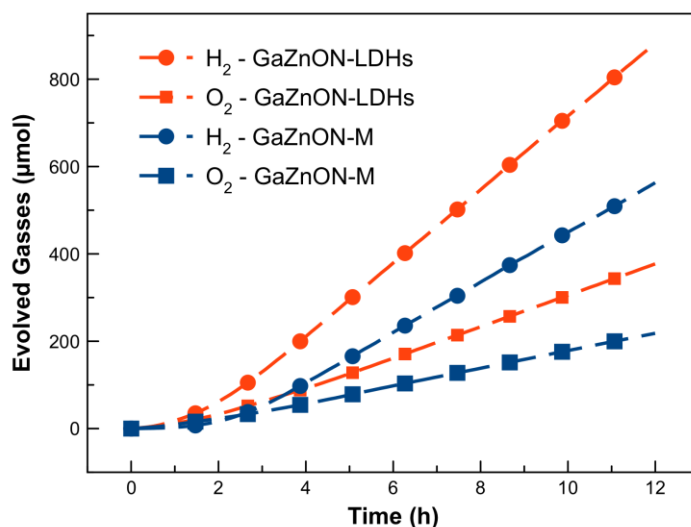


Figure 3.12: Comparison of the OWS performances of the GaN:ZnO samples prepared by processing of LDHs (GaZnON-LDHs) and mixed precursors (GaZnON-M).

The effectiveness of the LDHs precursor in the preparation of GaN:ZnO photocatalyst (GaZnON-LDHs) was investigated by comparing its visible light OWS activity to that of the GaZnON-M photocatalyst with same precursor composition. Continuous hydrogen and oxygen evolution were observed for both samples, as demonstrated in Figure 3.12. Short induction period

in the first hour of the experiment could be attributed to the experimental lag because of the photo-reactor and tubing volume.

GaZnON-LDHs photocatalyst outperformed the GaZnON-M sample with over 50% visible light evolved hydrogen. This improvement is attributed to the high crystallinity and uniformity of LDHs precursor at the atomic level, in addition to its higher surface area for solid-state reaction within the interlayer space of the LDHs structure.

3.8 Durability analysis

Durability is one of the most important features of catalysts because it directly impacts their commercial feasibility and appeal to market; therefore, durability analysis is one of the major evaluation studies for materials with applications in catalysis. For photocatalytic hydrogen evolution process, the primary focus is placed on the development of new photocatalysts and their performances, while durability of the developed materials was not investigated in detail and often long-term performances have not been addressed in the literature. It is known that some metal oxides such as TiO_2 and WO_3 are highly stable in water splitting reaction condition [194]; on the other hand, some photocatalysts exhibited instability under band gap excitation. For instance, CdS and ZnO suffers from photo-corrosion by consuming photo-induced holes, as described in reaction (5) [54–56,195,196], or hematite ($\alpha\text{-Fe}_2\text{O}_3$), which is an abundant and very promising photo-anode material for PEC water splitting, is unstable in acidic environments [22,197].

Unlike oxide semiconductors, oxynitride photocatalysts are not highly stable under water splitting conditions due to existence of nitrogen in their lattice [77,78,198]. In the past decade, modification of crystalline structure and surface of the nitrides and oxynitride photocatalysts resulted in robust photochemical performances [40,174,199–201]. In 2012, an outstanding long-

term performance was reported for the traditionally synthesized GaN:ZnO solid solution by monitoring the OWS activity of the photocatalyst in a 6-month period under visible light irradiation [202]. Ohno and co-workers explored the long-term durability of the traditional photocatalyst in a Pyrex top-irradiated reactor with L-40 UV cut-off filter ($400 < \lambda < 500$ nm) contains 200 mg of photocatalyst in 200 mL H_2SO_4 solution ($\text{pH} = 4.5$). Due to the fact that mechanical stirring damages the surface of the photocatalyst, removes the co-catalyst NPs from the surface, causes particles breakage, and most importantly creates charge recombination sites on the surface of photocatalyst materials [203], long-term water splitting experiment was performed without mechanical stirring, over the bed of photocatalysts sediment. In their study, stoichiometry OWS was observed for 3 months with insignificant sign of degradation or surface oxidation. After 6 months, the photocatalyst lost 50% of the initial activity, which surface modification with co-catalyst NPs resulted in up to 80% recovery of the original activity.

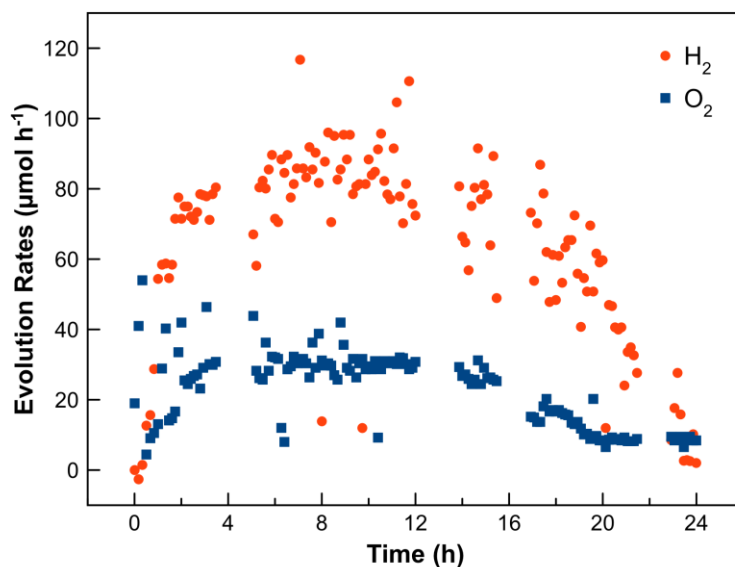


Figure 3.13: H_2 and O_2 evolution rates from the Rh-loaded GaN:ZnO solid solution photocatalyst.

To assess the durability of the synthesized nanoporous GaN:ZnO photocatalyst, the H₂ and O₂ evolution rates were monitored for longer periods. As shown in Figure 3.13, H₂ and O₂ evolution started at t = 0 and reached their highest rates at t ~4 h, when fairly stable evolution was recorded for the next 10 h. At this point, oxygen and hydrogen evolution rates decreased to the point where the water splitting reaction was terminated at t = 24 h. To understand the principle of the photocatalyst deactivation, the structure and surface properties of the fresh and spent photocatalyst were analyzed. Based on the obtained characterization data and materials reported in the literature, the following four deactivation mechanisms are suggested:

1) Disruption in crystalline structure

The XRD pattern of the fresh and used photocatalysts are displayed in Figure 3.14.

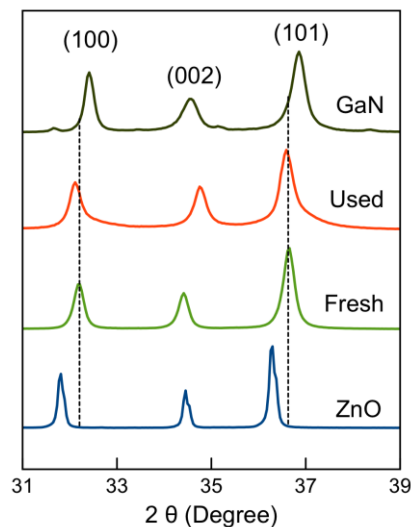


Figure 3.14: Diffraction pattern of the fresh and used GaN:ZnO photocatalyst (after 20 h) along with that of the standard ZnO and GaN.

The XRD data in Figure 3.14 indicates that the spent photocatalyst maintained the wurtzite crystalline structure after 20 h overall water splitting, exhibiting a similar pattern to the freshly synthesized GaN:ZnO, ZnO and GaN. The position of the major wurtzite peaks of the used and fresh photocatalysts have not changed considerably. The lattice parameters estimated for the fresh and used photocatalysts, summarized in Table 3.4, indicate nearly identical lattice parameters.

Table 3.4: Lattice parameters of the fresh and used photocatalysts estimated from the XRD pattern in Figure 3.14, using the equation (9) and (10).

Sample	Lattice constant (nm)		d-spacing (nm)	
	<i>a</i>	<i>c</i>	d_{100}	d_{101}
Fresh photocatalysts	0.320	0.519	0.278	0.245
Used photocatalysts	0.321	0.519	0.278	0.245

From Figure 3.14, it can be seen that the (100), (002) and (101) peaks of the used photocatalyst have widened slightly compared to those of the fresh photocatalyst. Besides, the clear border between the diffraction peaks have faded, suggesting potential lattice disruption, and phase transformation during the water splitting reaction. Such crystalline transformation, which could be responsible for the deactivation of photocatalyst, can be investigated through XPS analysis.

2) Partial surface oxidation

High resolution XPS spectra of the Ga2p and Zn2p peaks in Figure 3.15 shows consistent peak shifts from the fresh to the spent photocatalysts.

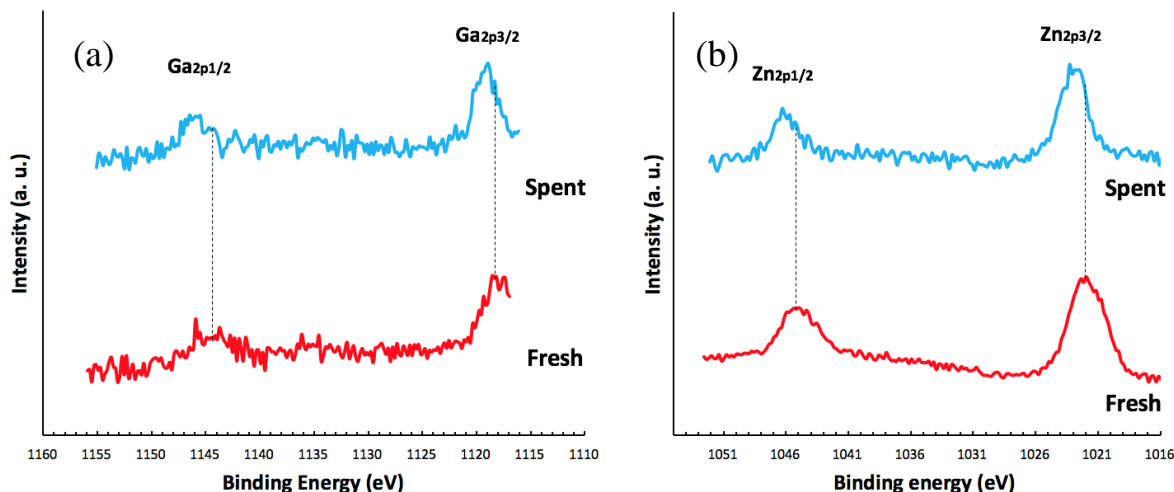


Figure 3.15: (a) Ga2p, and (b) Zn2p high resolution XPS spectra of the fresh and used GaN:ZnO photocatalysts.

The Ga2p_{1/2}, Ga2p_{3/2}, Zn2p_{1/2} and Zn2p_{3/2} peaks (1145.7 eV, 1118.5 eV, 1044.9 eV, and 1021.9 eV, respectively) of the fresh sample were shifted to the higher binding energies (1146.5 eV, 1118.9 eV, 1046.1 eV, and 1023.2 eV) after water splitting reaction. This shift indicates that the original bonds to Ga and Zn atoms on the photocatalysts surface have partially broken, and new phases have been formed. Evidently, the Ga–N and Zn–N bonds are partially collapsed, and replaced by Ga–O and Zn–O bonds. Such surface transformation could be assigned to photo-induced oxidation by holes and/or hydrolysis in aqueous media. This hypothesis is also in agreement with XRD data in Figure 3.14, in which the collapse in nitride phase may lead to partial decomposition of the photocatalyst structure, or generation of new phases.

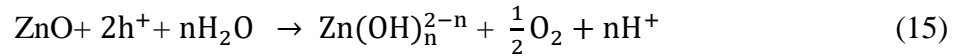
The Ga2p_{3/2} peak in GaN at 1118.0 eV [204]–1118.2 eV [205] located at a lower binding energy than that of Ga₂O₃ at 1119.5 eV [205]–1119.8 eV [206]. Since the location of the Ga2p_{3/2} of the spent photocatalyst (1118.9 eV) is laid between the reported values for GaN and Ga₂O₃, it

is believed that Ga in the used photocatalyst structure is bonded to both N and O; therefore, full-oxidization has not occurred.

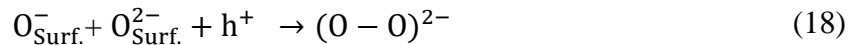
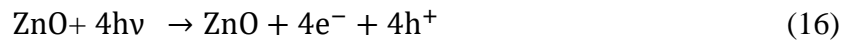
Surface decomposition may play an important role in the deactivation of photocatalysts. However, partial oxidation evidenced by slight peak shifts in the XPS spectra of Ga and Zn (similar to those presented in Figure 3.15) have been also reported for the traditionally prepared photocatalyst [187,202], which have exhibited outstanding stability for overall water splitting reaction. Therefore, it is believed that particles surface oxidation may not be responsible for the short-term deactivation.

3) Photo-decomposition of surface ZnO

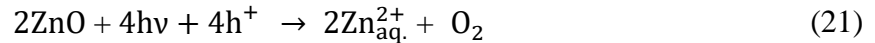
It is well-documented that ZnO suffers from instability under illumination [54–56]. Rudd and Breslin proposed the following reaction (15) for photo-decomposition of ZnO under band gap excitation [207]:



where n depends on the pH of the solution. According to Gerischer, the sequence of steps involved in the photo-decomposition of ZnO crystals consists of trapping of two holes on the surface followed by expulsion of Zn^{2+} from the surface, as described in reactions (16–20) [208]:



The overall reaction may be presented as:



Through similar mechanism, Zn–O bonds on the surface of the GaN:ZnO solid solution may interact with photo-excited holes on the surface and decompose. Gerischer studied the kinetic of each individual steps and proposed that the hole-trapping steps (reactions 17 and 18) is considerably slower than the oxygen production and Zn^{2+} expulsion steps (reaction 19 and 20), which may explain the low rate of oxygen evolution for several hours and rapid deactivation within the last 6 h of the experiment.

4) Formation of surface complexes

Despite the advantages offered by the short synthesis time, higher density of crystal defects and surface states considered as the disadvantage of the proposed fabrication route. In particular, surface defects and dangling bonds are very suitable sites for interaction with species inside the electrolyte. In general, oxygen can be considered as a shallow donor that occupies the surface of materials in high concentrations [209]. The adsorption of oxygen at the wurtzite surfaces of GaN has been reported [209,210], and oxygen was identified as a well-known contaminant in GaN growth process [211], which inferred the oxyphilic nature of GaN.

considering the lack of oxygen evolution during OWS, as also depicted in Figure 3.11, Figure 3.12 and Figure 3.13, it is hypothesized that surface adsorption (physisorption or chemical adsorption) of evolved oxygen plays an important role in deactivation of the photocatalyst. The surface trapped oxygen molecules could cover the evolution sites of the photocatalyst gradually, resulting in surface poisoning. Subsequently, the oxygen atoms on the surface can interact with

photo-excited electrons through reaction (22), and produce unwanted superoxide species, that could subsequently form other complexes such as peroxides.



To examine this theory, regeneration of the spent photocatalyst through physical approaches was attempted. The deactivated photocatalyst (after 20 h reaction) was collected and washed with pure water, ethanol and dilute hydrochloric acid solution. The photocatalyst then dried in the oven at 80 °C overnight and further treated at 550 °C for 1 h. the recovered photocatalyst was subjected to OWS tests in pure water for another two cycles where the regeneration procedure described above was performed between each cycle.

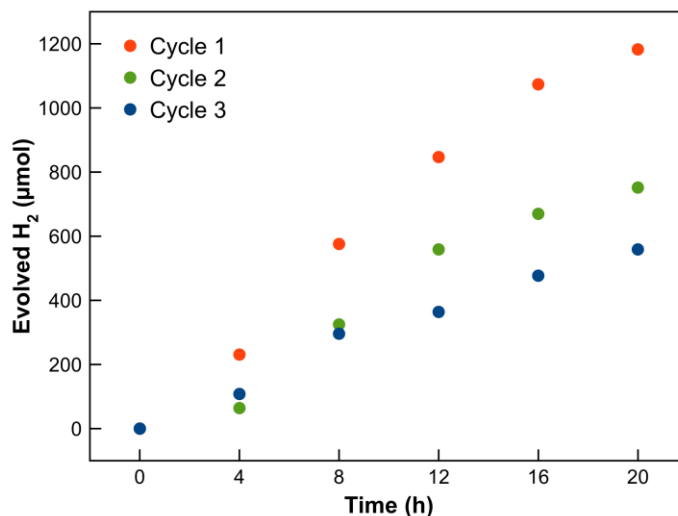


Figure 3.16: Evolved hydrogen from fresh (Cycle 1) and recycled photocatalysts (Cycles 2 and 3).

As demonstrated in Figure 3.16, the regenerated photocatalysts retained a portion of their initial activity (*i.e.* 64% in Cycle 2/Cycle 1 and 47% for Cycle 3/Cycle 1) because of physical treatments between the cycles. In addition, 74% of the hydrogen evolution rate was recovered from

Cycle 2 to cycle 3, suggesting an acceptable level of regeneration. It should be noted that the washing process may damage the photocatalyst's surface, and perhaps removes a portion of Rh NPs from photocatalyst structure, which could be partially responsible for the activity loss between the cycles. Refreshing the water splitting solution between the cycles likely helps the regeneration yield of the photocatalyst, since the intermediate species inside the electrolyte promote the photocatalyst's deactivation.

3.8.1 Deactivation mechanism

Four probable deactivation routes have been proposed, and each has been discussed through available experimental results, characterization data and materials in the literature. To our understanding, in practice, all four mechanisms contribute to deactivation of nanoporous GaN:ZnO photocatalyst to some degree. Permanent deactivation such as chemical transformation and disruption in crystalline structure likely occur within long-term reactions, as the one reported for the traditional GaN:ZnO. Changes in Ga2p and Zn2p binding energies could not be entirely responsible for deactivation of the photocatalyst, since similar surface transformations were observed for the stable GaN:ZnO [202].

The photocatalytic activity data of the nanoporous GaN:ZnO solid solution suggest that the deactivation process takes place on the surface, within a 6–8 h period. Apparently, the deactivation of the synthesized photocatalyst in this research is primarily accounted to partial Zn²⁺ dissociation and formation of surface complexes. Some recommendations are made in the last chapter of this thesis for further investigation of the photocatalyst deactivation scenario.

In conclusion, the results presented in this chapter indicate that the proposed synthesis using atomic-level uniform LDHs precursor and urea soft-template/nitrogen is a feasible facile

approach for the large-scale preparation of nanoporous GaN:ZnO solid solution with reasonable photocatalytic activity. A brief analysis comparing the synthesis cost and scalability of the nanoporous and traditional GaN:ZnO solid solutions is presented in the Appendix D.

Chapter 4: Utilization of Hydrogen and Oxygen Evolution Co-catalysts

The generation of photo-induced charges with sufficient energy levels corresponding to the redox reactions and their transport to the surface are the main tasks of photocatalyst materials. These charges can then interact with electrolytes, if suitable interfaces (active sites) can be formed. Even in the presence of redox active sites, the charge carriers must possess considerably higher energies to overcome the energy barriers on the photocatalyst–electrolyte interface. For the visible-light activated photocatalysts, such barriers substantially reduce the chances of electron-hole pairs participating in the redox reactions, thus decreasing the rate of the water splitting reaction significantly.

Even if the photo-induced charges reach the surface of the photocatalyst, they will recombine if suitable active sites for hydrogen evolution reaction (HER) and oxygen evolution reaction (OER) do not exist on the surface. For nitride and oxynitride semiconductors, considerable photocatalytic activity has been achieved after surface modifications with HER catalysts [87,95,101,208].

An efficient co-catalyst material reduces the overpotential (*i.e.* potential barriers) of the redox reactions, and achieves a large exchange rate [213]. A catalyst's exchange rate can be defined as the fractions of the charges transferred to the active sites that participate in the redox reaction at the catalyst–electrolyte interface [214]. In general, three elementary processes control the rate of catalytic redox reactions. Taking HER in water splitting as an example [215,216]:

- I. Adsorption of reactant (H^+) on the active site:



- II. Intermediate or product formation on the active site:



III. Product desorption from the active site:



To date, noble metals such as Pt, Pd, Rh, and Au have shown the highest HER catalytic activities, while IrO_x and RuO_x exhibit the most promising OER efficiencies [217,218]. Many studies have emphasized the development of efficient HER and OER catalysts for water electrolysis, which can be applied to the photocatalytic water splitting process. Despite their outstanding activity, noble metal catalysts are very expensive; therefore, their application in the design of functional devices is limited. In the last decade, considerable attention has been focused on reducing the noble metal content of the catalysts or replacing them with Earth-abundant compounds.

Effective oxidation and reduction catalysts have to meet certain conditions, such as 1) suitable particle size and morphology [219], 2) favourable reactive exposed crystallographic facets [220], 3) uniform dispersion on and stable linkage to the photocatalyst surface [221], and 4) suitable electrical characteristics to effectively attract photo-excited charges [222].

To the best of our knowledge, Rh-Cr₂O₃ core-shell is the most effective HER co-catalyst for the traditional GaN:ZnO. The solid solution photocatalyst ($x = 0.18$) decorated with 1 wt% Rh-1.5 wt% Cr-oxide reached the apparent quantum efficiency of 5.9% at 420–440 nm under 450 W Hg lamp [154]. This AQE is among the highest efficiencies that has been reported in the literature for OWS using a single photocatalyst material [11]. In this chapter, the effect of co-catalyst materials and their loading condition on the photocatalytic performance of the nanoporous GaN:ZnO are investigated.

4.1 Co-catalysts deposition method

In general, co-catalyst nanostructures can be deposited via ex-situ immobilization or in-situ crystallization. These methods are categorized based on the application of pre-synthesized catalyst materials (ex-situ) or the growth of catalyst nanostructures from their precursor directly on the nucleation sites of photocatalyst surfaces (in-situ) [223]. Owing to its effectiveness in the preparation of stable NPs on the photocatalyst surface [116], in-situ crystallization through photo-deposition and impregnation was applied for surface decoration of the nanoporous GaN:ZnO solid solution.

The impregnation method (also called incipient wetness [95]) involves the formation of metal precursor thin film on the surface of the support photocatalyst, followed by its thermal transformation to metallic (or metal oxide) islands. Ideally, the volume of the metal's salt solution will be sufficient to form a uniform layer on the active surface area of the photocatalyst (*i.e.* surface and pores). In practice, a few milliliters of the salt solution can be mixed with photocatalyst powder to form a paste that can be slowly dried (evaporation) to obtain a uniform metal complex film on the surface [99,153]. Higher volumes of precursor solution, which form a suspension rather than a paste, result in long processing times and aggregation of the metal complexes. The photo-deposition technique, on the other hand, utilizes the photo-induced electrons for direct reduction of a metal salt to its metallic state, and post-processing steps are usually not required. The mechanisms of impregnation and photo-deposition techniques on the surface of a photocatalyst are schematically illustrated in Figure 4.1.

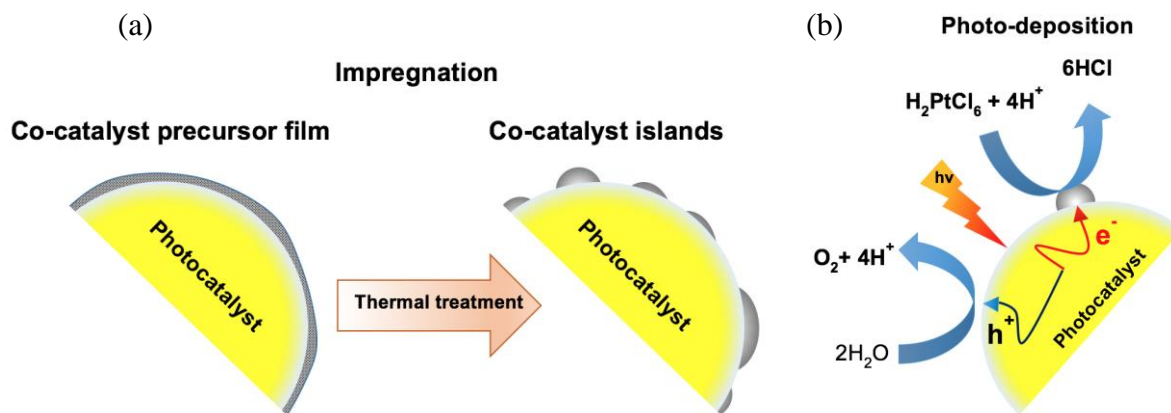


Figure 4.1: Schematic illustration of techniques used in this research for deposition of co-catalyst active sites on the surface of the photocatalyst (a) impregnation, and (b) photo-deposition of Pt.

To explore the impacts of the impregnation and photo-deposition methods, Pt (1–10 wt%) and nanoporous GaZnON-LDHs-3 ($x = 0.32$) were used as the model co-catalyst and photocatalyst support, respectively. The OWS activities of the Pt-loaded samples in Figure 4.2 reveal superior photocatalytic performance for the samples decorated by the photo-deposition technique throughout the entire range of experiments. The rates of H_2 evolution in Figure 4.2 indicate that the activity of the impregnation route-loaded photocatalyst could at best reach ~22% (for 5 wt% Pt) of the analogous activity loaded through the photo-deposition method.

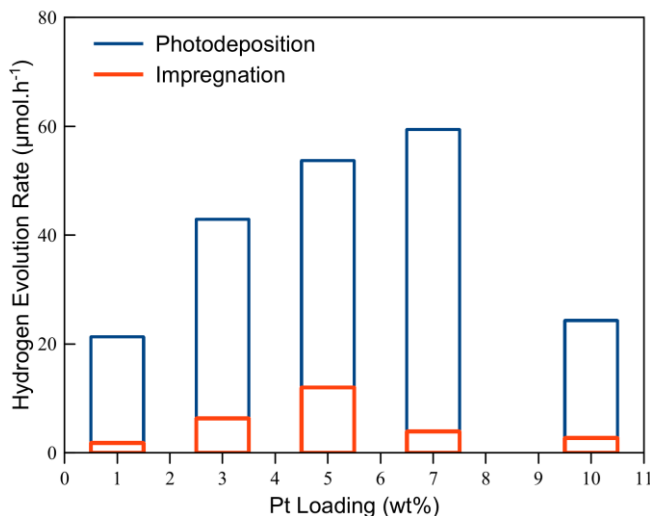


Figure 4.2: Comparison between impregnation and photo-deposition methods for the photocatalysts surface modification with Pt co-catalyst. Comparative studies of HER deposition technique (this figure) and HER photocatalysts materials/loading (Figure 4.5) were conducted using the same GaZnON-LDHs 3 photocatalyst sample. Details of the sample preparation for comparative studies are described in Chapter 2.

Interestingly, the optimal loading (to reach the highest hydrogen evolution rate) for the samples decorated through the impregnation method can be observed at 5 wt% Pt, while the photo-deposited samples exhibited a higher capacity up to 7 wt%. This improved capacity could be attributed to the selective surface occupation of Pt NPs during photo-deposition, compared to the random deposition of clusters and aggregates during impregnation. The effectiveness of photo-deposition for surface modification has been reported previously in the literature [99,153]. It is believed that the co-catalyst precursor film formed during the surface wetness step could be interrupted during the evaporation and thermal treatment steps, as displayed in the sequence of steps in Figure 4.3 (a–c).

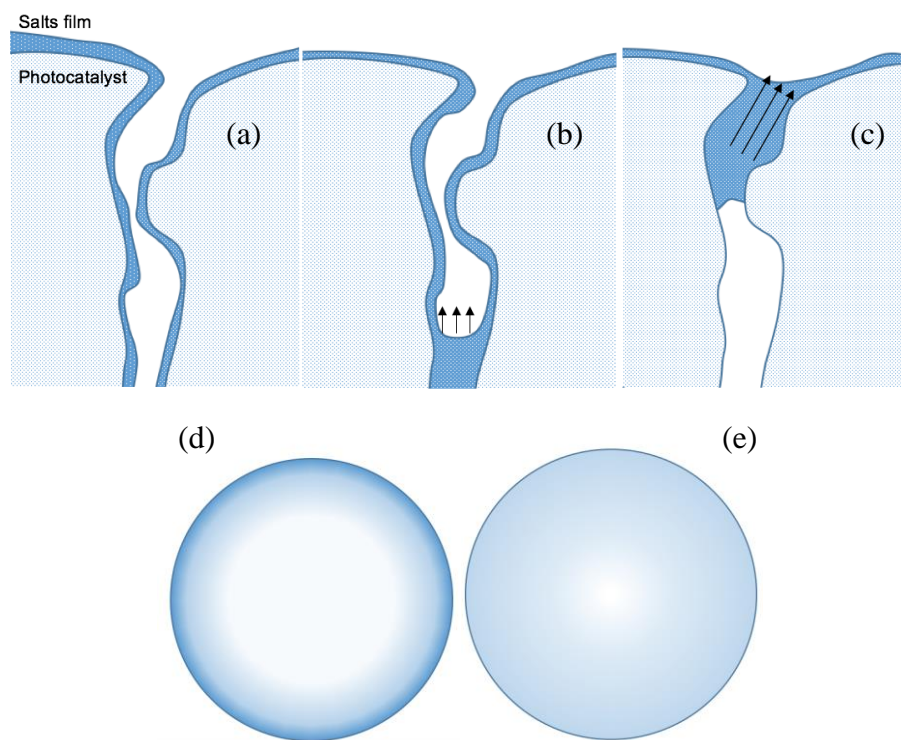


Figure 4.3: (a-c) Interruption of the co-catalysts precursors film during the impregnation on a porous structure; steps showing co-catalysts salt is dislodged from the pores during evaporation and thermal treatment. Comparison between co-catalyst active sites density (d) Egg-shell structure, and (e) uniform deposition.

The uniform film covering the photocatalyst surface in the mixing step, shown in Figure 4.3 (a), can be interrupted during drying and/or post-thermal treatment. The temperature gradient between the bulk and surface of the photocatalyst dislodges the catalyst salt from the pores to the surface layer, as illustrated in Figure 4.3 (b), causing the formation of a dense catalytic layer on the near-surface region, as displayed in Figure 4.3 (c). Such a dense layer on the outer surface of the photocatalyst results in a compositional imbalance, known as an “Egg-shell” structure [224–226], as shown in Figure 4.3 (d). On the other hand, as demonstrated in Figure 4.3 (e), the presence of photo-excited electrons within the entire photocatalyst structure leads to the deposition of co-

catalyst NPs uniformly on the surface and inside the pores. This uniform distribution explains the superior performance of the GaN:ZnO samples loaded through the photo-deposition method.

4.2 Optimal loading of co-catalyst active sites

Although co-catalyst active sites facilitate charge transfer from the bulk to the surface and enhance the rate of photocatalytic reactions, their loading amount must be optimized with respect to photocatalyst performance. Most co-catalyst materials are optically opaque, so they absorb the incident light that is meant to be the driving force of water splitting. It is documented that that excessive loading of co-catalyst active sites reduces the photocatalytic activity by shading the surface [227]. Unlike water electrolysis, in which the typical loading amounts of the HER and OER catalysts are above tens of wt% [217], co-catalyst loading for photocatalytic water splitting cannot exceed a few wt%. For the traditional GaN:ZnO solid solution, several HER and OER photocatalysts have been explored for water splitting application: Rh, Pt, Pd, and NiO_x have shown the highest HER, while IrO₂, RuO₂, and Ru molecular complexes have shown the highest OER activities [77,99,100]. However, the optimal loading of various co-catalyst materials is rarely addressed in the literature. It has been stated that 1–1.5 wt% is the optimal loading amount of Rh co-catalysts for the GaN:ZnO, whereas the photocatalytic activities do not vary significantly above this limit [228].

In this study, the optimal loading of Rh, Pt, NiO_x HER, and IrO_x, Mn₃O₄ OER catalysts was studied with respect to the rates of H₂ and O₂ evolution.

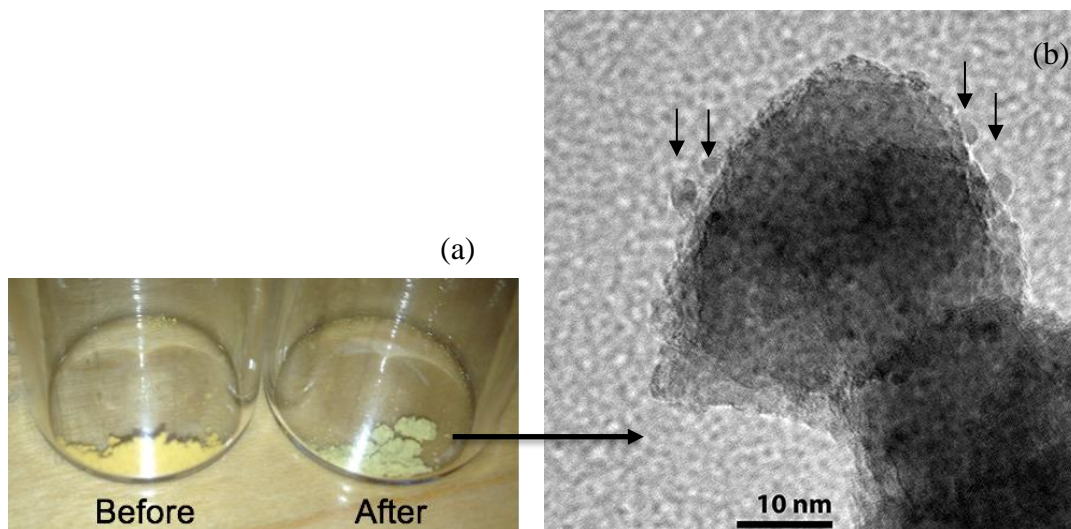


Figure 4.4: Changes in the appearance of the photocatalyst before and after 1 wt% Rh loading (a). Individual Rh NPs, marked by black arrows in the HRTEM image (b).

Upon photo-deposition, the color of the processing solution is darkened, suggesting the deposition of catalyst NPs on the surface of the nanoporous photocatalyst, as illustrated in Figure 4.4 (a). A high-resolution transmission electron microscopy (HRTEM) image of the 1 wt% Rh-loaded sample displayed in Figure 4.4 (b) confirms the deposition of individual Rh NPs with sizes ranging from 2–4 nm.

Figure 4.5 shows the hydrogen evolution for the GaN:ZnO photocatalyst loaded with Rh, Pt, and NiO_x co-catalysts at different loading amounts. The experiments revealed that Rh-loaded samples outperformed Pt- and NiO_x-decorated samples at 1, 3, and 5 wt% loading, while the Pt-GaN:ZnO sample exhibited superior performance at 7 and 10 wt%.

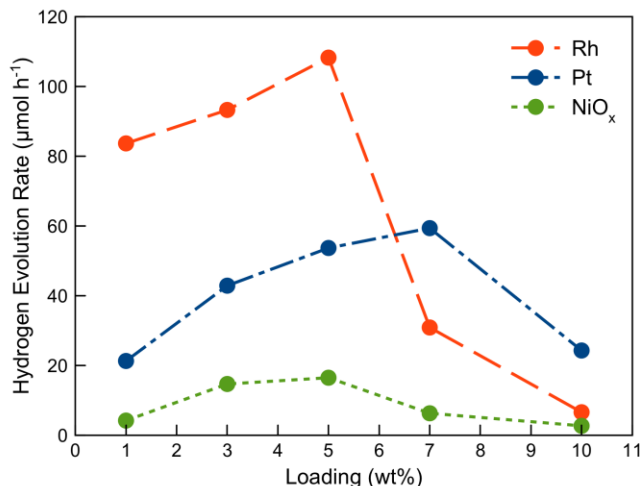


Figure 4.5: Dependency of the visible-light H₂ evolution rate to HER co-catalyst materials and their loading amount. Comparative studies of the HER deposition technique (this figure) and HER photocatalysts materials/loading (Figure 4.2) were conducted using the same GaZnON-LDHs 3 photocatalyst sample. Details of sample preparation for comparative studies are described in Chapter 2.

As expected, NiO_x-loaded photocatalysts showed the lowest photocatalytic activity. It should be noted that replacing highly active noble metals with Earth-abundant compounds is highly desirable, and recent studies suggest that engineered nanostructures of Co, Ni, and Mo-based HER catalysts can yield hydrogen evolution performance comparable to that of the state-of-the-art noble metal-based catalysts [219,229,230].

In contrast to the data reported in the literature, up to 7 wt% of Pt and 5 wt% of Rh and NiO_x can be loaded on the surface of nanoporous solid solution photocatalysts without reducing their photocatalytic performance. To the best of our knowledge, this increased loading limit is due to the higher surface area of the photocatalyst (36.4–53.1 m² g⁻¹, compared to 3.7–8.1 m² g⁻¹ reported for the GaN:ZnO prepared by the traditional method [70]). Hypothetically, the majority of the co-catalyst NPs are deposited inside the NPs within the nanoporous construction of the

photocatalyst. The structural characterization of the nanoporous photocatalyst presented in Chapter 3 provided solid evidence for the high degree of porosity of the prepared samples. The selected high angle annular dark field (HAADF) tomography images obtained by scanning transmission electron microscopy (STEM) in Figure 4.6 demonstrate the highly porous structure of the photocatalyst particles, with no sign of aggregation. Such a unique structure enhances the loading limit of the co-catalyst materials without shading the surface from the incident photons, but most importantly it reduces the recombination losses by shortening the charge carrier's diffusion path to the surface via the three-dimensional (3-D) porous structure. Therefore, the proposed synthesis technique, in addition to the benefits discussed in Chapter 3, provides a topological approach for effectively enhancing the number of HER active sites and promoting the charge transport process. Such advanced structures become more interesting given the fact that for practical uses, devices with low weights and high activity can be achieved via a nanoporous structure.

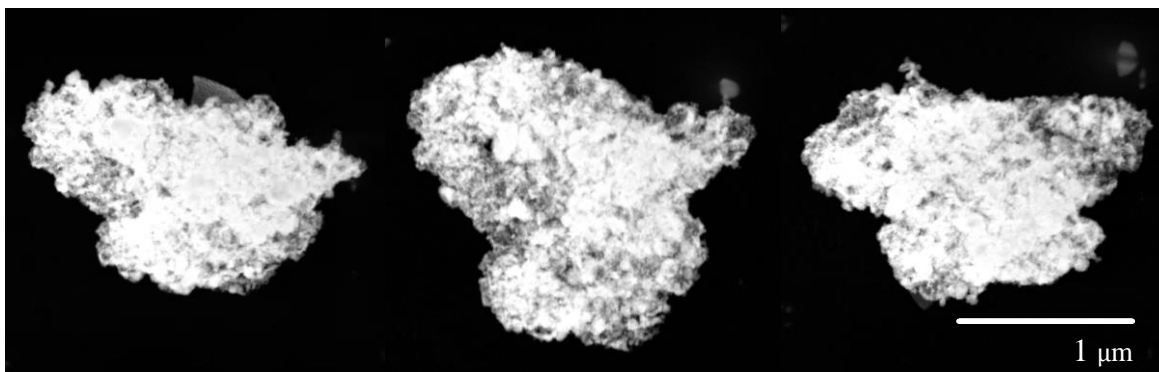


Figure 4.6: Selected angles HAADF STEM tomography images of a nanoporous GaN:ZnO particle.

The overall water splitting activity of the GaN:ZnO photocatalyst loaded with HER catalysts only indicates the suitable position of the VB state at more positive potentials, with

respect to the water oxidation reaction, as well as the existence of OER active sites on the surface of the pristine photocatalyst.

The GaN:ZnO photocatalyst decorated with 0.5 wt% IrO_x did not achieve an appreciable OWS activity from pure water due to the absence of HER active sites that 1) enhance the photo-recombination of holes with accumulated electrons in the bulk and on the surface, and 2) disrupt the charge balance of the semiconductor, which may result in the production of unwanted species and photo-decomposition of the photocatalyst surface. To analyze the OER co-catalyst performance, the oxygen evolution of samples decorated with IrO_x and Mn₃O₄ was measured in 5 mM of silver nitrate (as electron acceptor reagent) aqueous solution.

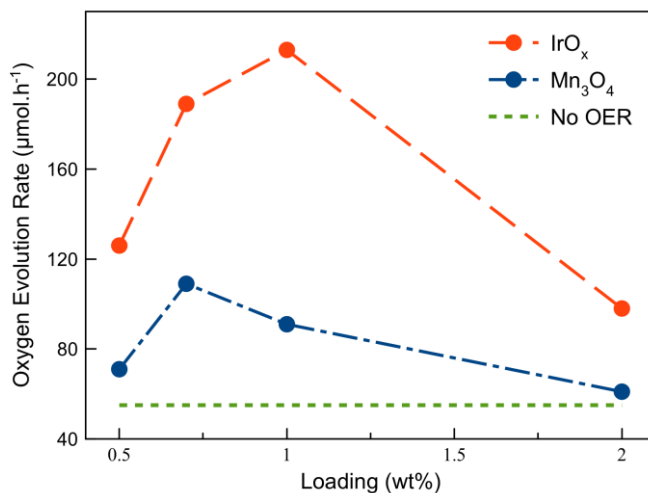


Figure 4.7: Effect of OER co-catalysts materials and loading on the O₂ evolution from 5 mM AgNO₃ solution. Oxygen evolution results of the bare and surface modified photocatalyst were obtained using the same GaN:ZnO- GaZnON-LDHs 3 photocatalyst samples, which were decorated with IrO_x and Mn₃O₄ at various loadings. Details of sample preparation for comparative studies are described in Chapter 2.

Sacrificial oxygen evolution results in Figure 4.7 confirm the presence of intrinsic OER active sites on the surface of the nanoporous GaN:ZnO photocatalyst, as the bare photocatalyst demonstrated notable oxygen evolution activity. Samples loaded with IrO_x and Mn₃O₄ co-catalysts showed superior oxygen evolution performance compared to that of the blank GaN:ZnO, revealing the effective OER catalytic capability of the two. Similar to HER catalysts, the optimal loading of OER catalysts depends on the catalyst material (0.7 wt% for Mn₃O₄ and 1.0 wt% for IrO_x), which is likely attributed to the final size of the nanoparticles. It should be noted that the optimal OER catalyst loading in AgNO₃ solution may not be identical to the one for the OWS since the kinetics of the reactions and the charge transfer mechanisms are vastly different.

Comparing the optimal loadings of the HER (5–7 wt%) and OER (0.7–1.0 wt%) co-catalysts indicates that the surface capacity of the photocatalyst for the OER sites is significantly lower than that of the HER sites. Although higher capacity semiconductor surfaces for HER co-catalysts have been reported previously [100], due to the nanoporous construction of the photocatalyst and through the mechanism discussed earlier, higher optimal loading is expected for the OER active sites. During the AgNO₃-mediated oxygen evolution, 15–30 min after illumination, the yellowish color of the solution changes to dark grey, indicating the rapid deposition of silver NPs on the surface of the photocatalyst. This rapid deposition shades the surface from the incident photons, resulting in termination of oxygen evolution in 2–4 h. Since silver and OER catalyst NPs are deposited through photo-deposition (reaction of precursor with the photo-excited electrons), the same sites on the surface of the photocatalyst have likely been used for their nucleation. Hypothetically, the rapid deposition of Ag nanoparticles onto IrO_x or Mn₃O₄ active sites could have deactivated a great portion of the OER active sites in the initial stages of reaction, as

schematically displayed in Figure 4.8. Thus, the actual impact of the OER catalyst on the O_2 evolution activity of the photocatalyst cannot be measured.

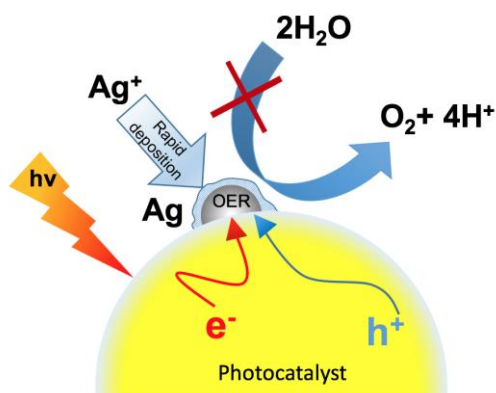


Figure 4.8: Rapid deactivation of OER co-catalyst by formation of Ag deposits onto photo-deposited OER sites during sacrificial O_2 evolution in $AgNO_3$ solution.

The average oxygen evolution rate measured for the 1 wt% IrO_x -loaded photocatalyst ($\sim 213 \mu\text{mol h}^{-1}$) is significantly higher than the highest recorded oxygen evolution from the OWS reaction using 1 wt% Rh-GaN:ZnO photocatalyst. Such improvement is attributed to the high OER rate on the IrO_x active sites as well as the presence of Ag^+ acceptor ions in the solution, which react efficiently with the electrons at lower potentials ($+0.80 \text{ eV vs. NHE}$ at standard condition [231]), compared to the H^+ ions. The role of Ag^+ electron acceptor can also be noticed in the sacrificial O_2 evolution rate of the blank photocatalyst ($\sim 55 \mu\text{mol h}^{-1}$), which is greater than the highest O_2 evolution ($\sim 35 \mu\text{mol h}^{-1}$) observed from OWS.

The promising performance of IrO_x as an OER catalyst encouraged us to explore the activity of the GaN:ZnO photocatalyst co-loaded with IrO_x (OER) and Rh (HER) active sites for OWS. Table 4.1 describes the prepared samples along with the IrO_x loading method and the obtained OWS result under visible light.

Table 4.1: Impacts of OER and HER catalysts co-loading, and the OER catalyst deposition method on the OWS performances of the nanoporous GaN:ZnO photocatalyst. The OWS data of the bare and surface modified photocatalyst were obtained using the same GaZnON-LDHs 3 photocatalyst samples, which were decorated with HER and OER co-catalyst materials at various loadings. Details of the sample preparation for comparative studies are described in Chapter 2.

Sample	Rh	Ir	Method	Activity ($\mu\text{mol h}^{-1}$)	
				H ₂	O ₂
1	-	-	-	3.2	1.1
2	1 wt%	-	-	67.3	25.9
3	-	0.5 wt%	Photo-deposition	8.1	3.4
4	1 wt%	0.5 wt%	Photo-deposition	31.0	17.6
5	1 wt%	0.5 wt%	Impregnation	36.2	16.1
6	1 wt%	0.02 wt%	Impregnation	61.7	26.1

As stated earlier, and as can be seen in Table 4.1, the blank GaN:ZnO photocatalyst (sample 1) does not show considerable OWS activity due to the lack of HER active sites. Upon loading of 1 wt% Rh co-catalyst (sample 2), the activity enhances, as Rh active sites effectively reduce H⁺, and holes participate freely in the oxygen evolution reaction. Decorating the surface of the GaN:ZnO photocatalyst with 0.5 wt% of IrO_x (sample 3) increases the OWS activity of the photocatalyst slightly, compared to the blank sample, due to its weak HER characteristics [77]. The photocatalyst co-loaded with IrO_x and Rh (sample 4–6) exhibits lower OWS activity compared to that of the Rh-loaded photocatalyst (sample 3). Reducing the Ir content of the photocatalyst to 0.02 wt% (Sample 6) enhances the photocatalytic activity of the co-loaded photocatalyst but does not exceed that of the Rh-loaded GaN:ZnO (sample 3). The reduced activity of the samples due to the incorporation of the OER catalyst appears to be related to the overlapping of the OER and HER sites on the surface and within the porous structure, causing the accumulation of photo-induced

holes and electrons at the overlapped HER and OER sites. The slight improvement in the OWS activity from sample 4 to sample 5 could have occurred because the photo-deposited OER and HER catalysts (samples 4) attract electrons and holes to the same sites on the surface and cause their recombination. Replacing the photo-deposition (sample 4) with impregnation (sample 5) for loading of the OER catalyst reduces the co-deposition of HER and OER catalysts on the same surface sites. However, as illustrated in Figure 4.3, this may cause the formation of an OER catalytic shell at the surface of the photocatalyst.

The H_2/O_2 ratios calculated from the OWS performances of the examined samples in Table 4.1 approach the stoichiometric value of 2.0 upon IrO_x catalyst loading. It is believed that the presence of the OER active sites efficiently promotes the water oxidation reaction and therefore reduces the density of the trapped charges on the surface. Such a mechanism can favourably contribute to an improvement in photocatalyst lifetime and a reduction of the side product formation on the surface.

4.3 Undesired reverse reaction catalyzed by HER active sites

It is generally accepted that the surface sites of most noble metal co-catalysts are also suitable for catalyzing the formation of water from photo-generated H_2 and O_2 , the so-called water splitting back reaction [11]. The reverse reaction can be completely suppressed via two approaches: 1) use of sacrificial reagents, or 2) physically separate photo-active sites (PEC configuration) [10]. However, some studies have shown improvements in the OWS efficiencies of suspended photocatalysts, presumably because of suppression of the H_2 and O_2 reaction by applying modifications to the electrolytes or the surface of the photocatalyst [101–103].

The OWS data in this research implies efficient H₂ and O₂ evolution using Rh NPs as co-catalysts. To our understanding, the insignificance of the reverse reaction is related to the nanoporous structure of the photocatalyst. It is believed that the accessibility of evolved O₂ and H₂ to the Rh active sites inside the nanopores is hindered by limited mass transfer through the channels.

One interesting strategy for suppressing undesired water formation is surface modification with materials that are permeable to some species while blocking the access of others. Cr₂O₃ thin film, as a shell surrounding the core HER catalysts, appears to be permeable to H⁺ and H₂ and blocks O₂ access to the core catalysts; therefore, this suppresses the reverse reaction [91,94,187].

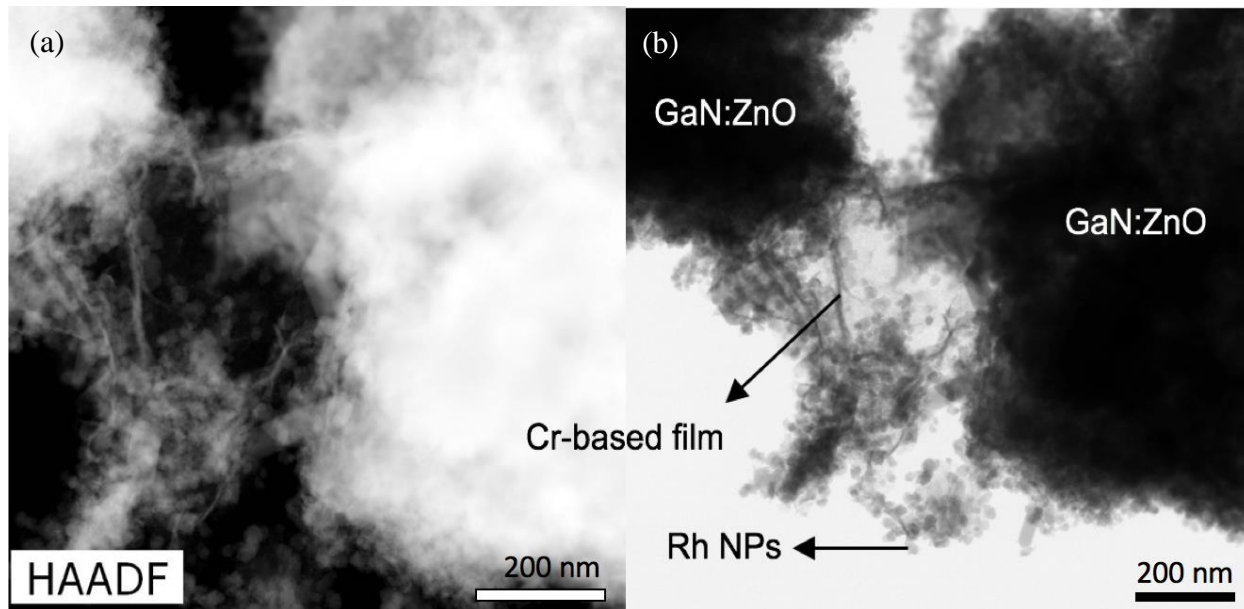


Figure 4.9: STEM (a) and HRTEM (b) image showing the formation of Rh aggregates wrapped in Cr-base film, and blocked the space between two photocatalyst surfaces.

In the case of nanoporous GaN:ZnO, the OWS performance declines by 30–45% upon surface modification with Cr₂O₃ shell. As shown in Figure 4.9, photo-deposition in the presence

of K_2CrO_4 promotes the formation of structures containing embedded Rh NPs, which block the spaces between photocatalyst surfaces, rather than their uniform distribution inside the pores and on the surface. The EDX elemental profile in Figure 4.10 reveals that Cr is the dominant element in the region between the two surfaces of the photocatalyst, as shown in Figure 4.10 (f). The Rh signals were detected on the photocatalyst surface and within the gap, as displayed in Figure 4.10 (e). The rest of elements (Ga, N, Zn, and O) are distributed uniformly in the bulk, as demonstrated in Figure 4.10 (a-d).

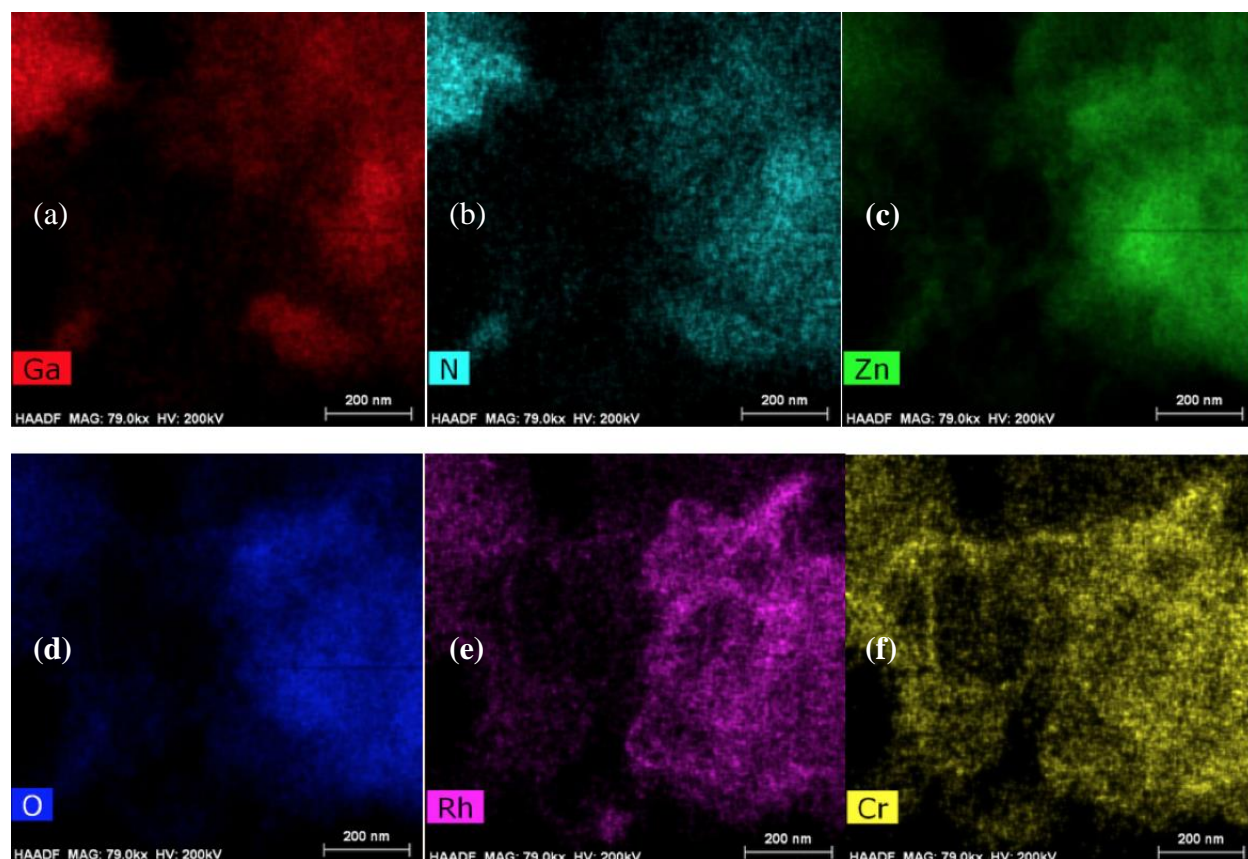


Figure 4.10: STEM-EDX compositional profile of the region displayed in Figure 4.9. Ga (a), N (b), Zn (c), O (d), Rh (e), and Cr (f).

The high density of Cr in the aggregation area suggests its role in the formation of the Cr layer that wraps Rh nanoparticles. This film is apparently responsible for blocking the nanopores entry, which is the basis of the nanoporous GaN:ZnO photocatalytic activity.

In conclusion, the findings of our study suggest a mechanism for effectively enhancing the capacity of photocatalyst materials for deposition of active sites, without compromising the light absorption. Moreover, the nanoporous structure exhibited a significant contribution in reducing the carrier diffusion path, thus reducing the photo-recombination losses.

Chapter 5: GaN:ZnO-Reduced Graphene Oxide (rGO) Composite

Graphene, as an allotrope of carbon, is an isolated monolayer sheet contains atoms tightly packed into sp^2 honeycomb lattice hybridized C–C bond with a π -electron cloud, is considered as one of the most important materials in the current century [123]. Surface and structure modification of graphene resulted in various materials such as graphene oxide (GO), doped graphene, graphene nanoribbons, and graphene quantum dots (QDs) with a wide range of morphological, optical, chemical, and electronic properties.

One convenient route to prepare graphene is through reduction of GO. Graphene oxide was synthesized in 19th century by Brodie and Staudenmaier, and later by Hummer [155]; however, its preparation, properties, and applications are still under debate [124]. Different graphite oxidation routes result in various oxygen functionalities, with a range of densities and distribution on the two-dimensional GO platform [123]. Optical measurements of the charges life-time in GO shows ns-scale decays, indicating the insulating/semiconducting behavior of GO, depending on its oxygen composition [232]. Highly oxidized graphene oxide is an insulating material [125]. Reduction of GO to reduced graphene oxide (rGO) is a facile and scalable route to tune the band gap of the semiconducting nanosheets-like compounds in a wide range: from insulating material to semi-metal with excellent charge carriers mobility $\sim 200,000 \text{ cm}^2 \text{ V}^{-1} \text{ s}^{-1}$ [114]. Mathkar et al. successfully controlled the band gap of GO nanosheets from 3.5 eV (O-rich GO) to 1.0 eV (C-rich GO or rGO) as demonstrated in Figure 5.1, by removing the oxygen functionalities [233]. Through thermal, electrical, chemical or photochemical reduction routes, rGO with tailored chemistry and electrochemical properties can be produced at large scale. In particular, photo-induced reduction, as an in-situ approach, offers many benefits such as room temperature processing, less contamination, and minimum pre- and post-treatments.

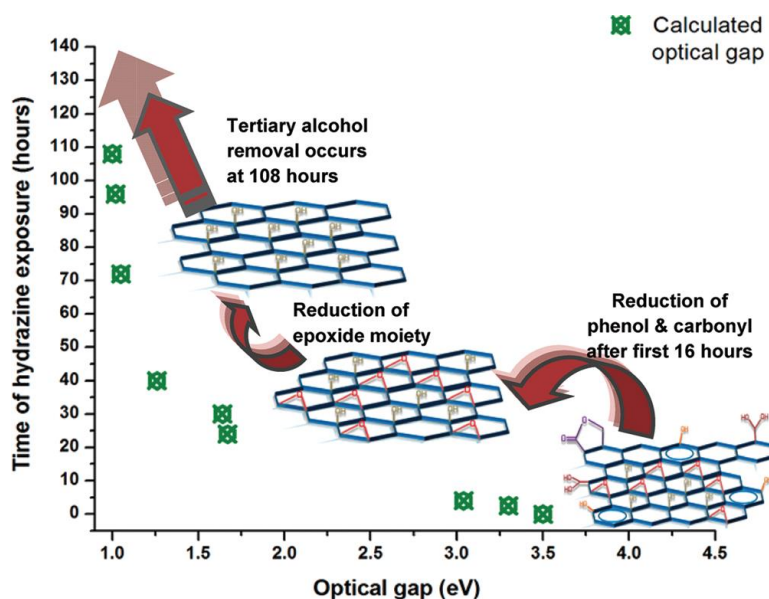


Figure 5.1: Chemical reduction of GO in hydrazine vapor. Band gap energy and schematic structure of the nanosheets at various stages of reduction are also depicted [233]. Reprinted with permission from (J. Phys. Chem. Lett., 2012, 3 (8), pp 986–991). Copyright (2012) American Chemical Society.

In the last decade, effectiveness of graphene-based composites (GBCs) in facilitating the transportation of charge carriers for production of solar fuels, particularly via water splitting, has been demonstrated for metal oxides, nitrides, sulfides, ternary composites and plasmonic metal nanostructures [15,114]. However, the majority of studies rely on the intrinsic characteristics of the semiconductors [15], whether graphene was employed as the electron acceptor, light absorber, electron mediator, or redox active sites [130]. Thus, a general mechanism to confirm the improvement in photocatalytic activities because of graphene incorporation cannot be developed. In this chapter, potentials of GaN:ZnO-rGO composite for enhancing the efficiencies of OWS is explored. The solid solution photocatalyst was prepared through nitridation of Ga₂O₃ and ZnO (the traditional solid-state technique) and applied as the model photocatalyst.

Pre-exfoliated graphite flakes were oxidized through the modified Hummers method to single sheets of GO with high density of oxygen containing functional groups. For the first time, the nanocomposite of the GaN:ZnO photocatalyst and GO nanosheets was synthesized through a facile self-assembly route, and subsequently transformed to the rGO composite under visible light irradiation. Various techniques were employed to characterize the physical, chemical and photochemical properties of the precursors and prepared samples.

5.1 Formation of functional GaN:ZnO-rGO composite

The X-ray diffraction (XRD) pattern of the prepared GaN:ZnO solid solution in Figure 5.2 (a) exhibits the diffraction pattern of wurtzite crystalline structure, located between that of the ZnO and GaN, as displayed in Figure 5.2 (b), confirming the formation of solid solution between the two.

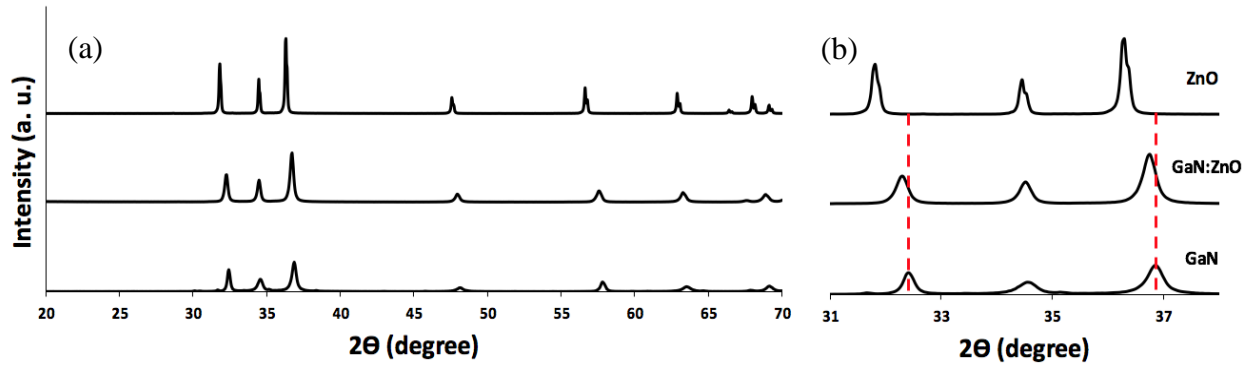


Figure 5.2: XRD pattern of GaN:ZnO solid solution, GaN, and ZnO (a) wurtzite structure, and (b) diffraction pattern shift.

The bulk $x = [\text{Zn}]/[\text{Zn}+\text{Ga}]$ of the photocatalyst, obtained from energy dispersive X-ray (EDX) spectroscopy, was estimated ~ 0.10 , which is slightly lower than those reported for the samples prepared under similar conditions ($x = 0.13\text{--}0.15$ [25,27,70]). This deviation is likely

attributed to hydrodynamic differences in the synthesis apparatuses. Due to the low velocity of ammonia ($v = 3.3 \times 10^{-3} \text{ m s}^{-1}$), the solid-gas diffusion rate is significantly low; therefore, slight changes in the synthesis apparatus may affect the properties of the prepared oxynitride photocatalyst substantially.

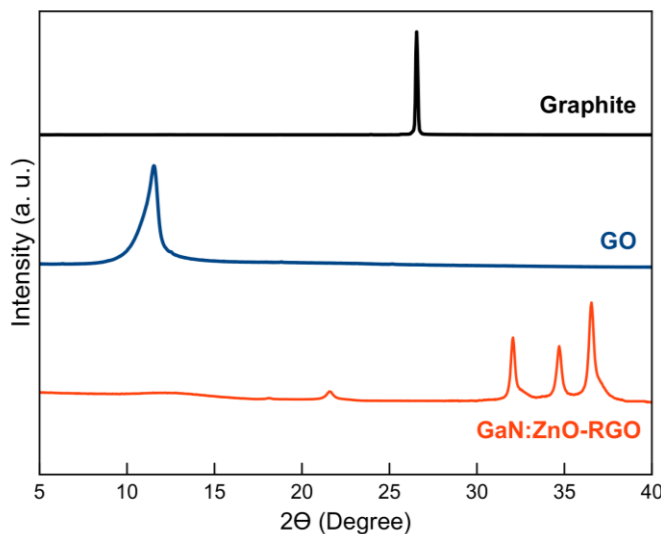


Figure 5.3: XRD pattern of pristine graphite, prepared GO, and GaN:ZnO-rGO composites.

Series of XRD data were acquired from the graphite precursor, GO and the prepared rGO composite, as demonstrated in Figure 5.3. XRD data confirmed the oxidation of graphite to GO, since the (002) peak of graphite at 27.5° , indicating an interlayer spacing of 0.33 nm corresponds to the distance between the densely packed graphitic layers, has shifted to 11.5° for GO, revealing that the interlayer spacing increased to 0.77 nm as the result of oxidization. This shift is caused by the introduction of oxygen-containing groups on the basal plane [123] and suggests the extensive oxidation of graphite. The XRD pattern of the prepared GaN:ZnO-rGO composite shows the rGO peak at 21.6° (interlayer spacing = 0.41 nm), in agreement with data reported in the literature [234,235], along with the wurtzite GaN:ZnO solid solution peaks at the higher angles. It is noticed

that the wurtzite peaks in rGO composite have widened slightly, compared to those of the as prepared GaN:ZnO. In addition, shoulders have appeared at the higher angles. These changes could be assigned to partial crystallographic damages caused by intense ultra-sonication during the GO composite synthesis.

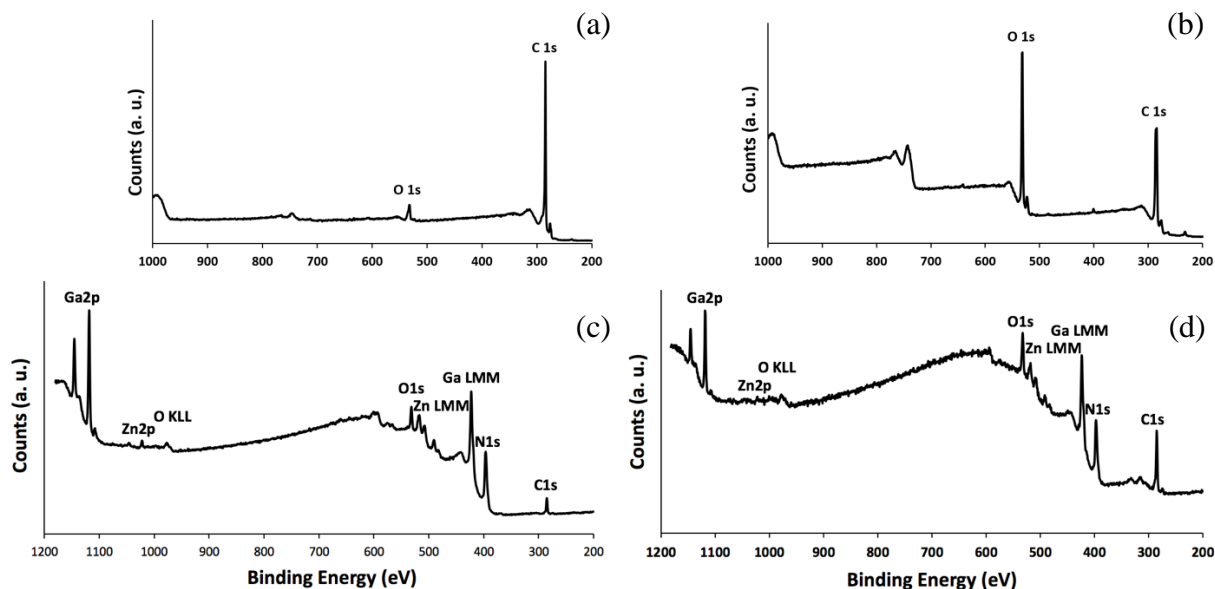


Figure 5.4: XPS spectra of (a) graphite, (b) GO, (c) GaN:ZnO, and (d) GaN:ZnO-rGO composite.

The subsequent oxidation and reduction steps can be characterized through analyzing the surface states of the prepared samples. X-ray photo-electron spectroscopy (XPS) survey spectra of graphite, the prepared GO, GaN:ZnO and GaN:ZnO-rGO composite are presented in Figure 5.4. C/O atomic ratios of 12.36, 2.05, and 3.50 are estimated for graphite, prepared GO, and GaN:ZnO-rGO composite, shown in Figure 5.4 (a, b and d) respectively, suggesting the effectiveness of the Hummer's oxidization of pre-exfoliated graphite, as well as the in-situ photo-assisted approach in reduction of GO. Graphite XPS survey spectra in Figure 5.4 (a) contain a major C 1s peak only, whereas the minor O 1s peak at ~532 eV is attributed to partial exfoliation and oxidization of the

natural graphite during ultra-sonication and surface adsorption from ambient. The surface composition of the prepared GO in Figure 5.4 (b) contains two major peaks for C1s (290–282 eV) and O1s (530–535 eV) as the result of an intense oxidization. The surface composition of GaN:ZnO solid solution and its rGO composite in Figure 5.4 (c and d) reveals higher concentration of carbon and oxygen (evidenced by relatively intense C1s and O1s peaks of rGO composite) as the result of reduced graphene oxide incorporation.

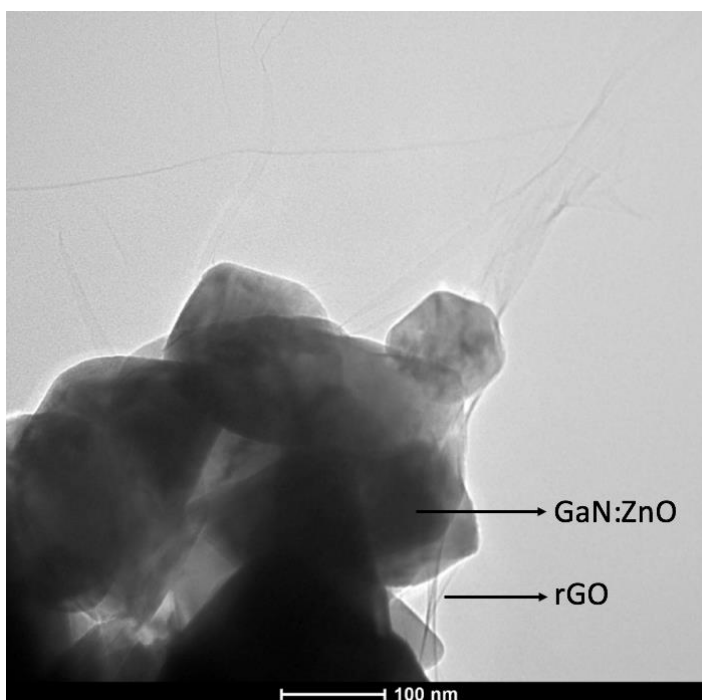


Figure 5.5: TEM image of GaN:ZnO-rGO composite showing the photocatalysts particles are wrapped in a monolayer rGO nanosheet.

Interestingly, the intensity of the Ga2p and Zn2p peaks have reduced from GaN:ZnO in Figure 5.4 (c) to its rGO composite in Figure 5.4 (d), suggesting that portion of the photocatalysts particles are wrapped in rGO nanosheets; therefore, not detectable by XPS. This embedded

structure between photocatalyst particles and rGO nanosheets can be seen in the transmission electron microscopy (TEM) image displayed in Figure 5.5, showing 100–250 nm particles are fully wrapped in a single layer rGO nanosheet. Such structure provides effective and stable electrochemical interfacial contact between the photocatalyst particles and conductive support. Besides, the optical transparency of monolayer graphene (> 97.5% optical transmittance [119]) maintains the photocatalytic activity of the composite by allowing the light photons to pass through the nanosheets and reach to the surface of the photocatalyst particles.

High degree of oxidation-reduction is further evidenced through high resolution C1s band characteristics of the samples. The C1s peak of graphite in Figure 5.6 (a) transforms into a complex spectra showing two maxima for GO in Figure 5.6 (b). This signal is deconvoluted to three peaks: C=C and C–C (47%, 284.5 eV), C–O (40%, 286.5 eV), and O–C=O (13%, 287.3 eV), indicating the occupation of nanosheets surface with high density of oxygen functionalities. As shown in Figure 5.6 (c), after photo-reduction, the densities of functional oxygen-containing groups are decreased significantly to C=C and C–C (75%, 284.5 eV), C–O (12%, 286.5 eV), and O–C=O (13%, 287.3 eV) and the broken sp^2 network was repaired.

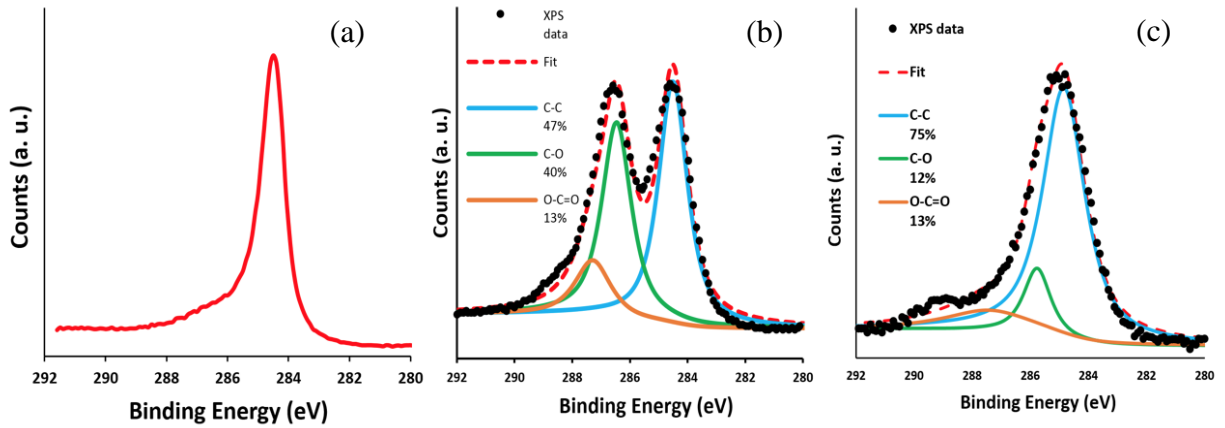


Figure 5.6: High resolution C1s spectra of (a) graphite, (b) GO, and (c) GaN:ZnO-rGO composite.

The remaining oxygen containing groups in the structure of the rGO composite is advantageous not only for maintaining the solubility of the composite for most applications, but also for stabilizing the interaction and charge transfer between composite components. This is important, knowing that the removal of oxygen functionalities transfers the characteristic of GO towards pristine graphene which is hydrophobic with negligible solubility in most solvents. In the course of reduction, the hydrophilic functionalities are removed; therefore, the electrostatic repulsion between negatively charged nanosheets is weakened, leads to Van der Waals restacking [236,237]. Further reduction leads to formation of aggregates with wrinkled, and crumpled morphologies [238–240]. Formations of these aggregates are irreversible and results in loss of high surface area of graphene [241].

5.2 Structure of the prepared GaN:ZnO-rGO composite

The preparation of GO nanosheets through the Hummers method using large natural graphite flakes leads to GO colloidal solution containing graphitic aggregates [242]. The impact

of graphite grain size on the quality of the prepared GO by reducing the graphitic phase residues has been addressed in the literature, concluded the effectiveness of pre-exfoliation [243,244].

After 3 h of ultra-sonication, graphite flakes with size larger than 500 μm in Figure 5.7 (a), transformed to pre-exfoliated graphite containing reduced size flakes as demonstrated in Figure 5.7 (b). Application of the pre-exfoliated graphite flakes as the starting material of the modified Hummers method results in fully-exfoliated GO nanosheets with smooth and clear surface, with no sign of contamination, as shown in Figure 5.8.

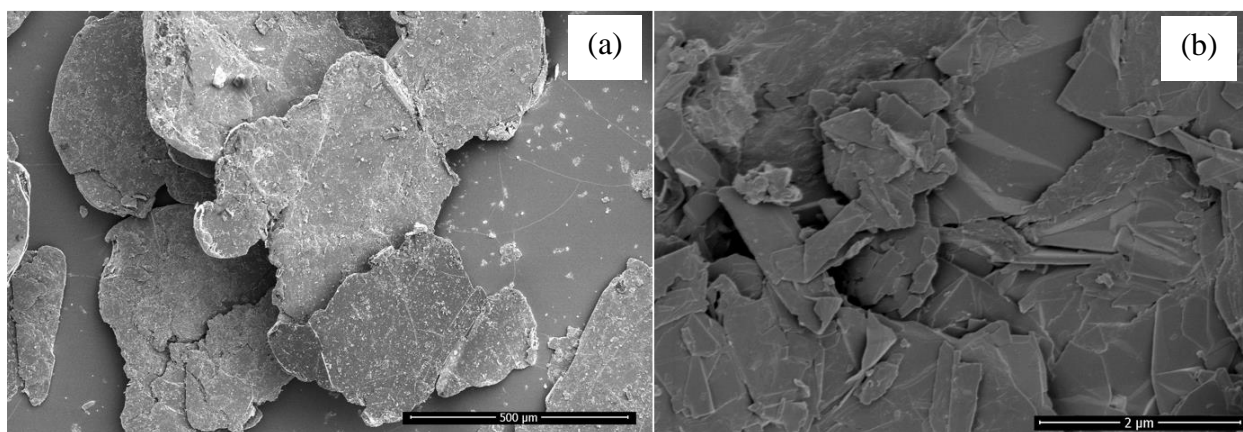


Figure 5.7: SEM image of graphite flakes (a) before and (b) after ultra-sonication for 3 h in pure water.

Majority of the prepared GO nanosheets have sizes over 10 μm and identified as single nanosheets with a wrinkled surface texture, as shown in the TEM and scanning electron microscopy (SEM) images in Figure 5.8 and Figure 5.9 (a), respectively.

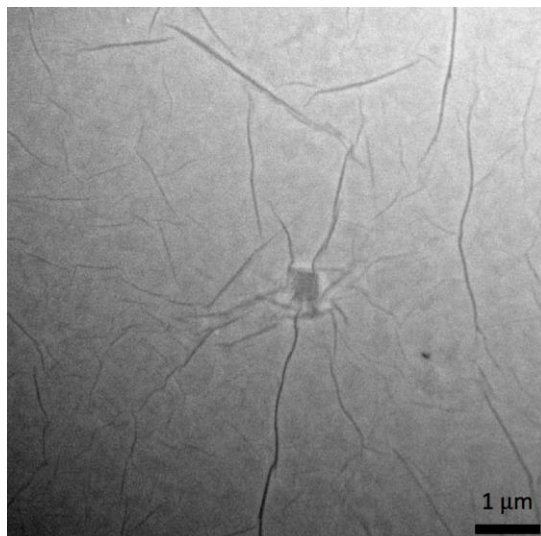


Figure 5.8: TEM image of a monolayer GO nanosheet prepared through modified Hummers method using pre-exfoliated graphite as the starting material.

The synthesized GaN:ZnO solid solution photocatalyst particles found to be uniform in shape, with sizes between 50 to 300 nm, shown in Figure 5.9 (b). Surface of the particles are clean with no sign of roughness. SEM analysis indicated that the majority of the solid solution particles tend to form large clusters up to 1 μm in size; yet, a portion of the sample contains individual particles or smaller clusters.

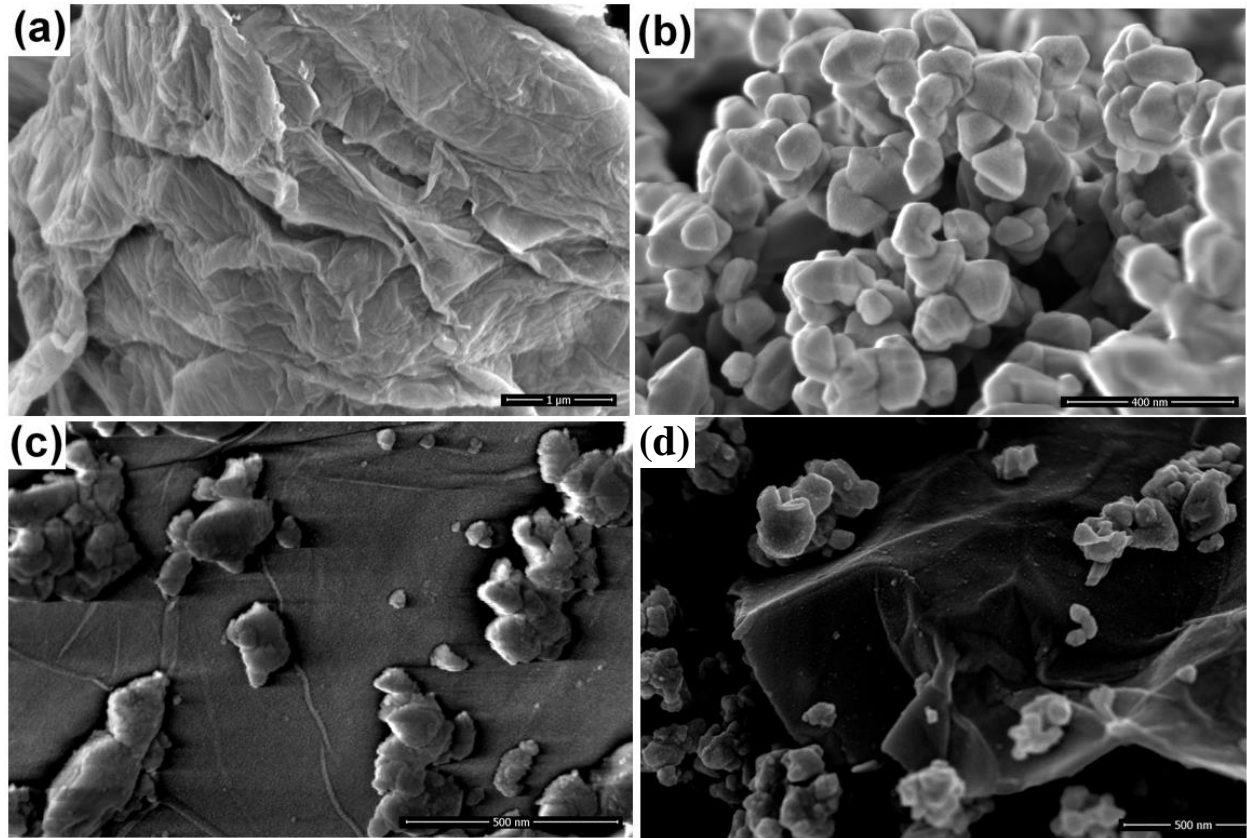


Figure 5.9: SEM images of the prepared (a) GO, (b) GaN:ZnO, (c) GO composite, and (d) rGO composite.

SEM image of the GaN:ZnO-GO composite displayed in Figure 5.9 (c), reveals the presence of individual and reduced-size clusters of the solid solution particles, less than 250 and 700 nm in size, respectively, distributed uniformly over the surface of GO. Dispersion of individual particles/smaller clusters in the GaN:ZnO-GO composite is attributed to the application of ultrasound treatment in the preparation of the composite sample. Also, the electrostatic attraction between negatively charged GO and surface of the photocatalysts particles during the electrostatic self-assembly may contribute to the relatively uniform distribution of the GaN:ZnO particles. SEM micrograph in Figure 5.9 (c) also revealed that the morphology of the GaN:ZnO particles is slightly

changed and roughness on the surfaces has appeared. The rough surface of the particles can be assigned to particle-particle breakage and attrition during ultra-sonic treatment. Such surface damages could enhance recombination losses by trapping the photo-induced charges. Despite the partial surface deformation of the particles, nanosheets surface remained clean and smooth. As shown in Figure 5.9 (d), the nanosheets have wrinkled further due to the removal of hydrophilic tails after photo-reduction. This wrinkled structure is known as an intrinsic feature of large graphene nanosheets [122,130].

The prepared rGO composite was examined for its structure and distribution of the compounds via scanning transmission electron microscopy (STEM) analysis, as the obtained micrographs and the compositional profiles are shown in Figure 5.10 and Figure 5.11, respectively. STEM images indicate that the rGO nanosheets are crumpled around the particles of GaN:ZnO. Ideally, this structure can be engineered through surface functionalization with conductive molecular linkers to improve the distribution of solid solutions particles, as well as suppress the formation of wrinkles at nanosheet edges. Alternatively, the mixed metal oxide precursor can be grafted on the surface via in-situ crystallization and treated at high temperature for nitrogen doping. This approach not only enhances the effective charge transport between photocatalyst and conductive support via chemicals interfacial bonds, but also, changes the electronic properties of graphene towards N-doped graphene which is known as a highly conductive 2-D material, consisting of n- and p-type island on the surface that are highly active for O₂ and H₂ evolution, respectively [245].

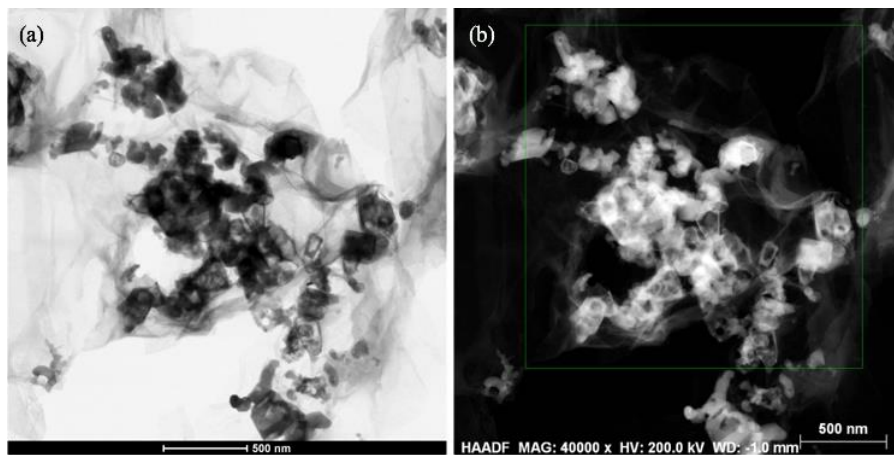


Figure 5.10: Dark (a) and bright (b) field STEM images of the GaN:ZnO-rGO composite.

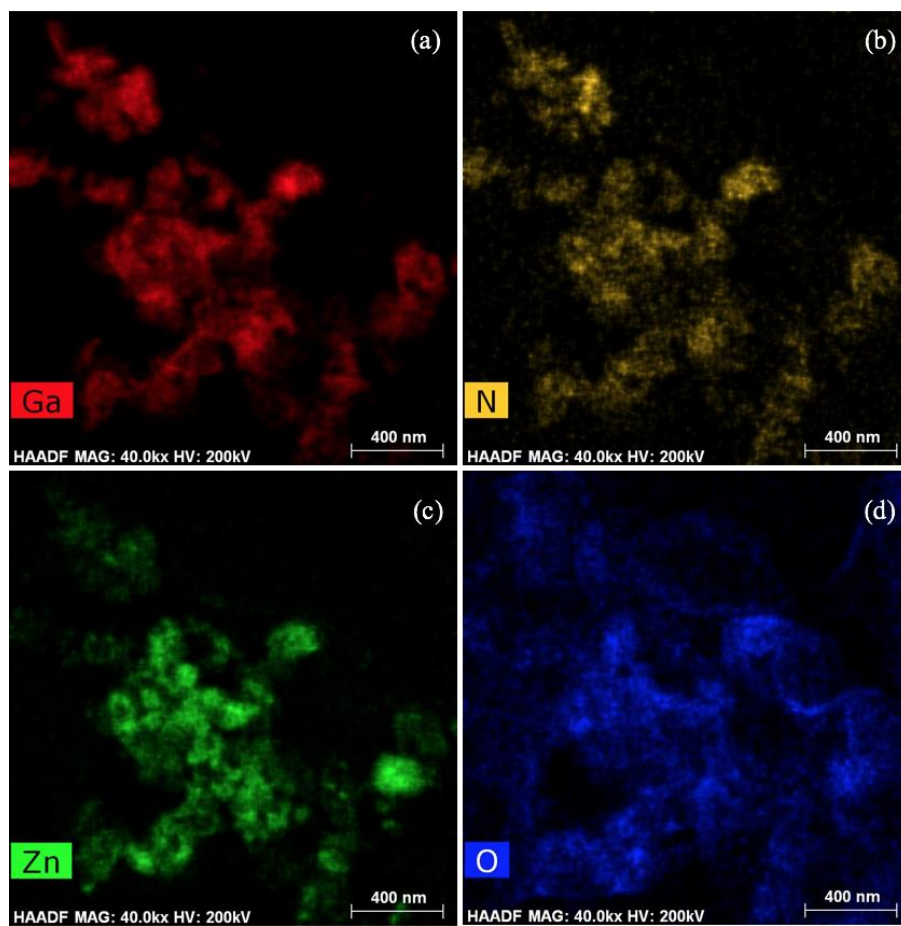


Figure 5.11: EDX elemental profile of the area selected in Figure 5.10 for (a) Ga, (b) N, (c) Zn and (d) O.

EDX compositional profiles in Figure 5.11 imply a uniform distribution of Ga, N, and Zn elements in the area assigned to the solid solution photocatalyst in Figure 5.10, and not in the rGO region. Presence of oxygen within the entire sample area is expected, due to the existence of oxygen functionalities on the rGO surface.

5.3 Photo-deposition of co-catalyst active sites

Visible-light photo-deposition was conducted to decorate the surface of the prepared GaN:ZnO-rGO composite with 1.5–2.5 wt% (metallic basis) Rh-Cr₂O₃ as HER co-catalyst. Bulk concentration of Rh and Cr was measured as 0.51 wt% and 0.83 wt%, respectively, while XPS data estimated the deposition of 0.41 wt% of Rh, and 2.16 w% of Cr on the surface. Increase of the Rh/Cr ratio from 0.19 on the surface to 0.61 in the bulk suggests that the Cr₂O₃ particles (or layer) have deposited on the Rh nanoparticles, forming a shell structure; therefore, they covered the Rh core co-catalyst from surface XPS detection.

It is important to confirm if the co-catalysts active sites have deposited on the surface of the rGO nanosheets, since it indicates that the photo-excited electrons can be injected to the conductive support, reached to a sufficient density, and participate in the reduction reaction at the rGO-electrolyte interface. Potentially, the fast charge transfer not only reduces the recombination losses, but also separates the O₂ and H₂ evolution sites, and decrease the rate of reverse reaction.

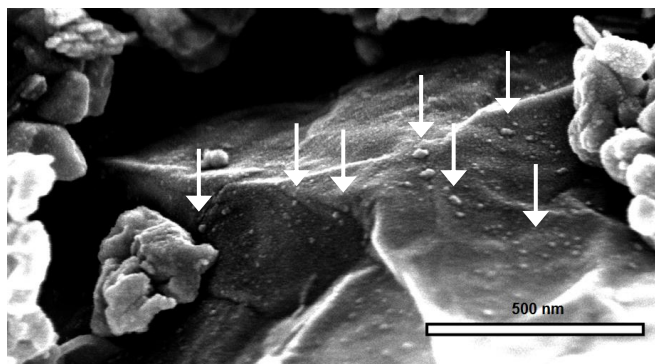


Figure 5.12: High resolution SEM images of the GaN:ZnO-rGO composite loaded with Rh-Cr₂O₃ NPs. White arrows show co-catalysts clusters.

A uniform pattern comprised of small particles and aggregates, less than 10 and 20 nm respectively, was observed on the surface of the rGO nanosheets of the composite loaded with Rh-Cr₂O₃ NPs, shown in Figure 5.12. The surface texture of GO composite in Figure 5.9 (c) have changed after deposition of co-catalyst NPs in Figure 5.12, inferring that the small particles and islands are deposited Rh-Cr₂O₃ co-catalysts. Surface patterns and contamination for chemically reduced samples or functionalized nanosheets are common. These textures are the residues of the processing chemicals that were deposited over the filtering and drying steps. Photo-reduction technique is extremely beneficial, where the obtained rGO composite is expected to be contamination-free. Since the GaN:ZnO-rGO composite prepared in this study was processed through photo-reduction of GaN:ZnO-GO, and not chemically, any contamination-related surface pattern is not expected. Therefore, the observed NPs and aggregates on the surface of rGO in Figure 5.12 are believed to be co-catalyst NPs, thereby confirming the sufficient electron density on the surface of rGO for reduction of the Na₃RhCl₆ and K₂CrO₄ precursors to the Rh-Cr₂O₃ active sites.

To investigate the deposition of co-catalyst NPs on the rGO surface, the Rh-loaded composite was examined through TEM. Acquiring a high quality TEM image from ultra-fine Rh NPs on the rGO nanosheets surface is a complicated task. Unlike Pt NPs, which appear as dark spots on the fairly transparent surface of graphene [246], Rh NPs form light spots that might be confused with structural wrinkles and pinholes on the rGO surface, as displayed in the HRTEM image of the Rh-loaded rGO composite in Figure 5.13.

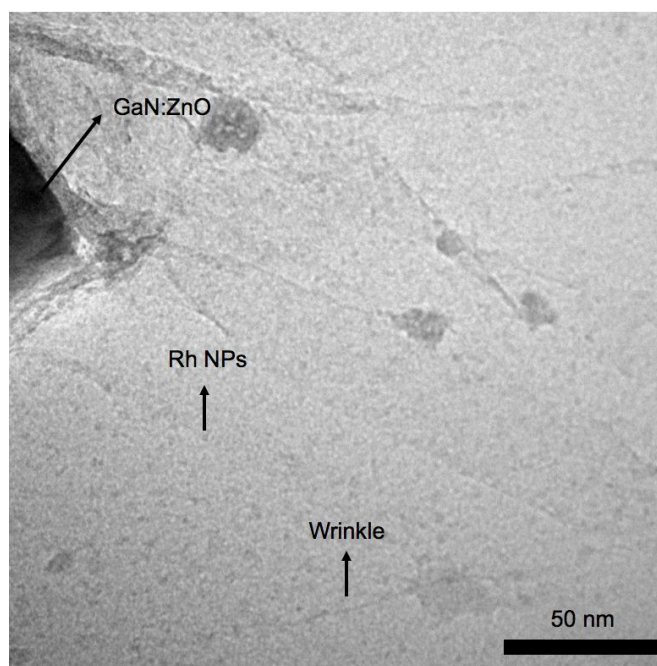


Figure 5.13: HRTEM image of the Rh-GaN:ZnO-rGO composite.

To obtain a certain visual evidence of Rh co-catalyst NPs on the surface of nanosheets, STEM mode at high resolution was employed, and the composition of the sample was mapped for Rh, as illustrated in Figure 5.14. Unlike the relatively indistinguishable Rh NPs via TEM in Figure

5.13, the STEM image in Figure 5.14 (a) clearly shows the texture of the nanosheets, along with ultra-fine Rh nanoparticles as bright spots.

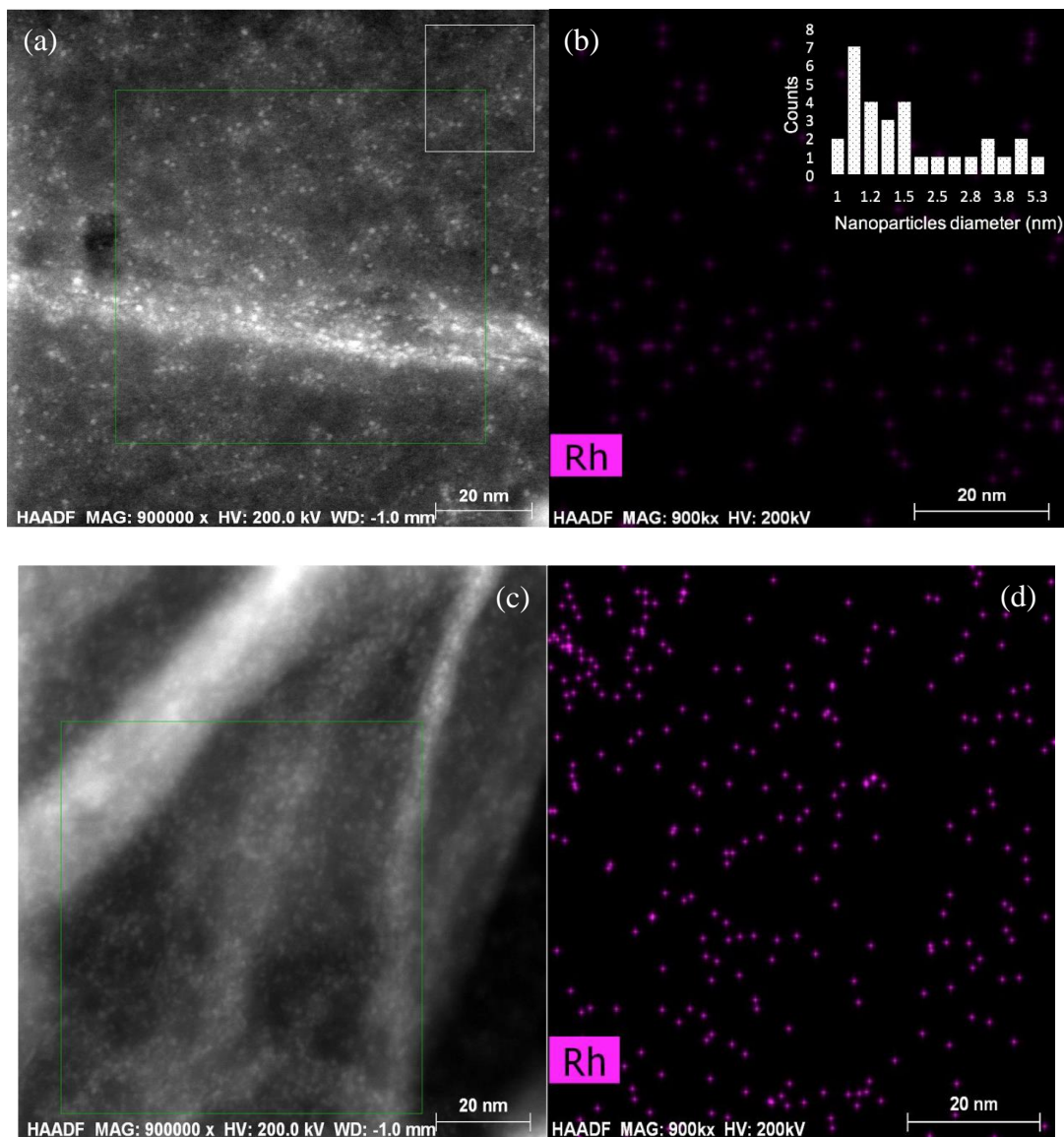


Figure 5.14: High resolution STEM image of the rGO surface loaded with Rh NPs (a and c), and Rh elemental map of the area indicated with the green rectangle in a and c (b and d). The inset in (b) displays the estimated Rh nanoparticle size distribution from the area indicated with the white rectangle in (a). The size distribution of the nanoparticles is presented as obtained with no statistical estimation. Image processing was conducted using ImageJ 1.50i.

The size distribution of Rh NPs between 1.0–5.3 nm were estimated from the area indicated by a white rectangle in Figure 5.14 (a), and demonstrated in the inset of the Figure 5.14 (b). The surface texture of the rGO nanosheets is further visible in the high resolution STEM image in Figure 5.14 (c), as such the wrinkles are clearly distinguished from the co-catalyst NPs. Figure 5.14 (a and c) suggest a very uniform deposition of Rh NPs on the rGO surface with no sign of aggregation. The compositional map of the areas indicated by the green rectangles in Figure 5.14 (a and c) are presented in Figure 5.14 (b and d), respectively. The Rh elemental data confirm that the bright dots can be accurately overlapped with the Rh elemental map, testifying the effective charge transfer to the rGO nanosheets and subsequent photo-deposition of Rh NPs from its salt solution under visible-light excitation.

5.4 Life-time of the photo-excited charges

To investigate the rate of photo-induced charge recombination of the prepared composite in comparison to the bare photocatalyst, photoluminescence (PL) analysis was carried out. As demonstrated in Figure 5.15, the GaN:ZnO solid solution PL emission spectra contains a peak at 450 nm. This value is lower than the previously reported data [186], considering the different composition of the prepared solid solutions. The rGO composite exhibited a slight (<10 nm) shift in the peak emission, and an emission tail to the higher wavelengths (~670 nm), compared to the blank photocatalyst, which might be attributed to the contribution of graphene into the emission spectra [247]. The extended emittance can also be assigned to the long absorption tail of graphene, compared to the sharp absorption edge of GO [248].

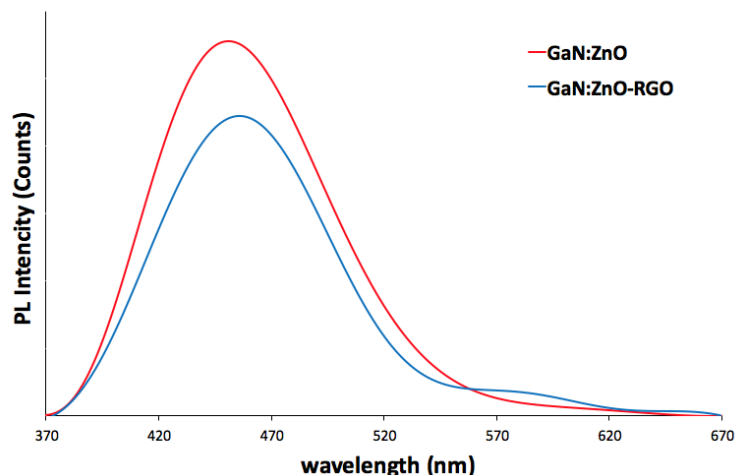


Figure 5.15: PL emission of GaN:ZnO solid solution and GaN:ZnO-rGO composite.

Due to the efficient charge transfer from the solid solution photocatalyst to the surface of the rGO nanosheets with higher electron mobility, the lifetime of the photo-excited charges has enhanced; therefore, the PL spectra of the rGO composite shows lower intensities than the one measured for the bare solid solution photocatalyst. The results of the PL measurements confirm the role of rGO as an effective support material in improving the lifetime of the photo-induced charges.

5.5 Photocatalytic performance

The impact of graphene integration was investigated through OWS performance of the prepared composite. As illustrated in Figure 5.16, stoichiometry rate of hydrogen and oxygen evolution was observed for GaN:ZnO hybridized with 2 wt% GO, continued steadily for several hours. The rate of overall water splitting for GaN:ZnO-rGO composite is clearly higher than that of the bare photocatalyst, due to the effective photo-induced charge separation, with calculated

apparent quantum efficiencies (AQE) of 0.14% and 0.25% for the GaN:ZnO solid solution photocatalyst and GaN:ZnO-rGO composite, respectively.

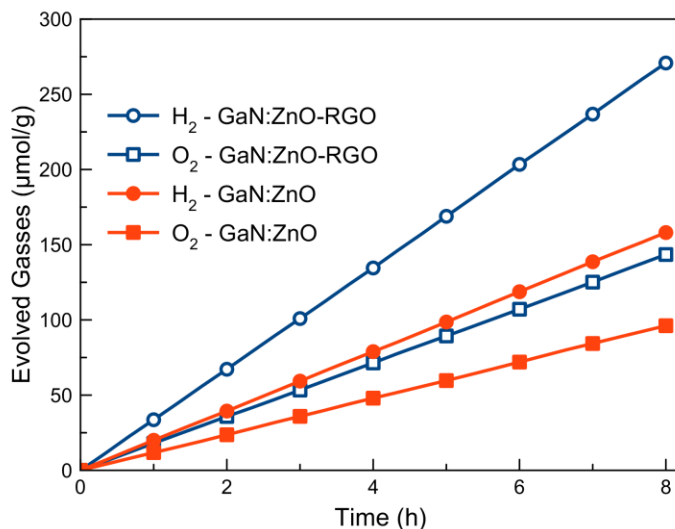


Figure 5.16: Overall water splitting performance of GaN:ZnO solid solution and its corresponding 2 wt% rGO composite.

Improvement in the overall water splitting activity of the GaN:ZnO-rGO composite presented in this study becomes more interesting, knowing that the ultimate functional energy conversion devices for practical applications are likely designed in the form of an immobilized film of photocatalyst deposited on an appropriate conductive substrate.

To identify the optimal GO loading, photocatalytic water splitting tests were performed using the GaN:ZnO-rGO photocatalyst with various GO compositions.

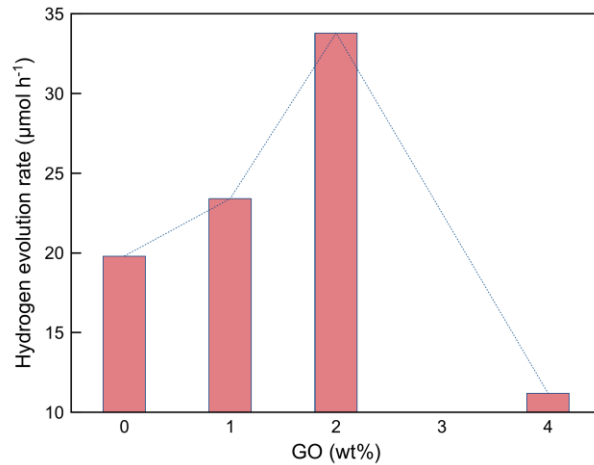


Figure 5.17: Effect of GO content of the composite on the visible-light hydrogen evolution. OWS data of the bare and reduced graphene oxide hybridized photocatalyst were obtained using the same traditional photocatalyst sample. Details of sample preparation for the comparative studies are described in Chapter 2.

As illustrated in Figure 5.17, the hydrogen evolution rate was increased significantly from the blank GaN:ZnO solid solution photocatalyst to its corresponding rGO composite by over 25%, and 70% by 1 and 2 wt% of GO loading, respectively. Adding further conductive nanosheets reduces the overall water splitting performance significantly, due to inefficient light absorption by the multi-layer-rGO composite.

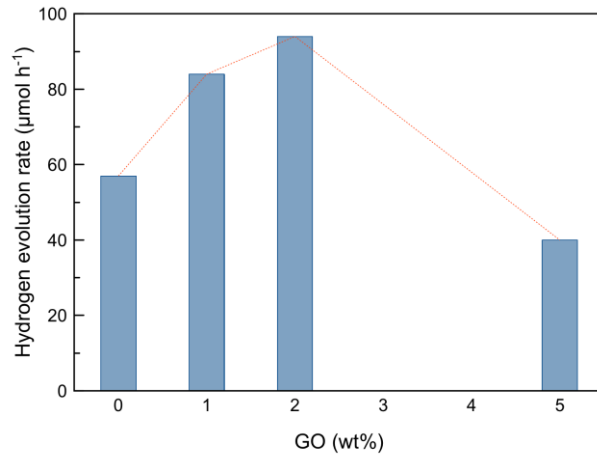


Figure 5.18: Effect of GO loading on the visible light H₂ production of the rGO composite of nanoporous GaN:ZnO solid solution. OWS data of the bare and reduced graphene oxide hybridized photocatalyst were obtained using the same GaZnON-LDHs 3 photocatalyst sample. Details of sample preparation for the comparative studies are described in Chapter 2.

The maximum OWS activity for the nanoporous solid solution photocatalyst hybridized with rGO was also observed at 2 wt% GO loading, as presented in Figure 5.18. Similar to the traditional photocatalyst, the nanoporous GaN:ZnO-rGO composite reached to 1.65-folds of the original activity once hybridized with 2 wt% GO.

The material characterization results and the photocatalytic performances presented in this chapter confirms the effective role of graphene in promoting the separation of the photo-induced charges. It is likely that rGO nanosheets have contributed to visible light hydrogen evolution through additional mechanisms (*e.g.* light absorption, local thermal effect, and catalytic). Therefore, further investigation on the characteristics of the prepared GaN:ZnO-rGO composite may result in higher water splitting efficiencies.

The photocatalytic system prepared and studied in this chapter can be further optimized through advanced fabrication techniques, such as ex-situ blending of functionalized components or in-situ crystallization.

Chapter 6: One-Dimensional Gallium Zinc Oxynitride Solid Solution

Nanostructures are defined as the systems with at least one dimension at the nanoscale [249]. Inorganic nanostructures have steadily received growing interest due to their peculiar and fascinating properties, compared to their bulk counterparts [137]. Such characteristics can be observed once the dimension of a material is reduced significantly, thus their electronic and optical properties deviate substantially from those of the bulk structures (quantum confinement) [250]. In addition to high active surface area, reducing the photo-recombination losses by decreasing the photo-excited charge diffusion length to the surface can be realized through morphology engineering. One-dimensional (1-D) nanostructure thin films such as nanowires (NWs), nanotubes (NTs) and nanofibers (NFs) could provide high surface area, fast photo-induced charge separation, short diffusion path, and strong light absorption. In the last decade, tremendous research efforts dedicated to the fabrication of functional devices based on semiconductor thin films. Among various materials, ZnO and GaN and their alike materials (such as GaAs and CdSe) have been the center of attentions, since their direct band gap enables wide range of optoelectronic applications [137]. In this chapter, the development and characterization of GaN:ZnO solid solution thin film is investigated. Among the approaches attempted in this research, atmospheric pressure chemical vapor deposition (APCVD) is proposed as an efficient and versatile route, and optimized for the preparation of GaN:ZnO thin film with tailored morphologies and chemistries.

6.1 Charge separation and recombination in 1-D nanostructures

In general, photo-induced charges can be recombined in three regions, as illustrated in Figure 6.1: inside the bulk (J_{br}), near the surface (J_{dr}), and at the surface (J_{sr}). The rate of these

processes is a strong function of semiconductors morphology, and can be reduced significantly during photocatalysts fabrication.

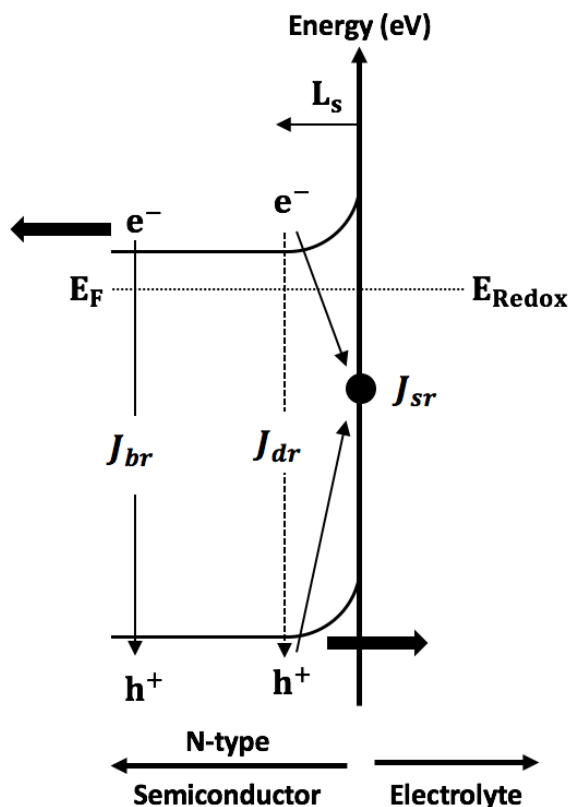


Figure 6.1: Charge separation in n-type semiconductors depletion layer (space-charge region). Figure also displays the charge recombination in the bulk (J_{br}), depletion layer (J_{dr}), and surface states (J_{sr}) of the semiconductor.

The Fermi energy (E_F) state of a semiconductor is defined as the energy level in which at thermodynamic equilibrium would have a 50% probability of being occupied by electrons [251]. Fermi-level of n-type semiconductors lies within the forbidden band, close to their conduction band (CB) potential. When a semiconductor is brought into contact with an electrolyte, an interface with imbalance electrical potentials is formed between the two. The equilibration of this interface

needs the flow of charges from one phase to another, which brings the Fermi energy level of the semiconductor and the redox potential of the electrolyte to an equal energy state. Thus, as displayed in Figure 6.1, a band-bending occurs near the surface of the semiconductors. The potential of the band-bending is directly proportional to the differences between the Fermi-level of the semiconductor and the redox potential of the electrolyte [252]. This band-bending forms a depletion in the density of the majority charge carriers (electrons in n-type semiconductors) near the surface that creates an electrical field in this region [253–255]. This electrical field drives the photo-excited charge separation efficiently in a thin layer near the surface of the semiconductor, the so called depletion layer (*i.e.* space-charge region) [253–256]. Ideally, photo-excited electrons and holes can be completely separated, if they are generated inside the depletion layer. In the other words, to reduce the charge recombination, the thickness of the depletion layer (L_s) must be comparable to the length in which light photons can penetrate inside the semiconductors lattice and generate electrical charges. Under a constant illumination, the photo-penetration depth (δ_p) can be assumed constant [257]. Photo-penetration depth is defined as the distance from the surface at which the intensity of the radiation inside the material falls to $\frac{1}{e}$ (about 37%) of its original value [258]. Photo-penetration depth is a function of photon's energy (wavelength) and according to the Beer-Lambert law (26) is inversely proportional to the absorption coefficient:

$$I(z) = I_0 e^{-\alpha z} \quad (26)$$

In 1-D nanostructure materials, the thickness of the depletion layer (L_s) is comparable to their diameter. As demonstrated in Figure 6.2 for an n-type semiconductor nanowire, decreasing the diameter (d) enhances the portion of the photo-excited charges that could be separated

efficiently. Ideally, in a 1-D semiconductor with $2L_s \sim d$, complete separation of the photo-excited charges can be realized through the mechanism displayed in Figure 6.2.

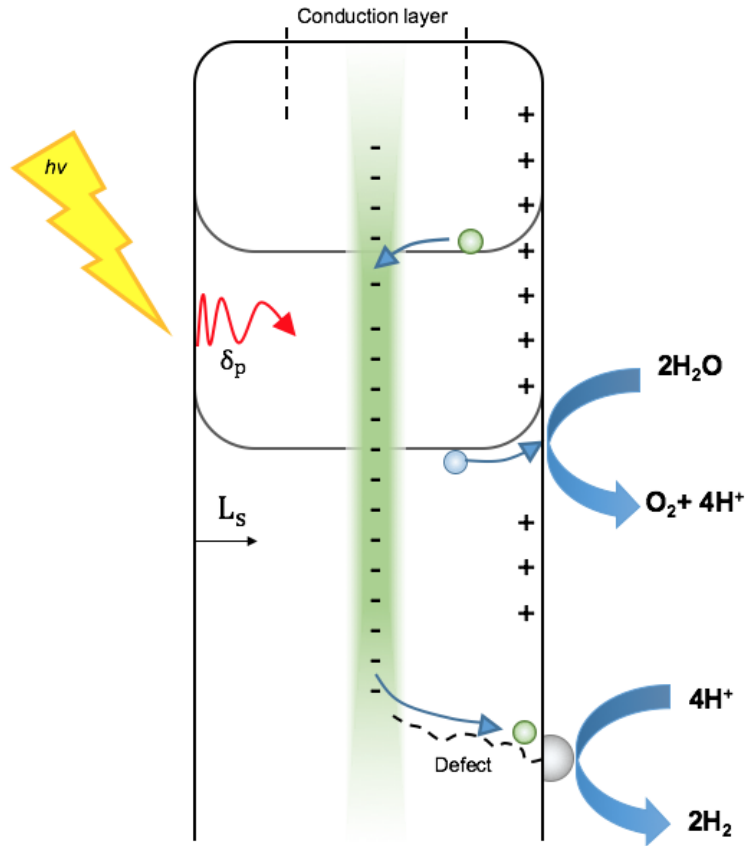


Figure 6.2: Charge separation mechanism in an n-type semiconductor nanowire. Figure also shows the OWS process using nanowire photocatalyst.

It should be noted that reducing the diameter of NWs is beneficial to a certain degree. Depending on the thickness (d) and doping concentration (e.g. $N_D \sim 10^{17} \text{ cm}^{-3}$ for GaN nanowires [259]) various characteristics can be expected from NWs:

- 1) Nanowires with thin conducting channels ($2L_s < d$), as displayed in Figure 6.2.

- 2) Completely depleted nanowires ($2L_s \geq d$) in which the charge separation is weakened due to lack of sufficient electrical field. The critical diameter to avoid fully depleted NWs is a function of semiconductor material, density of dopants, as well as morphology, and must be measured experimentally [260]. Diameters around 80 nm for GaN NWs [259] and 100 nm for ZnO NWs [260,261] have been reported as the critical dimension to avoid fully depleted nanowires.

In case of photocatalytic water splitting, as demonstrated in Figure 6.2 for an n-type nanowire, the photo-excited holes on the surface can readily interact with water molecules; while the accumulated electrons in the conductive highway at the center of the nanowire can reach to the surface through the crystalline defects or potential gradients driven by the high work function of the metal active sites, and produce hydrogen.

In spite to their fascinating properties, high density of surface states (large J_{sr}), attributed to their larger specific surface areas, and low mass transfer compared to slurry systems, could limit the functionality of the immobilized 1-D nanostructures for photocatalytic applications. [254]. It might be possible to control these losses by reducing the surface defects through surface treatments, and engineering the light harvesting devices for enhanced mass transfer.

6.2 Approaches to fabricate GaN:ZnO thin film

Inorganic 1-D nanostructures are not thermodynamically stable relative to their bulk material; thus, promoting the crystal growth towards one dimension is the most challenging task in their fabrication [262]. In general, 1-D nanostructures can be prepared by top-down (downsizing an existing structure) or bottom-up (evolution of solid crystals from vapor, liquid, or solid phase) approaches [263,264]. It is believed that the performance of the 1-D nanostructures

synthesized through bottom-up approach can go beyond those prepared via top-down routes, at a lower cost [137].

The concept of 1-D nanostructure formation through a bottom-up approach is about crystallization; the process involves two key steps: nucleation and growth [137]. When the concentration of building blocks is sufficiently high, they accumulate to form a cluster (nuclei) via homogenous nucleation. Further supply of building blocks results in growth of structures towards a favorable growth direction [262]. In this research, a focus is placed on the bottom-up fabrication of GaN:ZnO solid solution:

- 1) To fabricate 1-D Ga-Zn materials and further modify their chemistry to 1-D GaN:ZnO photocatalyst, and
- 2) To directly synthesize the 1-D GaN:ZnO.

Many techniques have been developed to prepare 1-D photocatalysts including hydrothermal synthesis, microwave-assisted route, sol-gel method, electro-deposition and vapor phase transfer [265]. The preparation of 1-D binary solid solutions is a complicated task, owing to the distinct thermodynamic properties of the reactants. Regardless of the fabrication technique, the growth mechanism strongly depends on the concentration of the building blocks at the growth region (tip) and the availability of a surface with suitable crystalline structure [265]. In the last few years, some techniques have been proposed for the fabrication of 1-D nanostructure consisting of Ga and Zn compounds. Table 6.1 summarizes the proposed methods along with the strategies developed in this research.

Table 6.1: Summary of the 1-D GaZnON fabrication routes proposed in the literature and the techniques developed in this research (shaded area).

Entry	Method	procedure	Morphology	Mechanism	Ref.
1	Diffusion of ZnO-GaN core-shell	Multi-step	NTs	Epitaxial casting	[106]
2	Diffusion of Ga ³⁺ into ZnO NWs	Multi-step	Core-shell NRs	Vapor-phase casting	[152]
3	Sol-gel GaZnO crystallization	Multi-step	NRs	Solid-state growth	[62]
4	Au-catalyzed CVD	Multi-step	NWs	VLSE	[64]
5	Ga ³⁺ decorated ZnO NWs	Multi-step	NWs	Impregnation	Here
6	Ga-Zn NWs solution growth	Multi-step	1-D	Selective capping	Here
7	Au-catalyzed APCVD	Single-step	Multiple	VLSE	Here

The proposed fabrication routes in the literature can be categorized into the following approaches:

- 1) Utilization of ZnO NWs as the template for grafting Ga³⁺ species, followed by post-thermal treatment (method 1 and 2 in Table 6.1), and
- 2) Use of Ga-Zn oxide phase in form of NPs or NWs for growth of, or phase transformation to, oxynitride 1-D nanostructures (method 3 and 4 in Table 6.1).

Inspired by the proposed techniques in the literature, three strategies were developed in this research for the fabrication of 1-D GaZnON (method 5–7 in Table 6.1). Among these methods, direct Au-catalyzed APCVD (method 7 in Table 6.1) exhibited the most promises, which is the focus of this chapter. The synthesis route based on the nitridation of ZnO-Ga³⁺ NWs and Ga-Zn NWs (method 5 and 6 in Table 6.1, respectively) are also discussed here.

6.3 Impregnation of ZnO NWs with Ga³⁺

Template-based methods have been extensively studied for the fabrication of materials with tailored morphologies [134,261]. Since the methods for the preparation of ordered single crystal ZnO nanowire arrays are well-documented, ZnO NWs were used as the 1-D template for the fabrication of Ga³⁺-ZnO NWs. This core-shell-like structure can be subsequently processed to GaN:ZnO solid solution NWs through post-thermal treatment. Hahn et al. (method 1 in Table 6.1) utilized ZnO nanowires as the template for epitaxial casting of GaN shell [106]. The ZnO core was later diffused into GaN shell at high temperature in NH₃ environment, resulted in GaN:ZnO NTs with $x = 0.10$. The GaN:ZnO NTs were found to have ~1.5–2-times higher sacrificial visible light hydrogen evolution activity, compared to the powder photocatalyst with similar composition. Zhong and co-workers (method 2 in Table 6.1) employed a similar approach, as such the Ga₂O₃ molecules were extracted at high temperature (1150 °C), anchored to the surface of the ZnO nanowires and formed ZnO-Ga³⁺ core-shell NWs. Nitridation of the core-shell NWs under ammonia flow resulted in ZnO-GaN:ZnO core-shell NWs that exhibited stable visible light anodic performance for PEC water splitting [152].

Both procedures described above have been conducted in well-controlled high temperature conditions [106,152]. Due to the difficulties associated with such precisely controlled procedures, development of a facile template-base fabrication route was attempted in this research. The ZnO NW arrays were prepared in a mild condition ($T = 93$ °C and atmospheric pressure, from the method described in [142,156] with modifications) and used as the template for Ga³⁺ impregnation. The scanning electron microscopy (SEM) image in Figure 6.3 (a) exhibits uniform growth of ZnO NWs on the seeded quartz substrate with diameter between 140–300 nm and average length of 4.0

μm . The inset of Figure 6.3 (a) shows the hexagonal tip of the prepared NWs, indicating their single crystal structure with favored growth direction towards the wurtzite c -axis.

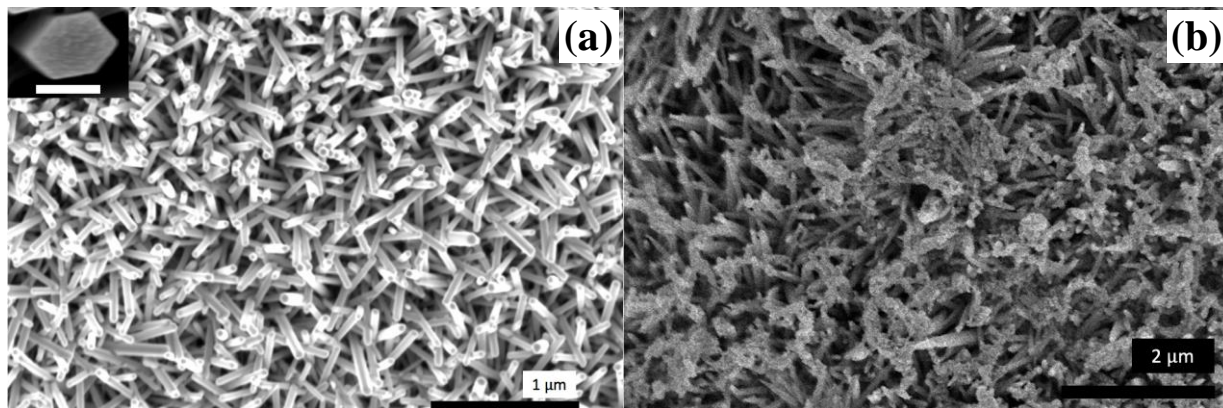


Figure 6.3: SEM image of (a) ZnO NWs prepared by chemical bath method. inset shows the hexagonal tip of a ZnO NW, scale bar = 100 nm, and (b) ZnO-Ga³⁺ thin film prepared by impregnation of ZnO NWs using 5 mM Ga(NO₃)₃·xH₂O solution.

Impregnation of the prepared ZnO NWs by concentrated (35 mM) Ga(NO₃)₃·xH₂O solution resulted in semi-uniform layers (SEM image is presented in Appendix E) with no sign of 1-D morphology. Use of dilute (5 mM) Ga(NO₃)₃·xH₂O solution for the surface modification of ZnO NWs maintained the 1-D structure of the film; however, aggregates and clusters, presumably of Ga³⁺ compounds, formed on the surface of the ZnO thin film, as demonstrated in Figure 6.3 (b). Apparently, Ga³⁺ salts deposited on the specific sites of the ZnO NWs, rather than uniformly distribute on the surface of individual NWs. Although impregnation was performed at room temperature, this aggregation could be attributed to rapid nucleation of Ga salt solution. Such dispersion is unwanted and leads to formation of a thin film with local compositions and morphologies. Portion of the ZnO thin film was removed (or deformed) during room temperature

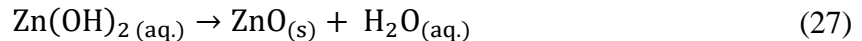
impregnation, which could be attributed to the low adhesion of the ZnO NWs to the quartz substrate.

Indeed, the surface decoration of the ZnO NWs template with Ga³⁺ species is a very appealing approach for fabrication of GaN:ZnO NWs, owing to its room temperature processing and scalability. This approach can be further optimized by applying various Ga salts at different concentrations. Alternative surface decoration techniques such as dip coating and spin coating can also be utilized for effective fabrication of ZnO NWs-Ga³⁺.

6.4 Direct growth of Ga-Zn 1-D nanostructures

Mild temperature growth of ZnO NWs has been developed in order to fabricate NW arrays on the conductive substrates sensitive to high processing temperatures such as indium tin oxide (ITO) or fluorine-doped tin oxide (FTO) coated glass substrates [142].

The Zn²⁺ is solvated by water, and forms several hydroxyl species, such as Zn(OH)⁺, Zn(OH)₂, and Zn(OH)₄²⁻ [267]. The stability of these complexes depends on the pH and temperature of the solution. Solid ZnO nuclei can be formed thorough the dehydration of these hydroxyl species, as shown in equation (27) [268,269]. Some reagents, often amines, exhibited strong control over the morphology of the formed film towards the 1-D growth.



The fabrication of ZnO NWs can be realized by hydrolysis of zinc nitrate using hexamethylenetetramine (HMT) as the morphology-regulating reagent. Similar procedure was applied in this research for the fabrication of ZnO NWs shown in Figure 6.3 (a). Direct growth of Ga-Zn 1-D nanostructures was attempted through the similar approach, by incorporation of gallium nitrate salt as the source of Ga, and use of zinc acetate as an alternative Zn source. Table

6.2 summarizes the growth conditions and the morphology of the structures observed on the substrate and inside the growth solutions. SEM images of the samples indicated in the Table 6.2 can be found in Appendix F.

Table 6.2: Summary of the experiments, as well as the morphology of the materials on the substrate and inside the processing solution for direct growth of Ga-Zn NWs through the chemical bath technique. Stoichiometric amount of $\text{Ga}(\text{NO}_3)_3 \cdot x\text{H}_2\text{O}$ and HMT were used as the source of gallium and selective capping reagent, respectively. SEM images of the samples are presented in Appendix F.

Entry	ZnO salt	Observation
1	Zinc nitrate	Rapid precipitation occurred within the first hour of the experiment. Star-like and 1-D micro-structures were observed inside the growth solution.
2	Zinc acetate	Precipitation of 1-D structures with low aspect ratio was observed inside the growth solution. Non-uniform micro-scale crystalline structures were grown on the substrate.

Similar to the method proposed for the ZnO NWs growth [142], HMT found to be effective for maintaining the growth towards one-dimension inside the processing solution, and on the substrate. Substituting zinc nitrate (Entry 1 in Table 6.2) in the original method with zinc acetate (Entry 2 in Table 6.2) resulted in vastly different morphologies, suggesting the significant dependency of the growth mechanism to the employed precursors. HMT was replaced by ethanolamine (ETA) in order to explore its capability to tailor the growth mechanism; however, ordered morphologies were not observed.

Direct growth of Zn-Ga NWs via solution-based route is an attractive route for the preparation of binary solid solution oxide, nitride, and oxynitride NWs at mild conditions. However, optimizing the growth mechanism requires extensive experimentation. Effect of various metal salts, selective capping reagents, and operating conditions (*e.g.* temperature and concentration) must be investigated thoroughly to develop an improved method for the preparation of high quality thin films.

6.5 CVD growth of GaN:ZnO 1-D nanostructures

Chemical vapor deposition is the most extensively explored the so called “top-down” route for the preparation of 1-D materials with tailored characteristics. In principle, it is possible to process any solid material into a thin film through vapor phase deposition [137]. CVD growth is well-known for its simplicity, where the vapor phase is generated by evaporation, followed by gaseous reactions at the source or transient temperature, and production of deposits on the surface of a substrate at a temperature lower than the source temperature. Such mechanism is called indirect vapor phase growth, since in addition to evaporation and condensation steps (direct vapor phase growth), some intermediate reactions occurs in the fluid phase. [137].

CVD technique has been categorized by different means:

- 1) Based on the configuration, such as operating pressure (*e.g.* atmospheric, vacuum and ultra-high vacuum), heat source (*e.g.* hot-wall and cold-wall), and precursors (*e.g.* gaseous, liquid and solid, as well as, metal-organic and metal-inorganic) [270].
- 2) Based on the growth mechanism, such as vapor-solid (VS), also called vapor-solid-solid (VSS), and vapor-liquid-solid (VLS) mechanism [137,262,271,272].

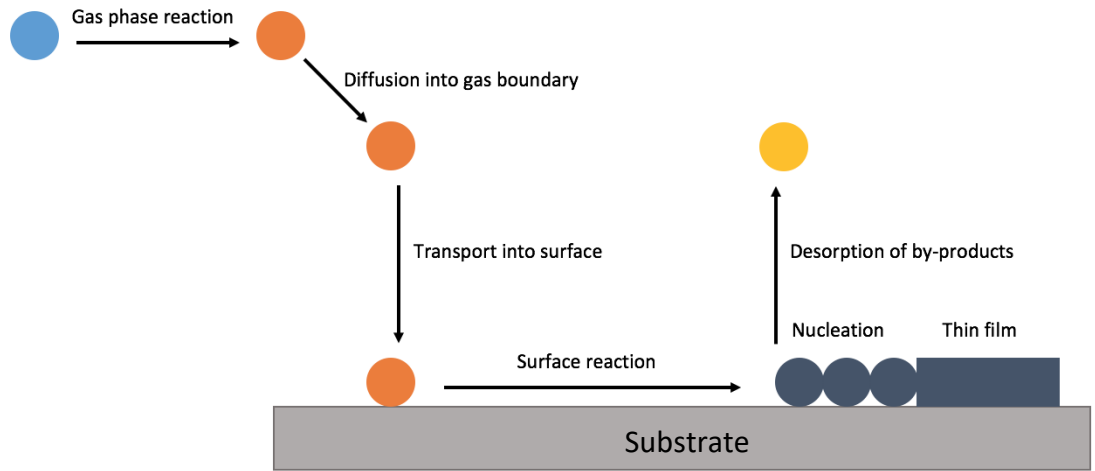


Figure 6.4: Vapor-solid (VS) growth mechanism.

Figure 6.4 explains the VS mechanism, in which the products of the gas phase reaction and/or gaseous precursors are diffused into the gas boundary layer, transported into the substrate surface, diffuse toward the surface, and nucleate to form a solid thin film [272].

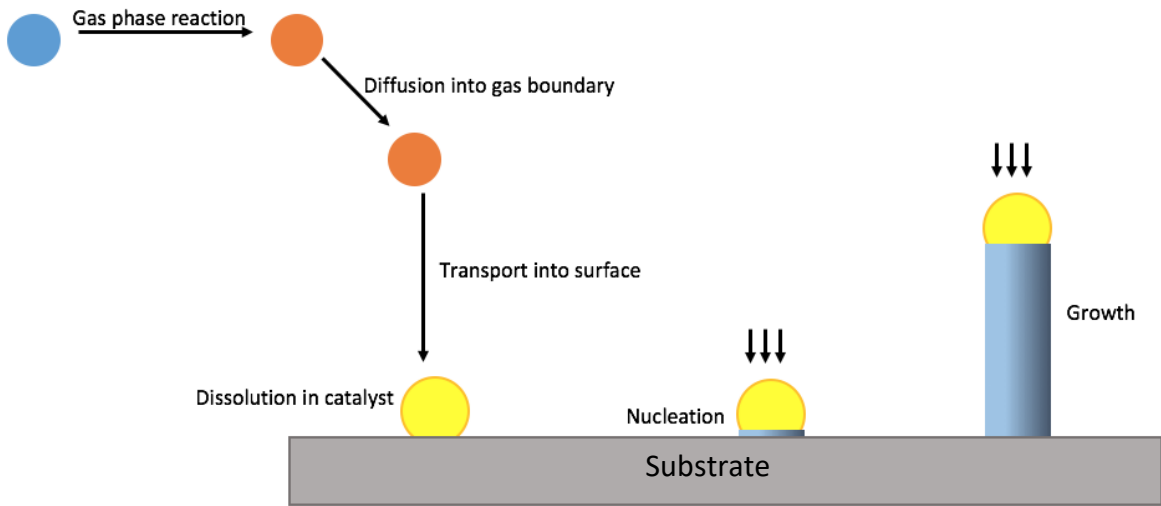


Figure 6.5: Vapor-liquid-solid (VLS) growth mechanism.

Vapor-liquid-solid growth path is much more complex than the vapor-solid mechanism. The VLS route was originally developed by Wagner and Ellis to produce micrometer-sized whiskers in the 1960s [273], later justified thermodynamically and kinetically by Givargizov [274], and recently re-examined by Lieber, Yang, and other researchers to generate nanowires and nanorods from a rich variety of materials [262]. VLS mechanism is the most successful method for the fabrication of dense and uniform 1-D nanostructures of inorganic materials [137]. In this mechanism, as displayed in Figure 6.5, the gaseous compounds diffuse to the gas boundary layer, dissolve into a metallic catalyst droplet (formation of catalyst-building blocks alloy), commence nucleation upon reaching to a critical composition, and elongate toward the favorable crystallographic plane (crystal growth) [271]. In addition to maintaining the nucleation and growth rates, the metal droplet serves as a platform to produce a morphologically uniform layer of building blocks, and strictly suppress the lateral growth of individual wires or whiskers.

- 3) Based on the nucleation mechanism: epitaxial and non-epitaxial growth. In epitaxial route, the CVD growth of the thin film cannot be realized, unless the crystalline structure of the substrate, or coated layer on the substrate, is relatively matched to that of the deposited film [249,262]. It has been reported that the nanowires of ZnO and GaN can be fabricated through epitaxial growth, whether on a pre-deposited seed layer or on a substrate with match crystalline structure such as GaN *c*-plane, or Si (100) substrates [262,275–281].

CVD synthesis is typically operates within the laminar regime [270]; therefore, the geometry of the reactor, concentration profile of the gaseous compounds, operating pressure and temperature are critical factors to be considered for optimized growth. In this research, APCVD technique was employed for the fabrication of 1-D nanostructure of GaN:ZnO on amorphous and

single crystal substrates. NH_3 was used as both carrier gas and nitrogen source; while a mixture of Ga_2O_3 and ZnO (1:1 wt) was applied as the source material. With this configuration, various parameters that affect the hydrodynamics, and kinetic of the CVD growth process have been studied through experiments. Schematic illustration of the APCVD apparatus, along with the concentration profile of the reactants and the synthesis configuration is displayed in Figure 6.6. The preparation conditions and parameters studied for optimized growth of nanostructures are summarized in Table 6.3. Since the actual growth temperature during the hot-wall CVD process cannot be measured accurately, as a common practice in the literature, the distance of the substrates from the center of the furnace (D), along with the source temperature (T_s) are used for reporting the growth conditions. Through the experiments, standard conditions indicated in Table 6.3 were maintained for identifying the best growth configurations.

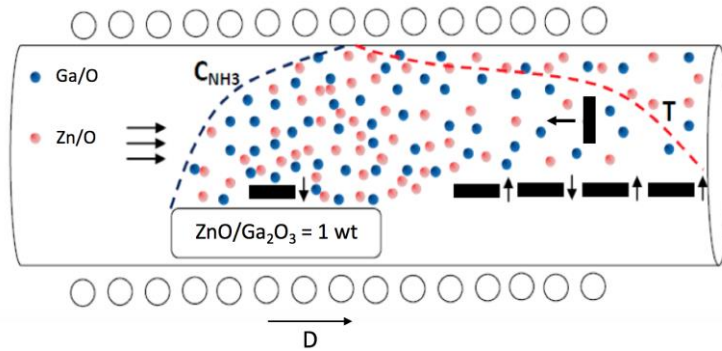


Figure 6.6: Schematic illustration of the utilized APCVD apparatus. Figure also displays the schematic profile of the reactants concentration and growth temperature.

Table 6.3: Conditions and study range of the parameters (shaded area) for the APCVD growth of the 1-D GaN:ZnO solid solution.

Parameter	Study range	Standard configuration
NH ₃ flow rate	-	250 mL min ⁻¹
ZnO/Ga ₂ O ₃	-	1 wt
Catalyst	-	10 nm Au
Substrate	Quartz and Si (100)	Si (100)
Source temperature (T _s)	900–1100 °C	1000 °C
Distance from center (D)	0, 8, 13, 21 cm	8 cm
Growth time (t)	5–60 min	30 min
Orientation	Face up/down and vertical	vertical

Due to the large number of experiments, the effect of some parameters such as ZnO/Ga₂O₃ ratio as the CVD source material and Au catalyst film thickness (L_{Au}) were not investigated. The flow rate of NH₃ could also be considered as a controlling parameter. NH₃ concentration is significantly above the stoichiometry of the gas phase reaction. Thus, transportation of the gaseous reactants and products, as well as maintaining the laminar regime can be safely considered as the primary role of NH₃.

6.5.1 Non-epitaxial CVD growth of GaN:ZnO 1-D nanostructures

In order to explore the role of substrates surface crystallography, as stated in Table 6.3, amorphous quartz (non-epitaxial) and single crystal Si (epitaxial) substrates were examined for the fabrication of GaN:ZnO thin film. The rest of the operating conditions were adjusted to the standard configurations stated in Table 6.3.

Au-coated amorphous quartz substrates was used for the non-epitaxial APCVD growth of GaN:ZnO thin film. In a typical synthesis, a clean substrate was coated with 10 nm Au catalyst and placed in the down-stream of the Ga₂O₃-ZnO source material (see Figure 6.6) for 30 min under ammonia flow.

Depending on the substrates temperature, which is determined by the distance of the quartz glass from the center of the furnace (D), the color and density of the deposited materials vary, ranging from yellow and low density deposits to white and high density layer, as demonstrated in Figure 6.7.

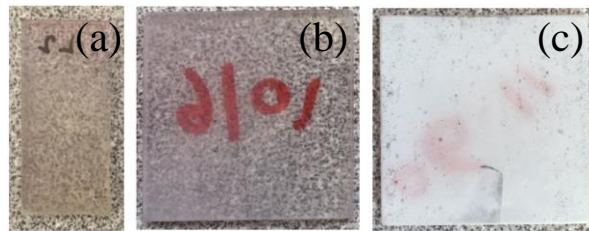


Figure 6.7: Digital photos of the quartz substrates process at the downstream of Ga₂O₃-ZnO source ($T_s = 1000$ °C) for 30 min (a) D = 8 cm, (b) D = 13 cm, and (C) D = 21 cm.

Different appearance of the quartz substrate processed at D = 8 and 13 cm in Figure 6.7 (a and b) suggests the deposition of phases with distinct chemistries and morphologies. Intense white color of the deposited layer in Figure 6.7 (c) is likely attributed to rapid deposition of ZnO-rich structures at low growth temperatures (D = 21). At this condition, the growth mechanism is presumably not catalyzed by Au NPs, since the gaseous compound were rapidly transformed to solid aggregates through secondary nucleation, and subsequently covered the Au NPs.

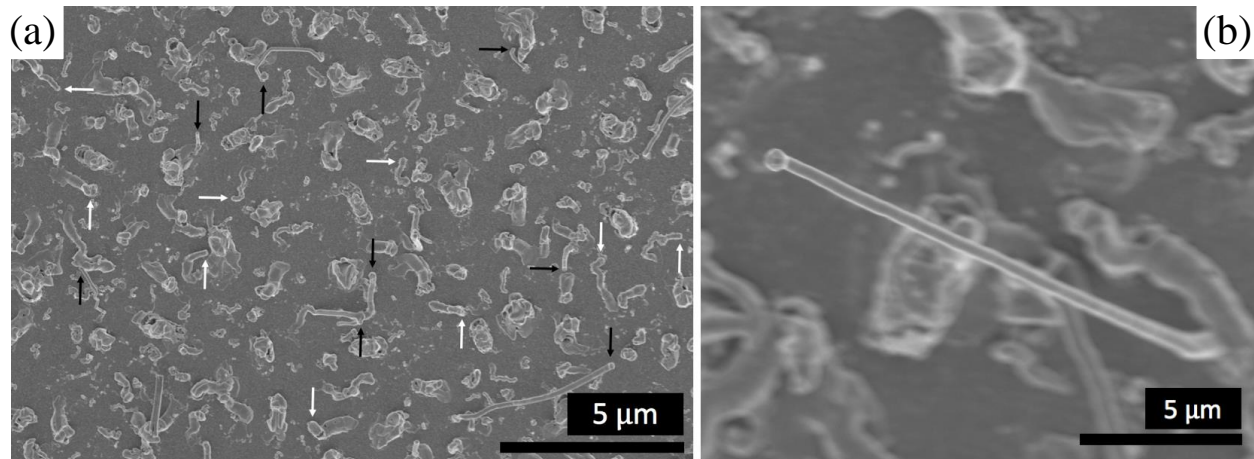


Figure 6.8: SEM image of the quartz substrate at $D = 8$ cm in the downstream of $\text{Ga}_2\text{O}_3\text{-ZnO}$ source ($T_s = 1000$ °C) for 30 min. (a) low resolution image. Arrows show the Au-catalyzed growth. Black: complete growth, white: surface growth (crawling). (b) High resolution image of an individual Au-capped NW.

SEM image of the quartz substrate at $D = 8$ cm in Figure 6.8 (a) shows the random growth of NWs, indicated by black arrows. Figure 6.8 (a) also revealed that the fabrication of NW arrays at high density cannot be realized through non-epitaxial route using the amorphous quartz substrate. It is generally accepted that to form well-defined crystals, a reversible pathway between building blocks on the surface of the solid and those inside the fluid phase must exist. This allows building blocks to maintain their positions according to the existing crystal lattice [137]. Lack of such crystalline support (non-epitaxial) results in random and slow growth of 1-D nanostructures, rather than dense and defined morphologies. As denoted by white arrows in Figure 6.8 (a), due to the lack of suitable crystalline sites on the surface of the quartz substrate during the CVD growth, Au catalyst NPs migrated on the substrate surface and formed horizontal NWs (surface growth), until they reach a crystalline deposit with match lattice dimensions (*e.g.* deposited ZnO, GaN or their solid solutions). Such growth mechanism called “crawling”, and occurs when epitaxial growth conditions cannot be satisfied. Growth of nanowires parallel to the

substrates surface is actually very useful, due to their potentials for optoelectronic devices fabrication and precise placement of individual nanowires [262].

High resolution SEM image in Figure 6.8 (b) shows an individual NW capped with an Au NP, confirming the VLS growth mechanism. The diameter of those NWs reached to a complete growth (vertical growth) measured between 100–120 nm, with 1.7–5.1 μm in length. The areal density of the NWs on the surface varied in a wide range, reaching up to $7.0 \times 10^6 \text{ cm}^{-2}$ in some regions.

6.5.2 Epitaxial CVD growth of GaN:ZnO 1-D nanostructures

For some semiconductors, by applying conventional epitaxial growth to VLS mechanism, the so called vapor-solid-liquid epitaxy (VLSE), synthesis of 1-D nanostructures can be realized [262]. Semiconductors generally have preferred growth direction; thus, by properly selection of the substrate, epitaxial growth of 1-D nanostructures occurs towards the favorable crystalline lattice. It is known that the crystalline structure of the Si (100) has the slightest mismatch with those of the GaN and ZnO *c*-plane. Due to this small crystallographic mismatch, direct fabrication of 1-D GaN:ZnO solid solution towards [002] *c*-axis is expected through the crystallographic layout schematically exhibited in Figure 6.9 for Si (100) substrate.

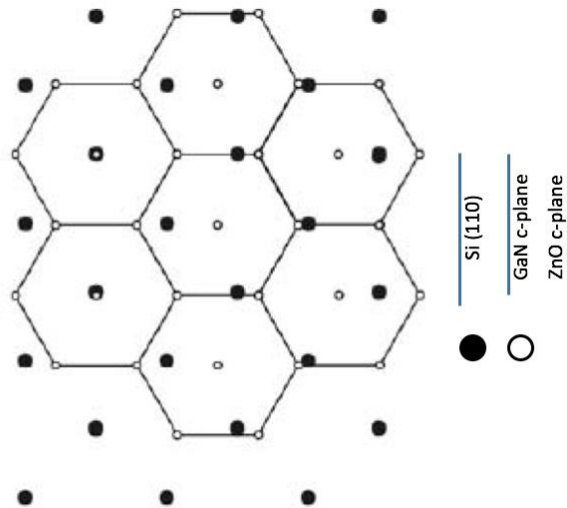


Figure 6.9: Schematic display of epitaxial GaN and ZnO nucleation on the Si (100) substrate. Image was taken from reference [282] and adapted for the purpose of this discussion. Reprinted with permission (adapted) from (New J. Phys., 9, 2007, 389–389). Copyright (2007) IOP Science.

For the fabrication of GaN:ZnO 1-D nanostructures, Au-coated Si substrates were located at $D = 8$ cm, and processed under ammonia flow at $T_s = 1000$ °C for 30 min. the growth conditions were adjusted in respect to the standard operating conditions described in Table 6.3.

The results of our experiments indicated the effectiveness of vertical substrates orientation. This could be related to the uniform temperature profile at the growth region, as well as the negligible effect of the gas boundary layer at the vertical position. Therefore, all the presented results, except at $D = 0$ which was carried out in the face-down orientation displayed in Appendix G, have been obtained from the substrates secured in a position perpendicular to NH_3 flow.

For homogenous nucleation and stable growth in the 1-D direction, sufficient vapor pressure of the building blocks in the growth region (catalyst droplet-fluid interface) is crucial. Typically, such conditions cannot be realized at atmospheric pressure; therefore, the majority of

the fabrication routes based on vapor phase transport are performed under vacuum operating conditions. At a given process temperature, the concentration of gaseous reactants is significantly lower in the atmospheric regime, compared to that in the vacuum condition; therefore, the fabrication of 1-D nanostructures is hardly possible. In a study by Kuykendall and co-workers, the fabrication of single crystal wurtzite $\text{In}_x\text{Ga}_{1-x}\text{N}$ nanowires across the entire compositional range ($x = 0$ to 1) was realized through atmospheric pressure CVD (APCVD) with thoughtful design of the CVD reactor [283]. It is apparent that despite their low vapor pressure at atmospheric condition, the available gaseous products can be directed to the substrate area and contribute to the VLSE growth of nanowires by modifying the CVD reactor hydrodynamics. A customized alumina holder was built to secure the substrate at the highest possible location inside the tube in a vertical position. As demonstrated in Appendix G, due to the special geometry of the sample holder, the downstream cross-section of the tube furnace was narrowed down to the substrate region; therefore, most of the gaseous products are available for the VLSE growth on the Au-coated Si substrate. The same outcome could be expected when CVD growth is performed in a narrow tube; however, due to operational obstacles such as the placement of source materials and substrate, this approach does not appear to be viable. This simple modification enhances the availability of gaseous reactants at the surface of the substrate significantly, sufficient to drive the homogenous nucleation and stable growth of oxynitride solid solution nanowires. Moreover, this modification substantially enhances the velocity (due to narrower channel) of the fluid phase, hence increasing the gas-liquid-solid diffusion considerably.

Low resolution SEM image of the processed Si substrate in Figure 6.10 (a), shows a uniform coverage of nanostructures at high density. Digital photo of the substrates in Figure 6.10

(b) also indicates a uniform coating of the nanostructures on the Si substrate. The clean area at the bottom was used for securing the substrate at the vertical position.

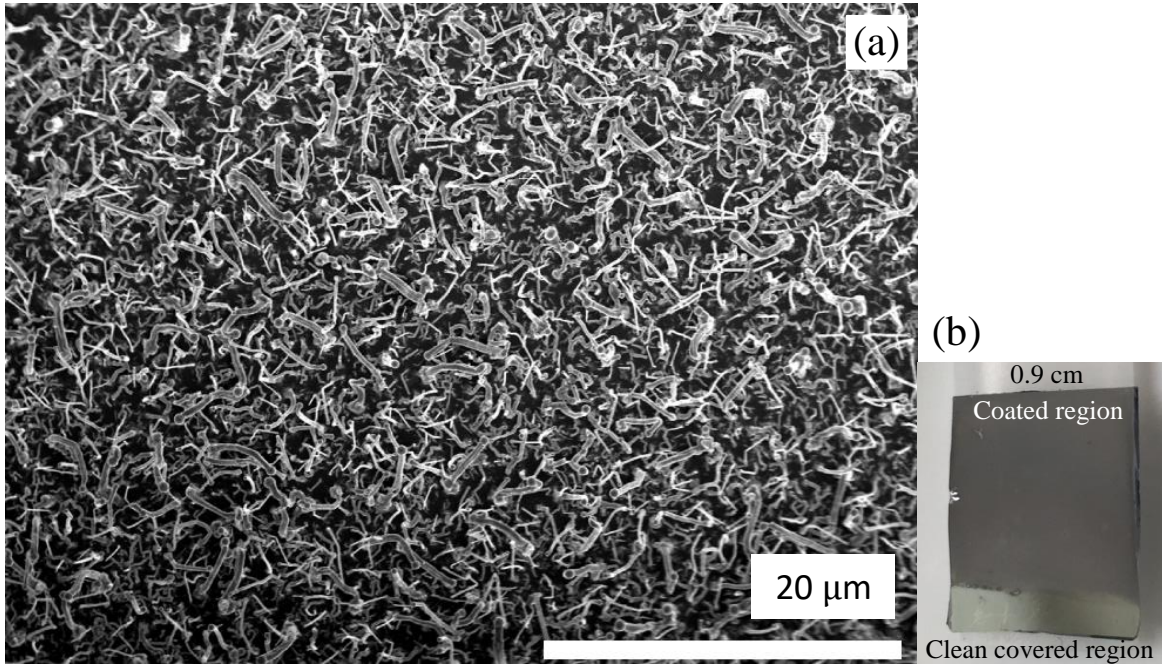


Figure 6.10: (a) Low resolution SEM image, and (b) digital photo of the Si (100) substrate processed at $T_s = 1000$ °C and $D = 8$ cm for 30 min.

Comparing the density and uniformity of the NWs on the Si (100) substrate in Figure 6.10 (a) to those on the quartz substrate in Figure 6.8 (a) reveals the effectiveness of the epitaxial growth of NWs through APCVD. The average areal density of the nanowires on the Si substrate is approximately $\sim 4.1 \times 10^7$ cm^{-2} , suggesting a good level of surface coverage, as compared to the wide range reported in the literature: from 1.5×10^4 cm^{-2} to 1.0×10^{10} cm^{-2} for the thin film of GaN nanowires prepared via catalyzed vacuum MOCVD [280] and MBE [38], respectively. Approximately 31% of the Au nanoparticles ($d_p = 80$ – 300 nm), estimated from the Au-coated Si substrate processed under the same conditions ($\sim 13.2 \times 10^7$ cm^{-2}), have been utilized for nanowire

growth. For a dense ZnO NWs prepared via vacuum CVD, this has been reported to be as high as 49% [276]. Such difference is likely attributed to the vapor pressure of the reactants (considering the atmospheric regime in this study) and morphology of the prepared NWs, as displayed in Figure 6.11, which appear to be kinked; bent in multiple locations towards the growth direction. It is worth mentioning that the overall morphology of the NWs (ordered or kinked) does not necessarily determine their functionality for a particular application, unless it significantly affects the crystalline structure, active surface area, and/or light absorption of the thin film catalyst. It is known that the disoriented or kinked nanowires are more effective for electrochemical applications, considering the hindered diffusion of the reactants within the ordered nanowire arrays. On the other hand, well-aligned nanowires are believed to have fewer structural defects, and superior light absorption.

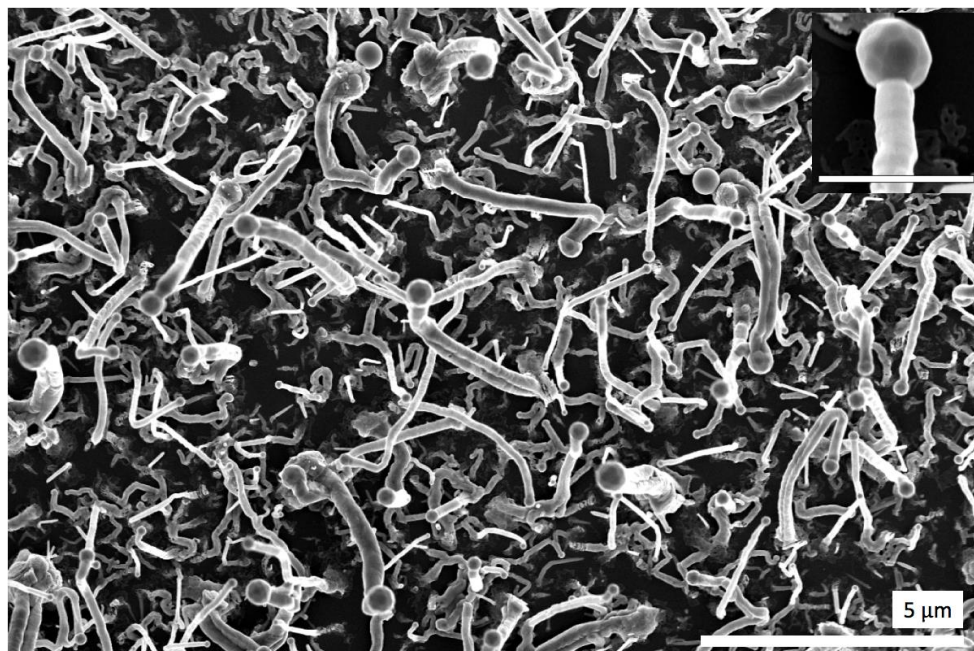


Figure 6.11: High resolution SEM image of the Si (100) substrate processed at $T_s = 1000$ °C and $D = 8$ cm for 30 min. Inset shows an individual Au-capped NW – scale bar = 500 nm.

The kinked structure of the NWs is attributed to the changes in the growth direction. Evidenced by the disoriented NWs in Figure 6.11, the synthesized nanowires can be identified as polycrystalline, with the synthesis mechanism initiated with homogenous nucleation towards the *c*-axis (epitaxial) and continuously changing towards the other hexagonal lattices. The origin of the kinked morphology of nanowires is not well understood and is still under debate. Such a structure could be explained through the following mechanisms:

- 1) Formation of local temperature-concentration domain in the regions around the Au catalyst that adjusts the growth direction. A nanowire grows faster along the direction with higher vapor pressure [262]; thus, slight temperature-vapor pressure gradients may affect the growth direction of the nanowires, particularly in APCVD configuration, in which variations in the temperature and pressure domains are likely. Operating pressure and temperature could also alter the VLS path, leading to the growth of straight (high temperature/ultra-high vacuum) or kinked (low temperature/vacuum and atmospheric) NWs [275, 276].
- 2) Dependence of the growth direction on the NWs diameter, whereas at diameters larger than a critical value, kinked growth could occur for the wurtzite NWs [286]. Based on the Wulff theorem, the overall shape of a crystal depends on the construction of the crystalline facets in the growth region (tip) and side-walls, giving a minimum total surface energy [287]. Hypothetically, the NWs growth direction could have change in order to maintain the minimum surface energy. This phenomenon has been argued previously as the cause of changes in the growth directions and diameters of NWs [100,277,280].

- 3) Drastic changes in the composition (*e.g.* Zn-rich or Ga-rich) of NWs or the formation of isolated wurtzite phases towards the NWs growth direction [290]. Since different materials diffuse to the Au droplets at various rates, sudden changes in the NWs composition could have affected the VLS kinetics and changed the growth direction. We have excluded this possibility later in this Chapter, showing a uniform composition along the growth direction.
- 4) Continuous migration of the Au catalyst from smaller droplets to the larger ones (Ostwald ripening), which leads to variations in the length, shape and sidewall properties of the NWs [291]. Hannon and co-workers highlighted that the size of Au droplets is not constant during VLS growth [291]. Their in-situ high resolution transmission electron microscopy (HRTEM) study revealed that gold diffusion can change the size of Au-droplets, resulting in adjustments in the shape of the NWs. Eventually, all Au catalyst are consumed by wetting the sidewalls, terminating the VLS growth.

NWs with an average diameter and length of $\bar{d} \sim 190$ nm and $\bar{L} \sim 3.8$ μm , respectively, were synthesized on the Si substrate at $D = 8$ cm and $T_s = 1000$ °C for $t = 30$ min. Accordingly, nanowires with $\bar{d} \sim 205$ nm and $L \sim 1.2$ μm were obtained by changing the location of the substrate to a farther distance ($D = 13$ cm). Presence of Au NPs on the tip of almost all the NWs in Figure 6.11 confirms their VLS growth mechanism.

It has been suggested that the size of the Au catalyst is relatively close to the diameter of the NWs [262]; however, it is shown in the inset of Figure 6.11 that the VLSE growth of NW with a diameter of 130 nm was catalyzed by a 250 nm Au NP. As highlighted by Ma et al., the VLS mechanism controls the shape and size of Au NPs as well as the exposed crystalline facets of the

NWs, maintaining stable growth [292]. In fact, the size and shape of the droplets is not constant, varying in response to the local growth conditions. In addition, the continuous migration of the Au droplets to the neighboring nanowires could result in a wide-ranging catalyst cap size distribution [291].

The synthesized NWs were characterized for their composition using energy dispersive X-ray (EDX) spectroscopy. Ga L α at 1.098 keV, Zn L α 1.012 keV, N K α at 0.392 keV, O K α at 0.525 keV, Au M α at 2.123 keV, and Si K α 1.740 keV energy lines were used to identify and quantify the elements in the prepared samples. Composition of the NWs sample prepared at D = 8 cm is summarized in Table 6.4. For higher resolution, energy lines up to 10 keV such as Ga K α peak at 9.251 keV, and Zn K α peak at 8.637 keV can also be analyzed; however, to reach a reliable 10 keV detection, an applied voltage ~20 keV is required, which integrates a significant background detection for samples with nanoscale dimensions.

Table 6.4: Elemental composition of the NWs synthesized at $T_s = 1000$ °C for 30 min (D = 8 cm).

Parameters	Values
Ga	47.4 atm%
Zn	5.6 atm%
N	38.6 atm%
O	7.1 atm%
Au	1.3 atm%
x	0.10
Zn/O	0.78
Ga/N	1.23
Zn/Ga	0.12

The obtained EDX data, presented in Table 6.4, indicate the formation of GaN:ZnO solid solution phase with ~20% deviation ($Zn/O = 0.78$ and $Ga/N = 1.23$) from the stoichiometric $(Ga_{1-x}Zn_x)(N_{1-x}O_x)$ composition, with $x = [Zn]/[Ga]+[Zn] = 0.10$. The low Zn-content of the solid solution is likely attributed to the high growth temperature at $D = 8$ cm (930–940 °C), which is suitable for VLS growth of GaN NWs but relatively higher than the ideal growth temperature of ZnO NWs [275–281]. The low composition of Au is related to the surface of the NWs, where the Au catalyst droplets wetted the nanowire sidewalls during VLS growth [291].

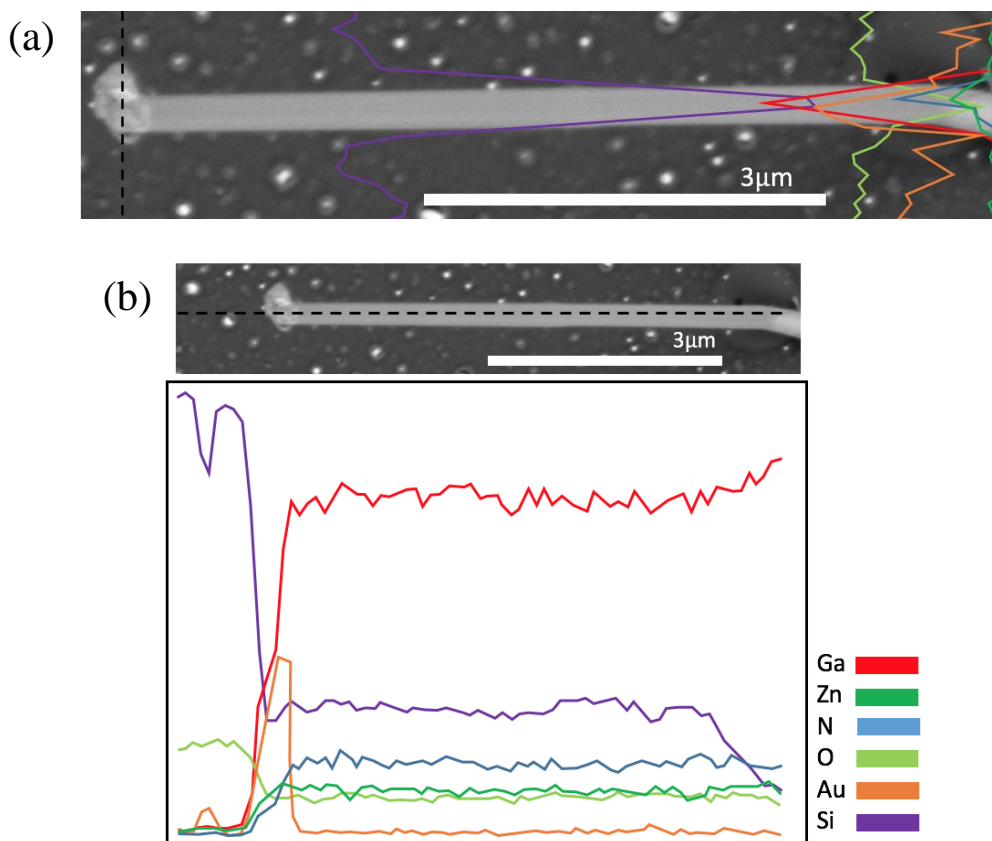


Figure 6.12: Elemental profile of the synthesized NWs along (a) tip cross-section acquired at 20 keV and (b) growth direction, obtained at 5 keV.

The EDX elemental profiles along the cross-section of the tip and growth direction are displayed in Figure 6.12. Although the Si $K\alpha$ signal (purple line) in Figure 6.12 (a) was significantly reduced at the NW-region, its relative high intensity compared to that of the Si signal in Figure 6.12 (b) indicates the dependency of the background detection to the applied voltages for the nanosize samples. The elemental profile in Figure 6.12 (b) is indicative of the uniform distribution of elements along the growth axis, with no sign of drastic changes in the NWs composition.

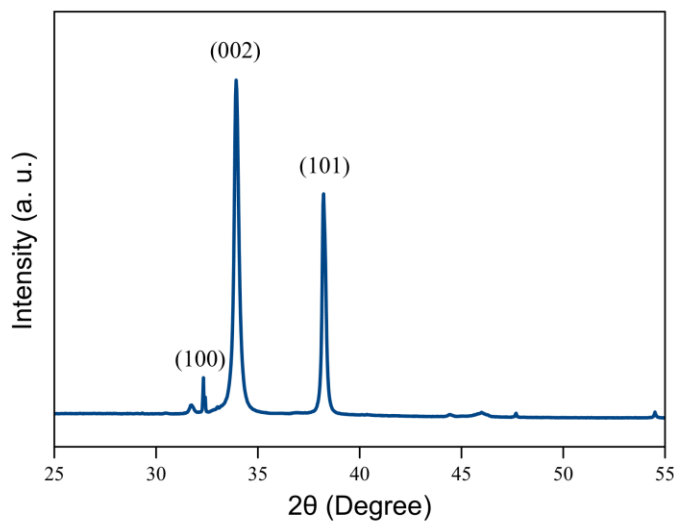


Figure 6.13: XRD pattern of the GaN:ZnO thin film fabricated at 1000 °C for 30 min at D = 8 cm on Si (100) substrate.

The highly crystalline hexagonal structure of the prepared GaN:ZnO NWs can be identified from the XRD pattern in Figure 6.13. As stated earlier, due to the negligible mismatch in the lattice dimension of the Si (100) and GaN/ZnO c -plane, epitaxial growth is expected towards the [002] direction. The high intensity of the (002) peak in the XRD pattern of the fabricated NWs, in

contrast to its bulk counterpart, testifies that the epitaxial growth of the NWs is primarily occurred towards the hexagonal c -axis. The intense (101) peaks are attributed to the secondary growth direction, as also observed in the SEM micrographs in Figure 6.10 (a) and Figure 6.11. The (100) peak can be related to the six symmetrical crystallographic planes parallel to the [002] axis, with various polarities, as marked in the scanning transmission electron microscopy (STEM) image of the NW displayed in Figure 6.14. Detection of an individual peak from the exposed facets on the outer surfaces of NWs is common and has been reported for various materials including GaN and ZnO [29,293,294].

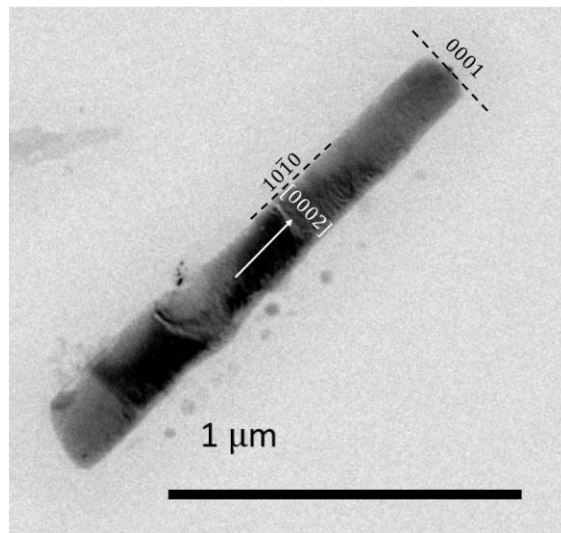


Figure 6.14: Low resolution STEM image of a NW prepared at at 1000 °C for 30 min at D = 8 cm, showing the growth direction, along the exposed facets on the side and tip.

The STEM image in Figure 6.14 shows the [002] growth direction and exposed facets of an individual NW with a length of 1.6 μm. In contrast to SEM observation in Figure 6.11, most of the NW samples observed by transmission electron microscopy (TEM) appeared to be short and

straight, with no sign of bending, suggesting the breakage of NWs at their bending points during the TEM sample preparation. Breakage of nanowires to the straight rod-shape materials is attributed to the structural defects at the points that the growth direction is changed between the [002] and [101]. Various strategies were applied to obtain nanostructures with less morphological damages so the shifts in the growth direction could be studied. In addition to the common ultrasonication method, the TEM samples in this research were prepared by freezing the deposited layer and scratching the substrate surface. However, undamaged nanowires, or those with [101] growth direction were not observed. To our understanding, the structures of NWs are formed by segments that mostly grow towards the *c*-axis, and a portion with [101] growth direction.

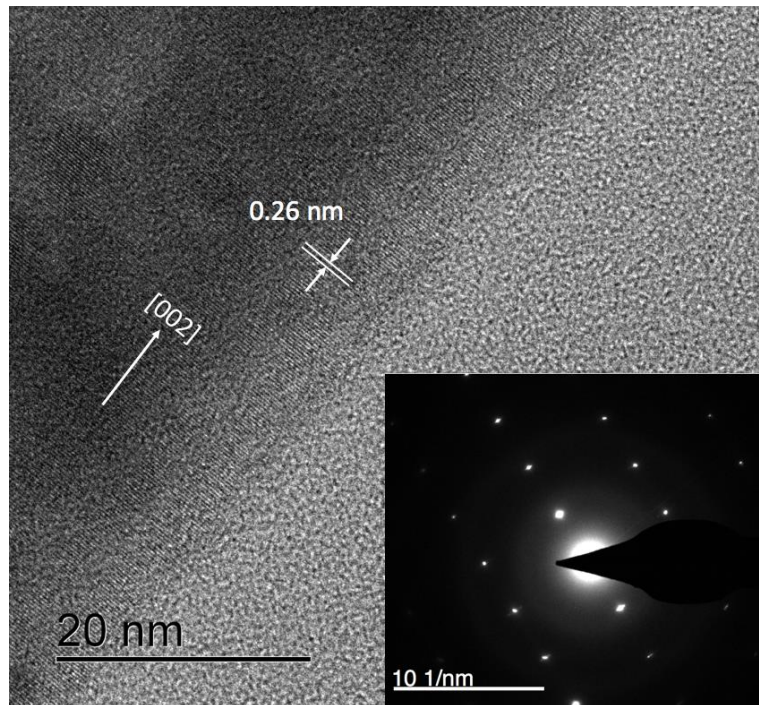


Figure 6.15: HRTEM images of a NW prepared at 1000 °C for 30 min at $D = 8$ cm on the Si substrate showing the growth direction and distance between the adjacent lattice fringes. Inset: SAED pattern.

Crystalline structure of the synthesized NWs was further studied through TEM analysis. The high resolution transmission electron microscopy (HRTEM) image in Figure 6.15 reflects a single crystal structure, consisting of well-ordered parallel lattice fringes with no sign of defects. In agreement with the XRD data, the lattice spacing of ~ 0.26 nm between adjacent planes corresponds to the distance between two (002) crystal planes. This observation is also confirmed by the selected area electron diffraction (SAED) pattern in the inset of Figure 6.15, exhibiting (002) plane single crystal diffraction pattern.

Interestingly, different crystallographic facets have been observed on the lateral surface of some NWs. Compared to the NWs with exposed $(10\bar{1}0)$ facets, as shown in Figure 6.14, a portion of NWs exhibited lateral walls consisting of $(10\bar{1}1)$ and $(10\bar{1}\bar{1})$ planes, evidenced by the $\sim 120^\circ$ angle between the two, as illustrated in Figure 6.16. Presence of such exposed facets have been reported for GaN:ZnO solid solution nanorods and GaN NWs prepared through solid-state growth and VLSE, respectively [62,292]. The transformation of the side-walls facets from the typical $(10\bar{1}0)$ to the combined $(10\bar{1}1)$ and $(10\bar{1}\bar{1})$ is related to the role of VLS mechanism, which continuously adjusts the crystallographic facets as well as the Au droplet size and shape to maintain the favorable growth direction and the hexagonal cross section of the NWs [292], which is visible in Figure 6.16.

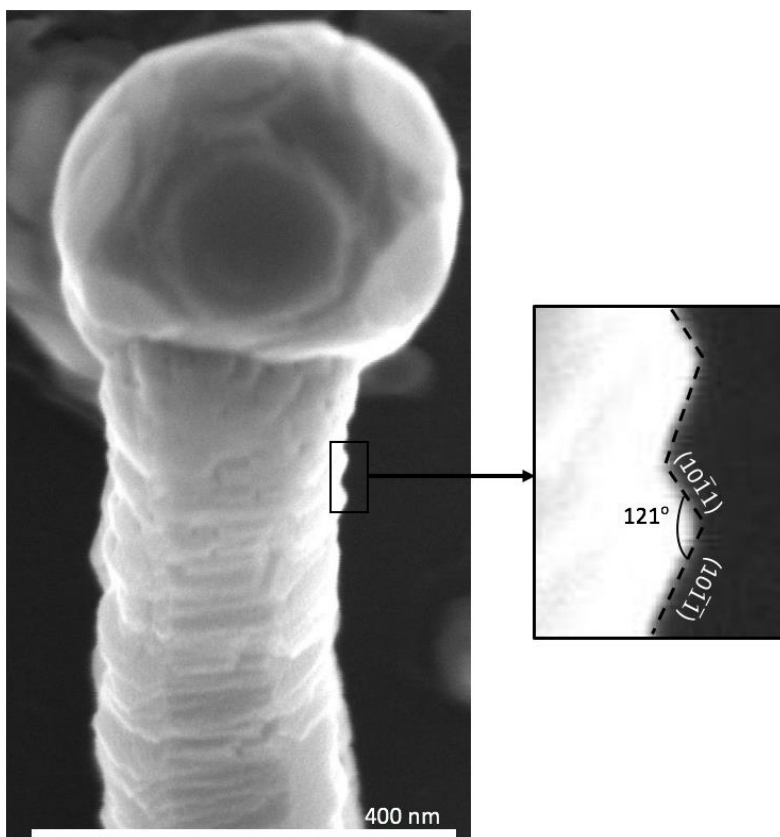


Figure 6.16: High resolution SEM image of a NW with exposed $(10\bar{1}1)$ and $(10\bar{1}\bar{1})$ facets.

It is highly desirable to control the surface polarity of nanowires since different crystallographic facets exhibit vastly different reactivity for particular catalytic reactions. For instance, it is known that anatase TiO_2 (001) is especially reactive for hydrogen evolution, compared to the thermodynamically stable (101) planes [295]. Moreover, despite the moderate plasmonic and catalytic activity of Au nanoparticles with mixed crystallographic facets, gold nanostructures with a dominant (111) orientation have been reported to be highly active for the overall water splitting reaction [220]. Although the activity of various crystallographic planes of GaN:ZnO solid solution has not yet been established, the development of a fabrication route with

control over the exposed crystallographic planes could open a new avenue of research for future studies that might lead to significant improvements in photocatalytic efficiencies.

6.5.3 Controlling the morphology of the thin film

For 1-D nanostructures, controlling the morphology of the synthesized thin film (*i.e.*, diameter and length) is considered to be the most important task. Tailoring the dimensions of the synthesized 1-D nanostructures has not been addressed for the majority of the fabrication routes reported in the literature, although its impact on the performance of functional nanowire materials is immense. There is strong evidence that the degree of supersaturation controls the morphology of a thin film [137], which can be tuned itself by several parameters during the vapor phase growth.

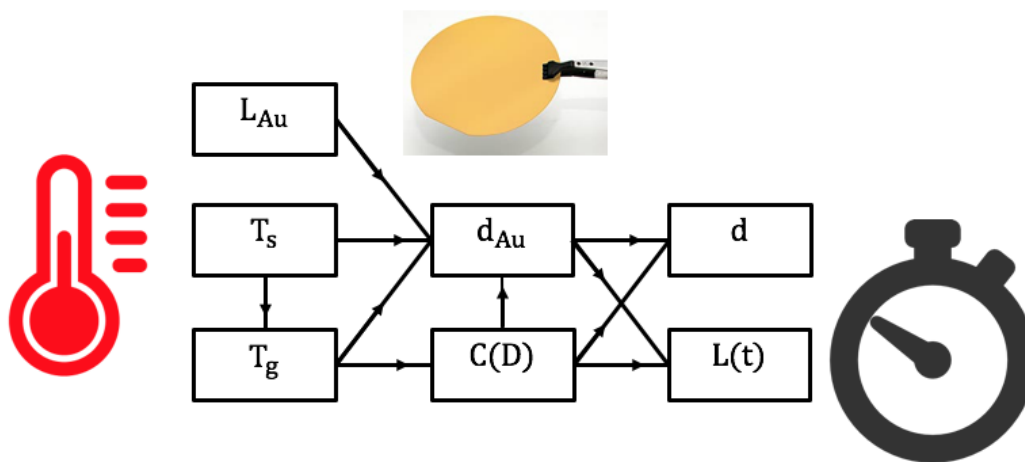


Figure 6.17: Dependence of 1-D nanostructures diameter (d) and length (L) to Au-catalyst film thickness (L_{Au}), source temperature (T_s), growth temperature (T_g), Au catalyst droplet size (d_{Au}), distance between precursor and substrate (D), and reactants concentration (C).

From a fabrication point of view, the temperature of precursor or source temperature (T_s), distance between the precursor and substrate (D) that determines the growth temperature (T_g), and

the duration of the CVD process (t) can be applied to control the dimensions of the synthesized nanowires. The dependence of growth parameters to these factors are depicted in Figure 6.17.

In vacuum CVD, sufficient vapor pressure of the reactant can be readily realized at high T_s ; hence, the primary dimension of the nanostructures can be safely considered as the growth temperature only. On the other hand, as suggested by our experiments, due to the low concentration of building blocks, the effect of both T_s and T_g are significant, and small variations in either could alter the VLSE kinetics. This functionality can be explained by the effect of these temperatures on homogenous nucleation as well as on nanowire growth. It is apparent for the VLS growth mechanism that the diameter of NWs is controlled by the size of Au catalyst droplets. Au catalyst is typically deposited on the surface at room temperature, as a thin film or as pre-synthesized NPs. In case of catalyst thin film, as applied in this research, Au droplets are formed in a wide range of sizes at elevated temperature. Moisala et al. reported that the melting temperature of Au particles varies drastically at smaller sizes ($d_p < 10$ nm) [296]. At low temperatures ($T < 800$ °C) Au droplets with size up to 10 nm can be formed; while, at $T > 900$ °C the entire Au film melts, and depending on the film thickness and exposure time to this temperature, droplets with sizes from ~10 nm to 1 μ m can be stabilized on the substrate. The dependency of Au melting temperature to the size of particles for some metal catalysts is presented in Appendix H.

To understand the processes that control the morphology of the thin films, the nanowires were prepared at various source temperatures and times ($T_s = 900, 1000,$ and 1100 oC for $t = 5, 30,$ and 60 min, respectively) as well as distances from the center of the furnace ($D = 0, 8, 13,$ and 21 cm). The rest of the operating conditions were kept unchanged in respect to the conditions stated in Table 6.3.

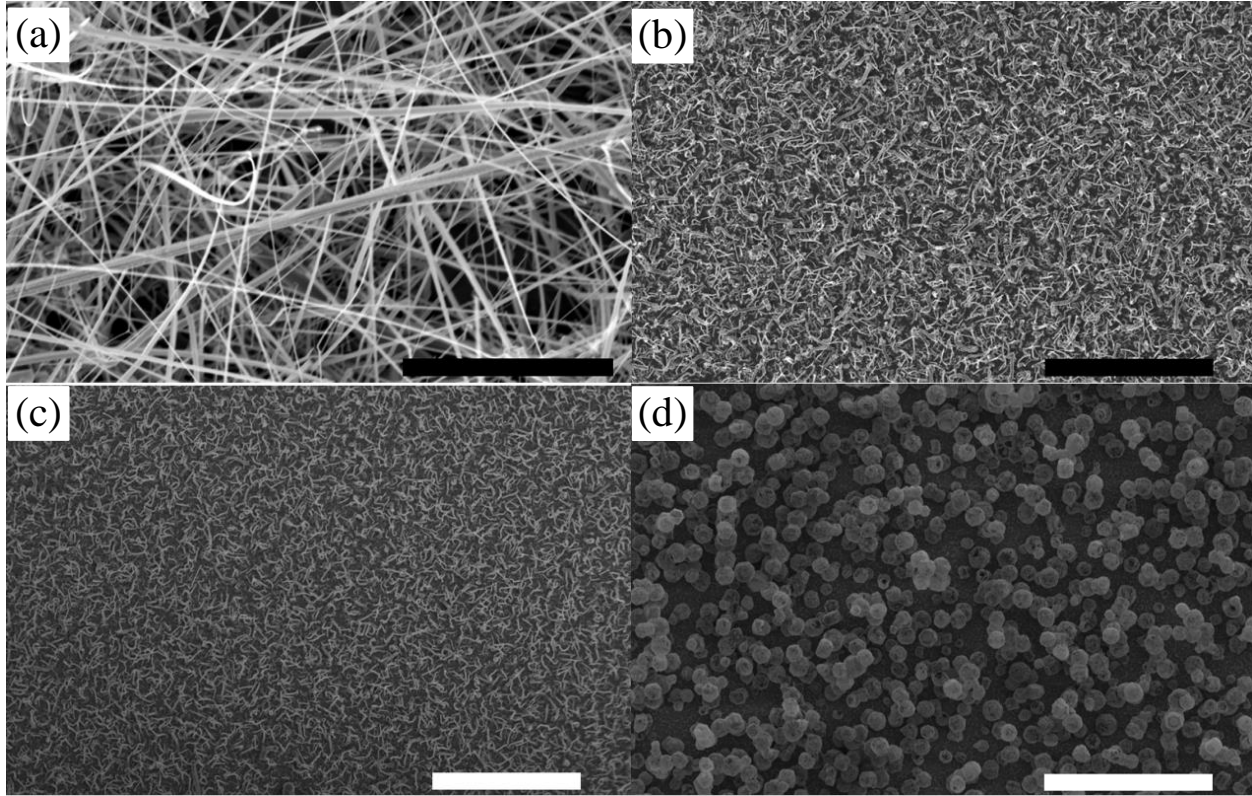


Figure 6.18: SEM image of the samples prepared via APCVD at $T_s = 1100\text{ }^\circ\text{C}$ and $t = 5\text{ min}$ on Si (100) substrate at various distances from precursor boat (a) NFs at $D = 0$ – scale bar = $5\text{ }\mu\text{m}$, (b) long NWs at $D = 8\text{ cm}$ – scale bar = $20\text{ }\mu\text{m}$, (c) short NWs at $D = 13\text{ cm}$ – scale bar = $10\text{ }\mu\text{m}$, and (d) hollow polyhedral cages at $D = 21\text{ cm}$ – scale bar = $50\text{ }\mu\text{m}$.

Figure 6.18 shows the nanostructures synthesized at $T_s = 1100\text{ }^\circ\text{C}$ for $t = 5\text{ min}$ on 10 nm Au-coated Si (100) located at various distances from the center of the furnace. The SEM micrographs in Figure 6.18 indicate the capability of the proposed APCVD method in the fabrication of structures with vastly different morphologies. At the center of the furnace ($D = 0$), when $T_s = T_g$, ultra-long and thin nanofibers (NFs), at $D = 8\text{ cm}$ NWs with $\bar{d} \sim 197\text{ nm}$ and $\bar{L} \sim 4.0\text{ }\mu\text{m}$, at $D = 13\text{ cm}$ NWs with $\bar{d} \sim 106\text{ nm}$ and $\bar{L} \sim 1.3\text{ }\mu\text{m}$, and at $D = 21\text{ cm}$ bulk structures with $\bar{d} \sim 5.7\text{ }\mu\text{m}$ can be prepared. Similar observation was made at $T_s = 1000\text{ }^\circ\text{C}$ and $900\text{ }^\circ\text{C}$ for $t = 30$

and 60 min, respectively, as such different morphologies were obtained from the substrates processed at various locations downstream from the source materials.

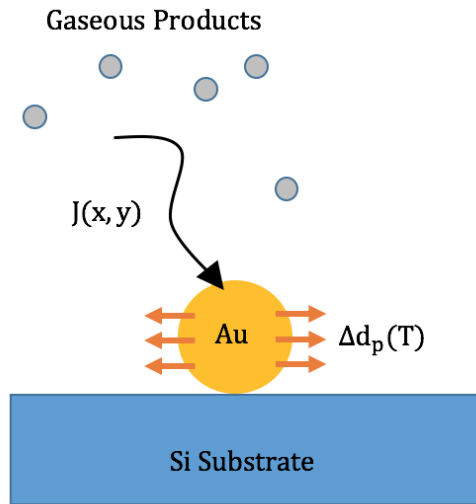


Figure 6.19: Dependency of the Au droplet size to the growth temperature and local concentration of the building blocks.

It is believed that the VLS nucleation and growth mechanism is dictated by the local concentration-temperature domain and size of the catalyst's particles [244,258,284,289,283]. As discussed earlier, during the nucleation stage, the size of Au droplets (d_{Au}) are a function of growth temperature, which adjusts the rate of Au droplets aggregation, resulting in larger clusters (Δd_p). The diffusion of the building blocks into Au droplet are controlled by the availability of the reactants (vapor pressure), as well as growth temperature (condensation). Therefore, as illustrated in the Figure 6.19, the size of Au droplets is controlled by the local concentration of reactants and growth temperature. Thus, lower temperature of the substrate (to reduce the rate of large Au cluster formation), and higher vapor pressure of the building blocks (to trigger the homogenous nucleation

by reaching the saturation concentration) result in structures with high aspect ratios. It should be noted that prediction of the diffusion rate of the building blocks to Au droplet (J) is hardly possible, since it is regulated by the availability of the building blocks (increases by approaching the center of the furnace) and condensation rate of the building blocks (inversely proportional to the growth temperature, increasing by distancing from the center of the furnace). Therefore, the dimensions of the synthesized nanowires are the outcome of these competing processes and must be studied through experimentation. By comparing this mechanism with the data obtained from experiments at various source and growth temperatures, four zones with unique temperature-concentration domain, each suitable for fabrication of different nanostructures were identified. These synthesis zones are illustrated in Figure 6.20.

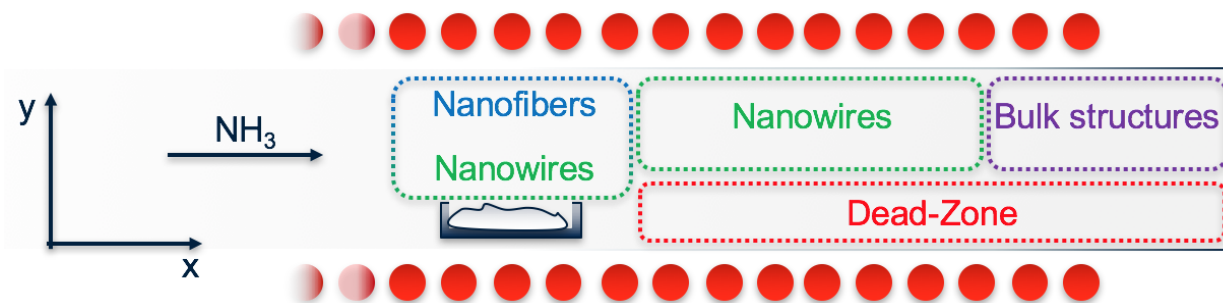


Figure 6.20: Various regions of the furnace for growth of structures with different morphologies.

1) Dead-Zone

At $y \sim 0$, due to relatively low concentration of the gaseous compounds (except NH_3), diffusion flux of the building blocks into the Au-catalyst (J) is insufficient for homogenous nucleation; while the rate of Au droplets aggregation (Δd_p) is the function of T_g , thus $J \ll \Delta d_p$. At this condition, large Au droplets are formed before reaching to the critical composition required

for the homogenous nucleation. Therefore, VLS growth conditions are not satisfied and 1-D nanostructures growth cannot be realized, as displayed in the SEM image in Figure 6.21.

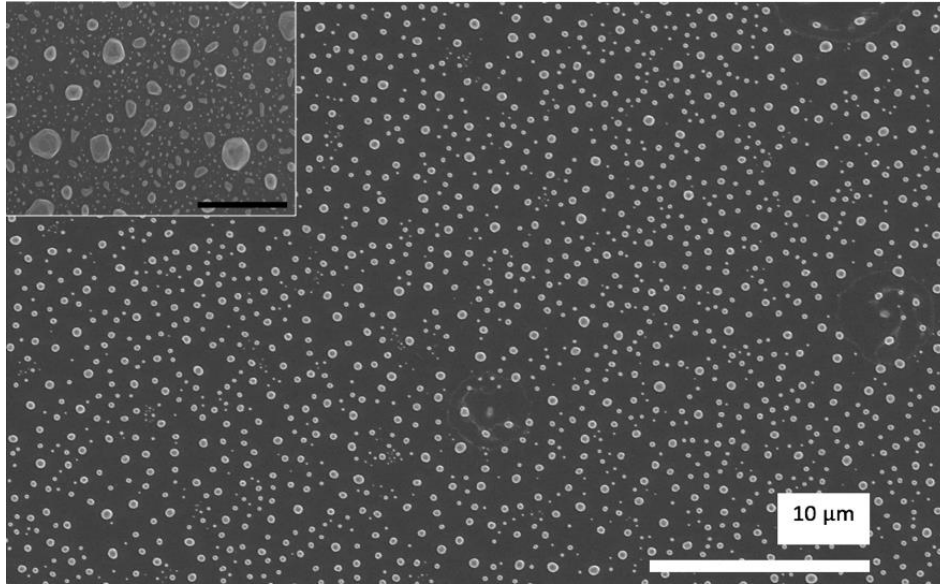


Figure 6.21: Low resolution SEM image of the Au-coated Si substrate processed at 1000 °C for 30 min in the dead-zone illustrated in Figure 6.20. Inset: SEM image of the Au coated Si substrate processed at 1100 °C for 5 min. scale bar = 3 μm.

In the absence of sufficient densities of the reactants to initiate nucleation, Au NPs with size as high as 700 nm and 1100 nm can be stabilized on the Si substrate at $T_s = 1000$ °C and 1100 °C, respectively, inside the dead-zone, as demonstrated in Figure 6.21 and its inset.

2) Nanofiber (NF) zone

When substrate is secured on the top of the precursor boat (face-down), as displayed in Appendix G, the growth and source temperature are equal ($T_s = T_g$). At this condition, an opposite mechanism, compared to the one observed for the dead-zone, regulates the VLS growth. When the

concentration of the building blocks reaches to their highest (C_{max}), the diffusion flux of the products into the Au-catalyst NPs (J) enhances significantly; thus, nucleation process begins shortly, leading to growth of ultra-thin (rapid nucleation) and ultra-long (rapid growth) NFs. Although high growth temperature increases the rate of Au droplets aggregation (Δd_p) which causes the formation of low aspect ratio structures, SEM micrograph in Figure 6.18 (a) indicates that the diffusion of gasses into Au-catalyst is the rate determining step. Therefore, the Au droplets were lifted from the substrate surface immediately (due to rapid nucleation), before engaging in the formation of larger aggregates ($J > \Delta d_p$). The fast growth towards the 1-D direction results in the formation of a dense film of NFs shown in Figure 6.18 (a), with smooth surfaces and diameters between 30 to 110 nm, as exhibited in Figure 6.22 (a).

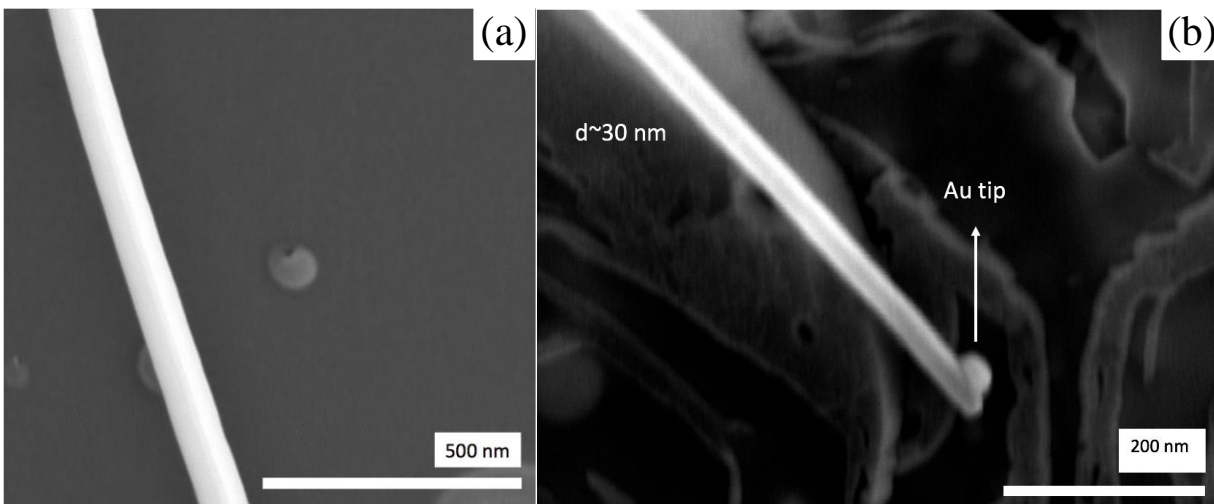


Figure 6.22: High resolution SEM micrograph of synthesized NFs on the Au-coated Si substrate processed at 1100 °C for 5 min in the NF-zone ($D = 0$) illustrated in Figure 6.20. (a) The smooth lateral surface, and (b) Au-catalyst on the tip of an individual NF.

High resolution SEM image in Figure 6.22 (b) shows an individual NF capped with an Au particle, confirming that the growth of NFs is catalyzed by the gold catalyst. Although the overall morphology of the NFs in Figure 6.18 (a) suggest their ultra-high aspect ratio, estimating the length of NFs from their high density film is hardly possible. The length of the NFs was approximated from the low resolution SEM image of the area that was not exposed to the gaseous reactants. As shown in Figure 6.23, the synthesized NFs exhibit ultra-high aspect ratio, with lengths over tens of microns. Such morphology is desired for many applications including energy conversion, owing to their high active surface area, short charges diffusion length, and strong light absorption (trapping) [299–302].

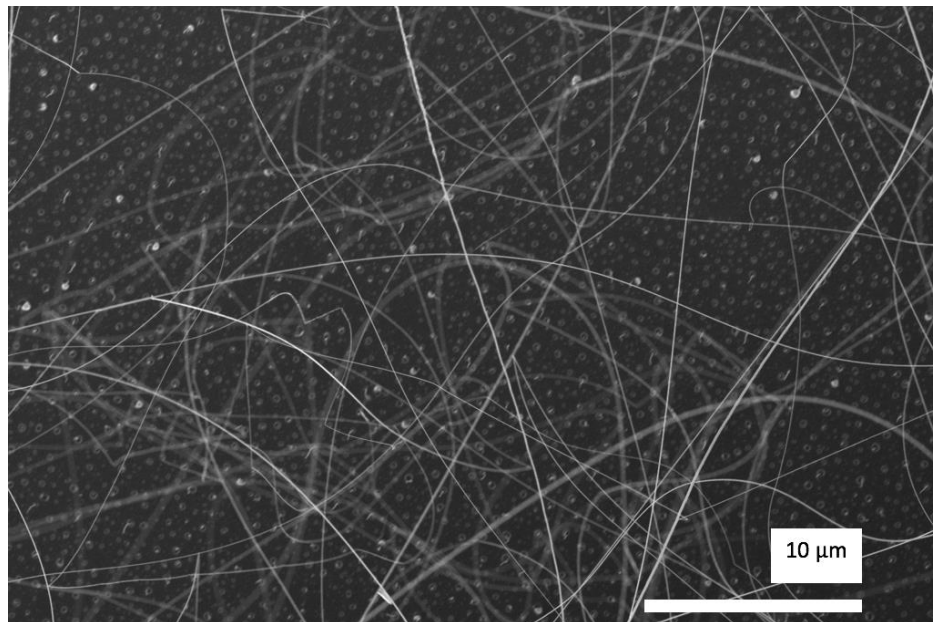


Figure 6.23: Low resolution SEM image of NFs synthesized on the Au-coated Si substrate processed at 1100 °C for 5 min in NFs-zone ($D = 0$) illustrated in Figure 6.20.

The compositional data of the synthesized NFs are summarized in Table 6.5. The synthesized solid solution NFs possess a GaN-rich chemistry with $x = 0.05$. Similar to the prepared NWs, the low Zn-content of the NFs is likely attributed to the high APCVD growth temperature, which is greater than the ideal ZnO NWs crystallization. Presence of Au on the surface of the solid solution NFs is expected, due to the surface wetting and diffusion of the catalyst [291].

Table 6.5: Composition of NFs synthesized at 1100 °C for 5 min at $D = 0$.

Parameters	Values
Ga	47.8 atm%
Zn	2.8 atm%
N	41.2 atm%
O	4.9 atm%
Au	3.3 atm%
x	0.05
Zn/O	0.58
Ga/N	1.16
Zn/Ga	0.06

Our experiments indicated that fabrication of GaN:ZnO NFs can be only realized at $D = 0$ and $T_g = 1100$ °C. Processing the Au coated substrate at $T_g = 900$ °C and 1000 °C results in the growth of NWs with $\bar{d} \sim 288$ and 141 nm and $\bar{L} \sim 4.3$ and 4.5 μm , respectively. Such variation in the nanostructures dimension suggests that J is the rate determining factor at high temperature range ($T_g=1100^\circ\text{C}$); while, at lower growth temperatures ($T_g = 900$ °C and 1000 °C) the VLS growth kinetics are controlled by both $J(x,y)$ and $\Delta d_p(T)$.

3) Nanowire (NW) zone

Distancing from the center of the furnace (precursor boat), the temperature of the substrate deviates from T_s ; while, the local vapor pressure of the reactants decreases, resulting in a moderate temperature-concentration domain. At this condition, gas diffusion flux into the Au nanoparticles (J) and Au droplets aggregation rate (Δd_p) are relatively balanced ($J \approx \Delta d_p$). Thus, sufficient densities of the building blocks are available to initiate the homogenous nucleation of 1-D nanostructures via VLSE mechanism (unlike dead-zone), yet the diffusion rate is not large enough (nucleation rate is not fast-enough) to keep the size of the Au droplets as small as those observed in the NF-zone. The outcome of these competing processes is the growth of NWs with various aspect ratios, as illustrated in Figure 6.18 (b) and (c) for $D = 8$, and 13 cm, respectively at $T_s = 1100$ °C for $t = 5$ min. Through the mechanism explained here and illustrated in Figure 6.19, by adjusting the location of the substrate ($D = 8$ and 13 cm) and growth conditions (60 min at $T_s = 900$, 30 min at 1000 , and 5 min at 1100 °C) thin films of NWs with average diameters ranging from 100 – 340 nm, average lengths between 0.5 – 4.0 μm , and x up to 0.11 can be synthesized on the Si substrate.

4) Bulk structure zone

In the region approaching the outlet of the heated zone, temperature decreases rapidly, inversely proportional to the deposition rate of the gaseous compounds. At this condition, the diffusion rate of gasses to Au catalyst is significantly high (due to condensation) and aggregation rate of gold droplets is minimal ($J \gg \Delta d_p$). Therefore, Au droplets are saturated rapidly and cannot maintain the VLS growth in 1-D direction, leading to the formation of bulk structures via secondary nucleation.

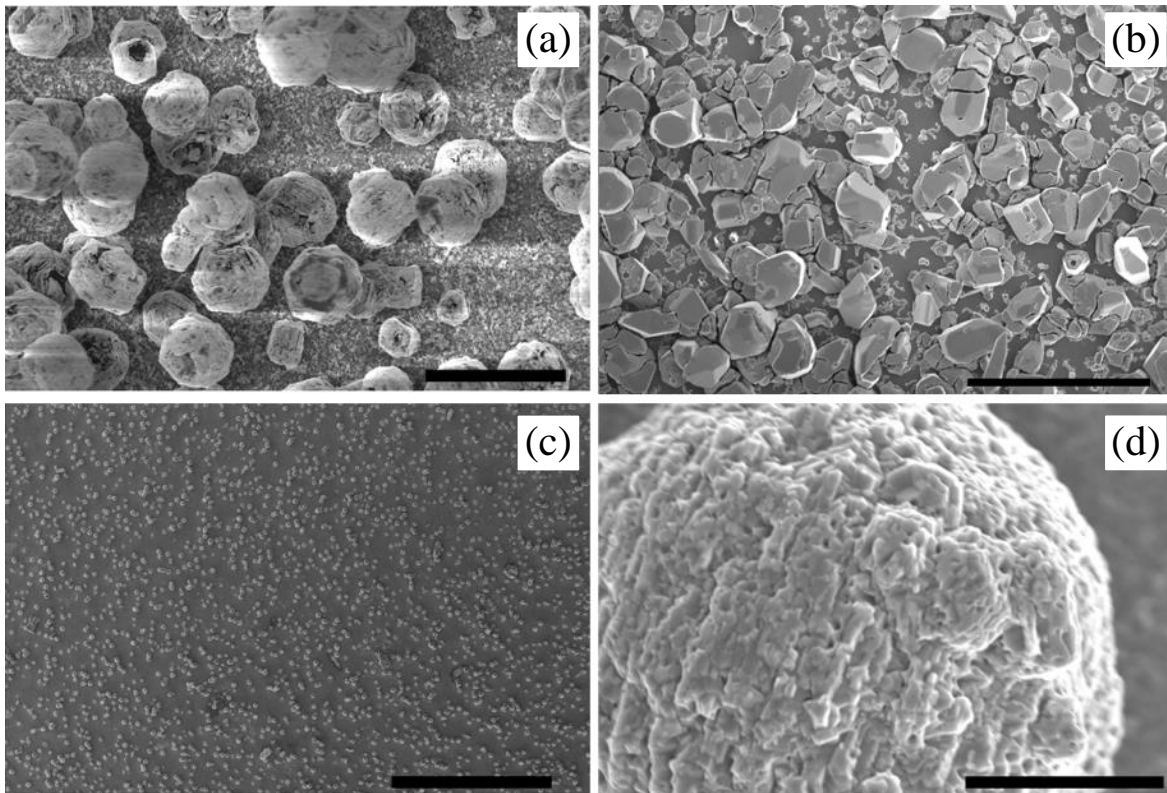


Figure 6.24: SEM images of the bulk structures on the surface of Si substrate prepared at various temperatures and durations in the bulk-structure zone displayed in Figure 6.20. (a) Polyhedral cages with hollow structure – scale bar = 10 μm , (b) thick film – scale bar = 20 μm , (c) and (d) low and high magnification images of micro-balls – scale bars = 200 μm and 2 μm , respectively. Low resolution SEM image of the polyhedral cages is presented in Figure 6.18 (d).

As a result of such rapid deposition, variety of bulk structures including polyhedral cages [303], shown in in Figure 6.18 (d) and Figure 6.24 (a), thick film, displayed in Figure 6.24 (b), and micro-balls, illustrated in Figure 6.24 (c) and (d) are formed on the Si substrate. Despite the uniform morphologies of these structures, indicating their well-defined crystalline structure, their consistent fabrication in the bulk-structure zone under same growth conditions was not realized. Apparently, the growth mechanism in this region is dictated by the temperature and CVD local

hydrodynamics, which is difficult to control accurately via APCVD process, unless a specially designed apparatus is used.

6.6 Photocatalytic performance

Visible-light OWS activities was observed from the NWs and NFs photocatalyst panels. However, to obtain data, a customized apparatus was required. Therefore, the synthesized NWs ($T_s = 1000\text{ }^\circ\text{C}$, $t = 30\text{ min}$, $D = 8\text{ cm}$; weight $\sim 3.2\text{ mg}$) and NFs ($T_s = 1100\text{ }^\circ\text{C}$, $t = 5\text{ min}$, $D = 0\text{ cm}$; weight $\sim 4.1\text{ mg}$) were explored for their photocatalytic activities through sacrificial hydrogen production under visible-light irradiation. For comparison, equal weight ($\sim 3.4\text{ mg}$) of powder nanoporous photocatalyst particles was dispersed in pure water, ultra-sonicated and drop casted on a Si substrate. The dried photocatalyst slide, denoted as GaZnON-P, was annealed at $350\text{ }^\circ\text{C}$ for 20 min to ensure an adequate adhesion to the surface of the substrate. All samples were prepared on Si substrates with area $\sim 0.81\text{ cm}^2$ and loaded with 1 wt% Rh co-catalyst through photo-deposition in 5 V% ethanol solution under visible light irradiation.

Acquiring a high quality image from the co-catalyst NPs on the surface of NWs is assumed to be simpler than the nanoporous particles, due to less complexities of their surface structures. However, because of their smooth surface and less defects, co-catalysts NPs may strip from their surface during the TEM sample preparation. Figure 6.25 shows the high resolution STEM and TEM image of an individual 6 nm Rh NPs on the surface of a GaN:ZnO NW. Surface structure of the NW in Figure 6.25 (a) is appeared to be smooth with minor sign of surface damages. In addition to the spherical Rh NP, the HRTEM image in Figure 6.25 (b) shows the single crystal structure of the synthesized NW, evidenced by the parallel crystalline fringes with no sign of defects.

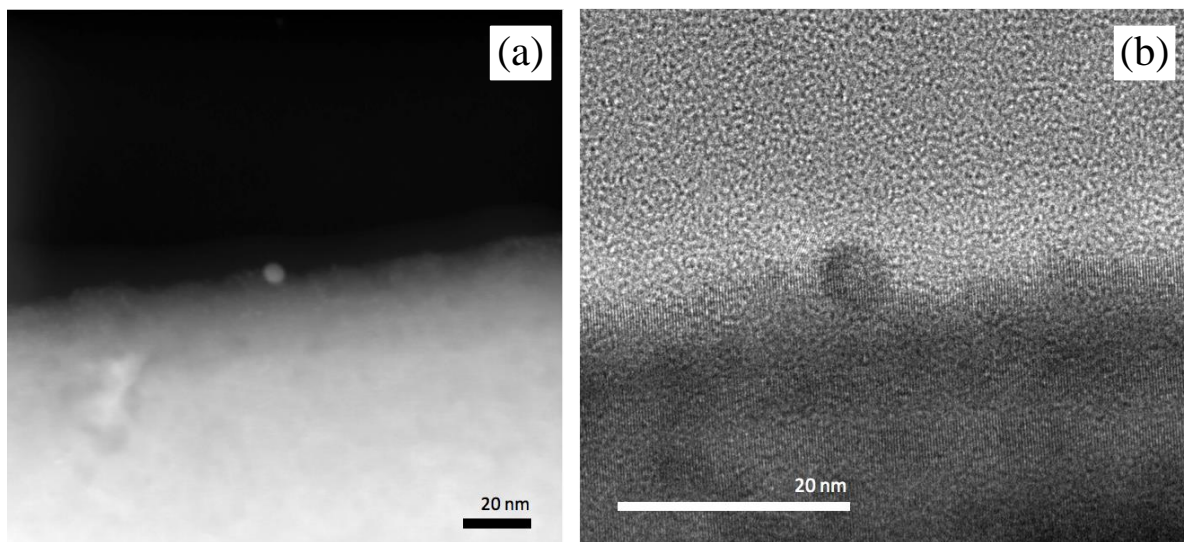


Figure 6.25: (a) STEM, and (b) HRTEM image of an Rh co-catalyst NP on the surface of a GaN:ZnO NW.

Visible light sacrificial hydrogen evolution of the photocatalyst panels was explored in 10 V% methanol solution and the results are illustrated in Figure 6.26. It is noticeable in Figure 6.26 that the total evolved hydrogen from the GaZnON-NW panel was more than 30% of the hydrogen generated by the GaZnON-P photocatalyst. The activity of the GaZnON-NF sample was the lowest recorded among the samples for sacrificial hydrogen evolution. The average rate of sacrificial hydrogen evolution of the GaZnON-NW panel was estimated $\sim 15.5 \mu\text{mol g}^{-1} \text{h}^{-1}$, which is higher than the one from the GaZnON-P panel $\sim 11.1 \mu\text{mol g}^{-1} \text{h}^{-1}$.

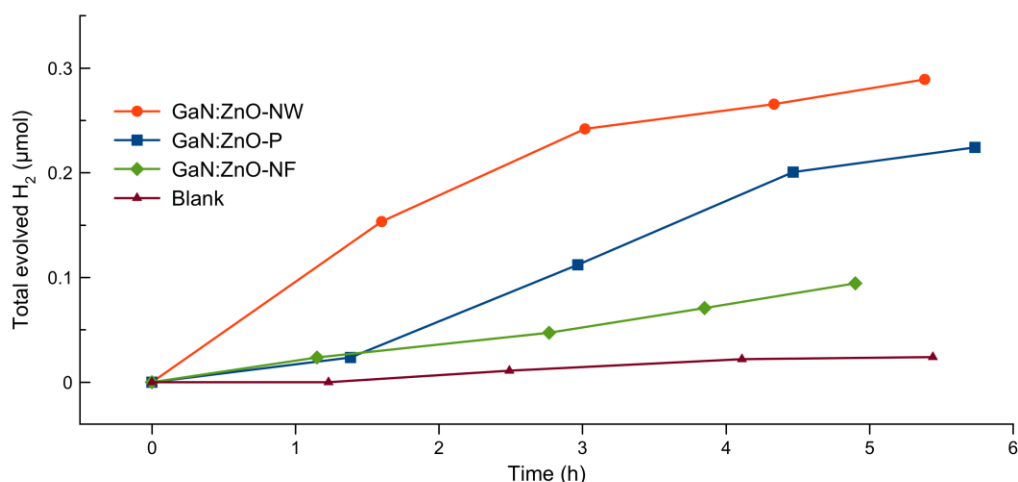


Figure 6.26: Sacrificial hydrogen evolution in 10 V% methanol solution for the GaN:ZnO nanowires (GaN:ZnO-NW), nanoporous particles (GaN:ZnO-P), and nanofibers (GaN:ZnO-NF). Data also displayed for the blank Si (100) substrate.

It is assumed that the 1-D structure of the NWs promotes the fast charge separation, resulting in their superior photocatalytic activities. In addition, as confirmed via TEM analysis in Figure 6.15 and Figure 6.25 (b), the defect-free structure of the NWs and their presumably higher surface area could be responsible for their improved hydrogen production. Unlike the GaZnON-NW sample, the GaZnON-NF photocatalyst exhibited low photocatalytic activity. NFs of semiconductors have reported to be highly active for electrochemical applications [299–302], owing to their ultra-high surface area and superior charge transfer. Greater portion of the photo-induced charges are expected to be generated inside the depletion layer of the synthesized NFs, since the photons penetration depth is favorably comparable to their depletion layer thickness. The followings may cause the low activity of the GaZnON-NF sample:

- 1) Compositional: EDX elemental data concluded that the synthesized NFs possess GaN-rich composition. Since the visible light absorption of the GaN:ZnO photocatalyst is attributed

to the Zn-content of the photocatalyst, low composition of zinc of the prepared NFs ($x \sim 0.05$) may limit their absorption to near UV region, therefore be responsible for their low visible light activity.

- 2) Structural: The diameter of GaN:ZnO NFs were estimated between 30–110 nm, which is relatively close to the range reported for the fully depleted GaN and ZnO NWs with critical diameter of ~ 80 nm [259] and 100 nm [260,261], respectively. The synthesized NFs could be fully depleted due to their small diameter; thereby charge separation mechanism driven by the electrical field in the space-charge region may no longer exist. Therefore, the low activity of GaN:ZnO NFs could be related to the high rate of photo-recombination.
- 3) Morphological (1): Ultra-high surface area of NFs may enhance the density of the surface states. These energy states could have trapped the photo-induced charges, and significantly enhanced the rate of surface recombination (J_{sr}).
- 4) Morphological (2): During the photocatalytic tests in aqueous media, it is possible that some of the NFs are dissociated from the surface. Ultra-high aspect ratio of the NFs makes them fragile and presumably reduces their stability on the surface of the photocatalyst panel.

Indeed, an extensive experimental study is required to obtain in-depth understanding of the synthesized NWs and NFs samples photocatalytic characteristics. In addition, the photocatalytic activities of the samples must be optimized through tailoring their morphological and structural properties. The analysis presented here is a brief study that indicates the promising performance of the GaN:ZnO solid solution NWs. Applying modifications to the proposed fabrication route in future work may lead to interesting water splitting performances from thin film photocatalyst panels.

Chapter 7: Conclusions and Recommendations

7.1 Conclusions

This research aimed to study:

- 1) The development of an efficient synthesis technique for the GaN:ZnO solid solution and evaluation of the characteristics of the synthesized photocatalyst.
- 2) The impact of the hydrogen and oxygen evolution co-catalyst materials and their loading conditions on the photocatalytic performance of the synthesized photocatalyst.
- 3) The role of graphene as the support material for GaN:ZnO solid solution photocatalyst in reducing the recombination of photo-induced charges.
- 4) The development of a method for the fabrication of GaN:ZnO solid solution in the form of 1-D nanostructures.

This section discusses the outcomes of this research and its contributions.

7.1.1 Development of a facile synthesis method for GaN:ZnO photocatalyst

In order to address the inefficiencies of the traditional GaN:ZnO solid solution synthesis technique (*e.g.* 10+ h at 850 °C under 250 mL min⁻¹ NH₃ flow), a facile technique was proposed. Two precursors were used for the preparation of GaN:ZnO solid solution: a uniform mixture of Ga₂O₃ and ZnO as well as the crystalline Ga³⁺ and Zn²⁺ layered double hydroxides (LDHs) as the atomic-level uniform mixed-metal precursor. Further, the ammonia nitrogen source in the traditional synthesis route was replaced by abundant and non-toxic urea. In addition to its role as the nitrogen source, the application of urea as a soft nano-template for the reduction of synthesis time by enhancing the surface area of solid-state reaction was explored.

Our material characterization and performance evaluation data led to the conclusion that a GaN:ZnO solid solution with reasonable photocatalytic activity can be prepared via the proposed technique within a few minutes, a fraction of the synthesis time reported using the traditional method. X-ray diffraction (XRD) and transmission electron microscopy (TEM) data confirmed the formation of wurtzite GaN:ZnO photocatalysts in a 12-min process. Despite this lower preparation time, the synthesized photocatalysts were characterized as poly-nano-crystalline materials, containing bulk and surface crystal defects, which are known to be undesirable for photocatalytic water splitting. The significant reduction in the synthesis time (12 min, compared to the original 10⁺ h) was found to be attributed to the distribution of the uniform precursors, particularly Ga³⁺ and Zn²⁺ LDHs, within the nano-template formed during urea thermal decomposition.

The synthesized samples were characterized using various techniques including scanning electron microscopy (SEM), energy-dispersive X-ray spectroscopy (EDX), ultraviolet-visible (UV-Vis) diffuse reflectance spectroscopy, and photoluminescence (PL) spectroscopy. The newly synthesized photocatalysts, characterized as nanoporous bulk particles, consist of nanopores distributed uniformly on the surface and in the bulk of the solid solution particles. The presence of these nanopores increases the active surface area of the photocatalyst at least 4.5 times, as compared to the surface area of the traditionally prepared photocatalysts.

One known drawback of the traditional preparation technique is the low Zn content of the solid solution photocatalyst, which is responsible for its visible-light activity. The Zn content of the nanoporous photocatalyst can be controlled in a wide range, and Zn-rich solid solution with $x = [\text{Zn}]/[\text{Zn}+\text{Ga}]$ up to 0.66 can be obtained.

The effect of the crystal defects and Zn content of the synthesized solid solution photocatalyst on the samples' PL emissions revealed the superior crystallinity of the samples prepared by LDHs precursor, which favourably reflected on their water splitting performances.

The synthesized photocatalysts with various compositions exhibited promising overall water splitting under visible-light irradiation. The highest apparent quantum efficiency (AQE) of 2.71% was achieved for the photocatalyst with $x \sim 0.32$, loaded with 1 wt% Rh co-catalyst nanoparticles. The performance of the newly synthesized photocatalyst is among the highest reported in the open literature for photocatalysts loaded with a single co-catalyst. Despite its promising photocatalytic activities, the nanoporous GaN:ZnO solid solution photocatalyst exhibited oxygen evolution lower than the expected stoichiometric rate and limited stability during water splitting. Four deactivation mechanisms were proposed based on the structural, photochemical, and physical routes. It was suggested that all four mechanisms contribute to the deactivation of photocatalysts to some degree.

Our study confirms the existence of a feasible path for the preparation of the solid solution of GaN and ZnO through a rapid solid-state reaction. The mechanism introduced in this work can be adapted for the synthesis of a wide range of advanced photocatalytic systems, particularly nanoporous nitride and oxynitride semiconductors.

The nanoporous GaN:ZnO solid solution photocatalyst developed in this study can be further optimized to achieve higher photocatalytic activity by applying modifications to the proposed synthesis route, as discussed in the recommendation section.

7.1.2 Utilization of hydrogen and oxygen evolution active sites

The importance of surface active sites for the evolution of hydrogen and oxygen has been emphasized for various photocatalysts, particularly oxynitrides. Co-catalyst nanoparticles (NPs) reduce the potential barriers on the surface and facilitate the transportation of the photo-excited electrons and holes to the surface–electrolyte interface. As part of this study, the impact of co-catalyst deposition methods, the role of co-catalyst materials, and their optimal loading amount were investigated with respect to the photocatalytic performances of the samples.

The effectiveness of the impregnation and photo-deposition methods was studied for the Pt model-catalyst. Our results, in agreement with data in the literature, demonstrated the superior activity of the samples decorated through photo-deposition. From the mechanism explained in this research (proposed in the literature), it is concluded that the photo-deposition method is particularly effective for nanoporous structures, owing to its uniform deposition of catalyst NPs at the targeted sites without blocking the pores.

The roles of various hydrogen and oxygen evolution sites were examined by comparing the photocatalytic activities of the GaN:ZnO samples loaded with Rh, Pt, NiO_x as HER, and IrO_x and Mn₃O₄ as OER catalysts. Visible-light hydrogen evolution of the loaded photocatalyst samples indicated the following order of HER catalytic activities: Rh→Pt→NiO_x. The higher surface area of the nanoporous photocatalyst resulted in a greater capacity for co-catalyst NP loading, without blocking the surface of the photocatalyst from the incident photons. The optimal loading without shading the photocatalyst surface was measured as high as 7 wt% for the Pt and 5 wt% for the Rh and NiO_x catalysts.

Our experimental and characterization data implies that the existence of nanopores in the structure of the newly synthesized photocatalyst offers several advantages, including the followings:

- 1) Providing a higher surface area for deposition of co-catalyst NPs, without shading the photocatalysts surface.
- 2) Reducing the photo-excited charge path to the surface by creating active sites inside the three-dimensional (3-D) structure.
- 3) Hindering the diffusion of evolved hydrogen and oxygen insides the narrow pores, and hypothetically decreasing the rate of the undesirable reverse reaction.

Therefore, this research has identified a morphological approach to address the key obstacles in photochemical water splitting, employing the nanopores as active water splitting regions.

The sample loaded with IrO_x co-catalyst demonstrated the highest oxygen evolution activity, reaching to over 200 μmol h⁻¹ sacrificial oxygen evolution in AgNO₃ solution. Despite the promising activities of the photocatalyst samples decorated with HER or OER catalysts, co-loading of nanoporous photocatalyst with H₂ and O₂ evolution catalysts resulted in lower overall water splitting efficiencies. A mechanism based on the overlapping of hydrogen and oxygen evolution sites on the surface and within the porous structure of the photocatalyst was suggested to explain the low activity of the co-loaded samples.

Finally, our attempts to suppress the undesirable reverse reaction through decorating the surface with Rh-Cr₂O₃ core-shell co-catalyst was not successful. The TEM and EDX elemental mapping data suggest that Cr was deposited as a film (rather than a shell structure surrounding the

core catalyst) on the surface of the photocatalyst, blocking the entry of nanopores and significantly reducing the active surface area of photocatalyst.

7.1.3 GaN:ZnO photocatalysts hybridized with reduced graphene oxide

Considering the outstanding photocatalytic activity improvements gained by the incorporation of graphene and its derivative materials into existing photocatalysts that have been reported in the literature, an advanced photocatalytic system of GaN:ZnO solid solution hybridized with reduced graphene oxide (GaN:ZnO-rGO) was fabricated and characterized. A Facile solution mixing approach was employed for the preparation of a composite via ultra-sound treatment of GaN:ZnO and graphene oxide (GO) solutions. The ex-situ fabrication route is believed to be driven by electrostatic attraction between negatively charged GO and GaN:ZnO particles. The prepared GO composite was subjected to in-situ photo-assisted reduction to obtain a conductive rGO composite. The XRD data confirmed the successful exfoliation of the graphite 3-D structure into micron-scale monolayer GO nanosheets through the modified Hummers method, and further, its reduction via visible-light irradiation. Removal of oxygen functionalities as the result of visible-light irradiation is indicative of the existence of electrochemical interaction between composite components, in which the photo-excited electrons from the bulk of the photocatalysts were transferred into the conductive nanosheets. This effective interaction was also confirmed by overall and high resolution XPS analysis, where the composition of oxygen reduced significantly, and the broken sp^2 network was healed after photo-induced reduction.

The synthesized composite photocatalyst showed a relatively uniform distribution of the photocatalyst particles on the surface of monolayer reduced graphene oxide nanosheets. Deposition of Rh co-catalyst NPs was evidenced through scanning transmission electron microscopy (STEM) analysis, which further confirms the sufficient charge density on the surface

of the nanosheets. It was also confirmed through PL analysis that the lifetime of the photo-excited charges was improved after hybridization with rGO. The synthesized composite with 2 wt% GO demonstrated superior activity for overall water splitting under visible-light irradiation, with over a 70% improvement in apparent quantum efficiency. Similar optimal GO composition and activity enhancements were also observed for the nanoporous GaN:ZnO photocatalyst graphene-based composite.

Our study is the first demonstration of GaN:ZnO-rGO composite fabrication and performance evaluation for OWS application. The characterization results presented in this study confirm the effective interaction between composite components, which results in higher water splitting efficiencies. The structural, morphological, and photochemical properties of the prepared composite photocatalyst can be further tailored through material fabrication to achieve higher quantum efficiencies.

7.1.4 Fabrication of GaN:ZnO 1-D nanostructure

One promising approach for enhancing the photocatalytic activities of semiconductor materials is their fabrication in the form of 1-D nanostructures such as nanofibers (NFs), nanowires (NWs), and nanotubes (NTs). In this research, the following approaches were investigated for synthesizing the thin film GaN:ZnO photocatalyst:

- 1) Nitridation of Ga³⁺ decorated ZnO NWs,
- 2) Direct growth of Ga-Zn NWs through solution-based method, and
- 3) Atmospheric pressure chemical vapour deposition (APCVD) via vapour–liquid–solid epitaxy (VLSE)

7.1.4.1 Nitridation of Ga³⁺ decorated ZnO nanowires

Gallium salt solutions with various concentrations (5–35 mM) were used for the impregnation of ZnO NWs as the template for preparation of Zn-Ga³⁺ NWs. SEM analysis suggested the destruction of the thin film's morphology and aggregation of Ga-species attached to the single-crystal ZnO NWs at high and low gallium salt solution concentrations, respectively. Although the fabrication of uniform solid solution NWs was not realized, this technique can be performed using various Ga salts and solvents for uniform surface decoration, and eventually the fabrication of GaN:ZnO NWs in mild conditions.

7.1.4.2 Direct solution-base growth of Ga-Zn nanowires

Chemical bath growth of ZnO NWs was modified by the addition Ga precursor to the growth solution containing various Zn salts and morphology-regulating reagents, to stimulate the direct 1-D growth of the Ga-Zn nanowires. The fabrication of Ga-Zn NWs was not realized, although crystalline structures with low aspect ratios were observed inside the growth solution and on the seeded quartz substrate. Further investigation of various Zn-Ga precursors, selective capping reagents, and growth conditions may lead to the development of a facile synthesis method for the growth of Ga-Zn NWs in mild conditions.

7.1.4.3 Atmospheric pressure chemical vapor deposition (APCVD) via vapor-liquid-solid epitaxy (VLSE) mechanism

Due to the complexity of the CVD growth of semiconductor thin films, several factors were studied, including substrate crystalline structure (non-epitaxial and epitaxial growth), source temperature, growth temperature, and growth duration.

An amorphous quartz substrate was employed for non-epitaxial VLS growth catalyzed by Au NPs. SEM images confirmed the growth of some NWs via the VLS mechanism on the quartz substrate. The VLS growth was controlled by self-seeding of wurtzite deposits as well as by horizontal crawling. The low density of obtained NWs on the surface of the substrate was determined to be the drawback of the non-epitaxial approach.

Single crystal Si (100) substrate, with slight crystallography mismatches to the GaN and ZnO *c*-plane, was used for epitaxial APCVD growth of the GaN:ZnO thin film. Uniform and high density NW arrays ($\sim 4.1 \times 10^7$ NW cm^{-2}) with diameters of ~ 190 and 205 nm and lengths of ~ 3.8 and 1.2 μm were obtained via epitaxial APCVD on the Si substrate processed at the various locations downstream of the Ga₂O₃ and ZnO mixture at 1000 °C for 30 min. Almost all the NWs were capped by Au NPs, confirming the VLS growth mechanism. SEM images revealed that the majority of NW possess a kinked structure, which suggests their polycrystalline VLSE growth. Some mechanisms were proposed for the formation of the kinked structure.

The prepared NWs were extensively characterized for their morphology, structure, and composition. XRD and EDX data revealed the formation of wurtzite oxynitride GaN:ZnO solid solution with combined (002) and (101) axis as the growth directions. The composition of the synthesized NWs exhibited $\sim 20\%$ deviation from the stoichiometric GaN:ZnO formulation, with $x = [\text{Zn}]/[\text{Zn}+\text{Ga}] \sim 0.10$ ($T_s = 1000$ °C for 30 min).

TEM analysis revealed that the smaller portion of the NWs consists of a single crystal structure of the GaN:ZnO solid solution with lattice dimensions in agreement to those of GaN and ZnO. The wurtzite *c*-axis [002] was identified as the primary favourable growth direction, as most of the analyzed samples exhibited the lattice constant match to this crystallographic plane. The proposed APCVD growth also exhibited potential for tailoring the crystalline facets of the exposed

lateral surfaces of the synthesized NWs, which might favourably contribute to their photocatalytic activities.

Four growth regions were identified at the center and downstream of the source materials. The diameters, aspect ratios, and compositions of the prepared 1-D nanostructures were successfully controlled within a wide range, as evidenced by the fabrication of GaN:ZnO NFs (with $d = 30\text{--}110$ nm, aspect ratio over 400, $x \sim 0.05$), NWs (with aspect ratios between 3.7–31.0 and x up to ~ 0.12), and bulk micro-structures using a single fabrication apparatus. The prepared thin films were characterized, and a mechanism based on the VLS growth kinetic was proposed for the formation of various morphologies in the growth regions.

Finally, the sacrificial hydrogen evolution of the GaN:ZnO NWs and NFs were compared to those of the powder nanoporous photocatalyst, indicating the superior photocatalytic activity of the NW photocatalyst. Hypothetical causes of low photocatalytic activities of the NFs were discussed from compositional, structural, and morphological viewpoints.

The APCVD method proposed in this research is among a few examples of the fabrication and extensive characterization of GaN:ZnO 1-D nanostructure fabrication. To our knowledge, the proposed fabrication route is the first report on the preparation of GaN:ZnO NFs. Moreover, using a simple vapour transfer approach at atmospheric pressure, our study is the first demonstration of the direct fabrication of GaN:ZnO thin films with a wide range of morphologies. Optimization of the growth process is expected to improve the photocatalytic activity of the immobilized photocatalyst thin films.

7.2 Recommendations

7.2.1 Apparatuses

Some modifications to the methods and applications of the new approaches are recommended to expand the knowledge about the synthesized samples.

1) Photo-reactor

Maintaining the photocatalyst concentration at approximately 1 g L^{-1} for a reliable comparison with the results presented in the literature is essential. Due to the limited yield of the solid-state preparation and the large number of comparative studies, a center- or top-irradiated reactor with 300–400 mL in reaction volume is ideal. For the safety of the apparatus, a focused light beam can be provided by a light source installed in an appropriate lamp housing with a standard cooling system. The use of a top- or side-irradiated photo-reactor with focused irradiation makes the performance evaluation of photocatalyst panels simpler and more efficient. In addition, the use of cold mirrors at the bottom and side of the photo-reactor is recommended to minimize the differences between apparent and actual quantum efficiencies.

2) Light source

The most common light sources used in the literature are 450 W Hg lamps and 300 W Xe lamps, secured in a standard lamp housing and equipped with multiple cut-off filters. Applying these light sources would provide an in-depth understanding of the photocatalytic activity of the prepared samples through reliable comparison to those reported in the literature.

Photocatalytic tests under monochromic irradiation are recommended, as the comparison between photocatalyst action plots (photocatalytic activity versus incident photon's wavelength) and absorption spectrum would provide valuable information on the optical and electrochemical characteristics of the photocatalyst. In addition, measuring photocatalyst activity under simulated

solar irradiation at AM1.5G would be beneficial for further understanding the optical and photochemical properties of the prepared photocatalyst samples for broader applications

3) Photo-electrochemical (PEC) analysis

Although GaN:ZnO solid solution photocatalyst (particles or NWs) cannot be prepared on a conductive substrate through in-situ routes, their immobilization on ITO- or FTO-coated glass substrate with solution-based approaches (*e.g.* drop casting and spin coating) makes the PEC measurements possible. It should be noted that such approaches would be highly sensitive to the porosity of the deposited film, and its interaction with the conductive layer on the substrate.

PEC analysis is a versatile technique for evaluating a wide range of photo-electrochemical characteristics. Simple photocurrent-voltage and Mott–Schottky measurements would determine the density of the charge carriers, charge transportation mechanism, density of dopants, and surface states of the photocatalysts film. Moreover, in-situ optimization of hydrogen and oxygen evolution co-catalyst performance can be carried out through water electrolysis using the PEC configuration. Such measurements could provide valuable information about co-catalyst deposition, structure, reactive facets, and dispersion.

7.2.2 Fabrication

Several fabrication techniques were used in this research, and various class of GaN:ZnO photocatalysts including nanoporous particles, graphene-based composites, and 1-D nanostructures were introduced. To further study the characteristics of the synthesized samples, the following studies are recommended.

7.2.2.1 Nanoporous GaN:ZnO solid solution

1) Heating rate of the solid-state synthesis

The use of urea as the source of nitrogen exhibited enormous potential for the facile preparation of oxynitrides. Since urea decomposition kinetics and the density of the gaseous products depend on the pyrolysis heating rate and temperature, the use of effective heating equipment is important. In this research, a pre-heated muffle furnace was used to reach the highest possible heating rate. However, securing the precursor materials inside a pre-heated furnace takes ~15–30 s, which reduces the temperature by 90–130°C. The use of customized heated chambers or furnaces with considerably high heating rates, such as electrical furnaces (*e.g.* induction furnaces), is highly recommended.

2) Solid-state synthesis environment

The presence of oxygen during high temperature solid-state synthesis affects the surface states and chemistry of the synthesized photocatalyst. Performing the solid-state synthesis proposed in this research in a customized heated apparatus with a nearly zero concentration of oxygen could change the solid-state reaction path as well as the characteristics of the synthesized photocatalyst drastically. This approach was attempted for a few trials in the Ar environment, and the obtained results suggested an optimal synthesis temperature lower than the one identified in the presence of oxygen. Again, the use of heating apparatuses such as induction furnaces is highly recommended, given their ultra-high heating rate and well-controlled reaction environment.

3) Hydrothermal synthesis of Ga-Zn mix-metal precursor

The hydrothermal method is a versatile technique for preparing highly crystalline nanomaterials with uniform chemistries. Hydrothermal synthesis has been studied extensively for the preparation of semiconductor photocatalysts with a variety of morphologies and characteristics [304–314]. Lee et al. reported the significant impact of the precursors' crystallite size and crystallinity in controlling the composition and band gap energy of the GaN:ZnO photocatalyst

[71]. The photocatalyst synthesized by this technique reached the highest Zn-content ($x = 0.87$) reported for the GaN:ZnO powder in the open literature. The utilization of the hydrothermal method for fabrication of the Ga-Zn mix-metal crystallites as the starting materials for the preparation of nanoporous (through nitridation by urea) and traditional (through nitridation by ammonia) GaN:ZnO may lead to interesting characteristics and improvements in photocatalytic efficiencies.

4) GaN:ZnO nanosheets

Reducing the electron diffusion path to the surface of the photocatalyst has been studied through various morphology modification techniques. One effective approach is the preparation of photocatalysts in the form of nanosheets. 2-D materials have shown outstanding performance because of the exposed reactive facets on their edges or surfaces.

The layered structure of the crystalline LDH precursor can be exfoliated through various solution-based approaches that have been proposed in the literature [315–320] to positively charged mixed-metal hydroxide nanosheets. Nitridation of $\text{Ga}^{3+}\text{-Zn}^{2+}$ hydroxide nanosheets at an elevated temperature may result in ultra-thin GaN:ZnO nanosheets with improved photocatalytic activity.

7.2.2.2 Surface modification with co-catalyst materials

The effects of various co-catalyst materials on hydrogen and oxygen evolution were studied in this research. In the following section, a few recommendations are provided for better understanding the role of the active sites in the water splitting reaction and unwanted reverse formation of water.

1) Role of Cr_2O_3 in nanoporous photocatalyst

Our attempts at suppressing the hydrogen and oxygen back-reaction by applying a Cr₂O₃ shell on the HER co-catalyst core was unsuccessful. We have proposed a mechanism for reducing the overall water splitting activity in the presence of Cr-species. Further investigation on this subject may reveal the Cr-base film formation mechanism and allow the technique applied in this study to be modified for higher photocatalytic activity. Step-wise photo-deposition of core and shell materials can be further studied, while surface decoration can be performed in sacrificial solutions such as methanol or ethanol. Further, ex-situ approaches can be employed for surface decoration with well-defined noble metal core catalysts in order to narrow down the study to the Cr₂O₃ shell deposition.

2) Co-loading of HER and OER co-catalysts

The hydrogen and oxygen evolution tests indicated the adverse effect of co-catalysts co-loading on the overall water splitting efficiencies of the nanoporous photocatalysts. A mechanism based on the overlapping of the hydrogen and oxygen active evolution sites was proposed, and modifications to the deposition procedures were applied. Further investigation on the co-loading of the photocatalyst surface with HER and OER catalysts may address the lower-stoichiometry evolution of oxygen through effective transportation of surface trapped photo-excited holes to electrolytes, possibly improving the stability of the photocatalyst. Again, ex-situ deposition could be carried out to reduce the possibility of the HER and OER active sites overlapping.

3) Earth-abundant co-catalyst materials

Although photocatalysts decorated with noble metal co-catalysts exhibited high photocatalytic efficiencies, reducing the noble-metal content of the co-catalyst or replacing the noble-metal catalysts with cost-effective Earth-abundant materials is desired. Despite the extensive studies on water electrolysis, the utilization of abundant HER and OER catalysts for photocatalytic water

splitting has not been explored sufficiently. Investigating the potential of highly active Earth-abundant catalysts to facilitate the rate of hydrogen and oxygen evolution for the synthesized nanoporous GaN:ZnO photocatalyst is recommended. The atomic scale incorporation of these catalytic sites on the high surface area of the nanoporous photocatalyst may result in considerable improvements in overall water splitting activities, at a lower cost.

7.2.2.3 Hybridization with graphene oxide

A facile, yet effective solution mixing-sonication approach was applied in this research for the fabrication of GaN:ZnO-graphene composite. Advances in nanoscale fabrication in the last few years have resulted in powerful hybridization routes that can be applied for the preparation of graphene-based composites of the GaN:ZnO solid solution.

1) Ex-situ surface functionalization

We have proposed that the electrostatic self-assembly preparation of composite photocatalyst was triggered by the attraction between GaN:ZnO surface and negatively charged GO. To further enhance this attraction and improve the interaction between nanosheets and particles, the surface of the prepared GaN:ZnO solid solution can be functionalized with conductive linkers. General routes for the surface functionalization of semiconductor photocatalysts with positively charged molecules and polymers have been proposed in the literature [221,321], which can be readily applied to the GaN:ZnO solid solution photocatalyst.

In addition, hybridization of GaN:ZnO with various graphene derivatives such as graphene quantum dots (QDs) may extend the light absorption of the composite photocatalyst and suppress its deactivation through the decomposition of unwanted surface compounds at the reactive edges of QDs.

2) In-situ crystallization

As stated earlier, Ga-Zn nanocrystallites can be prepared through hydrothermal synthesis. The incorporation of GO in this process leads to simultaneous in-situ growth of nanocrystallites on the surface of the nanosheets and a reduction of GO. The GaN:ZnO nanocrystallites in composite with N-doped graphene can be obtained by nitridation of the Ga-Zn precursor-rGO composite. In-situ growth of Ga-Zn nanocrystallites would potentially provide stable and effective interfacial contact between components of the final composite, supporting fast charge separation. An example of this approach was proposed very recently by Li et al., resulting in a 4.5-times improvement in photocatalytic hydrogen evolution [136].

3) Layered composite of GaN:ZnO-graphene

The preparation of positively charged Ga-Zn nanosheets can be realized through the approach proposed in 0. Self-assembly of these nanosheets into graphene oxide would ideally result in a layered composite structure with superior electrochemical interaction compared to its particulate counterparts. The composite of GaN:ZnO and highly reactive and conductive N-doped graphene can be obtained via high temperature treatment of oxy-hydroxide layered composite in a reductive NH_3 environment. Similar examples of such structures for photocatalysts such as TiO_2 and g- C_3N_4 have demonstrated outstanding performance, owing to their thoughtful designs and fabrication at the nanoscale [132,322].

7.2.2.4 Fabrication of 1-D GaN:ZnO

A number of approaches were studied in this research for the fabrication of GaN:ZnO thin film, with an emphasis placed on the APCVD method. In the following section, a few recommendations for the modification of the studied approaches and the development of new strategies are presented.

1) Surface modification of ZnO NWs with Ga³⁺ and solution-based growth of Ga-Zn nanowire

Two approaches based on the solution-based modification and growth were investigated for the fabrication of GaZnON NWs. The prepared ZnO NWs were used as the template for Ga³⁺ species, and the direct growth of Zn-Ga NWs under mild conditions was attempted. Although the primary results presented in this study did not imply successful preparation of compositionally or morphologically uniform GaZnON NWs, further investigation and optimization of the procedures are highly recommended. The effect of various Ga and Zn salts, surface decoration techniques, morphology control reagents, crystalline seed layers (thickness and orientation), and growth conditions (temperature and concentration) could be investigated extensively for the development of versatile fabrication routes under mild conditions.

2) Vacuum CVD growth of GaN:ZnO

As demonstrated in this study, GaN:ZnO nanostructures with 1-D morphologies can be synthesized via APCVD growth. The growth mechanism we have proposed in this research reflects the significant impact of the growth temperature and local vapour pressure of gaseous products on the morphology and chemistry of the thin film. We have shown that these factors can change the aspect ratio of the synthesized nanostructures by orders of magnitude (from NWs to NFs). Since the concentration of the building blocks at a certain growth temperature is determined by the operating pressure, vacuum CVD growth may have altered the growth mechanism proposed in this study, affecting the morphologies, dimensions, compositions, and eventually the photocatalytic activities of the synthesized nanostructures significantly.

3) Use of pre-synthesized gold NPs as the CVD catalyst material

Gold thin film was used in this research to produce catalyst nanoparticles for the growth of GaN:ZnO NWs and NFs. As demonstrated here, the size distribution of the CVD catalyst significantly affects the morphology of the synthesized thin film. In our opinion, the utilization of pre-synthesized Au NPs (in the form of colloidal solution) with a well-defined size and structure would considerably improve the quality of the thin film, and therefore is highly recommended for this study.

4) Wafer-scale growth

The large-scale growth of nanostructures through CVD is a challenging task. Our experimental results suggested a uniform growth of GaN:ZnO thin film on the surface of Si substrate at the centimeter-scale. Further investigation of the capability of the proposed technique for wafer-scale (inches) growth is recommended.

7.2.3 Photocatalytic performances

Despite the extensive material characterization carried out in this research, the causes of some photocatalytic performances are not fully understood. In the following, recommendations are provided to address this matter.

1) Instability of nanoporous GaN:ZnO solid solution

An oxygen evolution rate lower than the expected water splitting stoichiometry and termination of the overall water splitting were observed for nanoporous GaN:ZnO photocatalyst. Four mechanisms were proposed based on the data obtained from the material characterizations, activity tests, and materials in the literature. The origin of photocatalyst instability can be further investigated by 1) PEC analysis to identify the charge transfer mechanism, surface states, and dopant densities; 2) extensive surface characterization of spent photocatalyst at various stages of

the water splitting reaction through XPS, TEM, EDX, and SEM analysis ;3) characterization and performance evaluation of the nanoporous photocatalyst treated under ammonia at an elevated temperature; and 4) study of the effect of pH (particularly acidic) on the characteristics of the spent photocatalyst. The obtained data could be utilized for the development of a deactivation scenario. In addition, the implementation of various photocatalyst stabilization strategies proposed in the literature, such as techniques based on protection layers (*e.g.* amorphous Si-Ti oxy-hydroxide film [103]) is recommended.

2) Low photocatalytic activity of GaN:ZnO nanofibers

The preparation of NF semiconductors is very challenging yet highly desired due to their unique morphologies, which offer a number of advantages, such as a short charge diffusion path and high surface area. However, the GaN:ZnO NFs prepared in this research exhibited the lowest photocatalytic activity among the immobilized samples. It is hypothesized that the low activity of NF photocatalysts is attributed to their composition, structure, and morphology. Investigation of these causes, particularly through electrochemical measurements and post-material characterizations, is highly recommended. The obtained information may lead to the fabrication of highly active immobilized photocatalyst materials.

3) Effect of operating pressure and temperature

Temperature and pressure can significantly affect not only the half reaction potential but also the mechanism of the processes that occur during the water splitting reaction, such as the rate of undesired back-reaction as well as the transfer of photo-induced electrons at the photocatalyst–electrolyte interface. Studying the effect of operating conditions would provide valuable information regarding the operating temperature.

Bibliography

- [1] N.S. Lewis, D.G. Nocera, *Proc. Natl. Acad. Sci.* 103 (2006) 15729–15735.
- [2] N.S. Lewis, G. Crabtree, A.J. Nozik, M.R. Wasielewski, P. Alivisatos, H. Kung, J. Tsao, E. Chandler, W. Walukiewicz, M. Spitler, R. Ellingson, R. Overend, J. Mazer, M. Gress, J. Horwitz, C. Ashton, B. Herndon, L. Shapard, R.M. Nault, Basic Research Needs for Solar Energy Utilization. Report of the Basic Energy Sciences Workshop on Solar Energy Utilization, April 18-21, 2005, US Department of Energy, Office of Basic Energy Science, 2005.
- [3] D.G. Nocera, *Chem. Soc. Rev.* 38 (2009) 13–15.
- [4] H. Slater, *Renew. ENERGY WORLD.CoM* (2013).
- [5] E. Drury, A. Lopez, P. Denholm, R. Margolis, *Prog. Photovoltaics Res. Appl.* 22 (2014) 1302–1315.
- [6] N. Armaroli, V. Balzani, *Chem. - A Eur. J.* 22 (2016) 32–57.
- [7] G.W. Crabtree, N.S. Lewis, *Phys. Today* 60 (2007) 37–42.
- [8] M.G. Walter, E.L. Warren, J.R. McKone, S.W. Boettcher, Q. Mi, E.A. Santori, N.S. Lewis, *Chem. Rev.* 110 (2010) 6446–6473.
- [9] B. Adeli, F. Taghipour, *ECS J. Solid State Sci. Technol.* 2 (2013) Q118–Q126.
- [10] A. Kubacka, M. Fernández-García, G. Colón, *Chem. Rev.* 112 (2012) 1555–1614.
- [11] A. Kudo, Y. Miseki, *Chem. Soc. Rev.* 38 (2009) 253–278.
- [12] M. Pelaez, N.T. Nolan, S.C. Pillai, M.K. Seery, P. Falaras, A.G. Kontos, P.S.M. Dunlop, J.W.J. Hamilton, J.A. Byrne, K. O’Shea, M.H. Entezari, D.D. Dionysiou, *Appl. Catal. B Environ.* 125 (2012) 331–349.
- [13] A. Rachel, M. Subrahmanyam, P. Boule, *Appl. Catal. B Environ.* 37 (2002) 301–308.

- [14] R.J. Braham, A.T. Harris, *Ind. Eng. Chem. Res.* 48 (2009) 8890–8905.
- [15] Q. Xiang, B. Cheng, J. Yu, *Angew. Chemie - Int. Ed.* 54 (2015) 11350–11366.
- [16] P. Ji, M. Takeuchi, T.M. Cuong, J. Zhang, M. Matsuoka, M. Anpo, *Res. Chem. Intermed.* 36 (2010) 327–347.
- [17] X. Chen, S. Shen, L. Guo, S.S. Mao, *Chem. Rev.* 110 (2010) 6503–6570.
- [18] K. Takanahe, K. Domen, *Green 1* (2011) 313–322.
- [19] H. Zhou, Y. Qu, T. Zeid, X. Duan, *Energy Environ. Sci.* 5 (2012) 6732.
- [20] M. Kitano, M. Hara, *J. Mater. Chem.* 20 (2010) 627–641.
- [21] a Fujishima, K. Honda, *Nature* 238 (1972) 37–38.
- [22] H. Ahmad, S.K. Kamarudin, L.J. Minggu, M. Kassim, *Renew. Sustain. Energy Rev.* 43 (2015) 599–610.
- [23] J. Li, N. Wu, *Catal. Sci. Technol.* 5 (2015) 1360–1384.
- [24] M.V.B. George W. Crabtree, Mildred S. Dresselhaus, *Phys. Today* 57 (2004) 39–44.
- [25] K. Maeda, T. Takata, M. Hara, N. Saito, Y. Inoue, H. Kobayashi, K. Domen, *J. Am. Chem. Soc.* 127 (2005) 8286–8287.
- [26] K. Maeda, K. Teramura, D. Lu, T. Takata, N. Saito, Y. Inoue, K. Domen, *Nature* 440 (2006) 295–295.
- [27] K. Maeda, K. Teramura, T. Takata, M. Hara, N. Saito, K. Toda, Y. Inoue, H. Kobayashi, K. Domen, *J. Phys. Chem. B* 109 (2005) 20504–20510.
- [28] S.C. Lyu, O.H. Cha, E.K. Suh, H. Ruh, H.J. Lee, C.J. Lee, *Chem. Phys. Lett.* 367 (2003) 136–140.
- [29] Q.N. Abdullah, F.K. Yam, N.K. Hassan, M.A. Qeed, K. Al-Heuseen, M. Bououdina, Z. Hassan, *Ceram. Int.* 40 (2014) 9563–9569.

- [30] W. Wei, Y. Dai, K. Yang, M. Guo, B. Huang, *J. Phys. Chem. C* (2008) 15915–15919.
- [31] Q.Z. Liu, S.S. Lau, *Solid. State. Electron.* 42 (1998) 677–691.
- [32] F.A. Ponce, D.P. Bour, *Nature* 386 (1997) 351–359.
- [33] S.S. Kocha, M.W. Peterson, D.J. Arent, J.M. Redwing, M.A. Tischler, J.A. Turner, *J. Electrochem. Soc.* 142 (1995) L238.
- [34] I.M. Huygens, K. Strubbe, W.P. Gomes, *J. Electrochem. Soc.* 147 (2000) 1797.
- [35] H.J. Kim, J. Park, B.U. Ye, C.J. Yoo, J.L. Lee, S.W. Ryu, H. Lee, K.J. Choi, J.M. Baik, *ACS Appl. Mater. Interfaces* 8 (2016) 18201–18207.
- [36] N. Arai, N. Saito, H. Nishiyama, Y. Inoue, K. Domen, K. Sato, *Chem. Lett.* 35 (2006) 796–797.
- [37] K. Maeda, K. Teramura, N. Saito, Y. Inoue, K. Domen, *Bull. Chem. Soc. Jpn.* 80 (2007) 1004–1010.
- [38] D. Wang, A. Pierre, M.G. Kibria, K. Cui, X. Han, K.H. Bevan, H. Guo, S. Paradis, A.R. Hakima, Z. Mi, *Nano Lett.* 11 (2011) 2353–2357.
- [39] M.G. Kibria, H.P.T. Nguyen, K. Cui, S. Zhao, D. Liu, H. Guo, M.L. Trudeau, S. Paradis, A.R. Hakima, Z. Mi, *ACS Nano* 7 (2013) 7886–7893.
- [40] B. Alotaibi, H.P.T. Nguyen, S. Zhao, M.G. Kibria, S. Fan, Z. Mi, *Nano Lett.* 13 (2013) 4356–4361.
- [41] M.G. Kibria, F.A. Chowdhury, S. Zhao, B. Alotaibi, M.L. Trudeau, H. Guo, Z. Mi, *Nat Commun* 6 (2015) 6797.
- [42] M.G. Kibria, S. Zhao, F.A. Chowdhury, Q. Wang, H.P. Nguyen, M.L. Trudeau, H. Guo, Z. Mi, *Nat Commun* 5 (2014) 3825.
- [43] M.G. Kibria, F.A. Chowdhury, S. Zhao, M.L. Trudeau, H. Guo, Z. Mi, *Appl. Phys. Lett.*

- 106 (2015) 113105.
- [44] H. Le, S. Chua, E. Fitzgerald, K. Loh, ZnO Nanorods Grown on P-GaN Using Hydrothermal Synthesis and Its Optoelectronic Devices Application, 2007.
- [45] Y. Zhang, M.K. Ram, E.K. Stefanakos, D.Y. Goswami, J. Nanomater. 2012 (2012) 1–22.
- [46] D.-K. Hwang, M.-S. Oh, J.-H. Lim, S.-J. Park, J. Phys. D. Appl. Phys. 40 (2007) R387–R412.
- [47] M.-J. Chen, J.-R. Yang, M. Shiojiri, Semicond. Sci. Technol. 27 (2012) 74005.
- [48] Y.S. Choi, J.W. Kang, D.K. Hwang, S.J. Park, IEEE Trans. Electron Devices 57 (2010) 26–41.
- [49] C. Zhang, M. Shao, F. Ning, S. Xu, Z. Li, M. Wei, D.G. Evans, X. Duan, Nano Energy 12 (2015) 231–239.
- [50] X. Zhang, Y. Liu, Z. Kang, ACS Appl. Mater. Interfaces 6 (2014) 4480–4489.
- [51] T. Wang, R. Lv, P. Zhang, C. Li, J. Gong, Nanoscale 0 (2014) 1–5.
- [52] S.R. Kadam, V.R. Mate, R.P. Panmand, L.K. Nikam, M. V Kulkarni, R.S. Sonawane, B.B. Kale, RSC Adv. 4 (2014) 60626–60635.
- [53] Y. Wei, L. Ke, J. Kong, H. Liu, Z. Jiao, X. Lu, H. Du, X.W. Sun, Nanotechnology 23 (2012) 235401.
- [54] C. Han, M.-Q. Yang, B. Weng, Y.-J. Xu, Phys. Chem. Chem. Phys. 16 (2014) 16891–16903.
- [55] H. Fu, T. Xu, S. Zhu, Y. Zhu, Environ. Sci. Technol. 42 (2008) 8064–8069.
- [56] Z. Liwu, C. Hanyun, Z. Ruilong, Z. Yongfa, J. Phys. Chem. C 113 (2009) 2368–2374.
- [57] Wurtzite Cryst. Struct. - Wikipedia, Free Encycl. (n.d.)
http://en.wikipedia.org/wiki/Wurtzite_crystal_stru.

- [58] X. Duan, C.M. Lieber, *J. Am. Chem. Soc.* 122 (2000) 188–189.
- [59] S. Maensiri, P. Laokul, V. Promarak, *J. Cryst. Growth* 289 (2006) 102–106.
- [60] M. Yang, Q. Huang, X. Jin, *Solid State Sci.* 14 (2012) 465–470.
- [61] S. Yan, Z. Wang, Z. Li, Z. Zou, *J. Mater. Chem.* 21 (2011) 5682.
- [62] J. Li, B. Liu, W. Yang, Y. Cho, X. Zhang, B. Dierre, T. Sekiguchi, A. Wu, X. Jiang, *Nanoscale* 8 (2016) 3694–3703.
- [63] J. Wang, B. Huang, Z. Wang, P. Wang, H. Cheng, Z. Zheng, X. Qin, X. Zhang, Y. Dai, M.-H. Whangbo, *J. Mater. Chem.* 21 (2011) 4562.
- [64] W.Q. Han, Y. Zhang, C.Y. Nam, C.T. Black, E.E. Mendez, *Appl. Phys. Lett.* 97 (2010) 83108.
- [65] B. Adeli, F. Taghipour, *Appl. Catal. A Gen.* 521 (2016) 250–258.
- [66] H.L. Shi, Y. Duan, *Eur. Phys. J. B* 66 (2008) 439–444.
- [67] Y. Lee, H. Terashima, Y. Shimodaira, K. Teramura, M. Hara, H. Kobayashi, K. Domen, M. Yashima, *J. Phys. Chem. C* 111 (2007) 1042–1048.
- [68] S.H. Wei, A. Zunger, *Phys. Rev. B* 37 (1988) 8958–8981.
- [69] K. Maeda, K. Domen, *J. Phys. Chem. C* 111 (2007) 7851–7861.
- [70] K. Maeda, K. Domen, *Chem. Mater.* 22 (2010) 612–623.
- [71] K. Lee, B.M. Tienes, M.B. Wilker, K.J. Schnitzenbaumer, G. Dukovic, *Nano Lett.* 12 (2012) 3268–3272.
- [72] E.J. McDermott, E.Z. Kurmaev, T.D. Boyko, L.D. Finkelstein, R.J. Green, K. Maeda, K. Domen, A. Moewes, *J. Phys. Chem. C* 116 (2012) 7694–7700.
- [73] Z. Wang, J. Wang, J. Hou, K. Huang, S. Jiao, H. Zhu, *Mater. Res. Bull.* 47 (2012) 3605–3611.

- [74] H. Chen, W. Wen, Q. Wang, J.C. Hanson, J.T. Muckerman, E. Fujita, A.I. Frenkel, J.A. Rodriguez, *J. Phys. Chem. C* 113 (2009) 3650–3659.
- [75] H. Chen, L. Wang, J. Bai, J.C. Hanson, J.B. Warren, J.T. Muckerman, E. Fujita, J.A. Rodriguez, *J. Phys. Chem. C* 114 (2010) 1809–1814.
- [76] S.S. Menon, B. Kuppulingam, R. Ramesh, K. Baskar, S. Singh, *Adv. Sci. Lett.* 20 (2014) 1094–1097.
- [77] T. Takata, C. Pan, K. Domen, *Sci. Technol. Adv. Mater.* 16 (2015) 33506.
- [78] T. Takata, C. Pan, K. Domen, *ChemElectroChem* 3 (2016) 31–37.
- [79] S.C. Yan, S.X. Ouyang, J. Gao, M. Yang, J.Y. Feng, X.X. Fan, L.J. Wan, Z.S. Li, J.H. Ye, Y. Zhou, Z.G. Zou, *Angew. Chemie - Int. Ed.* 49 (2010) 6400–6404.
- [80] T. Hisatomi, K. Maeda, D. Lu, K. Domen, *ChemSusChem* 2 (2009) 336–343.
- [81] A.I. Khan, D. O’Hare, *J. Mater. Chem.* 12 (2002) 3191–3198.
- [82] F. Li, X. Duan, *Struct. Bond.* 119 (2005) 193–223.
- [83] G. Fan, F. Li, D.G. Evans, X. Duan, *Chem. Soc. Rev.* 43 (2014) 7040–7066.
- [84] F. Leroux, J. Besse, *Chem. Mater.* 13 (2001) 3507–3515.
- [85] V. Prévot, C. Forano, J.P. Besse, *Appl. Clay Sci.* 18 (2001) 3–15.
- [86] M. Lakraimi, A. Legrouiri, A. Barroug, A. De Roy, J.P. Besse, *J. Mater. Chem.* 10 (2000) 1007–1011.
- [87] C.O. Kappe, D. Dallinger, *Nat. Rev. Drug Discov.* 5 (2006) 51–63.
- [88] L. Perreux, A. Loupy, *Tetrahedron* 57 (2001) 9199–9223.
- [89] K. Maeda, K. Teramura, N. Saito, Y. Inoue, K. Domen, *J. Catal.* 243 (2006) 303–308.
- [90] J. Sato, N. Saito, Y. Yamada, K. Maeda, T. Takata, J.N. Kondo, M. Hara, H. Kobayashi, K. Domen, Y. Inoue, *J. Am. Chem. Soc.* 127 (2005) 4150–4151.

- [91] K. Maeda, K. Teramura, D. Lu, N. Saito, Y. Inoue, K. Domen, *Angew. Chemie - Int. Ed.* 45 (2006) 7806–7809.
- [92] Young-Jin Cho, Gun-hee Moon, Tomoki Kanazawa, Kazuhiko Maeda, Wonyong Choi, *Chem. Commun.* 52 (2016) 9636–9639.
- [93] J. Xu, C. Pan, T. Takata, K. Domen, *Chem. Commun.* 51 (2015) 7191–7194.
- [94] K. Maeda, K. Teramura, D. Lu, N. Saito, Y. Inoue, K. Domen, *J. Phys. Chem. C* 111 (2007) 7554–7560.
- [95] L. Delannoy, N. El Hassan, A. Musi, N.N. Le To, J.M. Krafft, C. Louis, *J. Phys. Chem. B* 110 (2006) 22471–22478.
- [96] M.N.S.M.R.B. Behnajady M.A., *Glob. Nest J.* 10 (2008) 1–7.
- [97] S.C. Chan, M.A. Barteau, *Langmuir* 21 (2005) 5588–5595.
- [98] G. Dukovic, M.G. Merkle, J.H. Nelson, S.M. Hughes, A.P. Alivisatos, *Adv. Mater.* 20 (2008) 4306–4311.
- [99] K. Maeda, N. Sakamoto, T. Ikeda, H. Ohtsuka, A. Xiong, D. Lu, M. Kanehara, T. Teranishi, K. Domen, *Chem. - A Eur. J.* 16 (2010) 7750–7759.
- [100] A. Xiong, T. Yoshinaga, T. Ikeda, M. Takashima, T. Hisatomi, K. Maeda, T. Setoyama, T. Teranishi, K. Domen, *Eur. J. Inorg. Chem.* (2014) 767–772.
- [101] K. Sayama, H. Arakawa, *J. Photochem. Photobiol. A Chem.* 94 (1996) 67–76.
- [102] R. Abe, K. Sayama, H. Arakawa, *Chem. Phys. Lett.* 371 (2003) 360–364.
- [103] C. Pan, T. Takata, M. Nakabayashi, T. Matsumoto, N. Shibata, Y. Ikuhara, K. Domen, *Angew. Chemie - Int. Ed.* 54 (2015) 2955–2959.
- [104] M. Yoshida, K. Takanabe, K. Maeda, A. Ishikawa, J. Kubota, Y. Sakata, Y. Ikezawa, K.

- Domen, J. Phys. Chem. C 113 (2009) 10151–10157.
- [105] K. Maeda, A. Xiong, T. Yoshinaga, T. Ikeda, N. Sakamoto, T. Hisatomi, M. Takashima, D. Lu, M. Kanehara, T. Setoyama, T. Teranishi, K. Domen, Angew. Chemie - Int. Ed. 49 (2010) 4096–4099.
- [106] C. Hahn, M.A. Fardy, C. Nguyen, M. Natera-Comte, S.C. Andrews, P.D. Yang, Isr. J. Chem. 52 (2012) 1111–1117.
- [107] Y. Tachibana, L. Vayssieres, J.R. Durrant, Nat. Photonics 6 (2012) 511–518.
- [108] Y. Lin, G. Yuan, S. Sheehan, S. Zhou, D. Wang, Energy Environ. Sci. 4 (2011) 4862.
- [109] T. Hisatomi, J. Kubota, K. Domen, Chem. Soc. Rev. 43 (2014) 7520–7535.
- [110] Q. Xiang, J. Yu, J. Phys. Chem. Lett. 4 (2013) 753–759.
- [111] X. An, J.C. Yu, RSC Adv. 1 (2011) 1426.
- [112] P. V. Kamat, J. Phys. Chem. Lett. 1 (2010) 520–527.
- [113] K.S.S. Novoselov, A.K.K. Geim, S.V. V Morozov, D. Jiang, Y. Zhang, S.V. V Dubonos, I.V. V Grigorieva, A.A.A. Firsov, Science (80-.). 306 (2004) 666–669.
- [114] Q. Xiang, J. Yu, M. Jaroniec, Chem. Soc. Rev. 41 (2012) 782.
- [115] M. Pumera, Energy Environ. Sci. 4 (2011) 668.
- [116] X. Huang, X. Qi, F. Boey, H. Zhang, Chem. Soc. Rev. 41 (2012) 666–686.
- [117] M. Inagaki, Y. a. Kim, M. Endo, J. Mater. Chem. 21 (2011) 3280.
- [118] K.P. Loh, Q. Bao, P.K. Ang, J. Yang, J. Mater. Chem. 20 (2010) 2277.
- [119] R.R. Nair, P. Blake, a. N. Grigorenko, K.S. Novoselov, T.J. Booth, T. Stauber, N.M.R. Peres, a. K. Geim, Science (80-.). 320 (2008) 2008.
- [120] S. Stankovich, D.A. Dikin, R.D. Piner, K.A. Kohlhaas, A. Kleinhammes, Y. Jia, Y. Wu, S.B.T. Nguyen, R.S. Ruoff, Carbon N. Y. 45 (2007) 1558–1565.

- [121] J. Ito, J. Nakamura, A. Natori, *J. Appl. Phys.* 103 (2008) 113712.
- [122] G. Lu, K. Yu, Z. Wen, J. Chen, *Nanoscale* 5 (2013) 1353.
- [123] W. Gao, *Graphene Oxide Reduct. Recipes, Spectrosc. Appl.* 39 (2015) 61–95.
- [124] P. Johari, V.B. Shenoy, *ACS Nano* 5 (2011) 7640–7647.
- [125] K.P. Loh, Q. Bao, G. Eda, M. Chhowalla, *Nat. Chem.* 2 (2010) 1015–1024.
- [126] Z. Zhang, J. Zhang, N. Chen, L. Qu, *Energy Environ. Sci.* 5 (2012) 8869.
- [127] X. Li, M. Rui, J. Song, Z. Shen, H. Zeng, *Adv. Funct. Mater.* 25 (2015) 4929–4947.
- [128] S. Yu, Y.-Q. Zhong, B.-Q. Yu, S.-Y.Y. Cai, L.-Z. Wu, Y. Zhou, *Phys. Chem. Chem. Phys.* 18 (2016) 20338–20344.
- [129] S. Stankovich, D.A. Dikin, G.H.B. Dommett, K.M. Kohlhaas, E.J. Zimney, E.A. Stach, R.D. Piner, S.T. Nguyen, R.S. Ruoff, *Nature* 442 (2006) 282–286.
- [130] N. Zhang, M.Q. Yang, S. Liu, Y. Sun, Y.J. Xu, *Chem. Rev.* 115 (2015) 10307–10377.
- [131] Y. Hou, Z. Wen, S. Cui, X. Feng, J. Chen, *Nano Lett.* 16 (2016) 2268–2277.
- [132] Y. Sun, C. Li, Y. Xu, H. Bai, Z. Yao, G. Shi, *Chem. Commun.* 46 (2010) 4740–4742.
- [133] S.S. Shinde, A. Sami, J.H. Lee, *Carbon N. Y.* 96 (2016) 929–936.
- [134] A. Mukherji, B. Seger, G.Q. Lu, L. Wang, *ACS Nano* 5 (2011) 3483–3492.
- [135] B. Adeli, F. Taghipour, *Chem. Eng. Technol.* 39 (2016) 142–148.
- [136] X. Li, Q. Zhang, H. Wang, Y. Li, *Appl. Surf. Sci.* 358 (2015) 57–62.
- [137] Y. Xia, P. Yang, Y. Sun, Y. Wu, B. Mayers, B. Gates, Y. Yin, F. Kim, H. Yan, *Adv. Mater.* 15 (2003) 353–389.
- [138] S. Hoang, P.X. Gao, *Adv. Energy Mater.* (2016) 1600683.
- [139] Y.J. Hwang, C. Hahn, B. Liu, P. Yang, *ACS Nano* 6 (2012) 5060–5069.
- [140] X. Pan, Y. Zhao, S. Liu, C.L. Korzeniewski, S. Wang, Z. Fan, *ACS Appl. Mater.*

- Interfaces 4 (2012) 3944–3950.
- [141] X. Cao, P. Chen, Y. Guo, J. Phys. Chem. C 112 (2008) 20560–20566.
- [142] L.E. Greene, M. Law, D.H. Tan, M. Montano, J. Goldberger, G. Somorjai, P. Yang, Nano Lett. 5 (2005) 1231–1236.
- [143] M.H. Huang, Y. Wu, H. Feick, N. Tran, E. Weber, P. Yang, Adv. Mater. 13 (2001) 113–116.
- [144] J. Goldberger, R.R. He, Y.F. Zhang, S.W. Lee, H.Q. Yan, H.J. Choi, P.D. Yang, Nature 422 (2003) 599–602.
- [145] X.M. Cai, A.B. Djurišić, M.H. Xie, Thin Solid Films 515 (2006) 984–989.
- [146] J.C. Wang, S.Q. Feng, D.P. Yu, Appl. Phys. A Mater. Sci. Process. 75 (2002) 691–693.
- [147] T. Kuykendall, P.J. Pauzauskie, Y. Zhang, J. Goldberger, D. Sirbuly, J. Denlinger, P. Yang, Nat. Mater. 3 (2004) 524–528.
- [148] C.H. Chiu, Z.Y. Li, C.L. Chao, M.H. Lo, H.C. Kuo, P.C. Yu, T.C. Lu, S.C. Wang, K.M. Lau, S.J. Cheng, J. Cryst. Growth 310 (2008) 5170–5174.
- [149] M.G. Kibria, H.P.T. Nguyen, K. Cui, S. Zhao, D. Liu, H. Guo, M.L. Trudeau, S. Paradis, A.R. Hakima, Z. Mi, ACS Nano 7 (2013) 7886–7893.
- [150] B. AlOtaibi, S. Fan, D. Wang, J. Ye, Z. Mi, ACS Catal. 5 (2015) 5342–5348.
- [151] C. Hahn, M.A. Fardy, C. Nguyen, M. Natera-Comte, S.C. Andrews, P.D. Yang, Isr. J. Chem. 52 (2012) 1111–1117.
- [152] M. Zhong, Y. Ma, P. Oleynikov, K. Domen, J.-J. Delaunay, Energy Environ. Sci. 7 (2014) 1693.
- [153] K. Maeda, K. Teramura, D. Lu, T. Takata, N. Saito, Y. Inoue, K. Domen, J. Phys. Chem. B 110 (2006) 13753–13758.

- [154] K. Maeda, K. Teramura, K. Domen, *J. Catal.* 254 (2008) 198–204.
- [155] W.S. Hummers, R.E. Offeman, *J. Am. Chem. Soc.* 80 (1958) 1339–1339.
- [156] M. Law, L.E. Greene, J.C. Johnson, R. Saykally, P. Yang, *Nat. Mater.* 4 (2005) 455–459.
- [157] R. Jenkins, J.L. de Vries, *X-Ray Spectrometry*, Marcel Dekker, 1971.
- [158] M. Lee, *X-RAY Diffr. Mater. Res. - From Fundam. to Appl.* (2016) 297.
- [159] I.I. Abu, K.J. Smith, *J. Catal.* 241 (2006) 356–366.
- [160] Meas. Serv. Div. Natl. Inst. Stand. Technol. (n.d.).
- [161] R. López, R. Gómez, *J. Sol-Gel Sci. Technol.* 61 (2012) 1–7.
- [162] W.Q. Han, Z. Liu, H.G. Yu, *Appl. Phys. Lett.* 96 (2010) 183112.
- [163] L. Zhao, G. Chen, Y. Zhou, Y. Yu, Q. Yu, Q. He, *Mater. Lett.* 128 (2014) 319–321.
- [164] H. Chen, L. Wang, J. Bai, J.C. Hanson, J.B. Warren, J.T. Muckerman, E. Fujita, J.A. Rodriguez, *J. Phys. Chem. C* 114 (2010) 1809–1814.
- [165] Y. Qiu, L. Gao, *J. Am. Ceram. Soc.* 87 (2004) 352–357.
- [166] C. Giordano, C. Erpen, W. Yao, B. Milke, M. Antonietti, *Chem. Mater.* 21 (2009) 5136–5144.
- [167] Y. Qiu, L.G. Å, *Chem. Lett.* 32 (2003) 774–775.
- [168] J. Buha, I. Djerdj, M. Antonietti, M. Niederberger, *Chem. Mater.* 19 (2007) 3499–3505.
- [169] Y. Zhang, J. Liu, G. Wu, W. Chen, *Nanoscale* 4 (2012) 5300.
- [170] J. Liu, T. Zhang, Z. Wang, G. Dawson, W. Chen, *J. Mater. Chem.* 21 (2011) 14398.
- [171] P.M. Schaber, J. Colson, S. Higgins, D. Thielen, B. Anspach, J. Brauer, *Thermochim. Acta* 424 (2004) 131–142.
- [172] A. Lundström, B. Andersson, L. Olsson, *Chem. Eng. J.* 150 (2009) 544–550.
- [173] N.K. Raman, M.T. Anderson, C.J. Brinker, *Chem. Mater.* 8 (1996) 1682–1701.

- [174] J. Liu, Y. Liu, N. Liu, Y. Han, X. Zhang, H. Huang, Y. Lifshitz, S.-T. Lee, J. Zhong, Z. Kang, *Science* (80-.). 347 (2015) 970–974.
- [175] A.G. Agrios, P. Pichat, *J. Photochem. Photobiol. A Chem.* 180 (2006) 130–135.
- [176] Q. Dong, Y. Fang, Y. Shao, P. Mulligan, J. Qiu, L. Cao, J. Huang, *Science* (80-.). 347 (2015) 967–970.
- [177] F. Li, X. Duan, *Struct. Bond.* 119 (2006) 193–223.
- [178] F. Yang, N.-N. Yan, S. Huang, Q. Sun, L.-Z. Zhang, Y. Yu, *J. Phys. Chem. C* 116 (2012) 9078–9084.
- [179] T.B. Nguyen, M.J. Hwang, K.S. Ryu, *Bull. Korean Chem. Soc.* 33 (2012) 243–247.
- [180] Y. Zhao, C. Li, X. Liu, F. Gu, H.L. Du, L. Shi, *Appl. Catal. B Environ.* 79 (2008) 208–215.
- [181] X. Liu, H. Bai, *Powder Technol.* 237 (2013) 610–615.
- [182] K. Shimura, H. Yoshida, *Phys. Chem. Chem. Phys.* 14 (2012) 2678–84.
- [183] X. Wang, S. Shen, S. Jin, J. Yang, M. Li, X. Wang, H. Han, C. Li, *Phys. Chem. Chem. Phys. Phys. Chem. Chem. Phys.* 15 (1938) 19380–19386.
- [184] S.R. Pendlebury, X. Wang, F. Le Formal, M. Cornuz, A. Kafizas, S.D. Tilley, M. Grätzel, J.R. Durrant, *J. Am. Chem. Soc.* 136 (2014) 9854–9857.
- [185] C. Wehrenfennig, G.E. Eperon, M.B. Johnston, H.J. Snaith, L.M. Herz, *Adv. Mater.* 26 (2014) 1584–1589.
- [186] T. Hirai, K. Maeda, M. Yoshida, J. Kubota, S. Ikeda, M. Matsumura, K. Domen, *J. Phys. Chem. C* 111 (2007) 18853–18855.
- [187] K. Maeda, K. Teramura, H. Masuda, T. Takata, N. Saito, Y. Inoue, K. Domen, *J. Phys. Chem. B* 110 (2006) 13107–13112.

- [188] Y. Zheng, L. Lin, B. Wang, X. Wang, *Angew. Chemie - Int. Ed.* 54 (2015) 12868–12884.
- [189] X. Wang, K. Maeda, A. Thomas, K. Takanabe, G. Xin, J.M. Carlsson, K. Domen, M. Antonietti, *Nat. Mater.* 8 (2009) 76–80.
- [190] X.-X. Zou, G.-D. Li, Y.-N. Wang, J. Zhao, C. Yan, M.-Y. Guo, L. Li, J.-S. Chen, *Chem. Commun. (Camb).* 47 (2011) 1066–1068.
- [191] Q. Su, J. Sun, J. Wang, Z. Yang, W. Cheng, S. Zhang, *Catal. Sci. Technol.* 4 (2014) 1556.
- [192] Y. Cui, J. Zhang, G. Zhang, J. Huang, P. Liu, M. Antonietti, X. Wang, *J. Mater. Chem.* 21 (2011) 13032.
- [193] A. Akhundi, A. Habibi-Yangjeh, *Appl. Surf. Sci.* 358 (2015) 261–269.
- [194] M. Ni, M.K.H. Leung, D.Y.C. Leung, K. Sumathy, *Renew. Sustain. Energy Rev.* 11 (2007) 401–425.
- [195] Y. Hu, X. Gao, L. Yu, Y. Wang, J. Ning, S. Xu, X.W. Lou, *Angew. Chemie - Int. Ed.* 52 (2013) 5636–5639.
- [196] Y. Tang, X. Hu, C. Liu, *Phys. Chem. Chem. Phys.* 16 (2014) 25321–9.
- [197] J. Zhu, M. Zäch, *Curr. Opin. Colloid Interface Sci.* 14 (2009) 260–269.
- [198] C. Pan, T. Takata, K. Domen, *Chem. - A Eur. J.* 22 (2016) 1854–1862.
- [199] M.G. Kibria, R. Qiao, W. Yang, I. Boukahil, X. Kong, F.A. Chowdhury, M.L. Trudeau, W. Ji, H. Guo, F.J. Himpsel, L. Vayssieres, Z. Mi, *Adv. Mater.* 28 (2016) 8388–8397.
- [200] J. Hou, H. Cheng, O. Takeda, H. Zhu, *Energy Environ. Sci.* 8 (2015) 1348–1357.
- [201] M. Higashi, K. Domen, R. Abe, *J. Am. Chem. Soc.* 134 (2012) 6968–6971.
- [202] T. Ohno, L. Bai, T. Hisatomi, K. Maeda, K. Domen, *J. Am. Chem. Soc.* 134 (2012) 8254–8259.
- [203] M. Matsumura, S. Furukawa, *J. Phys. Chem.* 89 (1985) 1983–1985.

- [204] M. Dinescu, P. Verardi, C. Boulmer-Leborgne, C. Gerardi, L. Mirengi, V. Sandu, *Appl. Surf. Sci.* 127–129 (1998) 559–563.
- [205] S.D. Wolter, B.P. Luther, D.L. Waltemyer, C. Önnby, S.E. Mohney, R.J. Molnar, *Appl. Phys. Lett.* 70 (1997) 2156.
- [206] L. Fu, Z. Liu, Y. Liu, B. Han, J. Wang, P. Hu, L. Cao, D. Zhu, *J. Phys. Chem. B* 108 (2004) 13074–13078.
- [207] A.L. Rudd, C.B. Breslin, *Electrochim. Acta* 45 (2000) 1571–1579.
- [208] H. Genscher, *J. Electrochem. Soc.* 113 (1966) 1174.
- [209] T.K. Zywiets, J. Neugebauer, M. Scheffler, *Appl. Phys. Lett.* 74 (1999) 1695.
- [210] R. Jones, J. Elsner, M. Haugk, R. Gutierrez, T. Frauenheim, M.I. Heggie, S. Öberg, P.R. Briddon, *Phys. Status Solidi* 171 (1999) 167–173.
- [211] A.F. Wright, *J. Appl. Phys.* 98 (2005) 103531.
- [212] J. Sato, N. Saito, Y. Yamada, K. Maeda, T. Takata, J.N. Kondo, M. Hara, H. Kobayashi, K. Domen, Y. Inoue, *J. Am. Chem. Soc.* 127 (2005) 4150–4151.
- [213] R. Kortlever, J. Shen, K.J.P. Schouten, F. Calle-Vallejo, M.T.M. Koper, *J. Phys. Chem. Lett.* 6 (2015) 4073–4082.
- [214] R. Schlögl, *Angew. Chemie - Int. Ed.* 54 (2015) 3465–3520.
- [215] A. Behranginia, M. Asadi, C. Liu, P. Yasaei, B. Kumar, P. Phillips, T. Foroozan, J.C. Waranius, K. Kim, J. Abiade, R.F. Klie, L.A. Curtiss, A. Salehi-Khojin, *Chem. Mater.* 28 (2016) 549–555.
- [216] Y. Li, J. Wang, X. Tian, L. Ma, C. Dai, C. Yang, Z. Zhou, *Nanoscale* 8 (2016) 1676–1683.
- [217] M. Carmo, D.L. Fritz, J. Mergel, D. Stolten, *Int. J. Hydrogen Energy* 38 (2013) 4901–

- 4934.
- [218] N. Mamaca, E. Mayousse, S. Arrii-Clacens, T.W. Napporn, K. Servat, N. Guillet, K.B. Kokoh, *Appl. Catal. B Environ.* 111–112 (2012) 376–380.
- [219] H. Fei, J. Dong, M.J. Arellano-Jiménez, G. Ye, N. Dong Kim, E.L.G. Samuel, Z. Peng, Z. Zhu, F. Qin, J. Bao, M.J. Yacaman, P.M. Ajayan, D. Chen, J.M. Tour, *Nat. Commun.* 6 (2015) 8668.
- [220] D. Mateo, I. Esteve-Adell, J. Albero, J.F.S. Royo, A. Primo, H. Garcia, *Nat. Commun.* 7 (2016) 11819.
- [221] S. Yang, X. Feng, S. Ivanovici, K. Müllen, *Angew. Chemie - Int. Ed.* 49 (2010) 8408–8411.
- [222] C.G. Vayenas, S. Bebelis, S. Ladas, *Nature* 343 (1990) 625–627.
- [223] J.J. Spivey, B. Rouge, *Metal Nanoparticles for Catalysis RSC Catal*, Royal Society of Chemistry, Cambridge, 2014.
- [224] J.R. (John R. Regalbuto, *Handbook of Catalyst Preparation*, Taylor & Francis, 2007.
- [225] L. Barthe, K. Philippot, B. Chaudret, N. Le Bolay, M. Hemati, *Powder Technol.* 257 (2014) 198–202.
- [226] S.E. Bozbağ, C. Erkey, *J. Supercrit. Fluids* 96 (2015) 298–312.
- [227] J. Yang, D. Wang, H. Han, C. Li, *Acc. Chem. Res.* 46 (2013) 1900–1909.
- [228] N. Sakamoto, H. Ohtsuka, T. Ikeda, K. Maeda, D. Lu, M. Kanehara, K. Teramura, T. Teranishi, K. Domen, *Nanoscale* 1 (2009) 106–9.
- [229] L. Fan, P.F. Liu, X. Yan, L. Gu, Z.Z. Yang, H.G. Yang, S. Qiu, X. Yao, *Nat. Commun.* 7 (2016) 10667.
- [230] J.-S. Li, Y. Wang, C.-H. Liu, S.-L. Li, Y.-G. Wang, L.-Z. Dong, Z.-H. Dai, Y.-F. Li, Y.-

- Q. Lan, *Nat. Commun.* 7 (2016) 11204.
- [231] X.-Z. Yuan, H. Wang, in: Springer London, London, 2008, pp. 1–329.
- [232] S. Vempati, T. Uyar, *Phys. Chem. Chem. Phys.* 16 (2014) 21183–21203.
- [233] A. Mathkar, D. Tozier, P. Cox, P. Ong, C. Galande, K. Balakrishnan, A. Leela Mohana Reddy, P.M. Ajayan, *J. Phys. Chem. Lett.* 3 (2012) 986–991.
- [234] P. Cui, J. Lee, E. Hwang, H. Lee, *Chem. Commun.* 47 (2011) 12370.
- [235] K. Zhang, Y. Zhang, S. Wang, *Sci. Rep.* 3 (2013) 3448-1–7.
- [236] X. Sun, Z. Liu, K. Welsher, J.T. Robinson, A. Goodwin, S. Zaric, H. Dai, *Nano Res* 1 (2008) 203–212.
- [237] Z. Liu, J.T. Robinson, X. Sun, H. Dai, *J. Am. Chem. Soc.* 130 (2008) 10876–10877.
- [238] Y. Liang, D. Wu, X. Feng, K. Müllen, *Adv. Mater.* 21 (2009) 1679–1683.
- [239] Y. Si, E.T. Samulski, *Nano Lett.* 8 (2008) 1679–1682.
- [240] H. He, C. Gao, *Chem. Mater.* 22 (2010) 5054–5064.
- [241] D. Li, M.B. Müller, S. Gilje, R.B. Kaner, G.G. Wallace, *Nat. Nanotechnol.* 3 (2008) 101–105.
- [242] L. Shahriary, A. a. Athawale, *Int. J. Renew. Energy Environ. Eng.* 2 (2014) 58–63.
- [243] L.Y. Meng, S.J. Park, *Bull. Korean Chem. Soc.* 33 (2012) 209–214.
- [244] M.H. Tran, C.S. Yang, S. Yang, I.J. Kim, H.K. Jeong, *Curr. Appl. Phys.* 14 (2014) S74–S79.
- [245] T.F. Yeh, C.Y. Teng, S.J. Chen, H. Teng, *Adv. Mater.* 26 (2014) 3297–3303.
- [246] Y. Tan, C. Xu, G. Chen, N. Zheng, Q. Xie, *Energy Environ. Sci.* 5 (2012) 6923.
- [247] G.-H. Nam, S.-H. Baek, C.-H. Cho, I.-K. Park, *Nanoscale* 6 (2014) 11653–8.
- [248] V.H. Pham, T.V. Cuong, S.H. Hur, E. Oh, E.J. Kim, E.W. Shin, J.S. Chung, *J. Mater.*

- Chem. 21 (2011) 3371–3377.
- [249] M. Law, J. Goldberger, P. Yang, *Annu. Rev. Mater. Res.* 34 (2004) 83–122.
- [250] H. Haug, S.W. (Stephan W.. Koch, *Quantum Theory of the Optical and Electronic Properties of Semiconductors*, World Scientific, 1994.
- [251] C. Kittel, P. McEuen, *Introduction to Solid State Physics*, Wiley, 1986.
- [252] G.G. Bessegato, T.T. Guaraldo, M.V.B. Zanoni, in: *Mod. Electrochem. Methods Nano, Surf. Corros. Sci.*, InTech, 2014, pp. 271–319.
- [253] A.I. Hochbaum, P. Yang, *Chem. Rev.* 110 (2010) 527–546.
- [254] F.E. Osterloh, *Chem. Soc. Rev.* 42 (2013) 2294–320.
- [255] J.M. Foley, M.J. Price, J.I. Feldblyum, S. Maldonado, *Energy Environ. Sci.* 5 (2012) 5203.
- [256] B. Liu, E.S. Aydil, *J. Am. Chem. Soc.* 131 (2009) 3985–3990.
- [257] Y. Zhou, G. Chen, Y. Yu, L. Zhao, Q. Yu, Q. He, *Catal. Sci. Technol.* 6 (2016) 1033–1041.
- [258] R. Feynman, R. Leighton, M. Sands, *The Feynman Lectures on Physics.*, Addison-Wesley, 2010.
- [259] R. Calarco, M. Marso, T. Richter, A.I. Aykanat, R. Meijers, A.V.D. Hart, T. Stoica, H. Luth, *Nano Lett.* 5 (2005) 981–984.
- [260] A. Fitch, N.C. Strandwitz, B.S. Brunschwig, N.S. Lewis, *J. Phys. Chem. C* 117 (2013) 2008–2015.
- [261] J. Bao, I. Shalish, Z. Su, R. Gurwitz, F. Capasso, X. Wang, Z. Ren, *Nanoscale Res. Lett.* 6 (2011) 404.
- [262] Y. Wu, H. Yan, M. Huang, B. Messer, J.H. Song, P. Yang, *Chemistry* 8 (2002) 1260–8.

- [263] R.G. Hobbs, N. Petkov, J.D. Holmes, *Chem. Mater.* 24 (2012) 1975–1991.
- [264] C. O'Regan, S. Biswas, N. Petkov, J.D. Holmes, *J. Mater. Chem. C* 2 (2014) 14.
- [265] K.S. Shankar, A.K. Raychaudhuri, *Mater. Sci. Eng. C* 25 (2005) 738–751.
- [266] G. Cao, D. Liu, *Adv. Colloid Interface Sci.* 136 (2008) 45–64.
- [267] I.W. Okpashi, V.E. Obi Bonaventure, C. Uchechukwu C Okoro, *J. Nanomed. Nanotechnol.* 6 (2015) 1–9.
- [268] S. Baruah, J. Dutta, *Sci. Technol. Adv. Mater.* 10 (2009) 13001.
- [269] Y. Sun, D.J. Riley, M.N.R. Ashford, *J. Phys. Chem. B* 110 (2006) 15186–15192.
- [270] H.O. Pierson, *Handbook of Chemical Vapor Deposition*, Noyes Publications, 1999.
- [271] Y. Wu, P. Yang, *J. Am. Chem. Soc.* 123 (2001) 3165–3166.
- [272] K.W. Kolasinski, *Curr. Opin. Solid State Mater. Sci.* 10 (2006) 182–191.
- [273] R.S. Wagner, W.C. Ellis, *Appl. Phys. Lett.* 4 (1964) 89–90.
- [274] E.I. Givargizov, *J. Cryst. Growth* 31 (1975) 20–30.
- [275] J.B. Baxter, E.S. Aydil, *J. Cryst. Growth* 274 (2005) 407–411.
- [276] S.-W. Kim, S. Fujita, S. Fujita, *Appl. Phys. Lett.* 86 (2005) 153119.
- [277] I. Levin, A. Davydov, B. Nikoobakht, N. Sanford, P. Mogilevsky, *Appl. Phys. Lett.* 87 (2005) 103110.
- [278] T.R. Kuykendall, M.V.P. Altoe, D.F. Ogletree, S. Aloni, *Nano Lett.* 14 (2014) 6767–6773.
- [279] V. Purushothaman, K. Jeganathan, *J. Nanoparticle Res.* 15 (2013) 1789.
- [280] J. Yang, J. Yoon, C. Kim, S. Hong, *Jpn. J. Appl. Phys.* 54 (2015) 02BD03.
- [281] S. Han, W. Jin, T. Tang, C. Li, D. Zhang, X. Liu, J. Han, C. Zhou, *J. Mater. Res.* 18 (2003) 245–249.
- [282] A. Dadgar, F. Schulze, M. Wienecke, A. Gadanez, J. Blasing, P. Veit, T. Hempel, A.

- Diez, J. Christen, A. Krost, *New J. Phys.* 9 (2007) 389–389.
- [283] T. Kuykendall, P. Ulrich, S. Aloni, P. Yang, *Nat. Mater.* 6 (2007) 951–956.
- [284] J. Westwater, *J. Vac. Sci. Technol. B Microelectron. Nanom. Struct.* 15 (1997) 554.
- [285] I. Zardo, L. Yu, S. Conesa-Boj, S. Estrade, P.J. Alet, J. Rossler, M. Frimmer, I.C.P. Roca, F. Peiro, J. Arbiol, J.R. Morante, I.M.A. Fontcuberta, *Nanotechnology* 20 (2009) 155602.
- [286] V. Zannier, V. Grillo, S. Rubini, *J. Phys. D. Appl. Phys.* 47 (2014) 394005.
- [287] J. Su, G. Cui, M. Gherasimova, H. Tsukamoto, J. Han, D. Ciuparu, S. Lim, L. Pfefferle, Y. He, A. V. Nurmikko, C. Broadbridge, A. Lehman, *Appl. Phys. Lett.* 86 (2005) 13105.
- [288] Y. Li, Y. Wang, S. Ryu, A.F. Marshall, W. Cai, P.C. McIntyre, *Nano Lett.* 16 (2016) 1713–1718.
- [289] S. V. Thombare, A.F. Marshall, P.C. McIntyre, *J. Appl. Phys.* 112 (2012) 54325.
- [290] K.A. Dick, S. Kodambaka, M.C. Reuter, K. Deppert, L. Samuelson, W. Seifert, L.R. Wallenberg, F.M. Ross, *Nano Lett.* 7 (2007) 1817–1822.
- [291] J.B. Hannon, S. Kodambaka, F.M. Ross, R.M. Tromp, *Nature* 440 (2006) 69–71.
- [292] Z. Ma, D. McDowell, E. Panaitescu, A. V Davydov, M. Upmanyu, L. Menon, *J. Mater. Chem. C* 1 (2013) 7294–7302.
- [293] O. Lupan, G. Chai, L. Chow, G.A. Emelchenko, H. Heinrich, V. V. Ursaki, A.N. Gruzintsev, I.M. Tiginyanu, A.N. Redkin, *Phys. Status Solidi Appl. Mater. Sci.* 207 (2010) 1735–1740.
- [294] J.-W. Zhao, Y.-F. Zhang, Y.-H. Li, C. Su, X.-M. Song, H. Yan, R.-Z. Wang, *Sci. Rep.* 5 (2015) 17692.
- [295] Q. Xiang, J. Yu, M. Jaroniec, *Nanoscale* 3 (2011) 3670–3678.
- [296] A. Moisala, a G. Nasibulin, E.I. Kauppinen, *J. Phys. - Condens. Matter* 15 (2003) S3011.

- [297] W. Lu, C.M. Lieber, *J. Phys. D. Appl. Phys.* 39 (2006) R387–R406.
- [298] L.C. Campos, M. Tonezzer, A.S. Ferlauto, V. Grillo, R. Magalhães-Paniago, S. Oliveira, L.O. Ladeira, R.G. Lacerda, *Adv. Mater.* 20 (2008) 1499–1504.
- [299] S. Chuangchote, J. Jitputti, T. Sagawa, S. Yoshikawa, *ACS Appl. Mater. Interfaces* 1 (2009) 1140–1143.
- [300] D. Lin, H. Wu, R. Zhang, W. Pan, *Chem. Mater.* 21 (2009) 3479–3484.
- [301] M.C. Wu, J. Hiltunen, A. Sapi, A. Avila, W. Larsson, H.C. Liao, M. Huuhtanen, G. Toth, A. Shchukarev, N. Laufer, . Kukovecz, Z. Konya, J.P. Mikkola, R. Keiski, W.F. Su, Y.F. Chen, H. Jantunen, P.M. Ajayan, R. Vajtai, K. Kordas, *ACS Nano* 5 (2011) 5025–5030.
- [302] N.C. Hildebrandt, J. Soldat, R. Marschall, *Small* 11 (2015) 2051–2057.
- [303] Z.L. Wang, *Mater. Today* 7 (2004) 26–33.
- [304] J. Ng, S. Xu, X. Zhang, H.Y. Yang, D.D. Sun, *Adv. Funct. Mater.* 20 (2010) 4287–4294.
- [305] B. Ma, F. Wen, H. Jiang, J. Yang, P. Ying, C. Li, *Catal. Letters* 134 (2010) 78–86.
- [306] R. Asai, H. Nemoto, Q. Jia, K. Saito, A. Iwase, A. Kudo, *Chem. Commun. (Camb)*. 50 (2014) 2543–6.
- [307] Y.C. Pu, G. Wang, K. Der Chang, Y. Ling, Y.K. Lin, B.C. Fitzmorris, C.M. Liu, X. Lu, Y. Tong, J.Z. Zhang, Y.J. Hsu, Y. Li, *Nano Lett.* 13 (2013) 3817–3823.
- [308] C. Liu, J. Tang, H.M. Chen, B. Liu, P. Yang, *Nano Lett.* 13 (2013) 2989–2992.
- [309] M. Shao, F. Ning, M. Wei, D.G. Evans, X. Duan, *Adv. Funct. Mater.* 24 (2014) 580–586.
- [310] H. Tuysuz, C.K. Chan, *Nano Energy* 2 (2013) 116–123.
- [311] L. Zhang, H. Bin Wu, Y. Yan, X. Wang, X.W. (David) Lou, *Energy Environ. Sci.* 7 (2014) 3302–3306.
- [312] J. Xu, X. Cao, *Chem. Eng. J.* 260 (2015) 642–648.

- [313] C.-C. Hu, T.-F. Yeh, H. Teng, *Catal. Sci. Technol.* 3 (2013) 1798.
- [314] X. Wang, M. Liu, Q. Chen, K. Zhang, J. Chen, M. Wang, P. Guo, L. Guo, *Int. J. Hydrogen Energy* 38 (2013) 13091–13096.
- [315] F. Song, X. Hu, *Nat. Commun.* 5 (2014) 1–9.
- [316] H. Liang, F. Meng, M. Cabán-Acevedo, L. Li, A. Forticaux, L. Xiu, Z. Wang, S. Jin, *Nano Lett.* 15 (2015) 1421–1427.
- [317] F. Song, X. Hu, *J. Am. Chem. Soc.* 136 (2014) 16481–16484.
- [318] J. Ping, Y. Wang, Q. Lu, B. Chen, J. Chen, Y. Huang, Q. Ma, C. Tan, J. Yang, X. Cao, Z. Wang, J. Wu, Y. Ying, H. Zhang, *Adv. Mater.* 28 (2016) 7640–7645.
- [319] Y. Hou, M.R. Lohe, J. Zhang, S. Liu, X. Zhuang, X. Feng, *Energy Environ. Sci.* 9 (2016) 478–483.
- [320] Z. Liu, R. Ma, M. Osada, N. Iyi, Y. Ebina, K. Takada, T. Sasaki, *J. Am. Chem. Soc.* 128 (2006) 4872–4880.
- [321] J. Liu, S. Fu, B. Yuan, Y. Li, Z. Deng, *J. Am. Chem. Soc.* 132 (2010) 7279–7281.
- [322] Q. Xiang, J. Yu, M. Jaroniec, *Nanoscale* 3 (2011) 3670–3678.

Appendices

Appendix A : Photo-reactor apparatuses

A.1 Center-irradiated photo-reactor

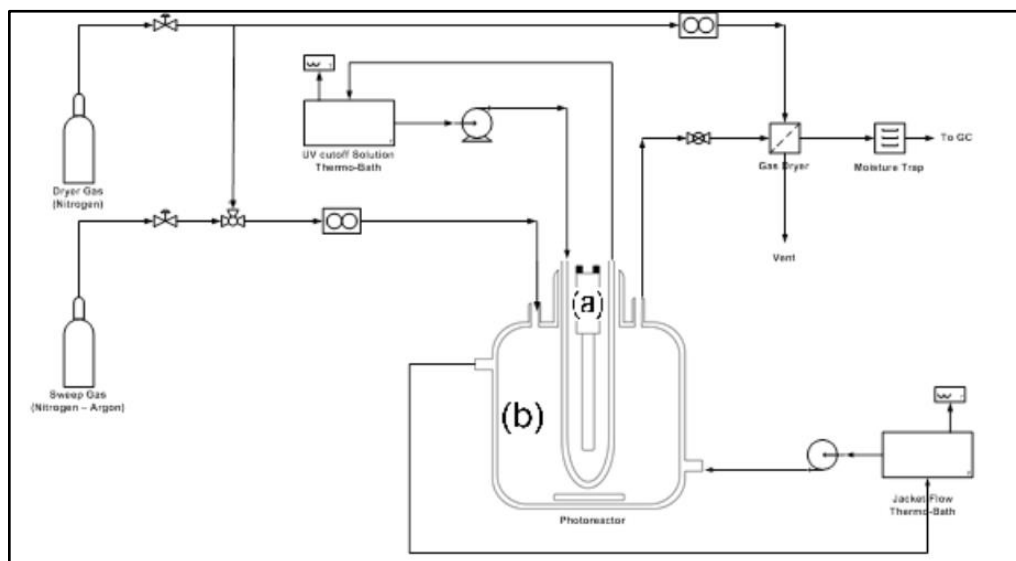


Figure A.7.1: Center-irradiated photo-reactor apparatus. (a) Light source and (b) 900 mL photo-reactor.

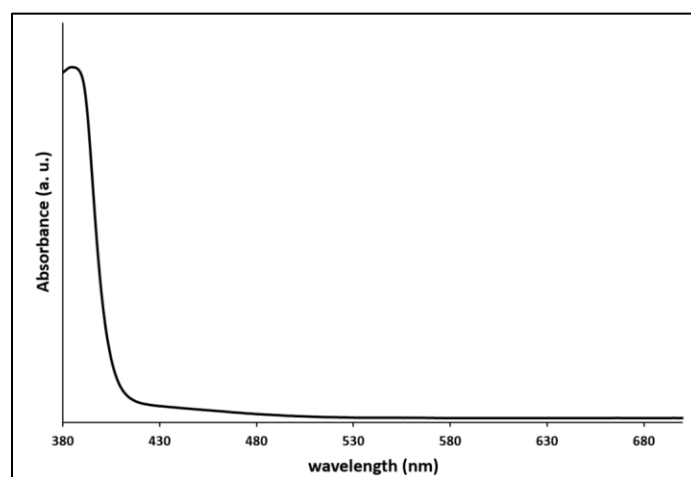


Figure A.7.2: UV-Vis absorption spectra of 2M NaNO₂.

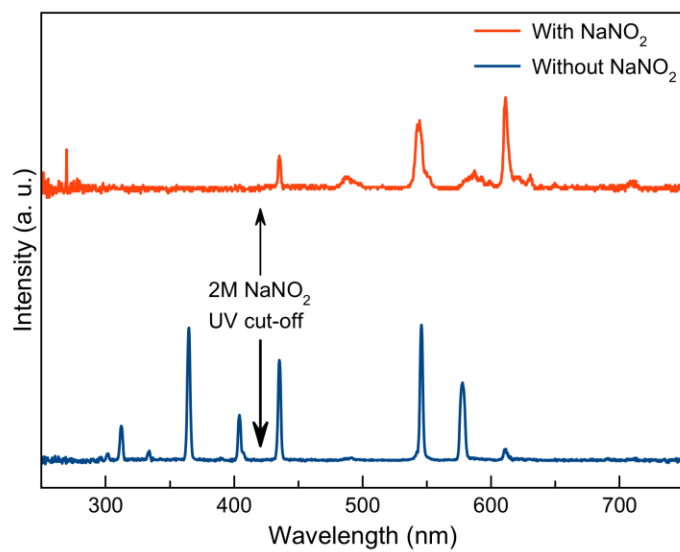


Figure A.7.3: UV-Vis output of the USHIO high pressure 100 W Hg lamp with and without use of the quartz sleeve and 2M NaNO₂ UV cut-off filter.

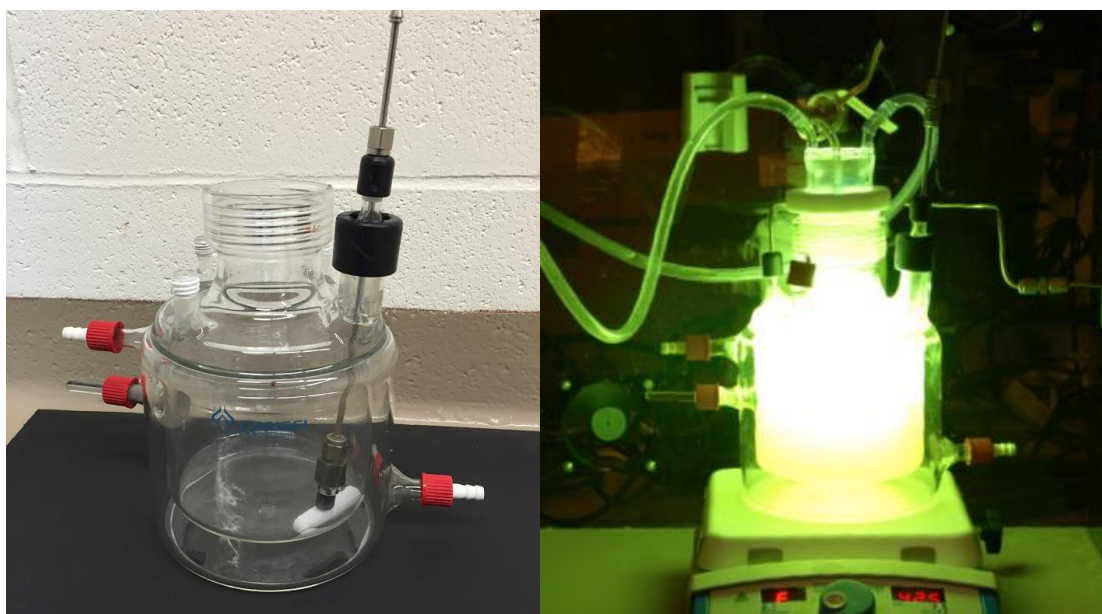


Figure A.7.4: Digital photo of the center-irradiated photo-reactor.

A.2 Pyrex side irradiated photo-reactor

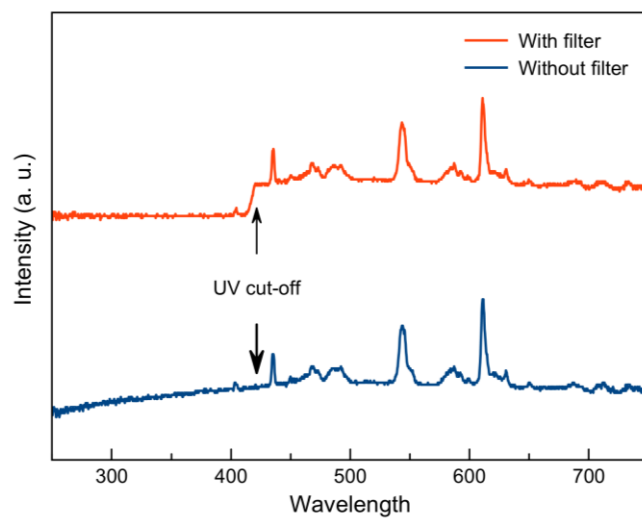


Figure A.7.5: UV-Vis output of the Osram XBO 75 W Xe lamp with and without use of the UV cut-off filter.

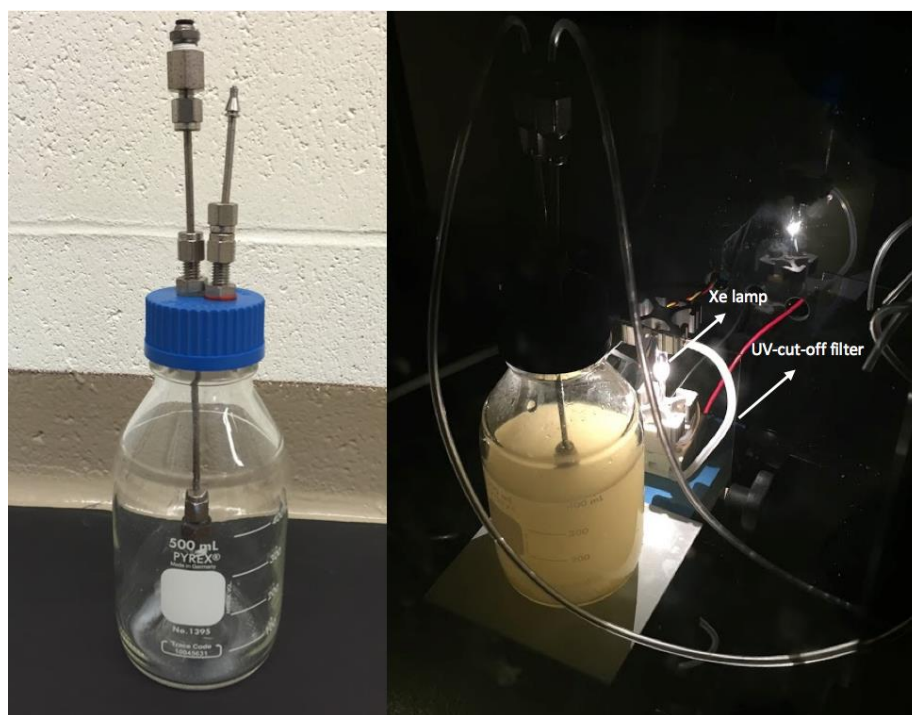


Figure A.7.6: The Pyrex side-irradiated photo-reactor.

A.3 Top irradiated photo-reactor

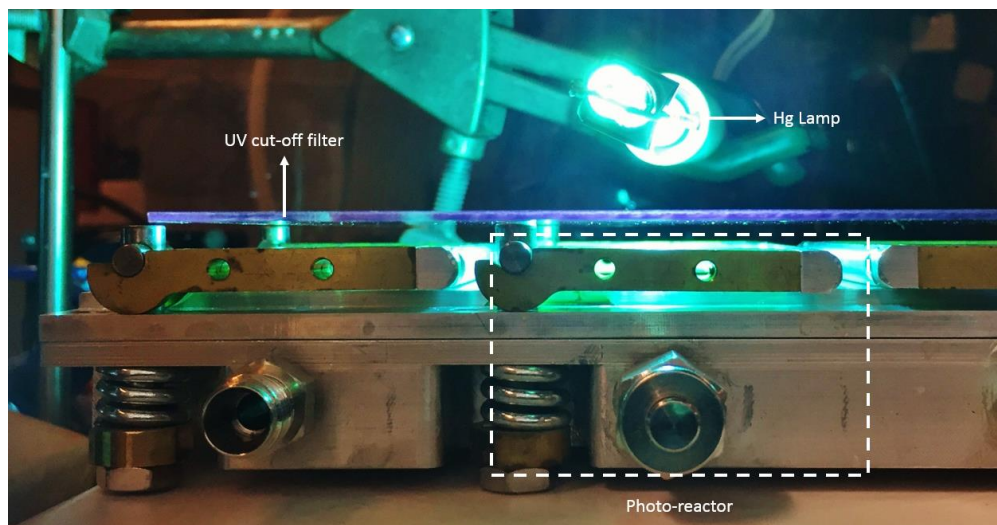


Figure A.7.7: Top-irradiated photo-reactor.

Appendix B : Microwave-assisted synthesis

B.1 Method

In a typical MW synthesis, stoichiometry amount of Ga_2O_3 and ZnO are mixed with appropriate amount of Zn and urea powders and ball-milled for 10 min, as described in 2.2.1.1. The prepaid precursor was loaded inside a 50 mL crucible, which was itself placed inside a 100 mL crucible, and the space between the two was filled with CuO as the heated medium. The crucibles were placed inside a domestic MW (Panasonic NN-SD671S) oven (on a fiberglass support) and treated under 600–1200 W for 6–15 min.

B.2 Photocatalytic performance

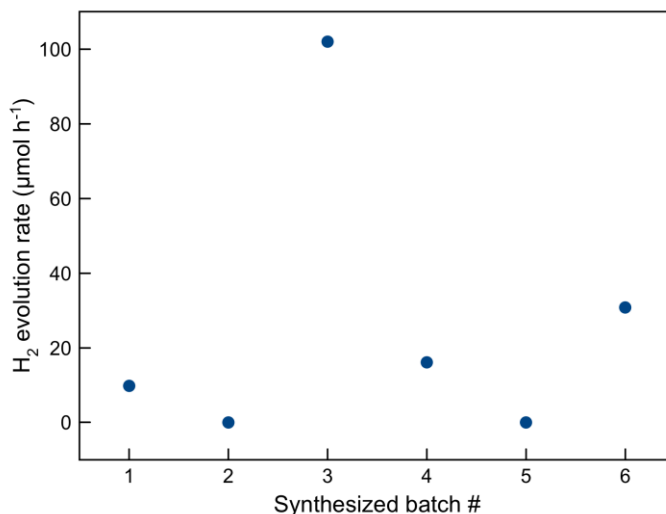
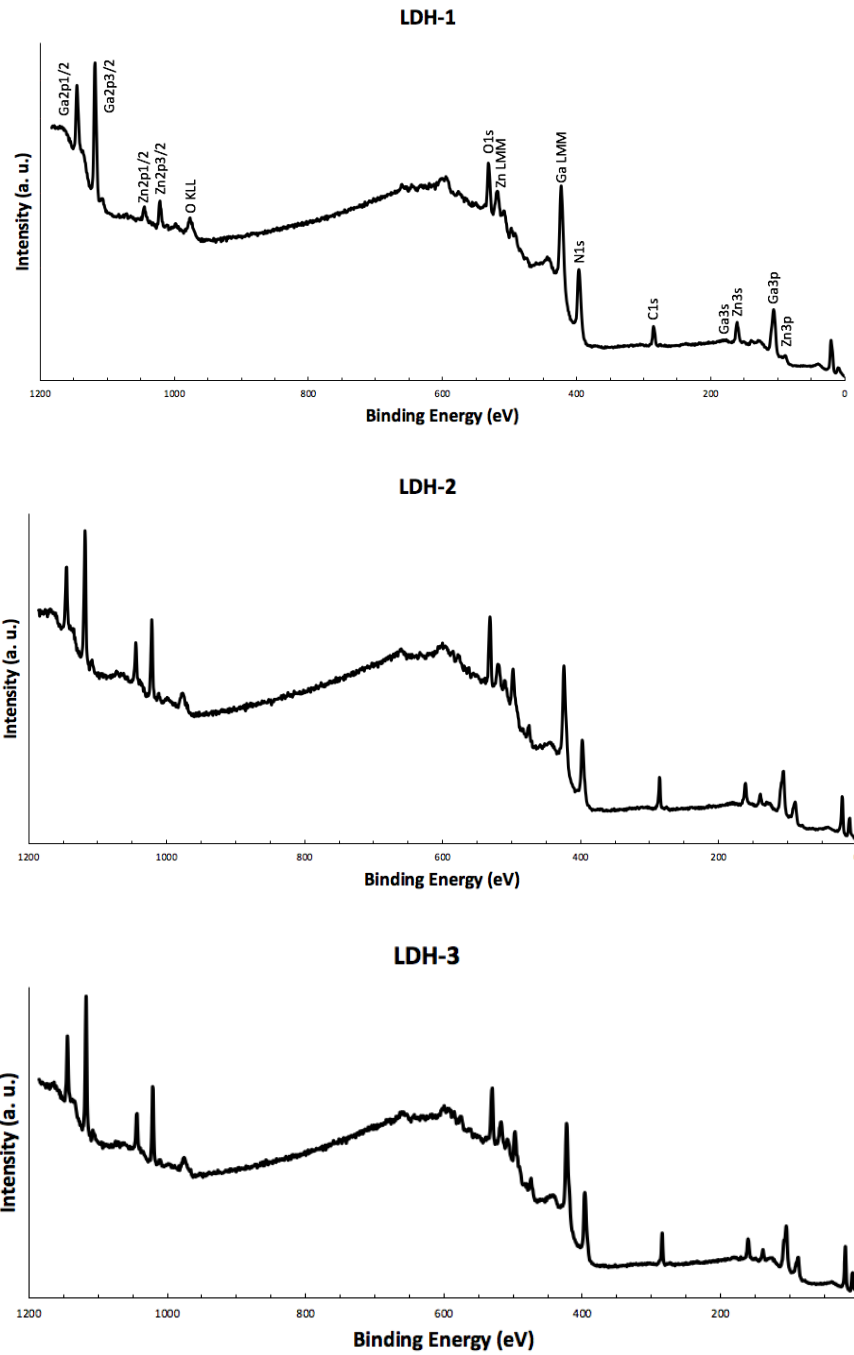


Figure B.7.8: Hydrogen evolution of the 3 wt% Pt-GaN:ZnO solid solution under visible light irradiation from pure water. All samples were prepared at 800 W for 12 min.

Appendix C : Surface and bulk elemental composition of nanoporous GaN:ZnO samples

C.1 XPS spectra



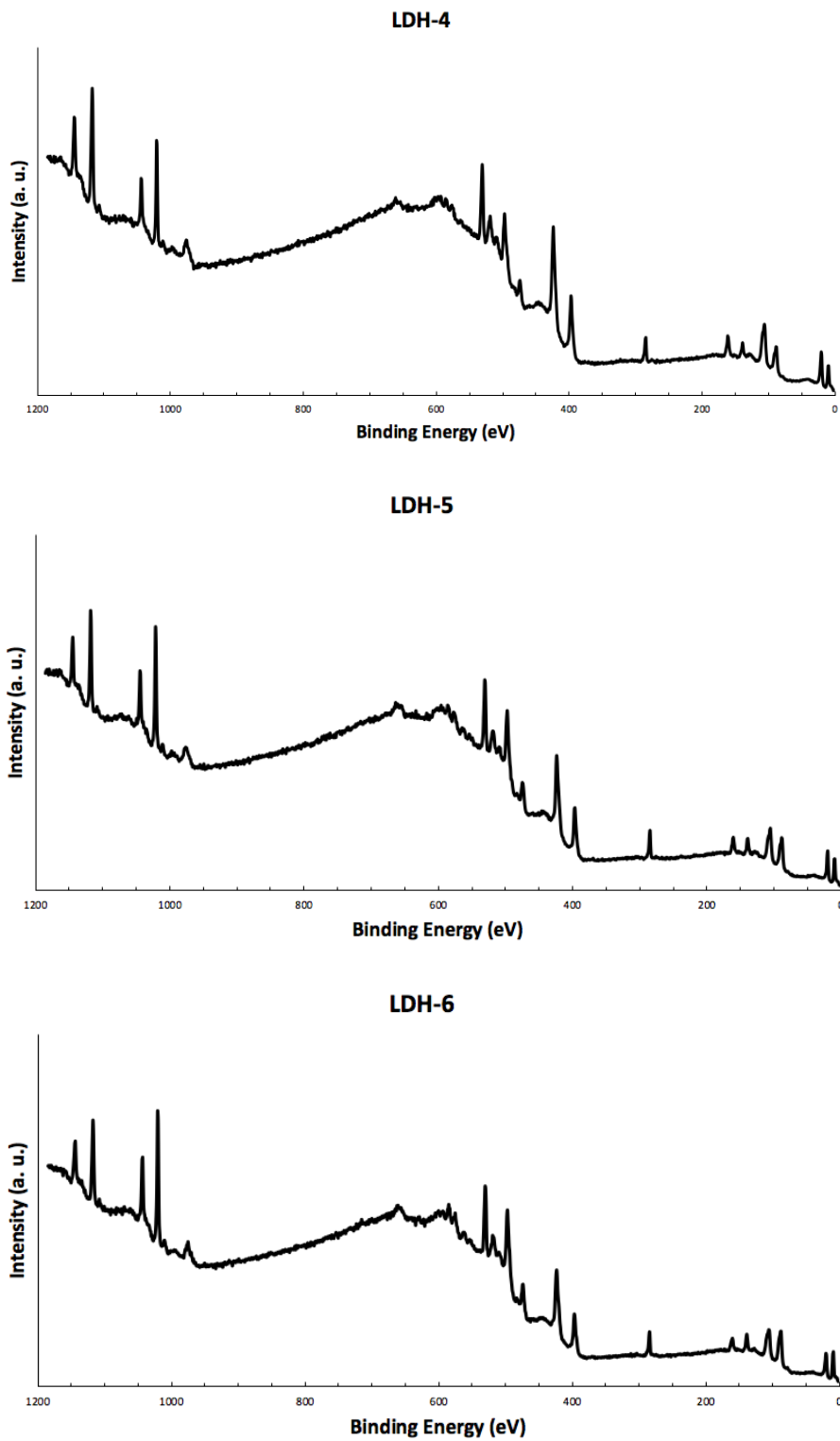
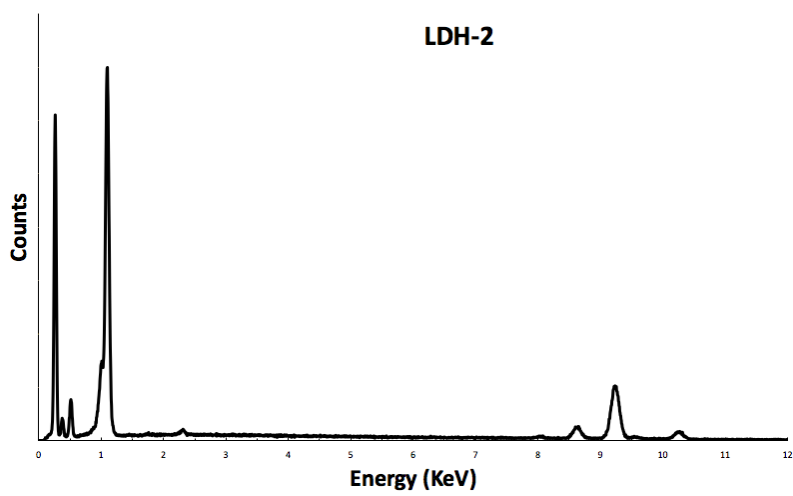
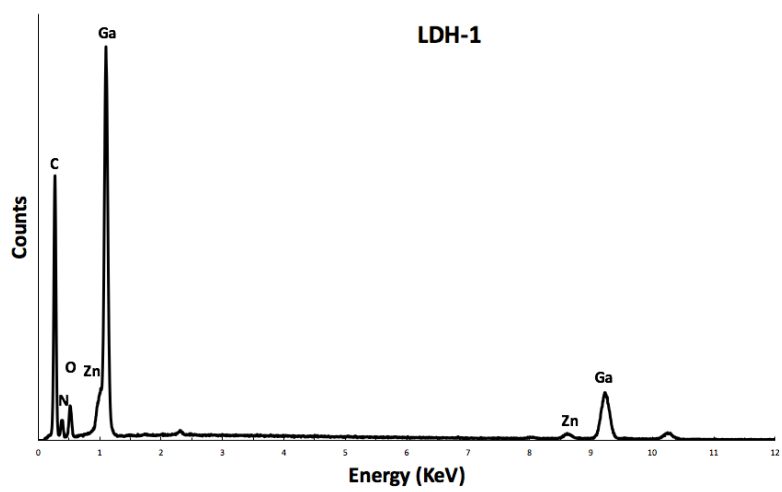


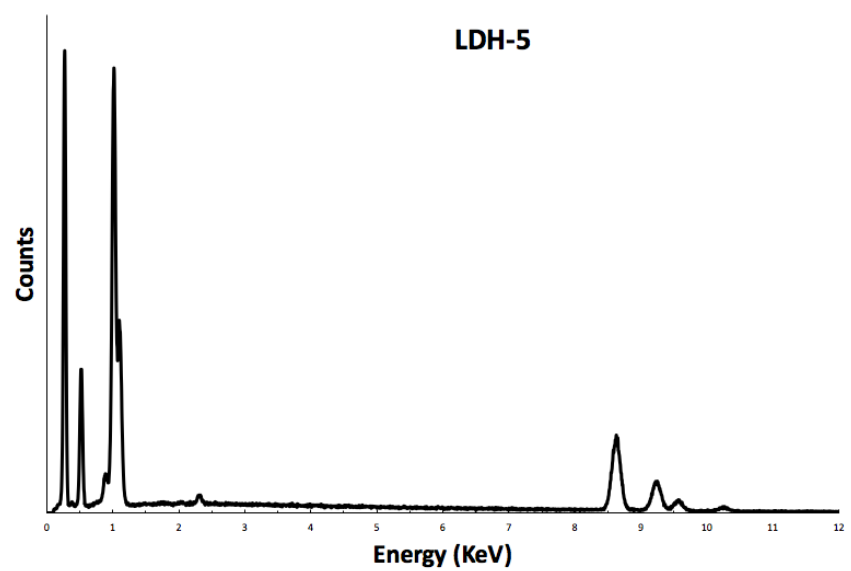
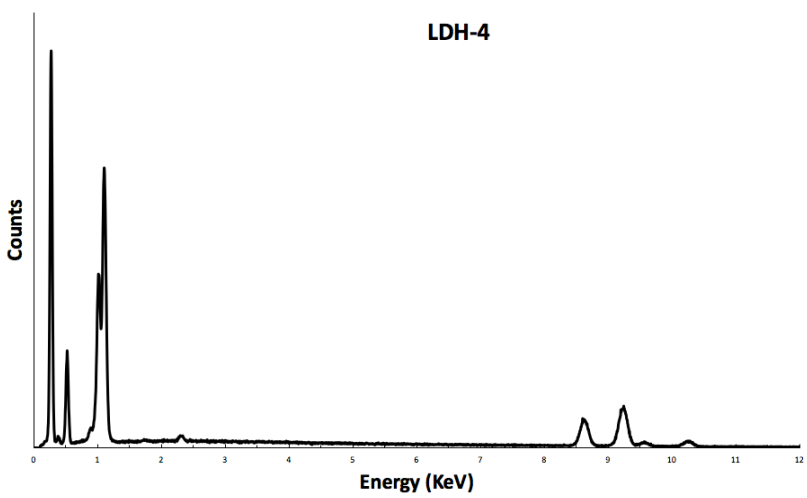
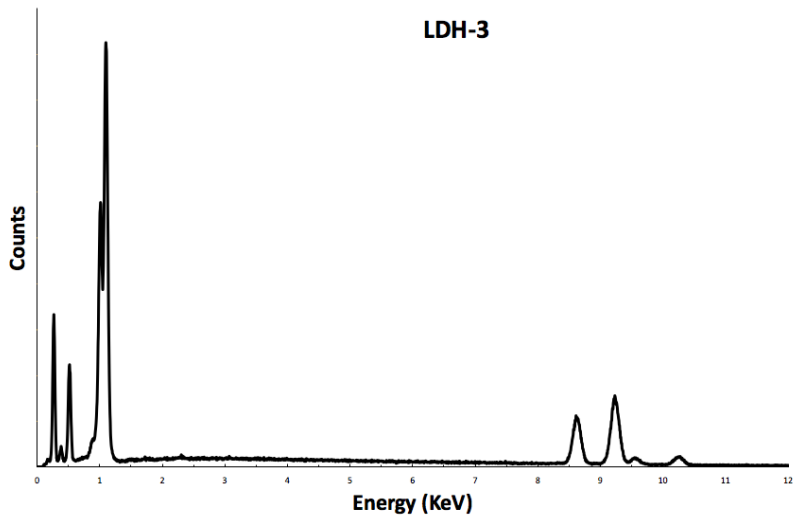
Figure C.7.9: XPS spectra of LHD-1 to LDH-6 photocatalysts. Surface x values are presented in Table 3.3.

Table C.1: Surface composition of prepared photocatalysts obtained by XPS.

Elements	LDH-1	LDH-2	LDH-3	LDH-4	LDH-5	LDH-6
N	35.32	32.86	35.4	29.52	31.31	28.37
O	35.39	36.02	39.05	43.97	42.34	44.02
Ga	25.23	24.78	17.83	17.12	13.5	12.92
Zn	4.06	6.34	7.72	9.39	12.85	14.69

C.2 EDX spectra





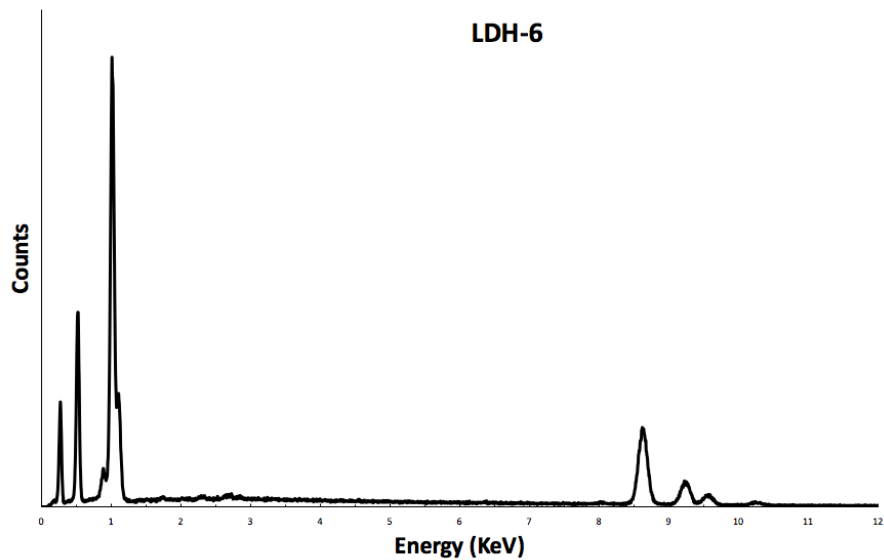


Figure C.7.10: EDX spectra of LHD-1 to LDH-6 photocatalysts.

Table C.2: Summary of the EDX bulk elemental analysis.

Elements	LDH-1	LDH-2	LDH-3	LDH-4	LDH-5	LDH-6
N	29.63	28.16	21.36	12.99	13.34	8.79
O	25.99	29.16	35.29	45.35	39.42	48.11
Ga	37.49	33.53	29.34	25.58	21.26	14.67
Zn	6.89	9.15	14.01	16.08	25.98	28.43

Appendix D : Cost analysis and scalability

In this Appendix, a brief cost analysis is conducted based on the synthesis routes described in Chapter 2 for nanoporous ($x = [\text{Zn}]/[\text{Zn}+\text{Ga}]$ in LDHs = 0.20) and traditional GaN:ZnO solid solutions. The prices of chemicals and gaseous ammonia were obtained from Sigma Aldrich Canada¹ and Praxair². The price of electricity was considered equal to the basic BC Hydro³ rate (8.29 cents per kWh). Table D.3 and Table D.4 summarize the amount of materials used for fabrication of the nanoporous and traditional GaN:ZnO photocatalysts, along with the total cost for one batch.

Table D.3: Amount of materials and their cost per batch of the nanoporous GaN:ZnO solid solution synthesis.

Materials	Used (mmol)	Used (g)	Unit mass (g)	Unit price (CAD)	Price (CAD/g)	Cost of materials (CAD/batch)
Ga ₂ O ₃	5.00	0.937	50.0	455.0	9.100	8.53
ZnO	2.50	0.204	250.0	40.5	0.162	0.03
Zn	2.50	0.163	250.0	41.5	0.164	0.03
CO(NH ₂) ₂	78.00	4.684	500.0	78.7	0.157	0.73
Na ₂ CO ₃	0.16	16.960	500.0	107	0.214	3.62
NaOH	0.32	12.800	500.0	98.6	0.197	2.52
HCL	26.0 (mL)	-	2.5 (L)	157.0	0.062 (CAD/ml)	1.61
Material cost per batch =						17.07 CAD

¹ <http://www.sigmaaldrich.com/canada-english.html> (accessed on October 2016)

² <http://www.praxair.com> (accessed on October 2016)

³ <https://www.bchydro.com/news/conservation/2012/kilowatt-hour-explained.html> (accessed on October 2016)

Table D.4: Amount of materials and their cost per batch of the traditional GaN:ZnO solid solution synthesis.

Materials	Used (mmol)	Used (g)	Unit mass (g)	Unit price (CAD)	Price (CAD/g)	Cost of materials (CAD/batch)
Ga ₂ O ₃	5.75	1.080	50.0	455.0	9.100	9.83
ZnO	11.50	0.940	250.0	40.5	0.162	0.15
NH ₃ gas	195.0 (L)	-	1260 (L)	579.0	0.460 (CAD/L)	89.70
Material cost per batch =						99.68 CAD

Table D.5: Cost of electricity for preparation of one batch of nanoporous and traditional solid solution photocatalysts.

Type of furnace	Power (kW)	Pre-heating period (min)	Synthesis time (min)	Synthesis energy cost (CAD)
Muffle furnace	1.0	90	12	0.14
Tube furnace	3.0	45	780	3.42

Table D.6: Total cost of synthesis of per gram of photocatalyst through urea-assisted technique proposed in this research and traditional solid-state reaction.

Synthesis	Material cost (CAD/batch)	Electrical cost (CAD/batch)	Obtained photocatalyst (g)	Synthesis cost (CAD/g)
Nanoporous	17.07	0.14	1.1	15.64
Traditional	99.68	3.42	1.3	79.31

Table D.5 compares the cost of the electrical energy required for the processing of precursor materials between the 12-min urea-assisted route and the traditional method. Table D.6

summarizes the total synthesis cost per gram of the photocatalyst material. Our analysis indicates that the preparation cost of the nanoporous photocatalyst is less than 20% of that for the traditional GaN:ZnO. From Table D.4 it is clear that the high cost of preparation for the traditional solid solution is attributable to its high consumption of ammonia gas (about 90% of the cost per batch). This cost can be significantly reduced by performing the traditional solid-state synthesis at compositional ranges closer to the reaction stoichiometry. For instance, the fabrication can be practiced in sealed ampoules or using low gas flow rates in reactors with smaller dimensions (hydrodynamics modifications).

Due to instrumental limitations and the high cost of the experiments, kilogram-scale fabrication of photocatalysts was not practiced in this research. Assuming that the kinetics of the solid-state reaction can support the kilogram scale, the following notes can be considered for scalability of the proposed and traditional synthesis routes:

- 1) It is apparent that the traditional solid-state technique cannot support large-scale production at this stage unless the rate of NH_3 consumption is reduced significantly.
- 2) The urea-assisted synthesis can be readily utilized for kilogram-scale production, as the synthesis can be performed in continuous rotary kilns, which enhance the mass transfer and have high heating rates. This process has been practiced widely for the tone-scale processing of minerals at high temperatures ($>1100\text{ }^\circ\text{C}$), such as in the cement industry.
- 3) The processes described in this research can be performed readily at a large scale, such as ball-milling (available at tone scale in the cement industry) as well as the solution-based preparation of LDHs and aging (available at tone scale in pharmaceutical industry).
- 4) Regardless of the fabrication method, the gaseous off-products must be handled properly due to the high concentration of hazardous ammonia and cyanides.

Appendix E : Morphology of the ZnO NWs impregnated with Ga³⁺ using concentrated Ga salt solution

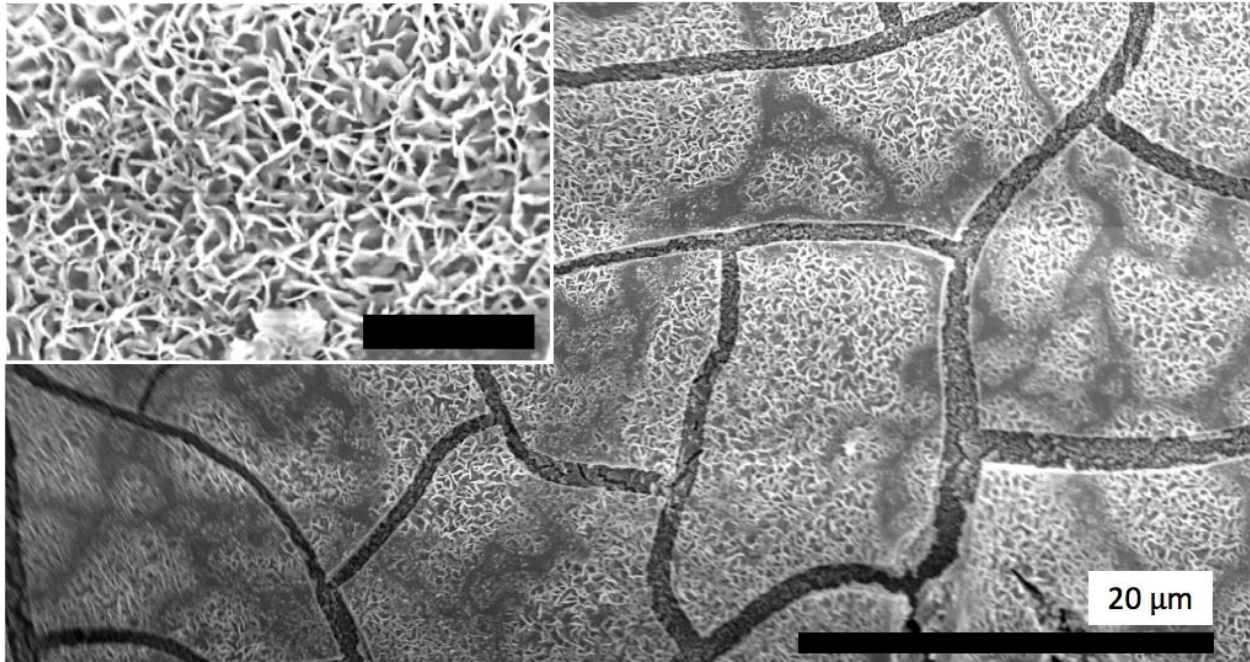


Figure E.7.11: Low resolution SEM image of the ZnO thin film impregnated with concentrated (35 mM) Ga(NO₃)₃.xH₂O solution. Inset shows the high resolution SEM micrograph of the continuous film, scale bar = 3 μm.

Appendix F : Morphology of the samples obtained through experiments described in Table 6.2: Direct growth of Zn-Ga NWs

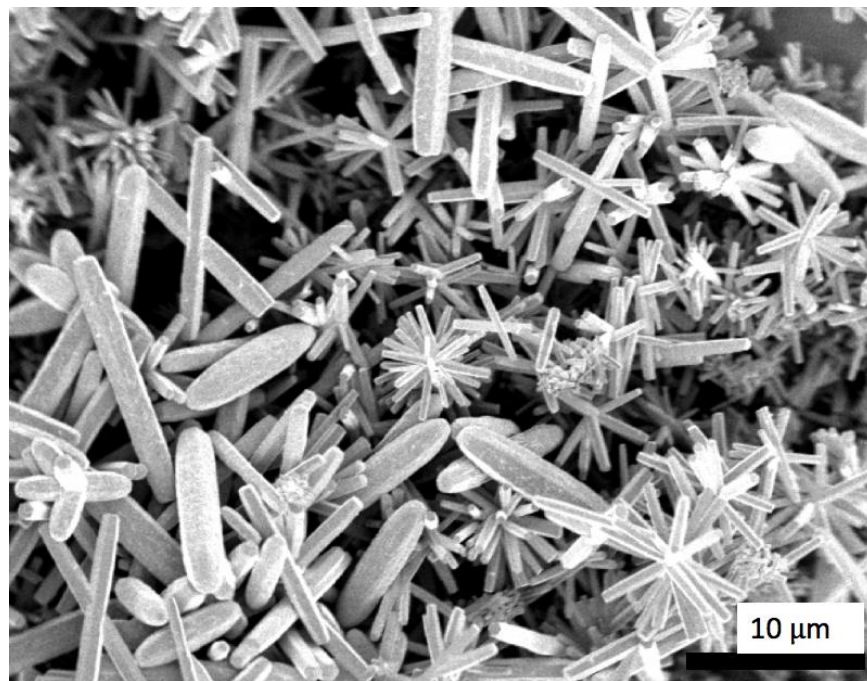


Figure F.7.12: SEM image of the structures precipitated inside the growth solution during chemical bath growth in HMT solution using zinc nitrate as Zn source (entry 1 in Table 6.2).

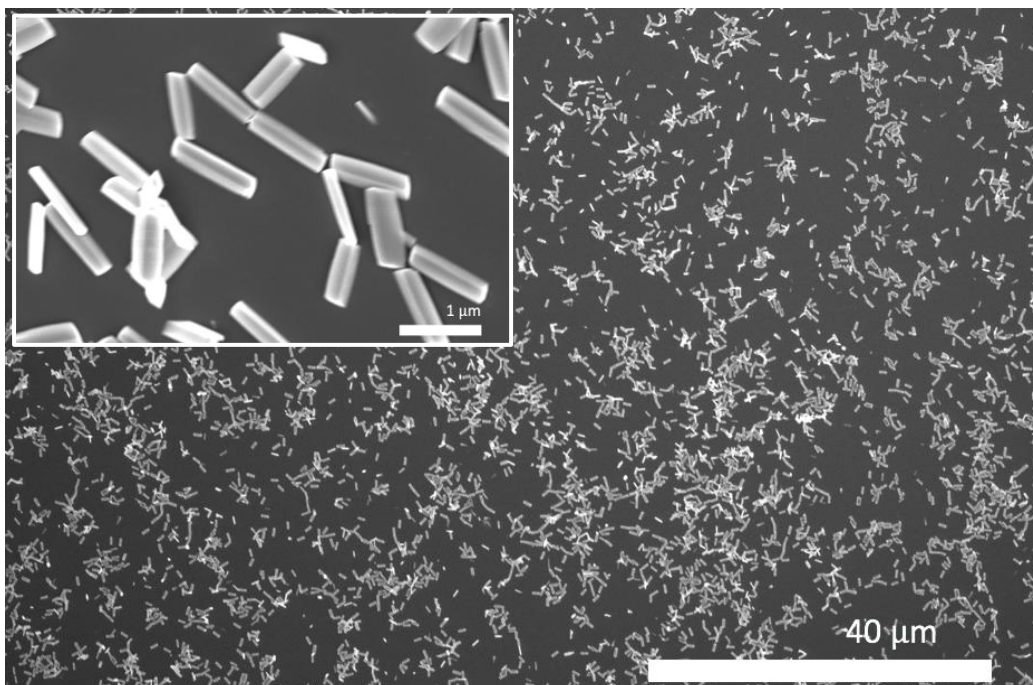


Figure F.7.13: SEM image of the structures precipitated inside the processing solution during chemical bath growth in HMT solution using zinc acetate as the Zn source (entry 2 in Table 6.2). Inset shows the high resolution SEM image of the precipitates.

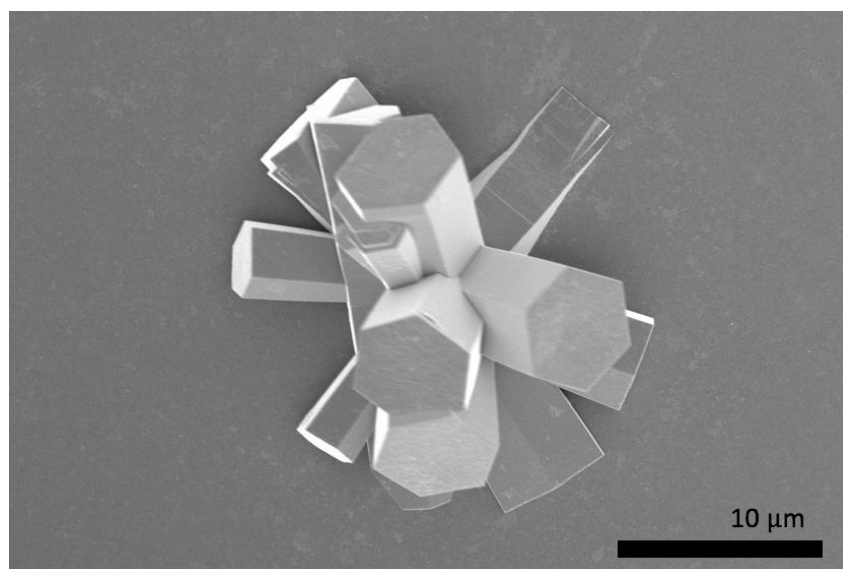


Figure F.7.14: SEM image of the structures observed on the ZnO-seeded quartz substrate during chemical bath growth in HMT solution using zinc acetate as the Zn source (entry 2 in Table 6.2).

Appendix G : Substrates orientation for epitaxial APCVD growth of 1-D nanostructures

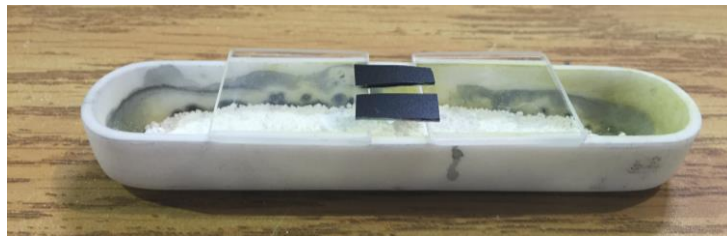


Figure G.7.15: Face-down substrates layout at $D = 0$.

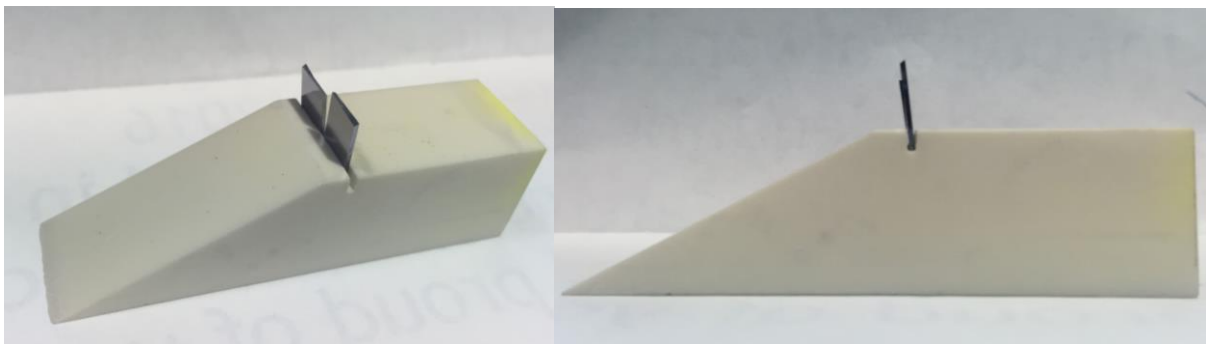


Figure G.7.16: APCVD substrate holder.

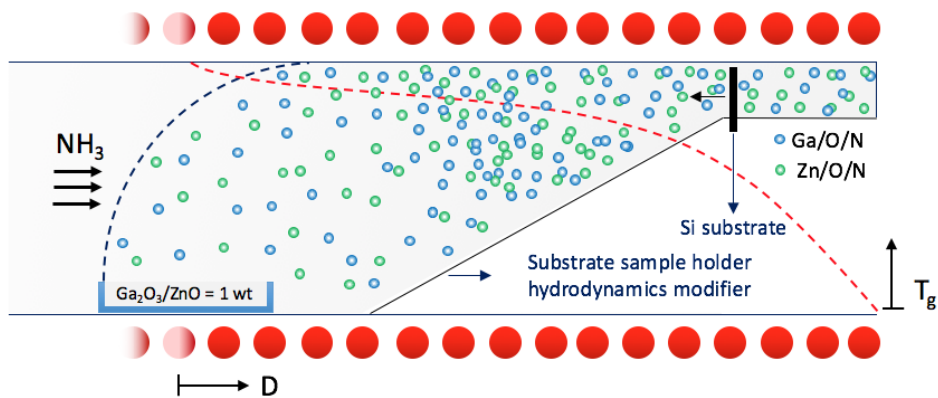


Figure G.7.17: Schematic illustration of the chemical vapor deposition hydrodynamics modification to enhance the density of the building blocks in the growth region using the vertical sample holder.

Appendix H : Formation of catalysts liquid droplets at different temperatures

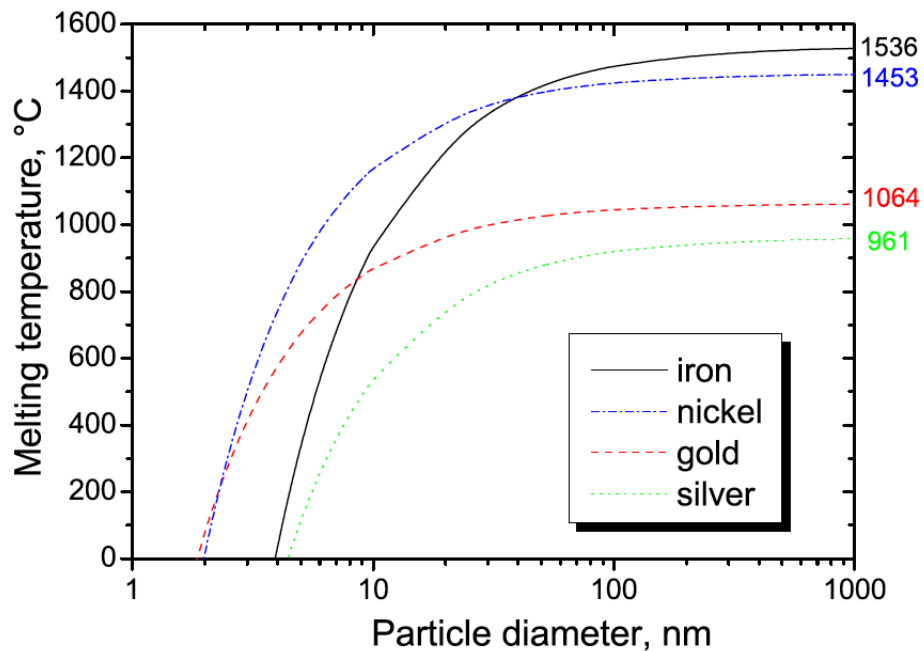


Figure H.7.18: Dependency of metal particles diameter to their melting temperature [296]. Reprinted with permission from (J. Phys.: Condens. Matter 15 (2003) S3011–S3035). Copyright (2006) IOP Science.